

https://dspace.org/

An Empirical Study and Application of Machine Learning to Assess the Impact of Wearable Devices Exposure on Humans in Underground Mine Environment

Ashraf, Muhammad Ahsan

2024
University of the Witwatersrand, Johannesburg
https://hdl.handle.net/10539/47633

Ashraf, Muhammad Ahsan . (2024). An Empirical Study and Application of Machine Learning to Assess the Impact of Wearable Devices Exposure on Humans in Underground Mine Environment [PhD thesis, University of the Witwatersrand, Johannesburg]. WIReDSpace. https://hdl.handle.net/10539/47633

Downloaded from a DSpace repository. https://dspace.org/

University of the Witwatersrand

PHD THESIS

An Empirical Study and Application of Machine Learning to Assess the Impact of Wearable Devices Exposure on Humans in Underground Mine Environment

Author:
Muhammad Ahsan Ashraf

Supervisor: Professor Turgay Celik

School of Electrical and Information Engineering

November 26, 2024



Declaration

I, **Muhammad Ahsan Ashraf**, declare that this Dissertation titled, "**An Empirical Study and Application of Machine Learning to Assess the Impact of Wearable Devices Exposure on Humans in Underground Mine Environment**" and the work presented in it are my own. I confirm that:

- This work was done wholly or mainly while in candidature for a research degree at this University.
- Where any part of this thesis has previously been submitted for a degree or any other qualification at this University or any other institution, has been clearly stated.
- Where I have consulted the published work of others, this is always clearly attributed.
- Where I have quoted from the work of others, the source is always given. With the exception of such quotations, this dissertation is entirely my own work.
- I have acknowledged all main sources of help.

Signed: 

Date: 27/11/2024

Abstract

The deployment of wearable wireless devices plays a crucial role in monitoring and enhancing the health and safety of underground miners. The widespread use of these devices has driven a significant expansion in their application, emphasizing the need to prioritize miners' health and well-being in underground environments. Wearable wireless devices rely on radio-frequency electromagnetic fields (RF-EMF) to transmit and receive signals. The proximity of RF-EMF to the human body in the confined spaces of underground mines has raised significant concerns about potential health risks, particularly due to the combination of limited space, elevated temperatures, and prolonged device usage. Therefore, investigating RF-EMF exposure in underground mining settings is imperative to assess its potential health effects. Non-Ionizing Radiation Protection (ICNIRP) regulates RF-EMF exposure regarding specific absorption rate (SAR) and temperature elevation in the tissues. This study assesses the impact of RF-EMF exposure for a widely adopted wearable device and IoT module, specifically the ESP32-WROOM employing a meandered inverted F-shape antenna (MIFA), within underground mine environments. The SAR was evaluated for MIFA at 2.4 GHz using a 4 mm human model for different mounting positions, distance between MIFA and body, power level, underground mine structure, and rock properties. Additionally, the study explores the temperature elevation in tissues caused by prolonged RF-EMF exposure, taking into account the varying temperatures and exposure durations typical of the underground mine environment. Furthermore, machine learning (ML) and deep learning models were incorporated to predict SAR and temperature elevation in tissues for different variations of associated exposure parameters. The experimental measurements were conducted for wearable devices in a mock mine tunnel using the Cornet ED88TPLUS RF-EMF Meter. The study concluded that (1) SAR remained below ICNIRP limits when the wearable device was positioned 12 mm away from the body, indicating that this distance is safe for minimizing RF-EMF exposure. (2) It was also found that the wrist is the optimal location for mounting the wearable device on a miner's body, outperforming torso placements in minimizing RF-EMF exposure. (3) The study further observed that RF-EMF exposure levels slightly increase due to the confined space of the underground mine environment, with marginal variation across different simulated rock properties. Therefore, it is recommended that ICNIRP limits be maintained in these settings

to mitigate RF-EMF exposure. (4) The primary contributor to temperature elevation in tissues was found to be the ambient temperature of the underground mine. However, the temperature rise due to RF-EMF exposure from the wearable device remained below ICNIRP limits for all simulated scenarios. (5) Additionally, temperature elevation increased exponentially, reaching its peak after one hour of continuous exposure under the same conditions. (6) The study also concluded that ML and deep learning models can predict SAR and temperature elevation, providing a fast and accurate solution for estimating RF-EMF exposure. Integrating these models into wearable devices could enable real-time RF-EMF exposure assessments, eliminating the need for separate equipment to measure the exposure. Further measurements were conducted at various distances from the wearable device, with power densities assessed to confirm that a 10 mm distance provides a secure buffer. Assessing RF-EMF exposure in underground mining environments offers valuable insights for enhancing risk management strategies and minimizing health risks associated with RF-EMF exposure.

Acknowledgements

I want to express my deep gratitude to Professor Turgay Celik for his guidance, enthusiastic encouragement, and valuable critiques during the planning and development of this research work. I am also grateful to Dr. Ahsan Mahboob, Head of the Sibanye-Stillwater Digital Mining Laboratory (DigiMine), for providing general guidance and data related to this research. I want to express my sincere gratitude to Mr. Alex Fenn, Head of Innovation at Sibanye-Stillwater, for his invaluable guidance and support during the initial stage of this research.

The author wants to thank and acknowledge the financial support provided by the Sibanye-Stillwater Digital Mining Laboratory (DigiMine), Wits Mining Institute.

Contents

Declaration i

Abstract ii

Acknowledgements iv

Contents v

List of Figures x

List of Tables xiv

Abbreviations xvi

Publications xvii

1 Introduction 1
- 1.1 Introduction . . . 1
- 1.2 The Need for Exposure Evaluation . . . 4
- 1.3 Effects of RF-EMF Exposure on Human Body Tissue . . . 4
  - 1.3.1 Thermal Effects . . . 6
  - 1.3.2 Non-Thermal Effects . . . 6
- 1.4 Contribution and Novelty of the Research . . . 7
- 1.5 Research Questions . . . 8
- 1.6 Objectives of the Research . . . 9
- 1.7 Thesis Outline . . . 11

2 Background: Literature Review 12
- 2.1 Wireless Communication Systems in Underground Mine . . . 13
  - 2.1.1 Wireless Propagation in Underground Mine . . . 14
  - 2.1.2 Wearable Wireless Devices in Underground Mines . . . 14
- 2.2 Related EM Quantities and Reference Levels . . . 18
  - 2.2.1 Specific Absorption Rate . . . 18
  - 2.2.2 Temperature Elevation in the Human Tissues . . . 20
  - 2.2.3 Fundamental Aspects of Bioheat Transfer . . . 21
  - 2.2.4 Pennes Model of the Bioheat Equation (BHE) . . . 22
  - 2.2.5 RF Exposure Restrictions and Reference Levels . . . 23
  - 2.2.6 RF Exposure Restriction for Underground Mines . . . 25
- 2.3 Classification of Studies Concerning RF-EMF Exposure Evaluation 26

2.3.1 Literature of RF-EMF Exposure in Confined Environment . 27
2.4 Conclusion of Literature 33
2.5 Research Gaps 42
2.6 Commercial EM Simulation Packages 44
2.6.1 High-Frequency Simulation Software (HFSS) 45
2.7 Packages for Human body Model 46

3 Methodology to Assess RF-EMF Exposure of Wearable Device 48
3.1 Research Methodology 48
3.2 Numerical Simulation and Predictions using ML Techniques 48
3.2.1 Methodology for Objective 1 50
3.2.2 Methodology for Objective 2 50
3.2.3 Methodology for Objective 3 51
3.2.4 Methodology for Objective 4 51
3.2.5 Methodology for Objective 5 52
3.2.6 Methodology for Objective 6 53
3.3 Methodology for Measurements 53
3.4 Ethical Clearance for Research 53
3.5 Considerations of Body Mounting Positions for Assessing RF-EMF Exposure from Wearable Devices 54
3.6 Human Body Model: Overview and Properties 56
3.7 Overview of the Approach Implemented for Systematic Evaluation of RF-EMF Exposure via Numerical Simulation 57
3.8 Summary 58

4 SAR Assessment for Wearable Devices 61
4.1 Introduction 61
4.2 Numerical Model of the Wearable Device 61
4.2.1 Performance Evaluation of MIFA 63
4.3 Exposure Assessment for a Wearable Device in a Free Space Environment 65
4.3.1 SAR for Wrist in a Free Space Environment 66
4.3.2 SAR for Waistline in a Free Space Environment 66
4.3.2.1 SAR for Wearable Device Positioned at the Side of the Waist in Free Space Environment 69
4.3.2.2 SAR for Wearable Device Positioned at the Back of the Waist in Free Space Environment 70
4.4 SAR Variability for Parameter Variations of RF-EMF Source 72
4.4.1 Analysis of SAR Variation with Distance between Antenna and Tissues 73
4.4.2 Transmitting Power and SAR variability 74
4.4.3 Device Orientation and SAR variability 75
4.5 SAR Assessment in Tunnel Environments: Analysis and Findings . 77
4.5.1 SAR for Wearable Device Positioned on the Wrist in Tunnel Environment 79

4.5.2 SAR for Waistline in tunnel . . . 80
4.5.2.1 SAR for Wearable Device Positioned on the Side of the Waist in Tunnel Environment . . . 80
4.5.2.2 SAR for Wearable Device Positioned on the Back of the Waist in Tunnel Environment . . . 80
4.5.3 Investigating SAR Variability in Relation to Tunnel Parameters . . . 81
4.5.3.1 SAR Variability Across Different Tunnel Properties 82
4.5.3.2 Impact of Distance on SAR Variability Between Wearable Devices and Tunnel . . . 84
4.6 Conclusion . . . 85

5 Assessment of Temperature Elevation in Tissues Induced by Wearable Device Exposure in Underground Mine Environment 87
5.1 Introduction . . . 87
5.2 Steady State Thermal Analysis of the Wearable Device Exposure . 87
5.2.1 Steady State Thermal Analysis for Wrist Position of the Wearable Device . . . 88
5.2.2 Steady state Thermal Analysis for Waistline Position of the Wearable Device . . . 89
5.2.3 Comparison of Steady-State Thermal Results from Wearable Device Exposure . . . 92
5.3 Transient Thermal analysis of the wearable device exposure . . . 94
5.3.1 For 1 hour of RF-EMF exposure . . . 95
5.3.2 For 5 hours of exposure . . . 97
5.3.3 For 8 hours of exposure . . . 97
5.4 Comparison of the Results . . . 99
5.5 Conclusion . . . 100

6 Background: Supervised Machine Learning 102
6.1 Introduction . . . 102
6.2 Supervised Machine Learning . . . 103
6.2.1 Performance Metrics of Supervised ML Models . . . 105
6.2.1.1 Root Mean Square Error . . . 106
6.2.1.2 Mean Absolute Error . . . 106
6.2.1.3 R-squared Error . . . 107
6.3 Supervised Learning Regression Models . . . 107
6.3.1 Linear Regression . . . 107
6.3.1.1 Learning Model . . . 108
6.3.2 K Nearest Neighbors . . . 109
6.3.3 Support Vector Machines . . . 111
6.3.4 Random Forest . . . 112
6.3.5 XGBoost . . . 113
6.4 Issues of Supervised Learning Algorithms . . . 115
6.5 Deep Learning Models . . . 115

6.5.1 Convolutional Neural Network (CNN) . . . 116
6.5.2 Recurrent Neural Network (RNN) . . . 117
6.5.3 Long short-term memory (LSTM) . . . 117
6.5.4 Fully Connected Neural Network (FCNN) . . . 118

7 Prediction of SAR & Temperature Elevation in Tissues using Machine Learning 120
7.1 Introduction . . . 120
7.2 Consideration of RF-EMF Exposure Parameters for Machine Learning 121
7.2.1 Parameters for SAR Predictions . . . 121
7.2.2 Parameters for Temperature Elevation Predictions . . . 122
7.3 Data Collection and Preprocessing . . . 122
7.3.1 For SAR Predictions . . . 122
7.3.2 For Temperature Elevation Predictions . . . 124
7.4 Implementation of Machine Learning Models for SAR Prediction . . 124
7.4.1 Data Splitting for Machine Learning Models . . . 124
7.4.2 Grid Search for Hyper Parameter Tuning . . . 125
7.4.3 Random Forest for SAR Predictions . . . 126
7.4.4 XGBoost for SAR Predictions . . . 128
7.4.5 K Nearest Neighbor for SAR Predictions . . . 130
7.4.6 Linear Regression for SAR Predictions . . . 130
7.4.7 Support Vector Machine for SAR Predictions . . . 131
7.4.8 CNN for SAR Predictions . . . 132
7.4.9 LSTM for SAR Predictions . . . 133
7.4.10 FCNN for SAR Predictions . . . 133
7.4.11 RNN for SAR Predictions . . . 134
7.4.12 CNN-LSTM for SAR Predictions . . . 134
7.4.13 T-Test for SAR Predictions . . . 135
7.5 Implementation of Machine Learning Models for Prediction of Maximum Temperature Elevation in Tissues . . . 139
7.5.1 Data Splitting for Machine Learning Models . . . 139
7.5.2 Random Forest for Temperature Elevation Predictions . . . 139
7.5.3 XGBoost for Temperature Elevation Predictions . . . 141
7.5.4 K Nearest Neighbor for Temperature Elevation Predictions . 142
7.5.5 Linear Regression for Temperature Elevation Predictions . . 143
7.5.6 Support Vector Machine for Temperature Elevation Predictions . . . 144
7.5.7 CNN for Temperature Elevation Predictions . . . 144
7.5.8 LSTM for Temperature Elevation Predictions . . . 145
7.5.9 FCNN for Temperature Elevation Predictions . . . 146
7.5.10 RNN for Temperature Elevation Predictions . . . 146
7.5.11 CNN-LSTM for SAR Predictions . . . 146
7.5.12 T-Test for Temperature Elevation Predictions . . . 147
7.6 Conclusion . . . 149

8 Measurement of RF-EMF Exposure of Wearable Device 152
8.1 Addressing the Gap for Comprehensive RF-EMF Exposure Measurement . . . 152
8.1.1 Schematic and Prototyping of the Wearable Device . . . 153
8.2 Components of the Wearable Device . . . 153
8.3 Measurements of RF-EMF Exposure . . . 156
8.3.1 Data Collection Procedure . . . 157
8.3.2 Consideration of Measurement Environment for RF-EMF Exposure Assessment . . . 157
8.3.3 Measurement Campaign . . . 158
8.3.4 Analysis of Measured Data . . . 158
8.3.5 Evaluation of Simulated Power Densities . . . 162
8.3.6 Analytical Calculation of Power Densities . . . 163
8.3.7 Comparison of Results . . . 164
8.4 Conclusion . . . 166

9 Conclusion 168
9.1 Key Findings and Insights: Addressing the Research Questions . . . 168
9.2 Improving Mining Safety: Insights from RF-EMF Exposure . . . 173
9.3 Limitation of the Research . . . 174
9.4 Future Directions . . . 175

List of Figures

2.1 Classification of methodologies for evaluating RF-EMF exposure . . 26
2.2 Human Body Model available in Ansys HBM package with male 4 mm resolution (left), female 4 mm resolution (center), and Neva VPH 3.0 female (right) 47

3.1 Flow chart of research methodology for numerical simulation and ML models. 49
3.2 Flow chart of research methodology for measurements 54
3.3 Different mounting positions of MIFA for evaluation of RF-EMF exposure, the box represents the part of the body selected for evaluation to reduce computation time. 56
3.4 System-level diagram of the Ansys Workbench used for RF-EMF exposure evaluation in underground mine environment in terms of (a) SAR, and (b) temperature elevation in tissues. 59

4.1 Dimensions (in millimeters) of the numerical model depicting the meandered inverted-F antenna (MIFA). 63
4.2 Reflection coefficient (S_{11}) of the MIFA at 2.4 GHz. 64
4.3 Far field radiation pattern of the MIFA at 2.4 GHz (a) 3D far-field radiation pattern and (b) 3D far-field pattern with antenna structure. 64
4.4 Performance parameters of the MIFA at 2.4 GHz (a) voltage standing wave ratio and (b) surface current density. 65
4.5 Simulation setup for wrist (a) MIFA mounted on the wrist of the human body (left), close side view representing the distance between skin and antenna (right) and (b) mesh view of the wrist. 67
4.6 Distribution of the electric field on the wrist at a frequency of 2.4 GHz. 67
4.7 Spatial distribution of SAR_{10g} on the wrist at 2.4 GHz. 68
4.8 Simulation setup of the MIFA on the side of the waistline. 70
4.9 Simulation results for MIFA placed on the side of the waistline (a) E field distribution and (b) SAR_{10g} 70
4.10 Simulation setup when MIFA is placed (a) on the backside of the waistline (b) simulated mesh of the scenario 71
4.11 Simulation results for MIFA placed on the backside of the waistline (a) E field distribution and (b) SAR_{10g} 71
4.12 SAR variability to the distance between antenna and tissue for MIFA placement on Wrist and Waistline. 74
4.13 SAR variability with different power levels for MIFA placement on wrist and waistline. 75

4.14 SAR variability with respect to antenna orientation for MIFA placement on wrist and waistline. 76
4.15 Processing of the LIDAR scanned model of the Wits mock mine tunnel. 78
4.16 Simulation setup of the MIFA on the wrist for the tunnel. 79
4.17 Simulation setup of the MIFA on the side of the waistline for the tunnel. 80
4.18 Simulation setup of the MIFA on the backside of the waistline for the tunnel. 81
4.19 SAR variability with permittivity of the rock for MIFA placement on wrist and waistline 83
4.20 SAR variability with the distance between body and tunnel structure for wrist and waistline scenarios. 84

5.1 Meshing of mechanical solver for the wrist scenario 89
5.2 HFSS imported loss in the mechanical solver for the wrist scenario . 89
5.3 Thermal distribution on the wrist at 30^0 C ambient temperature . . 90
5.4 Meshing of mechanical solver for the waistline side scenario 91
5.5 HFSS imported loss in the mechanical solver for the waistline side scenario 91
5.6 Thermal distribution for the waistline side scenario at 30^0 C ambient temperature 92
5.7 HFSS imported loss in the mechanical solver for the waistline side scenario 92
5.8 Temperature distribution of the MIFA antenna positioned on the back of the waistline at an ambient temperature of 30^0 C 93
5.9 Time vs. temperature variation in the skin tissues of the wrist for exposure of 1 hour with the ambient temperature of 40^0 C 96
5.10 Time vs. temperature variation in the skin tissues of the waistline for 1 hour with an ambient temperature of 40^0 C 96
5.11 Time vs. temperature variation in the skin tissues of the wrist for 5 hours with an ambient temperature of 40^0 C 97
5.12 Time vs. temperature variation in the skin tissues of the waistline for 5 hours with an ambient temperature of 40^0 C 98
5.13 Time vs. temperature variation in the skin tissues of the wrist for exposure of 8 hours with ambient temperature of 40^0 C 98
5.14 Time vs. temperature variation in the skin tissues of the waistline for 8 hours with an ambient temperature of 40^0 C 99

6.1 Major categories of machine learning. 103
6.2 Supervised machine learning model. 103
6.3 Types of Supervised machine learning. 104
6.4 Categories of the regression. 105
6.5 Linear regression. 108
6.6 Illustration of KNN regression for (a) K = 1 and (b) K = 5 110

6.7 Illustration of support vector regressor with radial basis function kernel function for epsilon (a) 0.01 and (b) 0.1 112
6.8 Random Forest Regressor with 100 tree estimators. 113
6.9 Example of the CNN model showcasing multiple layers, including the input and output sizes for each layer. 116
6.10 Example of the RNN model showcasing multiple layers, including the input and output sizes for each layer. 117
6.11 Example of the LSTM model showcasing multiple layers, including the input and output sizes for each layer. 118
6.12 Example of the FCNN model showcasing multiple layers, including the input and output sizes for each layer. 119

7.1 Feature importance for the prediction of SAR for Random Forest . 128
7.2 Feature importance for the prediction of SAR for XGBoost 129
7.3 Error between actual and predicted value of SAR for t-test when (a) random forest, (b) XGBoost, (c) KNN, (d) linear regression and (e) SVM models were used. 137
7.4 Error between the actual and predicted SAR values for the t-test across different deep learning models: (a) CNN, (b) LSTM, (c) FCNN, (d) RNN, and (e) CNN-LSTM. 138
7.5 Feature importance for the prediction of maximum temperature elevation for Random Forest 141
7.6 Feature importance for the prediction of temperature elevation for XGBoost 142
7.7 Error between actual and predicted value of temperature elevation for t-test when (a) random forest, (b) XGBoost, (c) KNN, (d) linear regression and (e) SVM models were used. 148
7.8 Error between the actual and predicted temperature values for the t-test across different deep learning models: (a) CNN, (b) LSTM, (c) FCNN, (d) RNN, and (e) CNN-LSTM. 150

8.1 Schematic diagram of the prototype wearable device. 154
8.2 Screenshot of Arduino IDE COM port displaying ESP32 IP, transmit power (as per the Wi-FiGeneric library i.e., 72 = 18 dBm = 0.063 W), temperature, and humidity data. 154
8.3 Screenshots of the mobile web server displaying temperature and humidity data from the wearable device. 155
8.4 Prototype of the wearable device utilizing ESP32. 155
8.5 Setup for measuring RF-EMF exposure of the wearable device in the tunnel. 159
8.6 RF-EMF exposure data collection at various distances between the RF-EMF meter and wearable device (a) 5 mm, and (b) 20 mm. . . 159
8.7 Plot of measured raw data at diverse distances between the RF-EMF meter and the wearable device (a) 5 mm, (b) 10 mm, (c) 15 mm, and (d) 20 mm 160

8.8 Plot of measure data at diverse distances between the RF-EMF meter and the wearable device (a) 5 mm, (b) 10 mm, (c) 15 mm, and (d) 20 mm 161
8.9 Simulated power density for all considered distance with MIFA. . . 162
8.10 Simulated power densities at distance (a) 5 mm, (b) 10 mm, (c) 15 mm and (d) 20 mm 163
8.11 Comparison of the measured, simulated, and analytically evaluated power density for different distances, where red area represents near field region and green area presents far-field region. 164

List of Tables

2.1 List of studies evaluating effects of underground mine environment on the propagation of EMR 15
2.2 List of different wearable devices developed for underground mines . 19
2.3 Basic restrictions prescribed by ICNIRP for 100 kHz to 300 GHz . . 24
2.4 Reference levels of electric and magnetic fields strengths prescribed by ICNIRP 25
2.5 List of studies evaluating RF-EMF exposure in confined environments 34
2.6 List of studies evaluating RF-EMF exposure in term of temperature elevation in tissues 39
2.7 Commercial software for high-frequency problems 44

3.1 Dielectric and thermal properties of human tissues at 2.4 GHz . . . 57

4.1 Comparison of MIFA RF-EMF exposure for different mounting positions at 2.4 GHz 72
4.2 Dielectric and thermal properties of the rock utilized in this study. . 79
4.3 Comparison of MIFA RF-EMF exposure for different tunnel scenarios at 2.4 GHz 81

5.1 Comparison of temperature elevation for wrist and waistline for different ambient temperature 94

7.1 Machine learning models hyperparameter configuration space. . . . 127
7.2 Comparison of performance metric of random forest 128
7.3 Comparison of performance metric of XGBoost 129
7.4 Comparison of performance metric of K Nearest Neighbor 130
7.5 Comparison of performance metric of Linear Regression 131
7.6 Comparison of performance metric of Support Vector Machine . . . 131
7.7 Comparison of performance metrics of deep learning models with different cross-validation folds 132
7.8 Comparison of performance metric of random forest for predictions of temperature elevation 140
7.9 Comparison of performance metric of XGBoost for predictions of temperature elevation in tissues 142
7.10 Comparison of performance metric of K Nearest Neighbor for temperature elevation prediction 143
7.11 Comparison of performance metric of Linear Regression for temperature elevation predictions 143

7.12 Comparison of performance metric of Support Vector Machine for temperature elevation prediction 144
7.13 Comparison of performance metrics of Deep learning models with different cross-validation folds 145

8.1 Measured maximum and average power density at different distances in the range of 2400 MHz to 2500 MHz. 161
8.2 Simulated power density for different distances. 162
8.3 Analytical power density for different distances. 163

Abbreviations

EMF	**E**lectro **M**agnetic **F**ield
SAR	**S**pecific **A**bsorption **R**ate
HFSS	**H**igh **F**requency **S**tructure **S**imulator
CST	**C**omputer **S**imulation **T**echnology
RF	**R**adio **F**requency
ELF	**E**xtremely **L**ow **F**requency
VLF	**V**ery **L**ow **F**requency
ICNIRP	**I**nternational **C**ommission of **N**on **I**onizing **R**adiation **P**rotection
IEEE	**I**nstitute of **E**lectrical and **E**lectronics **E**ngineers
FCC	**F**ederal **C**ommunication **C**ommission
TTE	**T**hrough-**T**he **E**arth
UWB	**U**ltra-**W**ide **B**and
WSN	**W**ireless **S**ensor **N**etwork
ISM	**I**ndustrial, **S**cientific and **M**edical
MIFA	**M**eander **I**nverted **F**-shape **A**ntenna
PCB	**P**rinted **C**ircuit **B**oard
IEC	**I**nternational **E**lectrotechnical **C**ommission
WHO	**W**orld **H**ealth **O**rganization
OC	**OC**cupational exposure
GP	**G**eneral **P**ublic
Wi-Fi	**Wi**reless **Fi**delity
LOS	**L**ine **O**f **S**ight
NLOS	**N**on-**L**ine **O**f **S**ight
RFID	**R**adio-**F**requency **ID**entification

Publications

Peer-reviewed journal papers directly related to this Dissertation

Muhammad Ahsan Ashraf and Turgay Celik, Evaluating radiofrequency electromagnetic field exposure in confined spaces: a systematic review of recent studies and future directions, *Radiation Protection Dosimetry*, 2024, p 1-19, https://doi.org/10.1093/rpd/ncae045

Muhammad Ahsan Ashraf and Turgay Celik, Machine Learning-Based Prediction of SAR and Temperature Elevation in Tissues Exposed to Radio Frequency Electromagnetic Fields, *IEEE Access* (In preparation)

Chapter 1

Introduction

1.1 Introduction

The proliferation of wireless communication devices in everyday life has heightened health concerns associated with radio-frequency electromagnetic fields (RF-EMF) exposure. These devices utilise various antennas to emit RF-EMF at different frequencies. When the human body is in proximity to these wireless devices, it entails two critical considerations: Firstly, the presence of the human body can affect the radiation properties of the antenna, thereby compromising its performance. Secondly, the human body can absorb RF-EMFs emitted by these devices, which can cause an increase in tissue temperature and subsequent health concerns. When RF-EMFs are exposed to the human body, they act as a lossy dielectric material and absorb the energy [1]. It can cause an increase in the kinetic energy of the tissues over time. If the operating frequency of the wireless device is close to the resonance frequency of the tissue, it transmits more energy to the human body and elevates its temperature [2].

The Specific absorption rate (SAR) is the standard term for regulating RF-EMF exposure to the human body. SAR is defined as the amount of power absorbed per tissue mass. The International Commission on Non-Ionizing Radiation Protection (ICNIRP) and the Institute of Electrical and Electronics Engineers (IEEE) provide guidelines to regulate RF-EMF exposure in terms of SAR and the rise in temperature of the tissues. The ICNIRP reported its first guidelines in 1998, which provided the basic restrictions of SAR up to 10 GHz and thresholds for electric

and magnetic fields up to 300 GHz [3]. These guidelines were amended in 2010 and 2020 [4] with the current literature and reported health effects of RF-EMF.

The mining industry has become increasingly important in modern life by providing valuable and essential mineral resources such as oil, gold, lead, copper, uranium, coal, and platinum [5]. In South Africa, the mining industry plays a vital role in the economy [6]. Unfortunately, there are numerous fatalities among miners working in underground mines every year. In 2018 and 2019, South Africa reported a total of 81 and 51 fatalities, respectively [7]. There has been a notable increase in fatalities, with 27 reported up to May 2021, surpassing the number recorded during the same period the previous year [8]. A significant factor contributing to these fatalities is the collapse of ground, accounting for approximately 37% of incidents [7], leaving miners trapped beneath rock debris or blocked tunnels. The absence of communication with miners after a disaster and prolonged rescue operations heightens the risk of further loss of life. Deploying reliable and robust communication and tracking of miners' locations can reduce the fatality rate in underground mines and provide fast and efficient rescue operations.

Wireless communication has various privileges over wired communication as it is reliable, low maintenance cost, easy to deploy, and adaptive [9]. Wireless communication plays an imperative role in monitoring different environmental and geotechnical parameters and tracking the location and vitals of the miners. In recent years, wireless communication systems have been deployed to monitor mining operations and environmental conditions, monitor vital signs and track miners' locations in underground mines. Tracking the location of the trapped miner is advantageous for effective rescue operations to save more human lives.

Wearable wireless devices are commonly used to monitor miners' vital signs and track their locations. These devices are typically mounted on the miner's body during a shift. The deployment of these wearable wireless devices in the proximity of the miners' bodies emphasises the thorough investigation of RF-EMF exposure in underground mines. Moreover, investigating RF-EMF exposure becomes crucial when wearable devices are utilised in underground mines' confined, reflective, and

high-temperature environments, mainly when used near the human body. The prolonged operation of these wearable wireless devices throughout the shift can potentially increase the risk of temperature elevation in tissue. The reflective nature of the surrounding environment in underground mines can further amplify exposure to RF-EMF.

Previously, the author investigated the exposure of RF-EMF on the human head and torso at frequencies of 433 MHz, 868 MHz, and 2400 MHz, utilising various underground mine scenarios [10, 11]. The findings indicated that SAR values were consistently higher within all underground mine scenarios than in free space. However, the RF-EMF exposure remained within the basic restrictions set by ICNIRP. Notably, a metal arch near the RF-EMF source heightened the tissue absorption rate. However, it is noteworthy that this study did not include factors such as the high temperatures of underground mine environments and the extended operational durations. Therefore, it is essential to rigorously study the impact of RF-EMF exposure to wearable devices worn by miners over extended durations, considering the elevated temperatures inherent to underground mine environments and the actual structure of underground mines.

This study investigates the impact of wearable devices in underground mines on SAR and tissue temperature elevation, considering realistic underground mine structures and rock properties. It also investigates the SAR variability regarding associated RF-EMF exposure parameters. The study also explores the effects of RF-EMF exposure on tissue temperature over an 8-hour shift and the high temperature of an underground mine. The SAR and tissue temperature elevation were also estimated using supervised machine-learning models, and their performance was compared. Additionally, a wearable device prototype was developed to measure RF-EMF exposure in the underground tunnel. The power density was measured using an RF-EMF exposure meter within the underground tunnel and compared with analytical and simulated power densities across various distances.

1.2 The Need for Exposure Evaluation

Wearable wireless devices are crucial in monitoring environmental and geotechnical parameters, vital signs, and the miner's location. Their increasing adoption in underground mines underscores their numerous advantages. Consequently, it is imperative to thoroughly investigate the precise RF-EMF exposure of these wearable devices in the harsh environment of underground mines without compromising underground mine conditions and characteristics.

Furthermore, miners typically wear these devices throughout their entire work shift. The proximity of RF-EMF in underground mines' confined, reflective, and high-temperature during prolonged operation can heighten miners' exposure levels to levels that exceed the regulated thresholds set by ICNIRP. This situation poses a significant risk to miners' health, making it essential to examine RF-EMF exposure in such challenging and complex conditions thoroughly.

Various studies have explored the effects of long-term RF-EMF exposure on temperature elevation in body tissues under normal conditions. However, no study has investigated these effects, considering the high temperatures in underground mines and the extended duration of exposure. This underscores the urgent need for further research to enhance our comprehension and mitigate potential health risks for miners.

1.3 Effects of RF-EMF Exposure on Human Body Tissue

The International Agency for Research on Cancer (IARC) of the World Health Organization has classified RF-EMFs from mobile phones as Group 2B, meaning they are possibly carcinogenic to humans. This classification raises concerns about RF-EMF exposure in public health [12]. Several studies summarize the effects of RF-EMF exposure on various human tissues. For instance, the review in [13] summarizes research focused on the effects of RF-EMF exposure on the central nervous system (CNS), including its impact on the blood-brain barrier

(BBB), neuronal activities such as effects on calcium channels, and autophagic processes. Similarly, a substantial body of literature published over the past sixty years demonstrates adverse effects associated with RF-EMF exposure, whether applied alone or in conjunction with other toxic stimuli. Numerous comprehensive reviews have examined the biological and health effects of RF-EMF exposure ([14–17]). Collectively, these reviews indicate that, for the high-frequency RF-EMF exposure below FCC guidelines can lead to:

- carcinogenicity (brain tumors/glioma, breast cancer, acoustic neuromas, leukemia, parotid gland tumors).
- genotoxicity (DNA damage, DNA repair inhibition, chromatin structure)
- mutagenicity, teratogenicity.
- adverse impacts on the neural, circulatory, immune, endocrine, and skeletal systems.
- neurodegenerative diseases (Alzheimer's Disease, Amyotrophic Lateral Sclerosis).
- neurobehavioral problems, autism, reproductive problems, pregnancy outcomes, excessive reactive oxygen species/oxidative stress, inflammation, apoptosis, blood-brain barrier disruption, pineal gland/melatonin production, sleep disturbance, headache, irritability, fatigue, concentration difficulties, depression, dizziness, tinnitus, burning and flushed skin, digestive disturbance, tremor, cardiac irregularities.

The impact of RF-EMF on the human body can be divided into two categories: thermal and non-thermal effects. Thermal effects arise from the rise in temperature due to energy transferred by RF-EMF. Conversely, non-thermal effects are not directly associated with temperature changes but with the energy absorbed. Further associated effects are discussed in detail below:

1.3.1 Thermal Effects

Different studies investigated the temperature variation in the whole body induced by RF-EMF exposure and associated potential health impairment. Increased body temperature of more than 1° C can damage human tissues. The excess heat in the body tissues is dissipated by the body's thermoregulatory response to maintain the body's average temperature, i.e., 37° C [18]. Severe health effects can occur when the body temperature is more than 40^0 C, which can cause heat strokes and irreversible cell damage due to thermoregulation physiology impairment [19]. Ramsey et al. observed that hyperthermia significantly affected workers' health behaviour when a worker is exposed to high temperature for 14 months [20]. In another study, Takashima et al. discovered that a SAR of 50 W/kg caused a temperature increase of more than 2 degrees Celsius after a 30-minute exposure at 2.45 GHz [21]. No significant biological changes were observed when a continuous or pulsed RF signal with a SAR of 100 W/kg was exposed to cells. However, a SAR of 200 W/kg inhibited cell growth, which exceeded the ICNIRP basic restriction of 2 W/kg.

1.3.2 Non-Thermal Effects

Exposure to low-level RF radiation below the ICNIRP basic restrictions typically does not pose thermal risks, as the body has mechanisms to regulate its temperature. However, several studies have investigated non-thermal effects arising from long-term exposure. The extensive use of mobile phones in daily life, mainly when held close to the head during calls, results in increased exposure to the brain compared to other parts of the body [22]. Consequently, various studies have focused on assessing the impact of mobile phone signals on the central nervous system and the brain. Short-term effects of RF radiation may include sleep disturbance, depression, headache, nausea, and visual disorders [23].

1.4 Contribution and Novelty of the Research

This research's primary contribution lies in utilising machine learning (ML) techniques to estimate SAR and temperature elevation in tissues for wearable devices deployed in underground mines across various parameters. Conducting numerical simulations is time-consuming and demands substantial computational resources. Additionally, altering any parameter necessitates repeating the entire simulation process. In contrast, a trained ML model can rapidly estimate exposure, even with variations in multiple parameters, outperforming numerical simulations in speed. However, to the author's knowledge, no prior study has applied ML techniques to estimate RF-EMF exposure to wearable devices within the underground mine environment. Furthermore, the research aims to address gaps in the existing literature by evaluating RF-EMF exposure in underground mine environments, considering factors such as high temperatures, realistic structure, prolonged exposure durations, and direct measurement within mine tunnels, which have not been explored in previous studies.

Understanding the variability of RF-EMF exposure parameters and associated factors in underground mine environments can help us better comprehend RF-EMF mitigation strategies, thereby improving health and safety standards for miners in these environments.

A novel aspect of this research lies in its evaluation of SAR and tissue temperature elevation for a realistic wearable device within underground mine environments, which, to the best of the author's knowledge, has yet to be previously explored in existing literature. In addition, implementing ML models for predicting SAR and tissue temperature elevation in the context of wearable devices represents another novel aspect of this research, which has not been previously explored in existing literature.

1.5 Research Questions

The use of wearable devices on the body of the miners in high ambient temperatures and confined space of the underground mines may exceed the reference limits of SAR and temperature elevation of the tissues prescribed by ICNIRP [4]. However, the RF-EMF exposure was investigated for workers considering high ambient temperatures, humidity, and clothing effect in [24, 25]. It was suggested that high ambient temperature marginally impacts RF-EMF exposure, but it does not include the actual structure of the surrounding environment and prolonged exposure. Considering the surrounding environment is crucial as a metal object near the RF-EMF source and the human body increases SAR in the tissues [26]. Furthermore, the propagation of the electromagnetic signals also depends on the surface roughness [27], tunnel size, and geometry [28–30]. Hence, understanding the actual conditions of the surrounding environment is crucial for accurately evaluating RF-EMF exposure. Investigating the variability of associated parameters necessitates extensive repetition of numerical simulations, which can be time-consuming. ML can be employed to predict SAR and temperature elevation to alleviate the burden of numerical simulations. Various studies have utilised ML models to estimate RF-EMF exposure in different confined environments [31–33]. Hence, implementing ML models to estimate RF-EMF exposure in confined environments is crucial, reducing the computation time and resources required for conventional simulation software. The main research question addressed in this research is: **What are the implications of wearable devices' exposure to human health in high ambient temperatures and prolonged usage in underground mines?** To answer the main research question, the following sub-research questions need to be addressed:

- What is the effect of wearable devices on SAR in the human body?
- How does the structure of the underground mine alter the SAR in the human body?

- How does temperature elevation in the body tissues co-relate to the RF-EMF exposure of wearable devices in high ambient temperatures of the underground mine?
- How does prolonged exposure to the wearable device impact the temperature elevation in body tissues at the high ambient temperature?
- How can ML techniques estimate SAR and temperature elevation in body tissues due to wearable devices?

1.6 Objectives of the Research

The following are the objectives of the research:

- Objective 1: Evaluation of SAR in the human body for wearable devices
  - The characteristics of wearable devices associated with RF-EMF exposure are essential. Therefore, the SAR will be evaluated by modelling the actual wearable devices.
- Objective 2: Evaluation of SAR for wearable devices considering real underground mine environment
  - The reflections due to the confined environment of the underground mine can alter miners' exposure to RF-EMF. Therefore, the actual underground mine structure will be considered using laser scanner technology available at the Sibanye-Stillwater Digital Mining (DigiMine) Laboratory.
- Objective 3: Assessment of temperature elevation in body tissues exposed to the wearable device under high ambient temperatures of underground mine
  - The body's temperature varies depending on the temperature of the surrounding environment, and RF-EMF exposure in such environments can introduce additional thermal load on the body tissues. Therefore,

it is crucial to investigate the temperature elevation of tissues due to exposure to the wearable device in high temperatures of underground mines.

- Objective 4: Effect of prolonged exposure to the wearable device on temperature elevation in tissues
  - Continuous exposure to RF-EMF can elevate the temperature of the exposed tissues for a prolonged duration. In underground mines, wearable devices are usually used for the whole work shift. Therefore, studying the temperature elevation in tissues when the body is exposed to RF-EMF for an extended time in a high temperature and confined environment is critical.
- Objective 5: Implementation of different ML techniques to estimate SAR and temperature elevation in tissues
  - Numerical simulations and dosimetric measurements are time-consuming and require more resources to evaluate human body exposure to RF-EMF. Therefore, different ML techniques will be implemented to estimate the exposure to wearable devices in the different underground mine environments.
- Objective 6: Recommendations regarding wearable devices' exposure in high ambient temperatures and prolonged usage in underground mines
  - Recommendations will be provided regarding SAR and temperature elevation of tissues on the above findings for different underground mine environment conditions, different characteristics of the wearable devices, and miners prolonged exposure to RF-EMF.

1.7 Thesis Outline

In this thesis, Chapter 2 offers background information and a literature review concerning the critical factors influencing the propagation of electromagnetic signals in underground mines, wearable devices utilised in these environments, and dosimetry studies conducted in confined spaces and for ML models. Chapter 3 discusses the research methodology, and the step-by-step procedure outlining the approach taken to achieve the research objectives is provided. It also discusses the system-level approach employed in the research. In Chapter 4, the investigation of SAR for wearable device antennas using realistic underground mine structures is presented, and the results regarding variations in parameters associated with RF-EMF exposure are discussed. In Chapter 5, temperature elevation in tissues is investigated for different ambient temperatures of the underground mine, and results were compared with ICNIRP guidelines. In Chapter 6, supervised machine learning literature is discussed along with various performance metrics of the ML models.

Similarly, Chapter 7 delves into implementing ML models for predicting SAR and temperature elevation in tissue. Chapter 8 presents and discusses the measurement of RF-EMF in the underground tunnel using a wearable device prototype. Chapter 9 discusses the conclusions drawn from the research findings, along with potential recommendations for future work.

Chapter 2

Background: Literature Review

This chapter conducted a comprehensive literature review, focusing initially on wireless communication systems in underground mines to understand their interaction with the mine environment and the critical factors involved. Following this, a review of the literature concerning wearable devices in underground mines was undertaken to understand common architectures, frequencies, and types of wearable utilized.

Subsequently, an extensive review of the literature about RF-EMF exposure evaluation in confined and free space environments was conducted. This literature was further classified based on the various research methodologies for assessing RF-EMF exposure. Through this review, research gaps in the field of RF-EMF exposure were identified.

Moreover, this chapter includes discussions regarding commercial packages utilized for the numerical evaluation of RF-EMF exposure in various environments. It also provides insights into the HFSS numerical software and human body models utilized in this study, along with a brief overview of ML models.

2.1 Wireless Communication Systems in Underground Mine

The accomplishment of communication systems ameliorates productivity, health, and safety in underground mines [34]. The excavation of minerals and ores advances consistently in underground mines. Therefore, the deployment of communication systems in excavated areas is significant. In this case, wireless communication systems have more advantages over wired communication systems owing to low cost, ease of deployment, mobility, and sustainability. Wireless communication systems are mainly comprised of the transmission of data through a wireless medium. However, the unfavourable and hazardous environment of the underground mine complicates the propagation of the wireless signals [35].

In underground mines, the applications of wireless communication systems are not limited to environmental monitoring parameters (such as gas concentration, temperature, and humidity), geotechnical parameters (such as rock stress, rock displacement, and seismic activities), tracking workers' location and monitoring their health vitals. Based on the application of wireless communication systems in underground mines, wireless communication systems can be divided into different categories, such as through-the-earth (TTE) systems, leaky feeder systems, wireless sensor network (WSN) systems, and ultra-wideband (UWB) systems. TTE systems operate at low frequencies and have large loop antenna systems on the surface to transmit a signal through the earth medium to the receiver integrated into cap lamps [36]. It provides alarming messages and tracking of the miners. In South Africa, the first TTE system was deployed in gold mines in 1946 [37]. At the same time, WSN systems communicate through Wi-Fi (IEEE 802.11), Bluetooth (IEEE 802.15.1), ZigBee (IEEE 802.15.4), and RFID technologies for short to medium-range communication [38] based on the application. UWB systems usually have wide bandwidth with low power and narrow pulses. These systems are usually used for tracking and location application in underground mines and provide more accurate measurement between transmitter and receiver [39].

2.1.1 Wireless Propagation in Underground Mine

Table 2.1 summarize the studies focused on the propagation of the EM signal in the underground mine environment. The effect on the propagation of EM signal for different parameters of the underground mine environment, such as surface roughness, dust, temperature, humidity, and shape of the tunnel, were studied [27, 40–42]. It can be concluded that surface roughness, the presence of dust particles, and the size of the tunnel are significant factors that affect the propagation of the wireless signals in the underground mine. In addition, the impact of different characteristics of EM signals such as frequency, orientation and gain of the antenna, skin depth, attenuation, and position of transmitter and receiver were also studied in [29, 43–47]. It can be concluded that frequency, the orientation of the antenna and the position of the transmitter and receiver are critical for the propagation of the wireless signal in underground mine tunnels. Most studies focused on industrial, scientific, and medical (ISM) frequency bands that use a 2.4 GHz frequency.

Table 2.1 shows that environmental factors in real underground mine settings have a substantial impact on EM signal propagation. Variables such as humidity, temperature, tunnel geometry, and the presence of machinery introduce unique propagation challenges that differ significantly from open or typical indoor environments. Incorporating these parameters is essential for accurately analysing EM wave propagation and assessing RF-EMF exposure in these conditions. The variations in propagation directly affect signal strength and exposure levels experienced by workers in such confined spaces.

2.1.2 Wearable Wireless Devices in Underground Mines

The health and safety of underground miners primarily rely on real-time monitoring of various activities and health vitals. Different environmental and geotechnical parameters were monitored through wearable devices for the health and safety of the miner. WSN techniques are widely employed to monitor various parameters

TABLE 2.1: List of studies evaluating effects of underground mine environment on the propagation of EMR

Reference	Author	Publication Source	Considered Parameters of the Mine Environment	Frequency Range	Summary
[40]	Zhao *et al.*	2008 IEEE International Symposium on Knowledge Acquisition and Modeling Workshop	Surface roughness	0 - 5 GHz	• Propagation loss increases with frequency due to wall roughness. • In coal mine, frequencies between 0.7 - 2 GHz provide low attenuation.
[43]	Cheng 2012a *et al.*	Applied Mechanics and Materials	Dust, frequency, droplet and temperature	0 - 3 GHz	• All parameters weaken the propagation of EM waves. • Attenuation increases with the increase in dust particles and moisture droplets.
[41]	Cheng 2012b *et al.*	International Journal of Antennas and Propagation	Humidity, permittivity, conductivity of circular and rectangular tunnel walls	0 - 3 GHz	• Tunnel dimensions have negligible effect on propagation in mine at mobile frequencies. • Humidity in the tunnel has less influence on permittivity. • Conductivity of the walls mainly depends on the conductivity of the pore water.
[44]	Rissafi *et al.*	IEEE Transactions on Antennas and Propagation	Propagation analysis for UWB channel in LOS and NLOS underground mine galleries	3 - 10 GHz	• Path loss exponents in underground mine galleries were higher than the indoor environment. • The omnidirectional antenna offers better signal coverage in NLOS galleries. • The directional antennas reduce time dispersion and increasing the channel capacity.
[45]	Hakem *et al.*	The 8th European Conference on Antennas and Propagation (EuCAP 2014)	Path loss, outage probability, delay spread and coherence bandwidth	2.4 GHz, 5.8 GHz, and 60 GHz	• The communication was better at 2.4 GHz. • The delay spread values are different from those in the indoor environment.

[28]	El Khaled *et al.*	IEEE Antennas and Wireless Propagation Letters	Effect of tunnel dimension on the path loss exponent	57 GHz - 59 GHz	• The channel capacity was higher for a 70 m gallery than a 40 m gallery. • The path loss exponent was less for a narrow (70 m) tunnel than a wider (40 m). • The omnidirectional antennas should be preferred for millimetre wave communication in underground mines.
[29]	Ranjan *et al.*	Wireless Personal Communications	Tunnel size, operating frequency, transmitter-receiver position, and antenna gain.	433 MHz, 915 MHz, 2.4 GHz, and 5.8 GHz	• Size and transmitter-receiver position strongly affect signal propagation. • Electrical parameters of the tunnel wall and antenna gain have moderate effects.
[30]	Hussain *et al.*	Physical Communication	Tunnel geometry, antenna placement, polarization and directivity		• Tunnel geometry, antenna placement, polarization, directivity, and configuration significantly impact the performance of wireless communication systems
[27]	Xusheng *et al.*	2018 IEEE International Conference on Real-time Computing and Robotics (RCAR)	Surface roughness, dust particles, propagation path loss	2.4 GHz	• Attenuation increases with the surface roughness and concentration of dust particles.
[46]	Tariq *et al.*	IEEE Access	Angular spread of multi-path signals	60 GHz	• Angular spread decreases along the distance between the transmitter and receiver and mainly depends on the tunnel's dimensions. • Directional antennas with beam steering characteristics are essential for underground mine communication at 60 GHz.
[47]	Issa *et al.*	2020 IEEE International Symposium on Antennas and Propagation and North American Radio Science Meeting	RSSI, SNR and path loss exponent	2.4 GHz	• LTE communication provides coverage of 50 m in underground mines.

[49]	Bedford *et al.*	IEEE Transactions on Antennas and Propagation	Hand-held LiDar scanner was used to model the caves to study the propagation of EM signals	2.4 GHz, 5.8 GHz	• A ray tracing method is a good choice for a cave with one bend than multi-bend caves. • A commercial ray tracing methods have drawbacks due to a lack of background knowledge.
[42]	Zheng *et al.*	Journal of Applied Geophysics	Dimensions of the tunnel, attenuation factor, dust particles, and roughness of wall	600 MHz, 900 MHz, 1.8 GHz, 2.4 GHz	• The width-to-height ratio should be considered when roadways are designed. • Dust particles, the roughness of the wall, and the tilt angle also attenuate the signal in the roadways.
[50]	Zhang *et al.*	IEEE Access	Attenuation, skin depth, conductivity and resistivity	3 Hz - 3 kHz	• The VLF (3 - 3kHz) band has a good agreement for propagation in the coal mine. • Conductivity of ore has a direct relation with the attenuation of the signal. • Skin depth has inversely relation with attenuation of the signal.

in underground mines continuously. Wearable devices serve a broad spectrum of functions beyond environmental monitoring, including gas detection, temperature, and air quality assessment, as well as vital signs monitoring such as heart rate, body temperature, breathing, and fatigue levels. Additionally, they are crucial in tracking miners' locations and optimizing rescue operations during emergencies [48].

Different wireless technologies have been implemented to develop wearable devices in underground mines. Table 2.2 summarizes studies on designing wearable devices for underground mines. Most studies integrate wearables into the miner's helmet, which is mandatory for underground miners. The following conclusion was drawn from the literature:

- Wearable type: Helmet or torso.
- Frequency: 2.4 GHz.
- Circuit board: Arduino platform.
- Antenna type: Whip and PCB antennas.
- Wireless connectivity: Bluetooth and Wi-Fi.
- Only a few studies tested wearable devices in the underground mine environment.

2.2 Related EM Quantities and Reference Levels

2.2.1 Specific Absorption Rate

The interaction of RF-EMF with biological tissues is complex, resulting in an inhomogeneous distribution of absorption within the tissues, even though the incident RF-EMFs are uniform. Since the distance between the RF-EMF source and human tissue is typically only a few centimeters, it is important to assess human

TABLE 2.2: List of different wearable devices developed for underground mines

Reference	Author	Publication Source	Wearable type	Antenna type	Frequency	Monitoring parameters
[51]	Minhas *et al.*	IEEE Systems Journal	Mobile node carried by miner	Whip antenna	433 MHz	Gas concentration, tracking of the miners, creating emergency alerts and node failures
[52]	Li *et al.*	2018 IEEE/ACM International Conference on Connected Health: Applications, Systems and Engineering Technologies (CHASE)	Helmet	Whip antenna (nrf24101)	2.4 GHz	ECG and eye blink sensor
[53]	Abro *et al.*	2018 International Conference on Computing, Electronics & Communications Engineering (iCCECE)	Jacket	PCB (MPIFA)	2.4 GHz	Temperature, humidity, pulse rate, gas detection, pressure, location tracking.
[54]	Indra *et al.*	2018 2nd International Conference on Electronics, Materials Engineering & Nano-Technology (IEMENTech)	-	-	433 MHz	Temperature, humidity and pressure.
[55]	Kim *et al.*	Applied Sciences	Helmet	RECON beacon	2.4 GHz	Proximity alarm system.
[56]	Ramya *et al.*	2021 International Conference on Design Innovations for 3Cs Compute Communicate Control (ICDI3C)	Helmet	Whip antenna	2.4 GHz	Gas, temperature, force and Infra-red sensor.
[57]	Suganya *et al.*	Journal of Physics: Conference Series	-	-	2.4 GHz	Different gases and temperature.
[58]	Reddy *et al.*	Annals of the Romanian Society for Cell Biology	-	MIFA (ESP8266)	2.4 GHz	Gas, tilt, temperature, and light.
[59]	Suganthi *et al.*	Materials Today: Proceedings	-	PCB antenna	2.4 GHz	Gas, acceleration, tilt angle and incline of the tunnel .
[60]	Ramya *et al.*	Indo-Iranian Journal of Scientific Research (IIJSR)	Helmet	Whip antenna	2.4 GHz	Gas, temperature, oxygen, opguard camera for fatigue monitoring.
[61]	Baek *et al.*	International journal of environmental research and public health	Eyeglasses	-	2.4 GHz and 5 GHz	personal proximity sensor.
[62]	Singh *et al.*	Computer Communications	Helmet	PCB antenna (ESP8266)	2.4 GHz	Heartbeat, gas, dust, temperature, humidity, flame and respiratory filter.
[63]	Porselvi *et al.*	2021 3rd International Conference on Signal Processing and Communication (ICPSC)	-	Whip antenna	Not specified (usually 868 MHz, 433 MHz)	smoke, respiratory, heartbeat.
[64]	Noorin *et al.*	2018 3rd IEEE International Conference on Recent Trends in Electronics, Information & Communication Technology (RTEICT)	Helmet	PCB antenna (ESP8266)	2.4 GHz	Gas, temperature, humidity, collision and helmet detection.

body exposure in the near field of the RF-EMF source. This assessment involves measuring the electric field within the human body.

The SAR quantifies the amount of RF energy absorbed in the human body when exposed to RF-EMF and used as an index term to regulate RF-EMF exposure [4]. It is defined as follows:

$$SAR = \frac{\sigma \cdot E^2}{2\rho} \qquad (W/kg) \tag{2.1}$$

Where σ is the conductivity of the human tissue (S/m), E is the electric field inside the human body (V/m), and ρ is the density of the tissue exposed (kg/m^3).

The SAR is typically used for frequencies ranging from 100 kHz to 10 GHz and is influenced by various factors, including frequency, geometry, and the dielectric properties of the tissues exposed to RF-EMF. Additionally, it depends on the distance between the RF-EMF source and the exposed tissues, the frequency of operation, input power, antenna polarization and orientation, as well as other environmental parameters related to RF-EMF exposure.

The SAR is averaged over a mass of 10 g, 1 g, or any custom tissue value. The SAR average over 10 g of tissue is referred to as SAR_{10g}, whereas for 1 g of the tissue, it is referred to as SAR_{1g}. The ICNIRP guidelines considered SAR_{10g} to provide basic restrictions of RF-EMF exposure [4]. Other important terms related to SAR include *peak spatial-average SAR* (psSAR) and *whole body average SAR* (SAR_{wb}. Peak spatial average SAR represents the maximum average SAR value in the tissue considered for RF exposure based on the specific average volume. The whole body average is defined as the energy absorbed in the body divided by its total mass and denoted as SAR_{wb}.

2.2.2 Temperature Elevation in the Human Tissues

In recent decades, there has been significant progress in understanding biological processes and improving our knowledge of the thermal properties of human tissues.

These advancements have contributed significantly to investigations into heat and mass transfer applications.

The bioheat transfer phenomenon has gained prominence in diagnosing the effects of RF-EMF exposure on human tissues. Advances in computational techniques and mathematical modelling has leveraged the researcher's ability to analyze the bioheat equation for temperature elevation due to RF-EMF exposure. Collaboration among multidisciplinary researchers, including medical professionals, physicians, and engineers, has propelled advancements in bioheat transfer. The fundamental aspects of the bioheat transfer equation are described below.

2.2.3 Fundamental Aspects of Bioheat Transfer

The thermoregulation system of the human body can maintain a core temperature near 37° C during thermal stress for a wide range of environmental conditions, such as high-temperature conditions. The blood flow rate varies depending on the needs and activities of the human body.

Blood plays a dual role in balancing thermal energy as a thermoregulation response; it can act as either a heat source or a heat sink. For instance, in winter, blood circulation from the heart to other organs increases to facilitate body warming. Researchers shown that the human body typically rises 12° C in 1 hour without losing heat by blood flow during exercise. The blood perfusion rate is the amount of blood supplied to a specific tissue region per minute per 100 g of tissues. It also represents the need for nutrients in a specific tissue area. Heat dissipation is also associated with a high blood perfusion rate during exercise and thermal stress. Hence, comprehending the thermal characteristics of biological tissues is crucial for understanding the heat transfer mechanisms within the body. It has gained significant importance with the rising exposure to RF-EMF at a wide range of wireless communication frequencies among individuals.

Temperature distributions in different human body tissues can be determined by solving the bioheat transfer equation, which includes blood perfusion, heat conduction, and external heating. The SAR distribution induced by RF-EMF or other external heating sources should be determined first to solve the bioheat equation. Then, all the calculations, initial conditions, and appropriate boundary conditions allow for calculating the temperature distribution.

2.2.4 Pennes Model of the Bioheat Equation (BHE)

The temperature distribution in the human tissues is calculated using the bioheat equation proposed by Pennes [65]. A series of experiments were conducted to measure the temperature distribution in nine subjects as a function of the radial position of the arm by maintaining the thermal equilibrium. Pennes proposed a model to characterize blood perfusion and metabolism within the tissue. The standard thermal diffusion equation with blood perfusion and RF-EMF heating is represented as [66]:

$$\begin{aligned} C(r)\rho(r)\frac{\partial T(r,t)}{\partial t} &= \nabla.(K(r)\nabla T(r,t)) + \rho(r)SAR(r) + Q(r,t) \\ &\quad - B(r,t)(T(r,t) - T_B(r,t)) \end{aligned} \tag{2.2}$$

Where C is the specific heat of the tissue, T is the temperature of the tissue, T_B is blood temperature, B is associated with blood perfusion, K is the thermal conductivity of the tissue, Q is the metabolic heat generation, ρ is the density of the tissue, SAR represents the specific absorption rate, and r and t represent the position and time.

The temperature elevation due to wearable antennas can be considered insufficient to activate the thermoregulation response, i.e., activation of sweating and increase in the blood flow rate [66]. However, the working conditions of the underground miner in higher temperatures and sweating conditions can elevate the temperature distributions in the tissue. Therefore, it is crucial to examine the temperature

distribution in the high-temperature environments where miners often work for over eight hours per shift.

2.2.5 RF Exposure Restrictions and Reference Levels

International and National organizations regulate RF-EMF exposure to the population using the World Health Organization (WHO) recommendations. The following well-known international organizations developed the norms to limit the exposure that is currently applied:

- International Commission on Non-Ionizing Radiation Protection (ICNIRP).
- Federal Communication Commission (FCC).
- Institute of Electrical and Electronic Engineers (IEEE).
- International Electro-technical Commission (IEC).
- European Committee for Electro-technical Standardization (CENELEC)

The safety limits secure the minimum harmful level of RF-EMF exposure according to scientific data and are updated every ten years. Different reduction factors are applied for the general public and occupational safety. A significant safety margin (50-fold) was implemented for the basic restriction of SAR. According to the basic restrictions reported by ICNIRP [4] in 2020, for the general public, the safety distance from the transmitting antenna was defined as 75 cm in [67], and 1 m in [68].

Experimental studies demonstrated that at the frequency range of 100 kHz - 6 GHz, an average whole-body SAR of 6 W/kg for 1 hour induces 1° C evaluation in temperature. Therefore, in the 2020 guidelines of ICNIRP [4], the minimum exposure level that induces 1° C of elevation in temperature is a whole-body SAR of 4 W/kg for 30 minutes of exposure at the frequency mentioned earlier. The

basic restrictions provided by ICNIRP have been summarized for SAR and temperature rise in Table 2.3 for the general public's uncontrolled environment and the occupational workers' controlled environment with their respective reduction factors. The whole-body SAR limits were set at 0.4 W/kg and 0.08 W/kg for occupational and general public exposure, respectively. Similarly, the safety limits for the head and torso were also described for different ranges of frequencies. In addition, ICNIRP introduces the reduction margin by 10 and 2 factors for the general public and occupational exposure, respectively. The reference level for electric and magnetic field strength was also summarized in Table 2.4 for occupational and general public exposure.

TABLE 2.3: Basic restrictions prescribed by ICNIRP for 100 kHz to 300 GHz [3]

100 kHz - 300 GHz		100 kHz - 6 GHz				6 - 30 GHz		30 - 300 GHz	
SAR_{WBA}		Head & Torso		Limbs		Head and Torso, Limbs			
Δ T after 30 min		Δ T after 6 min				Δ T after 6 min			
1°C		2°C		5°C		5°C			
SAR_{WBA} averaged over 30 min		**SAR 10g** averaged over 6 min				**PD** 4 cm^2		**PD** 1 cm^2	
4 W/kg		20 W/kg		40 W/kg		200 W/m^2		400 W/m^2	
OC	GP	OC	GP	OC	GP	OC	GP	OC	GP
Safety reduction factors									
10	50	2	10	2	10	2	10	2	10
SAR_{WBA} averaged over 30 min		SAR_{10g} averaged over 6 min				PD averaged over 6 min			
0.4 W/kg	0.08 W/kg	10 W/kg	2 W/kg	20 W/kg	4 W/kg	100 W/m^2	20 W/m^2	200 W/m^2	40 W/m^2

WBA: whole body average PD: power density OC: Occupational, GP: General public

TABLE 2.4: Reference levels of electric and magnetic fields strengths prescribed by ICNIRP [3]

Reference Levels	**Frequency**	**Electric field strength (V/m)**	**Magnetic field strength (A/m)**
General public	0.4 - 2 GHz	$1.375 \times f^{0.5}$	$0.0037 \times f^{0.5}$
	2-300 GHz	61	0.16
Occupational	0.4 - 2 GHz	$3 \times f^{0.5}$	$0.008 \times f^{0.5}$
	2-300 GHz	137	0.36

2.2.6 RF Exposure Restriction for Underground Mines

The ICNIRP identifies RF-EMF exposure into two tiers: occupational and general public exposure. Occupationally exposed individuals are exposed under controlled conditions with their respective occupational duties, trained to be aware of RF exposure risks and to employ mitigation measures. The general public is considered individuals of all ages and health statuses without knowledge and control over their exposure to RF-EM fields. Different exposure restrictions have been shown in Table 2.3 and Table 2.4. Similarly, in IEEE standard [69], the exposure limits are divided into two tiers: unrestricted and restricted environments. If the dose limits of the unrestricted environment are exceeded, RF safety training is required for the individuals to implement the dose limit of the restricted environment.

In underground mines, workers typically lack protective equipment and receive no RF safety training. Although underground mine environments are classified as occupational, according to ICNIRP, underground mines fall into the general public category when it comes to RF-EMF exposure. In [10], results suggested that RF-EMF exposure levels in underground settings were lower than in general public environments. Nevertheless, it is crucial to implement basic restrictions for worker safety based on current guidelines [4]. Additionally, assessing the long-term RF-EMF exposure experienced by miners requires further investigation.

2.3 Classification of Studies Concerning RF-EMF Exposure Evaluation

The increasing use of wireless communication has heightened human exposure to RF-EMF, prompting researchers from various fields to assess its potential health implications. Different research methodologies have been employed, tailored to the disciplines involved. For instance, medical researchers conducted experiments on tissues to observe RF-EMF impacts under various conditions. Social science researchers utilized methodologies such as questionnaires and interviews. Meanwhile, engineering researchers utilized numerical simulations and standard SAR measurements to evaluate RF-EMF exposure, comparing it with existing regulatory thresholds. Looking at the diverse methodologies used to assess RF-EMF exposure, they can be classified based on the methods employed, as depicted in Figure 2.1.

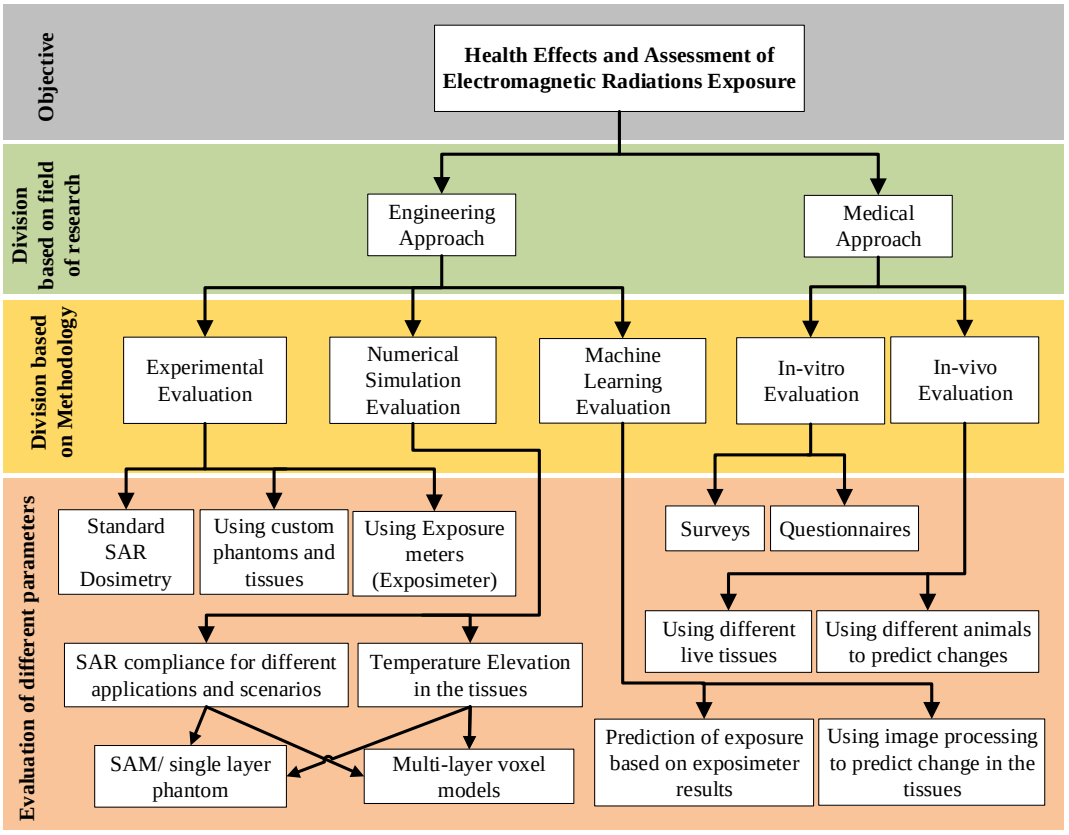

FIGURE 2.1: Classification of methodologies for evaluating RF-EMF exposure

Various studies explore human exposure to RF-EMF, focusing on physical quantities such as electric field strength (measured in volts per meter, V/m), magnetic field strength (measured in amperes per meter, A/m), and power densities (W/m^2) [70–73], and temperature elevation [74, 75]. This type of research is specified as **RF Dosimetry**, and associated quantities are referred to as dosimetry quantities. The studies use numerical simulation to investigate the exposure, referred to as numerical dosimetry. In contrast, the studies focus on measuring dosimetry quantities, referred to as RF exposure assessment [76]. **RF Epidemiology** statistically correlates human exposure to health effects by evaluating In-Vitro or In-Vivo RF exposures [77–79]. It also relies on dosimetry to obtain reliable results of dose-response [80, 81].

2.3.1 Literature of RF-EMF Exposure in Confined Environment

Different studies focused on determining exposure in enclosed environments such as in rooms, shopping malls, along corridors, offices, schools, universities, hospitals, trains, inside electric cars, elevators, and enclosed capsule environments [82–95].

Some studies solely discuss RF-EMF exposure in indoor or confined environments without comparing it to free-space conditions. Comparing exposure levels between confined and free-space environments under similar conditions is imperative to gain a comprehensive understanding of RF-EMF exposure in confined environments.

Many studies used exposimeter to measure RF-EMF exposure in indoor and confined spaces. However, accessing underground mine tunnel areas for such measurements poses significant challenges. As a result, numerical simulations have been employed to investigate RF-EMF exposure from mobile phones and Wi-Fi devices in various enclosed environments [89, 96, 97]. Table 2.5 summarizes the studies that evaluate RF-EMF exposure in different enclosed environments for different exposure settings and methodologies. Similarly, Table 2.6 summarizes the studies that evaluated RF-EMF exposure regarding temperature elevation in tissues.

In [82], ExpoM-RF was used to measure exposure in different areas of Seoul for 14 RF bands using children, fathers, and mothers. The body shadowing increases the exposure by 1.4 times, essential for accurate exposure measurements. The downlink is the major contributor to the exposure, and Wi-Fi is the major in all the frequencies. The exposure was higher in the metro, followed by foot/bicycle, bus/ car. It was also higher for a base station in South Korea than reported in the European countries. Similarly, the RF-EMF exposure was higher for the higher number of beams and high data rate in the transmission of MIMO communication [90]. In [91] , the outdoor exposure, 61% exposure is from FM broadcasting antennas, and 39% contribution is from mobile communication antennas whereas, in the case of indoor exposure, 89.1% contribution is from FM band and 10.5% from mobile telephony band and 0.4% is from Wi-Fi. During different days and hours, the variation in the electric field was between 0.27 dB and 2.26 dB in different frequency bands. The spatial distribution between indoors and outdoors was 3 dB to 7 dB. In [92], three hundred locations inside the campus were considered for indoor and outdoor measurements. The measured power density of the outdoor station is ¡1% of its threshold. The power density at the indoor base station reached 16% of the allowed limit, while for Wi-Fi, it remained below 1% of the permissible power density.

In [93], it was concluded that Wearing the glasses reduced the electric field value by a factor of four compared to not wearing them. The aluminium frame of the glasses serves as a shield, further reducing RF-EMF exposure. However, despite these measures, the electric field value in the tissues remained above the recommended threshold. The RF-EMF exposure was analysed in the capsule environment [94]. The signal distribution should be well estimated and mainly depend on the distance from the transmitter. No adverse health effects from using these devices in such a capsule environment were found. This study has limitations, notably the use of a simple phantom model that restricts the evaluation of exposure to different tissues. Additionally, the study did not assess long-term exposure effects. Similarly, in [95], the RF-EMF exposure values were higher for cellular communication and increased linearly with floor levels. However, the exposure levels are below the

legislated limits. A plane wave exposure at 1.5 GHz with a custom phantom was used to evaluate the exposure in the indoor environment [96]. The room was modelled using loamy and concrete materials using the CST material library. The results were lower than the prescribed safety levels. The exposure in different tissues was not evaluated, and no comparison was provided for free space and indoor environment. A metal pin, spectacles, and ring metal jewellery was used to analyse the impact of different distances between the dipole antenna and metallic objects [26]. It was suggested that all shapes of metals increase the SAR and temperature in the head tissues. The distance and length of the metal pin can increase and decrease the absorption in the head. The presence of a spectacles lens decreases the SAR in the eyeball. However, it increases the absorption around the skin near the spectacles. Two different human body positions were analysed for a model placed inside a permanent magnet guide rail [97]. The exposure mainly depends on the distance between the human body and the guided rail. The hotspot of the exposure was in the foot of the passenger.

In [98], the body-worn exposimeter lowers the RF-EMF exposure level due to the shielding of the body in different micro-environments of Belgium, Spain, France, Netherlands and Switzerland. The downlink is the major contributor to the RF-EMF exposure. The study has several limitations, including the time-consuming process of re-calibrating the device after each measurement, the weight of the body-worn device, and variations in frequency bands among exposure meters, which impedes direct comparison. In [99], the exposure to electric, magnetic and electromagnetic fields has exceeded their limits in many cases, not only for the worst-case simulation scenario. Electric field and magnetic flux density were in the range during measurements, and additional protection was required. The magnetic flux was higher on the surface of the current cables. Expanding the distance with the nominal power of the transformer enhances protection.

In [10], the SAR was higher in all underground mine environments compared to free space, but it was maximum in the presence of a metal arch. The SAR was higher in the head than the torso and head with the helmet. A safety helmet mitigates the exposure when a wearable device is mounted on the outside layer.

The SAR values were lower than the prescribed limits of ICNIRP and IEEE for all simulation scenarios. In [100], the downlink and broadcast, followed by uplink and Wi-Fi, were the main sources of RF-EMF personal exposure. Furthermore, personal RF-EMF exposure varied by the days of the week and during different time slots over the day. However, the measurements suggested that all personal RF-EMF exposure levels were substantially below the ICNIRP guideline limits for the general public. Similarly, in [101], the risk and exposure perceptions of people was compared related to RF-EMF associated with mobile phone base stations, as a function of different information provided (basic text, precautionary information, or personal RF-EMF exposure measurement) to the participants. A total of 383 individuals were recruited and divided into different categories. The findings indicated that individuals with basic knowledge and those provided with RF-EMF exposure data did not exhibit significantly different risk perceptions regarding RF-EMF exposure. In [102], the RF-EMF exposure of employees in libraries was assessed for Wi-Fi frequencies. The occupational exposure is close to the general population on average. The exposure was higher for Walkie-Talkie, and outside exposure depends on the geographic location of the source. The RF-EMF exposure was lower than occupational exposure limits for Wi-Fi, whereas indoor Wi-Fi was 10 times lower than the ICNIRP Limits.

A high level of RF-EMF exposure inside the apartment due to the presence of nearby base stations were measured in Sweden [103]. The results indicated that the apartment was unsuitable for long-term living based on current knowledge of the potential adverse effects of RF-EMF. Similarly, in another study, four EME SPY 140 exposimeters were used to evaluate RF-EMF exposure in Albacete (Spain) [104]. The level of RF-EMF exposure in 14 micro-environments was lower than ICNIRP limits. The major contribution of the exposure was from DECT communication, followed by mobile phone and Wi-Fi. The exposure was higher on Sunday compared to other days. Similarly, the exposure during the day was higher than in the night. However, the study was conducted from 2010 to 2014, may have limitations due to the dynamic nature of exposure frequencies in today's environment. The RF-EMF exposure by a base station in Leuven, Belgium was

analysed using a spectrum analyser at different locations and times during the day [105]. All measurements were below ICNIRP limits. The overall exposure was 0.64 V/m in outdoor environments, and for indoor, it was 0.32 V/m. Thus, outdoor exposure was higher by a factor of two than indoor.

In [106], the RF-EMF exposure of the pedestrian in a vehicle-to-vehicle (V2V) outdoor exposure was investigated numerically. Five scenarios were investigated near the car with two antennas mounted on the car, one on the back and a second on the front with a tilted direction. For all cases, the exposure value was less than the thresholds, but the front orientation of the antenna always yielded higher RF-EMF exposure than the back antenna. The skin was the most affected tissue due to the exposure. In another study, the RF-EMF exposure of Wi-Fi signals were measured using an exposimeter EME SPY 140 in the School of Spain [107]. The exposure was measured for indoor and outdoor environments, suggesting that on the weekend, the exposure was higher outside the building, which shows that the Wi-Fi exposure contribution was from neighbour's Wi-Fi, whereas during the weekdays, the exposure was higher inside the building, but was below the levels for both scenarios.

In [108] , the RF-EMF exposure was simulated for low frequencies with a virtual human body model standing partially outside a vehicle. The vehicle was modelled as a replica, and the monopole RF antenna was modelled at 16 MHz with transmit power of 25 W. The study investigated four scenarios to assess electric field exposure: A) without the human body, B) with the operator present, C) with the operator wearing a helmet, and D) with the operator wearing a helmet and using a cabled handset. Results indicated that while most areas complied with electric field limits, localized regions exceeded thresholds in scenario A. With the operator present, the induced electric field within the body reached 12 V/m. In scenario C, the induced electric field within the head increased by 10% compared to scenario B. In scenario D, slight increases in electric field and SAR near the ears were observed but remained within safety limits. Another study investigated the RF-EMF exposure in the office space in the New York City using electrosmog meter Cornet [109]. The results suggested that the break room has less exposure

due to fewer devices; at the entry and reception area, exposure was higher due to the close presence of the router, and a medium level of RF-EMF exposure was found in the remaining areas of the office. It is recommended that the minimum distance in an office space between any worker and the Wi-Fi router may not be less than 22 feet. In another study, the low-frequency magnetic field exposure of the subway train was evaluated for different exposure materials and RF-EMF shielding [110]. The exposure on the human body for different distances was also calculated. The magnetic flux in the train depends on the different materials, windows, and shielding layers. The magnetic flux for aluminium alloy was 6.3% of ICNIRP, 5.8% for CFRP carbon fibre material, and 5.4% in the case of stainless steel.

Similarly, in [111], the RF-EMF exposure level of Wi-Fi 2G and 5G band in Mexico were assessed. The main source of exposure was the 2.4 GHz Wi-Fi band which was below ICNIRP limits. According to the results of risk perception surveys, the Tamazunchale (Mexico) population was worried about the situation in comparison with several European populations, but their perception changed when they were informed about the results of the study. The exposure was higher during the day, and in the schools and the workspace.

In [31], eighteen head models were developed using a fast machine-learning (CondNet, CNN) approach, and variation in antenna performance was evaluated. The SAR, impedance, and return loss showed large variations compared to directivity and radiation patterns. In another study, a deep learning-based method was used to determine electromagnetic wave absorption in the human body [112]. The CNN was trained using the data obtained from finite-difference time-domain analyses at 3.5 GHz; the method accurately predicts average and maximum power density in various regions of the human head. In [32], a cluster analysis approach was applied to exposure measurements. The clusters were identified as children with high exposure living 120-200 m from 225 kV/ 400 kV overhead lines and mid-to-low exposure living 40 m from 400 V/ 20 kV substations. Similarly, a clustering algorithm was applied on the measured RF-EMF exposure data in 205 schools in Greece in the range of 27 MHz - 3 GHz [33]. The results showed no specific

pattern in total RF-EMF strength, whereas exposure was at least 3500 times less than in 97.5% of schools, and only 2.5% schools had exposure less than 500 times. In [113], a low-frequency RF-EMF was measured in the building inside the campus and different ML techniques were applied to estimate the exposure. The results suggested that 99% of the success rate was obtained for user data, and values of explained variance and R-squared were close to 1.0, showing that the model makes good predictions.

In [114], a CNN model was trained to learn a surrogate SAR model to find the relation between MRI images and local SAR. After training, the model predicts the SAR in milliseconds. In silico and in vivo validation has a good qualitative and quantitative match of predicted local SAR. Similarly, the SAR maps from 3T and 7T simulated MR images using CNNs for real-time SAR estimation in MRI were studied [115]. Various 2-D U-Net architectures were evaluated on realistic body models, achieving promising results. The proposed approach predicts SAR maps for 224×224 slices in under 30 ms, showing potential for real-time SAR prediction in clinical MRI settings without additional techniques or patient-specific calibrations. In [116], brain images were used to extract the change due to RF-EMF exposure using Ml techniques. The SVM method provides more accuracy than other ML classifiers. It provides the prediction extracting the brain image were almost 1.8 and .20 s, which is suitable for practical applications.

2.4 Conclusion of Literature

Table 2.1 concluded that the studies investigated the effect of different underground mine environment parameters on the propagation of EMR. It can be summarized that tunnel size, surface roughness, the concentration of dust particles, material, and frequency of EM signal are important factors influencing the propagation in the underground mine environment. The attenuation primarily relies on the loss profile of underground mine tunnels. Therefore, it is essential to incorporate actual underground mine environments and conditions to evaluate RF-EMF exposure in these settings.

TABLE 2.5: List of studies evaluating RF-EMF exposure in confined environments

Confined Environment Literature (Simulation and Measurement)							
Reference	**Author**	**Publication Source**	**Parameter**	**Methodology**	**Exposimeter/ Software**	**Area of study**	**Country**
[82]	Choi *et al.*	Science of the Total Environment	Power density	Measurements	ExpoM-RF	Seoul, Cheonan, & Ulsan	South Korea
[90]	Loh *et al.*	2021 15th European Conference on Antennas and Propagation (EuCAP)	Electric field	Measurement	Testbed and triaxial isotropic field probe, Agos ARIA-6000	The University of Surrey	United Kingdom
[91]	Paniagua *et al.*	Environmental research	Electric field	Measurement	EME SPY 200	Inside and outside dwelling (buildings, flat & house)	Spain
[92]	Keshmiri *et al.*	Radiation Protection Dosimetry	Electric field & power density	Measurement	Probe WPF18 connected to SMP	Campus area of Ferdowsi University of Mashhad	Iran
[93]	Jovanović *et al.*	Safety Engineering	Electric field and SAR	Simulation	CST software	-	-
[94]	Harris *et al.*	2020 Wireless Telecommunications Symposium (WTS)	Electric field and SAR	Simulation	Sim4life	Enclosed cylindrical capsule	-
[95]	Moraitis *et al.*	2020 14th European Conference on Antennas and Propagation (EuCAP)	Electric field and power density	Measurement	SRM-3000 by Narda	Eight-floor building	Greece
[96]	Bejenaru *et al.*	2020 International Conference and Exposition on Electrical And Power Engineering (EPE)	SAR	Simulation	CST software	Indoor room	-
[26]	Bhargava *et al.*	Case Studies in Thermal Engineering	SAR and Temperature elevation	Simulation	COMSOL Multiphysics	Metallic object	-
[98]	Huss *et al.*	Environment International	Power density	Measurement	Novel body-worn distributed meter, ExpoM-RF and EMSpy 200	Different countries	Belgium, Spain, France, Netherlands and Switzerland.
[97]	Lieli *et al.*	IOP Conference Series: Earth and Environmental Science	Electric and magnetic field	Simulation	COMSOL software	Electric Train	-
[99]	Göcsei *et al.*	Journal of Electrostatics	Electric and magnetic field	Simulation & measurement	COMSOl multiPhysics and EverTech EMDEX II	Industry	Hungary

[117]	Cerezci *et al.*	Radiation Protection Dosimetry	Electric and magnetic field	Measurements	ELT-400 and HOLADAY 3060, Narda 550 field meter and SRM 3006 spectrum analyzer	Indoor environment	Turkey
[10]	Ashraf *et al.*	Radiation Protection Dosimetry	SAR	Simulation	CST software	Underground mine	-
[100]	Zeleke 2018 *et al.*	International Journal of Environmental Research and Public Health	Electric field	Measurement	ExpoM-RF	Residential, school and office	Australia
[101]	Zeleke 2019 *et al.*	International Journal of Environmental Research and Public Health	Electric field	Measurement	Questionnaire and ExpoM-RF	Residence near the mobile base station in the metropolitan areas of Melbourne	Australia
[102]	Massardier-Pilonchery *et al.*	International Journal of Environmental Research and Public Health	Electric field	Measurement	EME SPY 200	Libraries and Media Libraries	France
[103]	Hardell *et al.*	Oncology Letters	Power density	Measurement	EME SPY 200	Rooms of the apartment	Sweden
[104]	Ramirez-Vazquez *et al.*	Environmental research	Power density	Measurement	EME SPY 140	Different 14 micro-environments such as buildings, shopping malls, hospitals, schools, universities, home offices and in the public transport	Spain
[105]	Iyare *et al.*	Environmental research	Electric field	Measurement	Dipole antenna and spectrum analyzer	City centre of Leuven	Belgium
[118]	Mannan *et al.*	Energy Reports	Electric field, magnetic field and power density	Measurement	HF-B3G (RF meter)	Residential, hospital, office, and school and entertainment centres inside Qatar Foundation	Qatar
[106]	Benini *et al.*	Sensors	SAR	FDTD simulation	Sim4Life	Vehicle	
[107]	Ramirez-Vazquez *et al.*	IEEE Access	Power density	Measurement	EME SPY 140	Inside and outside a school	Spain
[108]	Colella *et al.*	Frontiers in Public Health	Electric field and SAR	FDTD simulation	Sim4Life	Military vehicle	
[119]	Colella *et al.*	2022 Microwave Mediterranean Symposium (MMS)	Electric field	FDTD simulation	Sim4Life	Military vehicle	-

[109]	Wafik *et al.*	Journal of Al-Azhar University Engineering Sector	Volt/meter and μTesla	Measurement	Electrosmog meter Cornet	Inside Office of the building, New York	USA
[120]	Kapetanakis *et al.*	Applied Sciences	Electric field	Measurement	NARDA SRM-3006	Inside schools	Greece
[121]	Psenakova *et al.*	2019 IEEE 20th International Conference on Computational Problems of Electrical Engineering (CPEE)	SAR	FIT simulation	CST software	Inside shielded space	
[122]	Chiaramello *et al.*	IEEE Journal of Electromagnetics, RF and Microwaves in Medicine and Biology	Electric field	Simulation	WiCa Heuristic Indoor Propagation Prediction (WHIPP)	Residential	-
[110]	Wang *et al.*	Progress in Electromagnetics Research M	Magnetic flux and SAR	MoM and FIT simulation	FEKO and CST	Subway vehicle	-
[123]	Bustillo *et al.*	Journal of Physics: Conference Series	Average power density	Measurement	NARDA SRM-3000	Philippine General Hospital (PGH)	Philippine
[124]	Celaya-Echarri *et al.*	IEEE Access	Electric field	Simulation and Measurement	EME SPY 121 and 3D-Ray Launching algorithm using Matlab	Urban transport busses	-
[125]	Celaya-Echarri *et al.*	IEEE Access	Electric field	Simulation and Measurement	3D Ray Launching simulation, EME SPY EVO and EME SPY 200	Shopping malls	Poland
[126]	Celaya-Echarri *et al.*	IEEE Access	Power density	Simulation and Measurement	EME SPY Evolution and 3D ray tracing technique	Aircraft cabin	-
[127]	Martínez-González *et al.*	Environmental Research	Electric field	Measurement	NARDA NBM-550 broadband field meter and isotropic NARDA EF0691 E-field probe	Library reading room	Spain
[83]	Karpowicz *et al.*	2018 International Symposium on Electromagnetic Compatibility (EMC EUROPE)	Electric field strength	Measurements	EME SPY 200	Shopping malls, offices, schools, libraries, and public transport facilities	-
[128]	Onishi *et al.*	International Journal of Environmental Research and Public Health	Electric field	Measurement	Spectrum analyser and SRM-3006 NARDA	Outdoor and underground shopping malls	Japan

[111]	Ramirez-Vazquez *et al.*	International Journal of Environmental Research and Public Health	Power density	Measurement	EME SPY 140	Exposure of 63 volunteers from home, workplace, outside, schools, travel, and shopping	Mexico
[84]	Sagar *et al.*	Environment international	Electric field strength & power density	Measurement	ExpoM-RF and EME-Spy 201	94 selected environments	Switzerland, Ethiopia, Nepal, South Africa, Australia and United States of America
[85]	Smondrk *et al.*	19th International Conference Computational Problems of Electrical Engineering	SAR	FIT simulation	CST software	-	-
[86]	Michalowska *et al.*	2018 IEEE 4th International Symposium on Wireless Systems within the International Conferences on Intelligent Data Acquisition and Advanced Computing Systems (IDAACS-SWS)	Electric field	Measurement	ESM-140	Industry	-
[87]	Sen *et al.*	2018 International Conference on Innovation in Engineering and Technology (ICIET)	Electric field, penetration depth and absorbed power	Measurement	Anechoic chamber with tissues (goat)	Metallic chamber and free space	-
[88]	Kljajic *et al.*	2018 26th Telecommunications Forum (TELFOR)	Electric field, global exposure ratio (GER)	Measurement	NARDA NBM-550	Campus area of University of Novi Sad	Serbia
[89]	Bejenaru *et al.*	24th IMEKO TC4 International Symposium Electrical & Electronic Measurements Promote Inudstry	SAR	FIT simulation	CST software	-	-

Machine Learning Literature

Reference	**Author**	**Publication Source**	**Parameter**	**Methodology**	**Machine Learning Models**	**Area of study**	**Country**
[31]	Diao *et al.*	IEEE Access	SAR	Simulation	CNN	Eighteen head models	-
[112]	Di Barba *et al.*	Sensors	Power density	Simulation	CNN	-	-
[32]	Tognola *et al.*	International Journal of Environmental Research and Public Health	Magnetic field	Measurement	Cluster analysis	Indoor (schools)	-
[33]	Kiouvrekis *et al.*		Electric field intensity	Measurement	Clustering algorithm	Schools	Greece

[113]	Pala *et al.*	2017 XIIIth International Conference on Perspective Technologies and Methods in MEMS Design (MEMSTECH)	Electric field	Measurement	Linear regression, Gradient Descent (GD) algorithm and ridge regression models	Campus building	Turkey
[114]	Meliadò *et al.*	Magnetic Resonance in Medicine	SAR	MRI images	CNN	-	-
[129]	Maurya *et al.*	Medical & Biological Engineering & Computing	Power density	Measurement and Brain images	Naive Bayes, SVM, Neural Net and Random Forest	-	-
[115]	Gokyar *et al.*	IEEE Access	SAR	-	CNN	MRI	-
[116]	Gothai *et al.*	Computer System Science Engineering	Power density	Brain images	SVM, Naive Bayes, Artificial Neural Network and Unsystematic forest	-	-

TABLE 2.6: List of studies evaluating RF-EMF exposure in term of temperature elevation in tissues

Reference	Author	Publication Source	Parameter	Method	Objective	Summary
[130]	Kodera *et al.*	IEEE Access	SAR and Temperature	Simulation	Relation between SAR and temperature rise	The time duration of RF-EMF exposure is critical for SAR restriction.
[131]	Lwin *et al.*	2018 IEEE 7th Global Conference on Consumer Electronics (GCCE)	SAR and Temperature	FDTD simulation	Temperature rise in Brain tissues	The exposure was higher in the TE case than in the TM wave. The exposure also depends on the distance from the RF source.
[24]	Moore *et al.*	IEEE Transactions on Biomedical Engineering	SAR and Temperature	Numerical simulation	Clothing effect and high temperature of body	The results suggested that RF-RMF contributes an additional thermal load to the tissues and subsequently causes temperature elevation in tissues depending on ambient temperature, humidity, and type of clothing.
[25]	Moore *et al.*	Bioelectromagnetics	SAR and Temperature	Numerical simulation	Clothing effect and high temperature of body	The results suggested that different environmental conditions had minimal impact on the exposure metrics, and were below the guidelines.
[132]	Kaburcuk *et al.*	2018 International Applied Computational Electromagnetics Society Symposium (ACES)	SAR and Temperature	Numerical simulation	Impact of Smart glasses on EMR	The temperature rise in the head was 0.153° C at 4.9 GHz, and 0.299° C at 2.4 GHz, and the temperature rise occurred on the same side of the head where the antenna was installed.
[133]	Sacco *et al.*	IEEE Journal of Electromagnetics, RF and Microwaves in Medicine and Biology	SAR and Temperature	Numerical simulation	Impact of textile on EMR	The results suggested that the textile in contact with the skin increases the absorbed power density up to 41.5% and 34.4% at 26 GHz and 60 GHz, respectively. The temperature of the bare skin elevated by 52% at 26 GHz and 46% at 60 GHz.
[134]	Gultekin *et al.*	IEEE Access	SAR and Temperature rise	FDTD simulation and Measurement	Brain tissues as a function of frequency, power and time	This study suggests that RF heating increases rapidly with frequency, incident power, and exposure time.
[135]	Christopher *et al.*	Radiation Physics and Chemistry	SAR and Temperature rise	Measurement	Temperature elevation due to 4G cell phone	The results suggested that the temperature rise in the brain was 0.10° C at 30 mm depth, and SAR was 0.66 W/kg. The measured SAR lies within the safe limit of ICNIRP.
[136]	Matikka *et al.*	Physics in Medicine & Biology	SAR and Temperature changes	FDTD simulation	Temperature changes due to metallic implant	A remarkable increase in temperatures of tissues such as 8° C was seen with a 1 W power level, whereas no significant temperature increase was observed at lower power levels.

[137]	Gajda *et al.*	Biomedical Physics & Engineering Express	SAR and Temperature rise	Simulation	-	The proposed method was highly efficient for repeated temperature-rise calculations for parameter variation and showed good agreement with conventional simulations. The investigation includes a narrow, circularly symmetric beam incident with different waveforms on a planar skin/fat/muscle tissue model.
[138]	Cavagnaro *et al.*	IEEE Transactions on Biomedical Engineering	Temperature elevation	Simulation	Relation of exposure duration and temperature elevation	Findings indicated that the most significant correlation with temperature increase typically falls between 1 and 2 minutes for SAR. Generally, SAR exhibits a stronger correlation with temperature than volume absorption rate (VAR) across short and long durations and at higher frequencies. However, VAR demonstrates a better correlation in some cases.

Table 2.2 reviews the wearable devices used in an underground mine for monitoring the miners' different activities and health vitals. It can be concluded that most wearable devices use ISM frequency bands to transfer real-time information from the miner to the control room. Most wearable devices use 900 MHz, 2.4 GHz, and 5.8 GHz frequency bands and are worn on the head by integrating into the miner's safety helmet and on the miner's torso or wrist. Most wearable devices also use PCB and whip antennas to communicate with each other. The wearable devices used an ESP8266 chip for communication, which consists of a meandered PCB antenna. Therefore, PCB antennas can be used to model wearable devices to assess RF-EMF exposure on the miner for underground mine settings.

Table 2.5 summarizes research related to RF-EMF exposure in various confined environments. Both measurement and simulation methodologies have been employed to assess RF-EMF exposure to the general public. Different types of exposimeter or RF meters were used to measure exposure in indoor settings; however, these devices do not provide information on specific absorption rate (SAR) or temperature elevation in body tissues. Typically, they measure RF-EMF exposure in terms of electric field strength, magnetic field intensity, and power density.

Simulation studies utilize various commercial software to model confined environments and employ high-resolution human body models to investigate RF-EMF exposure. To the best of the author's knowledge, there are currently no studies that evaluate RF-EMF exposure in the high-temperature conditions of underground mines while incorporating a realistic underground mine environment. Furthermore, no measurements have been conducted in actual underground mine settings.

Table 2.6 summarizes the impact of RF-EMF exposure on the temperature rise in the exposed tissues. It is critical to investigate the temperature rise in the tissues in high-temperature environments as investigated in [24]. Considering the real environment and multi-layer human body tissues to elevate temperature rise is crucial as the bioheat equation depends on the thermal properties and SAR. In [24, 25], no real environment (such as metal or other objects in the surroundings) was

considered to evaluate RF-EMF exposure in the high-temperature environment. Instead, it concluded that the high temperature of the surroundings marginally elevates the temperature of the tissues. The temperature elevation in tissues also depends on the exposure time and properties of tissues.

Recently, the author studied RF-EMF exposure from wearable devices in underground mine environments [10]. The CST software was used to model different underground mine scenarios, and SAR values were compared. It was found that the SAR values were higher in all underground mine scenarios compared to the free space scenarios. The SAR values were also higher in the head than the torso and were lowest when a device was mounted outside the safety helmet. It was also suggested that absorption was higher in the deep tissues of the human body at low frequencies compared to the high frequency where absorption was superficial.

Importantly, the SAR values remained below the thresholds set by the ICNIRP for all simulated scenarios. However, the study did not evaluate the temperature rise in tissues due to RF-EMF exposure. Furthermore, there has been no investigation into how the high temperatures present in underground mines may affect tissue temperature. Previous studies also failed to consider the prolonged duration of exposure in the confined, high-temperature environment of underground mines.

Different studies use ML techniques to estimate RF-EMF exposure in humans, rats, and plants [116,129,139–141]. These studies predict RF-EMF exposure using ML techniques implementing image processing of the exposed tissues, and analyzing changes before and after exposure. In [142], unsupervised ML methods such as hierarchical clustering were applied to estimate the pattern of RF-EMF exposure in schools. The exposure was measured using an exposimeter and estimated using ML models.

2.5 Research Gaps

During the literature review for assessing RF-EMF exposure, three significant research gaps were identified:

- **Evaluation of exposure in high-temperature environment:** Various wearable devices were employed in high-temperature environments, such as underground mines. The high ambient temperatures in these mines can raise the average body temperature (around 37^0 C) even without direct exposure to RF-EMF. When the human body is exposed to the RF-EMF at such a high temperature of the surroundings, the thermal burden on tissues can increase further. Therefore, it is critical to evaluate RF-EMF exposure by considering the high temperature of the surrounding environments. To the author's best knowledge, no study evaluated the exposure of wearable devices considering such high temperatures and confined environments conditions of the underground mine.

- **RF-EMF Exposure for long duration in high-temperature environment:** The miner can wear these wearable devices during the whole shift of the work, usually 6 to 8 hours/day. Using these wearable devices for such a prolonged duration is critical as it can keep the temperature of the tissues elevated for the extended duration of the wearable device. Therefore, it is crucial to investigate RF-EMF exposure for a long duration to understand how long the temperature of the tissues continues to increase or decrease due to the body's thermoregulation response to the high temperature of the surroundings. However, no study investigated the elevation in the tissues for the long-duration usability of wearable devices in the high-temperature environment of the underground mine.

- **Implementation of the ML techniques to estimate RF-EMF exposure:** Extensive numerical simulations of RF-EMF exposure in underground mines demand significant time and computational resources, especially when accounting for the complex underground environment and a multi-layer human body model. Therefore, it is crucial to implement a methodology that requires less time and computational power to estimate RF-EMF exposure while considering various parameters of RF-EMF exposure. To address this, ML models are needed to assess long-duration RF-EMF exposure from wearable devices in the high-temperature conditions typical of underground

mines. However, to date, no studies have applied ML techniques to estimate RF-EMF exposure in such confined environments.

2.6 Commercial EM Simulation Packages

Advancements in high computations of computers and software enhance the capacity to simulate large models with more accuracy and less time. Different commercial software is available to solve high-frequency problems. Most of the solvers in the software can be interlinked to solve different problems. For example, thermal solvers can be linked to high-frequency solvers as antenna structures designed in high-frequency solvers can be used to determine the thermal behaviour of antenna performance. Each software tool is based on distinct numerical techniques and is tailored to specific types of problems. When selecting an effective simulator for a specific issue, it is essential to consider several key factors: functionality, accuracy, setup time, execution speed, and the cost of the license. These elements play a crucial role in determining the simulator's suitability for the intended application and overall effectiveness. Table 2.7 shows the well-known commercial simulators for high-frequency problems. The Ansys HFSS software was selected for this study

Table 2.7: Commercial software for high-frequency problems

Simulator	**Numerical method**	**Type of solution**	**Provider**
CST MWS	FIT	Time/ Frequency domain	SIMULIA
HFSS	FEM	Frequency	ANSYS
FEKO	MoM/ FEM/ FDTD	Frequency	Altair
SEMCAD X Matterhorn	FDTD		SPEAG
XFdtd	FDTD	Time	Remcom
COMSOL Multiphysics	FEM	Frequency	COMSOL
Momentum	IE-MoM		KEYSIGHT
IE3D	IE-MoM	Spatial	Zeland Software

due to several key factors. HFSS utilizes a finite element method (FEM) to tackle complex electromagnetic problems, enabling accurate simulation of high-frequency designs. Notably, HFSS includes built-in tools for calculating SAR, a critical metric in RF-EMF exposure assessment. It also supports diverse material definitions, including dielectric properties essential for accurately modelling biological tissues and simulating RF-EMF exposure with variations in permittivity and conductivity. Additionally, Ansys Workbench offers an integrated solution that links high-frequency analysis with mechanical (thermal) analysis. The cost was another consideration, as the School of Aeronautical and Mechanical Engineering at the University of Witwatersrand holds a campus license, facilitating convenient access to any Ansys module.

2.6.1 High-Frequency Simulation Software (HFSS)

Ansys HFSS is a 3D EM simulation software for simulating high-frequency problems and electronics such as antennas, RF or microwave components, filters, connectors, IC packages, and PCBs [143]. *HFSS* was one of the old tools in the market and was heavily used in industrial design environments; it extracts parasitic parameters and visualizes 3D EM near and far fields. All solution is based on FEM numerical technique [144]. *Ansys Electronic Desktop* is a complete package that consists of different solvers, such as *HFSS* for design, analysis, and simulation of electromagnetic components, *Q3D* for extracting lumped RLGC parameters and Spice models, *Circuit* is a schematic-based interface for circuit simulator, *EMIT* is used for mitigating radio frequency interference in electronic devices, *Icepak* is a fluid and thermodynamic simulator for electronic systems and components, *Maxwell* uses finite element analysis to solve 3D electrostatic, magneto-static, eddy current, and transient problems, *simplorer* is an integrated, multi-domain, mixed-signal simulator for complex technical systems and *Mechanical* analyses the vibration frequencies and thermal analyses to determine temperatures and heat flux.

2.7 Packages for Human body Model

Ansys HFSS offers different human male and female body models in several geometrical accuracies of millimetres [145] and a set of a library "Ansys Human Body Model V5" consisting of different human models and tissues properties [146]. The models contain more than 300 muscles, organs, tissues, and bones with an accuracy of 1, 2, and 4 mm, as shown in Figure 2.2. The properties of the human body materials are frequency dependent, such as permittivity and conductivity from 10 Hz to 10 GHz. These properties are included in the Ansys material library based on [1]. The user can modify the model for specific applications and parts. The user can remove specific model parts and objects if not needed. The model can be electrically large for high frequencies, making simulation very time-consuming and computationally extensive due to the massive size of the meshes [147].

The Visible Human Project (VHP) package includes a high-resolution female model that can be utilized in Ansys and other electromagnetic (EM) simulation software [148]. These models offer a high level of detail and precise geometry of internal body structures, making them valuable for implementing implantable antennas. Consequently, selecting the appropriate body part is crucial for minimizing simulation time and conserving computational resources.

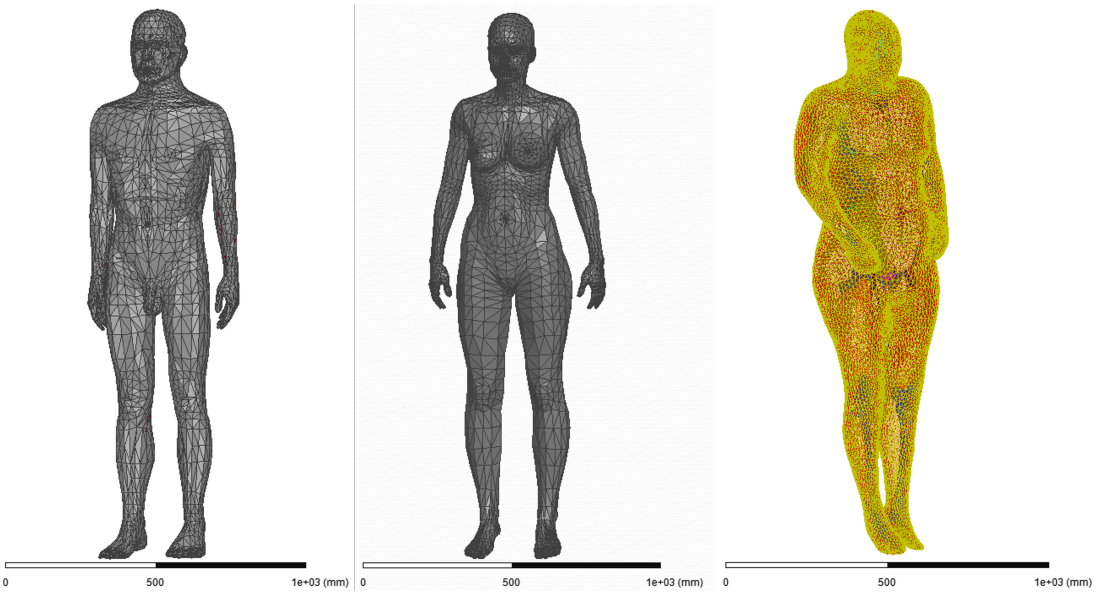

FIGURE 2.2: Human Body Model available in Ansys HBM package with male 4 mm resolution (left), female 4 mm resolution (center), and Neva VPH 3.0 female (right)

Chapter 3

Methodology to Assess RF-EMF Exposure of Wearable Device

This chapter comprehensively discusses the research methodology used to achieve the research objectives. It includes a detailed flowchart description outlining the methodology used for numerical simulations, machine learning, and measurements to assess RF-EMF exposure of wearable devices in underground mine environments. Furthermore, detailed elaboration is provided on the system-level approach employed in numerical simulations and specific insights into the human body model utilized.

3.1 Research Methodology

The research methodology was divided into two categories to evaluate the wearable device's RF-EMF exposure: numerical simulation and predictions using ML models and measurement. The methodology is further elaborated below.

3.2 Numerical Simulation and Predictions using ML Techniques

Numerical simulations were performed to evaluate SAR and temperature elevation in tissues for various mounting positions and scenarios involving the wearable device. The numerical simulations also incorporated the underground mine environment to assess more realistic RF-EMF exposure. Figure 3.1 illustrates the

flowchart outlining the methodology employed to accomplish each research objective for numerical simulation and ML models.

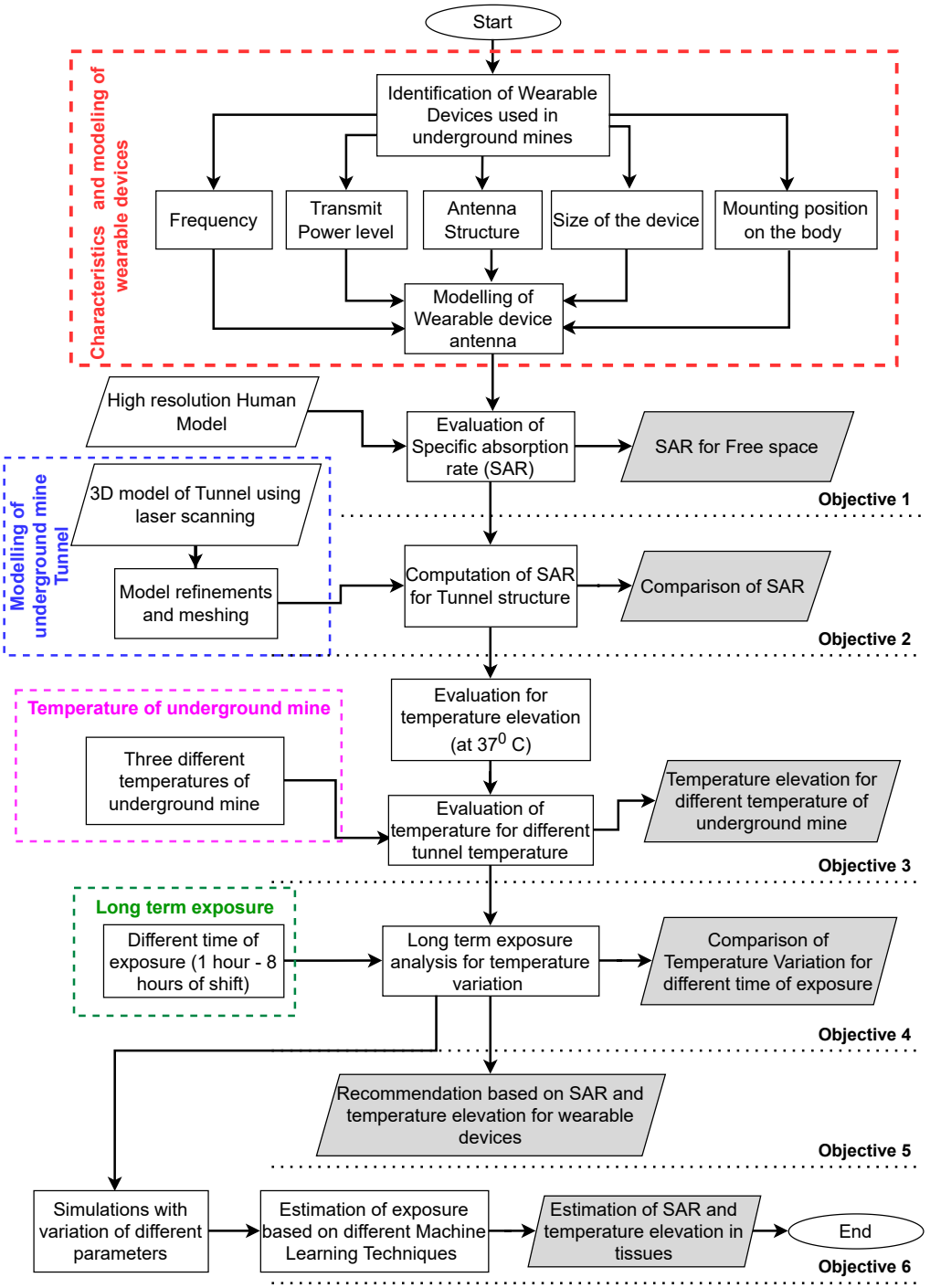

FIGURE 3.1: Flow chart of research methodology for numerical simulation and ML models.

3.2.1 Methodology for Objective 1

Numerical simulation using HFSS was employed to model wearable devices, incorporating their key characteristics such as frequency of operation, transmit power level, antenna structure, device size, and mounting position on the body. Many wearable devices utilize Arduino and ESP32 circuit boards operating at a frequency of 2.4 GHz within the ISM band, with varying power levels. According to the Independent Communications Authority of South Africa (ICASA) [149], a maximum power of 0.01 W can be utilized at 2.4 GHz for near-field communication, making it suitable for worst-case exposure investigations. Whip antennas or PCB antennas, often in the form of MIFA, are commonly used in wearable devices. Hence, a widely used PCB antenna such as MIFA was modelled at 2.4 GHz to assess SAR for different mounting positions of the wearable device on the human body.

The SAR was analyzed for the free space environment using a human models library named "Human Body Models (HBM)". It consists of a male model with dielectric properties ranging from 10 Hz to 10 GHz [146], available in HFSS software. The SAR values were compared for different parameters associated with RF-EMF exposure.

3.2.2 Methodology for Objective 2

The actual surrounding environment conditions must be considered to evaluate RF-EMF exposure. The presence of surrounding objects can significantly affect exposure metrics. As a result, a realistic model of the Wits mock mine tunnel was created using LiDAR technology. In [49], a laser scanner was utilized to model caves and study the propagation of electromagnetic signals. Similarly, a LiDAR laser scanner available in the Sibanye-Stillwater Digital Mining (DigiMine) laboratory was used for 3D scanning of the tunnel. The scanned 3D model was imported into the 3D CAD tool of Ansys (Geometry) for further CAD processing. Different material properties were assigned to the structure, and mesh refinement was

applied to the 3D tunnel model. Subsequently, the tunnel model was integrated into the primary file of objective 1 to assess SAR within the underground mine setting. Finally, SAR values were compared for different properties of the rock.

3.2.3 Methodology for Objective 3

The underground mines are usually hot environments where temperatures can reach 40 or 50^0 C. When tissues are exposed to RF-EMFs, they can raise the temperature of the tissues from their average temperature of 37^0 C. However, only the temperature of the surrounding environment higher than the average body temperature can increase the temperature of the human body. Therefore, it is essential to investigate RF-EMF exposure in high-temperature conditions when wearable devices are used in such environments.

To simulate the temperature elevation in tissues for different ambient temperatures of underground mines, such as 40^0 C or 50 ^{0} C, we used the "Mechanical" solver of the "Ansys Workbench" software with the modelled file of objective two. The electromagnetic losses were converted to thermal losses and defined as the heat source in thermal simulations. We analyzed the temperature variations for different mounting positions of MIFA for different ambient temperatures of the underground mine and compared the results with the ICNIRP guidelines [4].

3.2.4 Methodology for Objective 4

Wearable devices are frequently used in underground mines for extended shifts lasting up to 8 hours. This prolonged use can lead to prolonged exposure of tissues to RF-EMF. Considering the long-term effects of this exposure in such environments is crucial. This study investigated the effects of RF-EMF exposure to wearable devices on the human body for durations ranging from 1 to 8 hours under high ambient temperatures. The study utilized the thermal transient solver of *Ansys Mechanical*.

The simulation file of objective 3 was incorporated with time duration into the transient and static thermal solver of *Ansys Mechanical* for investigation of long-term RF-EMF exposure. The study analyzed the maximum temperature elevation in tissues with increasing exposure time and compared it for different exposure time settings.

3.2.5 Methodology for Objective 5

Numerical simulations are time-consuming processes requiring significant computational resources to evaluate RF-EMF exposure. This exposure depends on various parameters of the RF-EMF source, such as frequency, antenna gain, transmit power level, and distance from the human body to the antenna, as well as parameters associated with the underground mine environment, such as ambient temperature, tunnel dimensions, and exposure duration. Supervised ML models were utilized to estimate RF-EMF exposure of wearable devices, and varying associated parameters were used to address this.

Our research involved conducting a series of simulations, each with varying associated parameters. The ML model was trained to estimate SAR and temperature elevation in tissues. For instance, we varied the distance between the head and antenna (ranging from 5 mm to 15 mm), the transmit power of the antenna (from 0.1 mW to 1 mW), the orientation of the antenna, its mounting position on the body, the surrounding temperature (40^0 C or 50^0 C), and the exposure duration (1 to 8 hours) to train the ML and deep learning models. The trained ML and deep learning models were then used to estimate RF-EMF exposure for various combinations of these parameters. This approach offers a practical and efficient alternative to running complete simulation setups, which can be time-consuming.

Our primary objective was implementing various ML models and assessing their accuracy in estimating RF-EMF exposure for different parameters. By doing so, we aimed to provide a comprehensive understanding of the capabilities and limitations

of ML techniques in predicting SAR and temperature elevation due to RF-EMF exposure.

3.2.6 Methodology for Objective 6

Recommendations regarding RF-EMF exposure of wearable devices concerning high ambient temperatures, prolonged exposure times, and the confined environment of underground mines were provided based on SAR and temperature elevation in tissue, derived from both numerical simulations and ML models.

3.3 Methodology for Measurements

Figure 3.2 illustrates the flowchart used to measure RF-EMF exposure of wearable devices. Due to the challenges in accessing wearable devices deployed in underground mines, measurements were conducted in the Wits mock mine tunnel. A wearable device prototype was constructed using essential components, notably the ESP32 for Wi-Fi operation at 2.4 GHz.

RF-EMF exposure was measured using the Cornet RF-EMF exposimeter, focusing on power density (W/m^2) due to the unavailability of exposimeters measuring SAR or temperature elevation in human tissues. Measurements were conducted in the same settings to ensure consistency, following procedures outlined in previous studies for increased accuracy [82, 98, 100, 101]. Analysis was performed on measured values at varying distances from the ESP32 wearable device and RF meter. The measured results were also compared with simulated and analytically calculated power densities for MIFA.

3.4 Ethical Clearance for Research

Ethical clearance for this research and self-conducted measurements was obtained with reference number H22/10/01 under an ethical waiver.

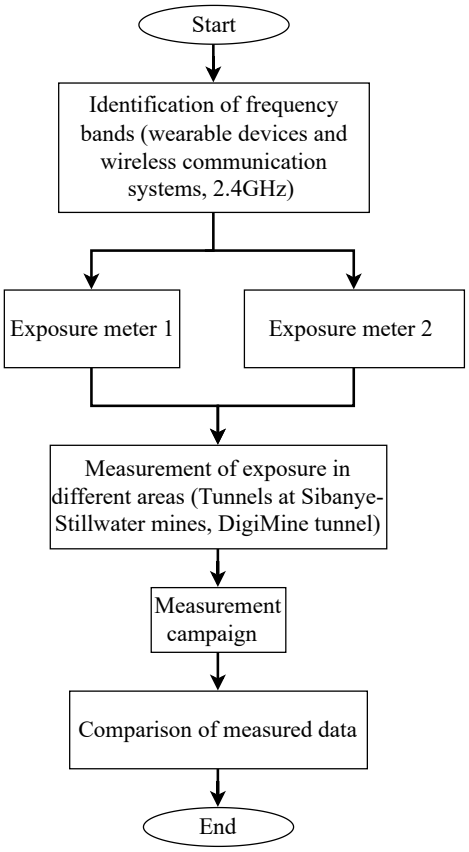

FIGURE 3.2: Flow chart of research methodology for measurements

3.5 Considerations of Body Mounting Positions for Assessing RF-EMF Exposure from Wearable Devices

Wearable devices can be positioned at various locations on the human body, each offering distinct advantages and considerations [150]. One standard placement is on the wrist, which is famous for smartwatches and fitness trackers due to its accessibility and non-intrusiveness [151, 152]. Wrist-worn devices allow convenient access to information and can track various biometric data. Another common placement location for wearable devices is the chest or torso, where devices like heart rate monitors and activity trackers are frequently worn [153]. This positioning ensures close contact with the skin, facilitating accurate vital signs and physical activity monitoring. Wearable devices can also be worn on the head, as

seen with smart glasses or virtual reality headsets, offering a direct line of sight for visual information and interaction [150]. For different applications, wearables can be embedded into clothing, such as smart apparel, enabling continuous monitoring without requiring direct skin contact. [154,155]. Additionally, the wearable can be worn on the fingers, ears, and ankles and can be embedded into textiles or accessories like jewellery. The choice of placement depends on factors like the device's intended purpose, comfort, user experience, and the type of data to be collected or displayed.

A comprehensive investigation into RF-EMF exposure across different mounting positions becomes imperative. Notably, a recent study examined RF-EMF exposure on the head of workers utilizing the ESP board, as reported by Zradziński et al. (2020) [156]. The findings revealed a substantial reduction in exposure by 300% when the device was mounted on the helmet's exterior, as opposed to being directly worn on the headband by the worker. However, it should be noted that the investigation did not employ a realistic human model. Similarly, in a prior study by the author, RF-EMF exposure for different frequencies was explored on the head and torso in underground mine scenarios [10]. While the scope was limited due to the dipole antenna, it was observed that placing the antenna outside the safety helmet resulted in even lower SAR values compared to the scenarios involving the torso. Therefore, the safety helmet can help reduce workers' RF-EMF exposure by introducing a distance between the head and the wearable antenna.

The mounting position of the MIFA on the body is shown in Figure 3.3. The arm and waistline segments highlighted in Figure 3.3 were selected for RF-EMF exposure assessment. This selection helps optimize computation time and resources by targeting specific areas instead of simulating the entire body model. Moreover, it is well known that the RF-EMF absorption is highest in tissues closest to the antenna compared to deep tissues [10].

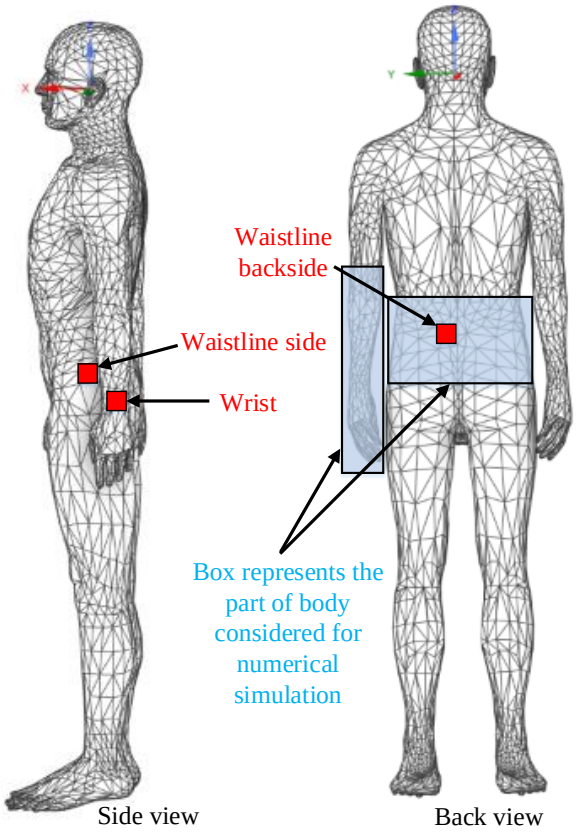

FIGURE 3.3: Different mounting positions of MIFA for evaluation of RF-EMF exposure, the box represents the part of the body selected for evaluation to reduce computation time.

3.6 Human Body Model: Overview and Properties

In section 2.7, we discussed the Ansys human body package, which provides various human body models explicitly designed for electromagnetic exposure assessments. For our investigation, we have chosen the male body model with 4 mm resolution as it strikes the right balance between computational efficiency and accuracy. By adopting a 4 mm human model, we can carry out simulations quickly without compromising on the realistic assessment of electromagnetic exposure of wearable devices. This approach also ensures compliance with relevant safety guidelines and regulatory standards. The dielectric and thermal properties of the tissues were considered from the ITIS database [157] as shown in Table 3.1.

TABLE 3.1: Dielectric and thermal properties of human tissues at 2.4 GHz [157]

Tissues	Permittivity	Electrical Conductivity (S/m)	Density (kg/m^3)	Heat Capacity (J/kg/°C)	Thermal Conductivity (W/m/°C)
Skin	38.1	1.44	1109	3391	0.37
Bladder	57.7	2.02	1071	3716	0.52
Colon	54.0	2.00	1088	3655	0.58
Kidney	52.9	2.39	1066	3763	0.53
Liver	43.1	1.65	1079	3540	0.52
Lung Inflated	20.5	0.79	394	3886	0.39
Pancreas	57.3	1.93	1087	3164	0.51
Prostate	57.6	2.13	1045	3760	0.51
Small intestine	54.5	3.13	1030	3595	0.49
Spleen	52.5	2.2	1089	3596	0.53
Stomach	62.2	2.17	1088	3690	0.53
Air	1	0	1	1004	0.03

3.7 Overview of the Approach Implemented for Systematic Evaluation of RF-EMF Exposure via Numerical Simulation

This section discussed a system-level approach for evaluating RF-EMF exposure in detail, employed to numerically assess SAR and tissue temperature elevation in tissues across various mounting positions and incorporating an underground mine model.

The wearable device antenna was modelled using the HFSS solver within the Ansys Workbench platform. This integration enables seamless data transfer, geometry manipulation, and solution sharing across diverse engineering modules. This study utilised HFSS, Geometry (previously named SpaceClaim), and Mechanical solvers for SAR evaluation, tunnel CAD model processing, and tissue temperature elevation analysis, respectively.

SpaceClaim facilitates geometry processing within this framework and shares the geometry with HFSS. The HFSS evaluates electromagnetic losses, and SAR values

are computed using a 4 mm tissue model and analyses the performance parameters of the MIFA antenna. Subsequently, these computed loss densities are imported into the Mechanical solver, where HFSS shares geometry and material properties alongside tissue losses. These losses are defined as heat sources within the Mechanical solver, which further incorporates temperature monitoring on tissues and boundary conditions. The system-level diagram of the Ansys Workbench used for SAR and temperature elevation in tissues for the underground mine environment is shown in Figure 3.4a and Figure 3.4b, respectively.

The steady-state solver within the Mechanical module furnishes maximum temperature in tissues with infinite time assumptions, while the transient solver offers temporal tissue temperature elevations. Computational time and memory requirements for the transient solver are contingent upon time step selections and the duration of RF-EMF exposure. All simulations were conducted utilising an i7-10700 CPU with 64GB of RAM.

3.8 Summary

In this chapter, the research methodology is explained to investigate the RF-EMF exposure of wearable devices in underground mine environments and the associated variability across different parameters related to RF-EMF exposure and the surrounding environment. A comprehensive discussion of each objective offers insights into the methodology implemented to achieve specific goals. Additionally, a detailed description of the measurement methodology is provided.

The different mounting positions of wearable devices are discussed, highlighting their advantages in investigating RF-EMF exposure through numerical simulation in both free space and underground mine environments. Specifically, wrist and two waistline scenarios were selected for evaluating SAR and temperature elevation in tissues. A detailed discussion on the human body model and tissue properties obtained from the ITIS database is also provided. Finally, it is essential to explain

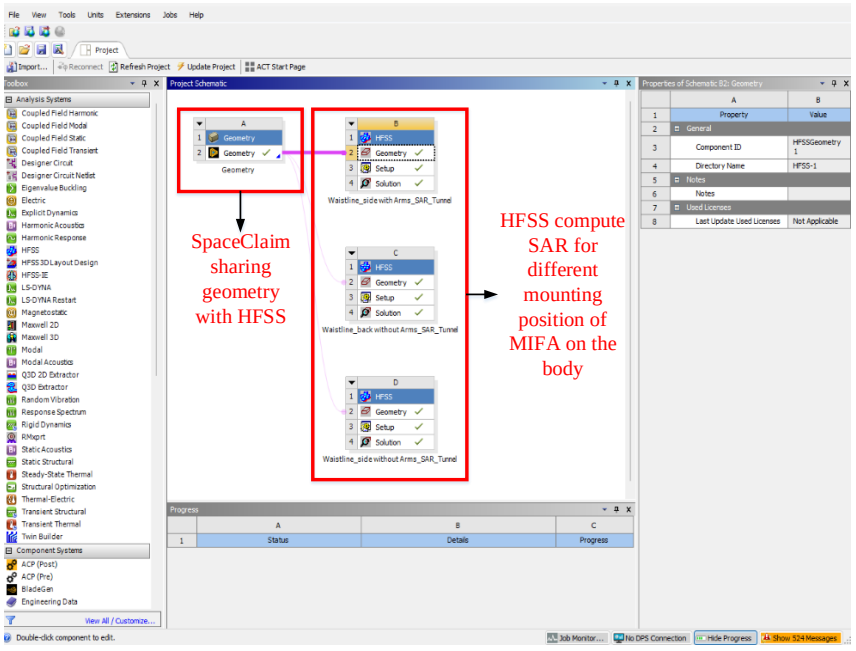

(a)

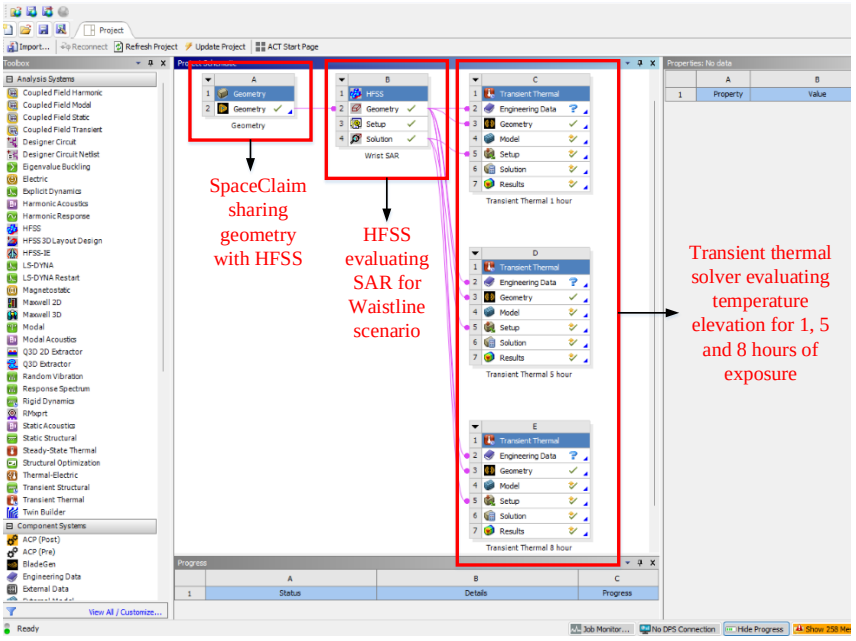

(b)

FIGURE 3.4: System-level diagram of the Ansys Workbench used for RF-EMF exposure evaluation in underground mine environment in terms of (a) SAR, and (b) temperature elevation in tissues.

the approach used for the systematic investigation of RF-EMF exposure in free space and underground mine environments.

Chapter 4

SAR Assessment for Wearable Devices

4.1 Introduction

In this chapter, a numerical evaluation of RF-EMF exposure of the wearable device was conducted for both free space and tunnel scenarios. Firstly, the modelling and considerations for evaluating the wearable device were explained in Section 4.2, including a discussion on human body models. Subsequently, the SAR for two mounting positions of the wearable device, namely wrist and waistline, was analyzed. The variability of SAR for different parameters of the RF-EMF source was also discussed and compared. Finally, in Section 4.5, the SAR values were analyzed for the tunnel scenario while considering variations in properties of the underground mine rock. The results were thoroughly discussed and compared with those of previous studies.

4.2 Numerical Model of the Wearable Device

The emergence of wearable technology has revolutionised various industries thanks to its ability to provide easy and efficient solutions for monitoring and tracking tasks. As wearable devices continue to gain popularity in hazardous work environments, it has become increasingly important to assess RF-EMF exposure to ensure the safety and welfare of workers.

The investigation of RF-EMF exposure for wearable devices, as detailed in [156, 158], utilized an ESP32-WROOM-based device developed by the Central Institute

for Labour Protection, Warsaw, Poland. Additionally, Chapter 2 highlighted the widespread use of the ESP8266 IoT board in wearable devices, which comes in various versions featuring two variations of the meandered F-shape antenna (MIFA). Given this context, the ESP32 board was chosen for the current study to assess RF-EMF in underground mine environments. This choice ensures consistency and allows for the validation of RF-EMF exposure investigations across different ESP board versions.

The wearable wireless device encompasses several components, such as a sensor, battery, antenna, and processing board (e.g., ESP32). For a comprehensive model of the wearable device, it is essential to include all components to replicate the model accurately. In evaluating the RF-EMF exposure of the wearable device, the antenna structure, which serves as the source of RF-EMF, holds paramount significance, as discussed in [156, 159, 160]. In the study by Zradzinski et al., a pilot test was conducted involving all components of the wearable device [156]. The test revealed insignificant differences in the maximum value of SAR_{10g} (0.2%) and proposed a simplified model structure with a MIFA antenna. Consequently, based on these findings, only the antenna structure will be considered for the modelling to assess the exposure metrics.

The wearable device ESP32-WROOM comes with an omnidirectional antenna called the MIFA. The MIFA operates in the ISM frequency band (2400-2483.5 MHz), supporting Wi-Fi and Bluetooth communication using international standards IEEE 802.11 and IEEE 802.15.1. The ESP-32 module provides maximum EIRP (Effective Isotropic Radiated Power) for Wi-Fi communication is 100 mW (20 dBm), and for Bluetooth, it is 8 mW (9 dBm) [161]. The numerical model of the MIFA antenna and ground was modelled with a copper thickness of 0.035 mm, conductivity of 5.8×10^7 S/m, a relative permittivity of 1, and a density of 8933 kg/m^3. The MIFA antenna was placed on the substrate FR-4 epoxy with permittivity of 4.4, a conductivity of 3.8×10^{-3} S/m, a loss tangent of 0.02, and a density of 1900 kg/m^3. The optimized dimensions of the MIFA are shown in Figure 4.1.

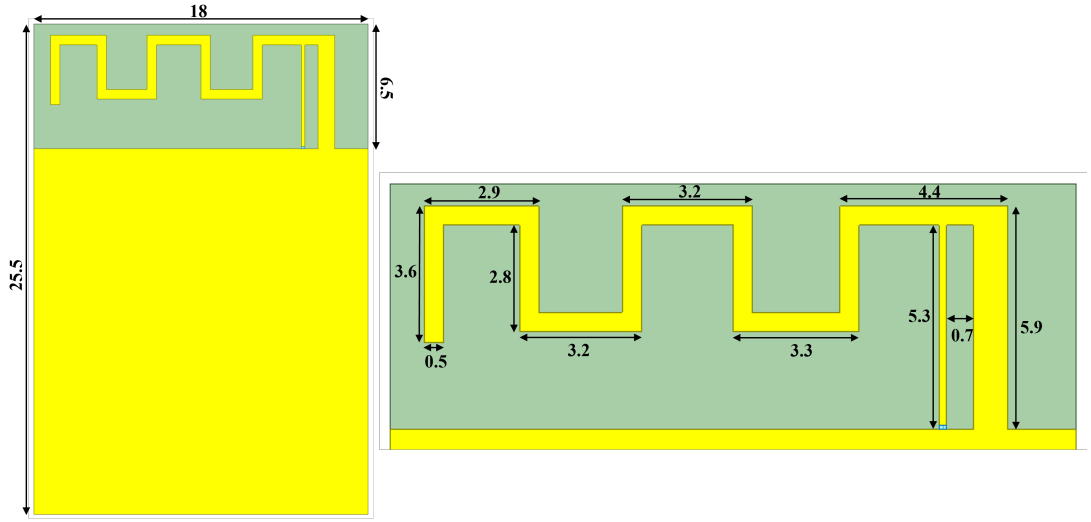

FIGURE 4.1: Dimensions (in millimeters) of the numerical model depicting the meandered inverted-F antenna (MIFA).

4.2.1 Performance Evaluation of MIFA

The numerical model of the MIFA was tested for its performance at 2.4 GHz (2400 MHz). The reflection coefficient, voltage standing wave ratio (VSWR), and far-field radiation pattern were plotted for verification. The reflection coefficient, also known as S_{11}, is a fundamental parameter that offers intuition into an antenna's impedance matching, efficiency, and overall performance within a given system [162]. It indicates the frequency range over which the antenna structure is appropriately matched, allowing it to radiate electromagnetic waves efficiently. Typically, a threshold of -10 dB is utilized to determine the extent of reflection from the antenna structure, where only 10% of the incident power is reflected [162]. The reflection coefficient was analyzed at 2.4 GHz to evaluate the behaviour of MIFA, as shown in Figure 4.2. The analysis revealed a bandwidth of 70 MHz, ranging from 2.37 GHz to 2.44 GHz.

Similarly, the far-field radiation pattern of the MIFA was also plotted, as shown in Figure 4.3a. It shows the omnidirectional radiation pattern of the MIFA with a maximum gain of 2.1 dB. The 3D radiation pattern with the MIFA structure is presented in Figure 4.3b, offering valuable insights into its radiation behaviour.

Other performance parameters of the MIFA antenna, such as Voltage Standing

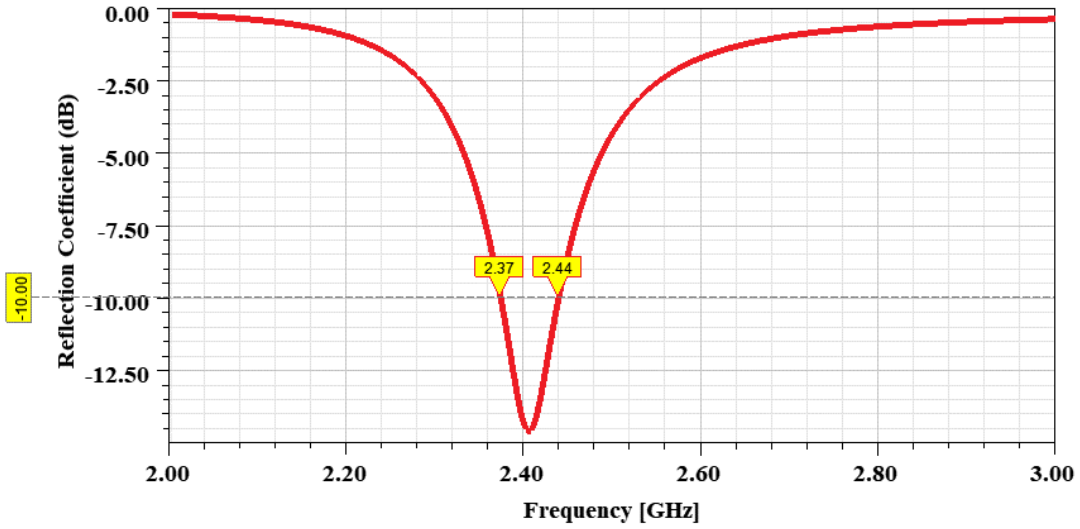

FIGURE 4.2: Reflection coefficient (S_{11}) of the MIFA at 2.4 GHz.

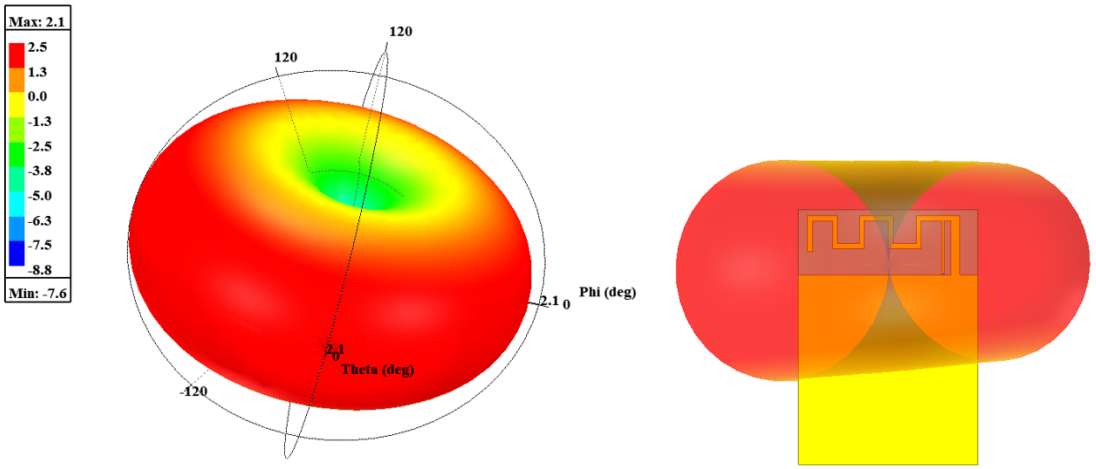

(a) (b)

FIGURE 4.3: Far field radiation pattern of the MIFA at 2.4 GHz (a) 3D far-field radiation pattern and (b) 3D far-field pattern with antenna structure.

Wave Ratio (VSWR) and surface current distribution, were also observed. The nominal value of the VSWR should be between 0 to 2 for better performance of the antenna. The VSWR of MIFA is shown in Figure 4.4a. It can be seen that the VSWR is below 2 for 2.37 GHz to 2.45 GHz. Similarly, the surface current distribution was plotted in Figure 4.4b. It provides insight into the distribution and behaviour of electromagnetic energy along the surfaces of the MIFA.

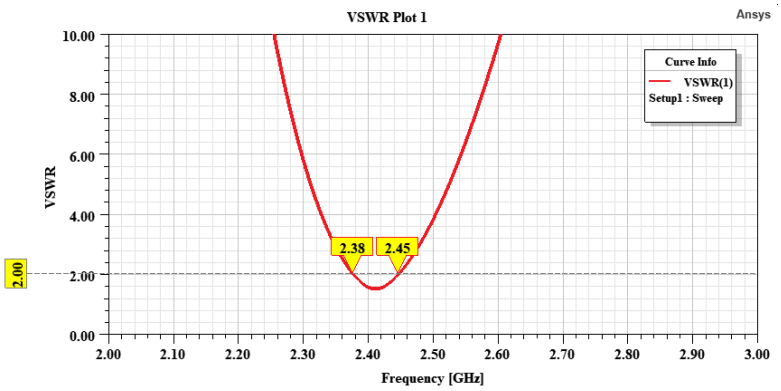

(a)

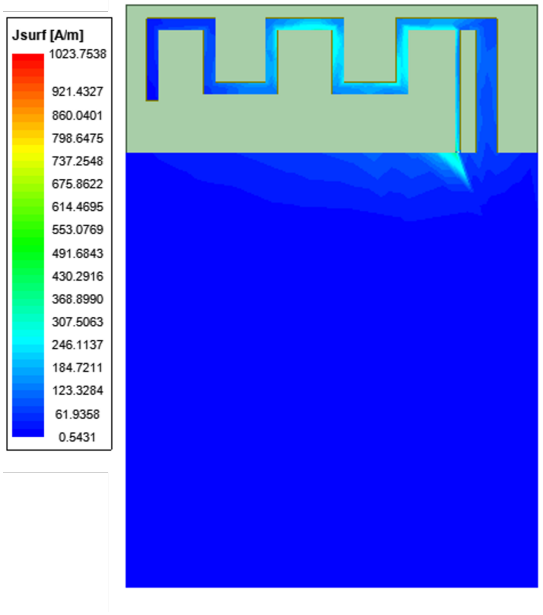

(b)

FIGURE 4.4: Performance parameters of the MIFA at 2.4 GHz (a) voltage standing wave ratio and (b) surface current density.

4.3 Exposure Assessment for a Wearable Device in a Free Space Environment

The SAR was investigated for various mounting positions of the wearable device on the body within a free-space environment. This setting offers valuable insights, as reflections from nearby objects have no impact. A detailed analysis of the SAR for each mounting position is provided below:

4.3.1 SAR for Wrist in a Free Space Environment

Various smartwatches are widely used for health activity monitoring and worker tracking purposes [152]. The wrist, classified as an extremity by the ICNIRP guidelines [4], benefits from a higher exposure threshold compared to other body regions, with a SAR for a 10-gram averaged mass of tissues in the limbs set at 4 W/kg [4]. Understanding SAR levels is critical for designing and positioning wearable devices on the wrist, ensuring electromagnetic exposure remains safe and safeguarding worker health. Mounting the wearable device on the wrist is significant for two reasons: first, due to its higher exposure thresholds compared to other body parts, and second, because it enables monitoring of various health parameters such as blood pressure, heart rate, sleep patterns, and location tracking, capabilities not easily achieved with other mounting positions like the waistline or head.

A wearable antenna was positioned just above the wrist on a human model to assess exposure, mimicking a typical wristband placement, as illustrated in Figure 4.5. The antenna was positioned 5 mm away from the human body for numerical assessment, focusing on the arm to streamline computational efforts. The numerical simulation of the wrist involved solving 82,119 tetrahedrons, as depicted in Figure 4.5b. Figure 4.6 illustrates the electric field distribution, with a maximum E-field of 151.96 V/m. Additionally, Figure 4.7 depicts the distribution of the maximum peak spatial average SAR for a 10-gram mass of skin tissues. Notably, the SAR_{10g} distribution reveals a hotspot on the wrist under the MIFA, with the wrist region experiencing the highest SAR exposure, reaching a maximum SAR value of 4.076 W/kg.

4.3.2 SAR for Waistline in a Free Space Environment

The waistline is crucial for evaluating SAR levels in wearable devices for several reasons. It is a preferred location for various types of wearable devices, such as fitness trackers, smart belts, and waistbands. Many users favor this position due

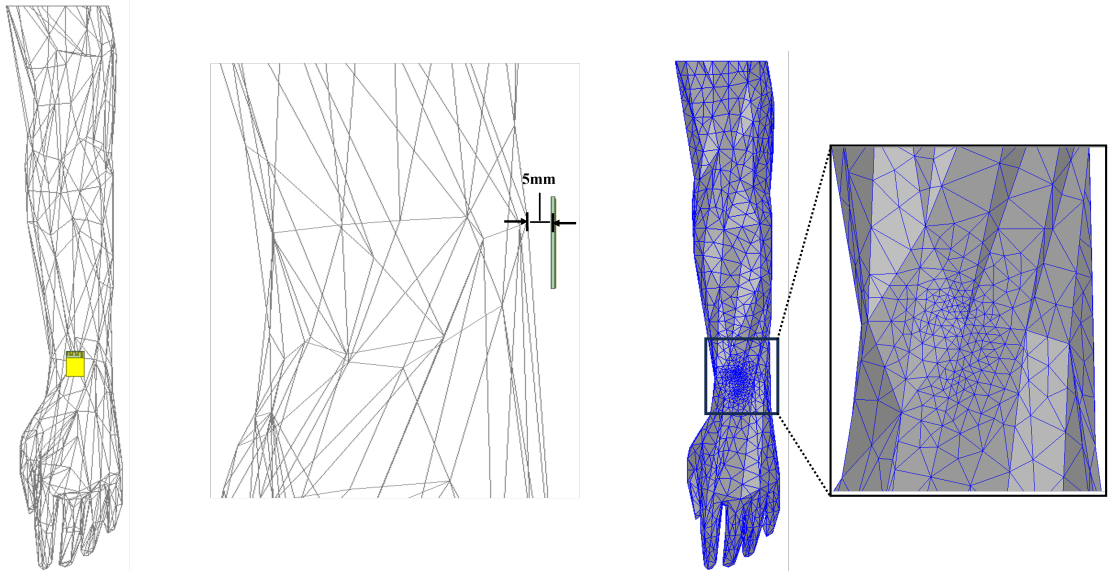

(a) (b)

FIGURE 4.5: Simulation setup for wrist (a) MIFA mounted on the wrist of the human body (left), close side view representing the distance between skin and antenna (right) and (b) mesh view of the wrist.

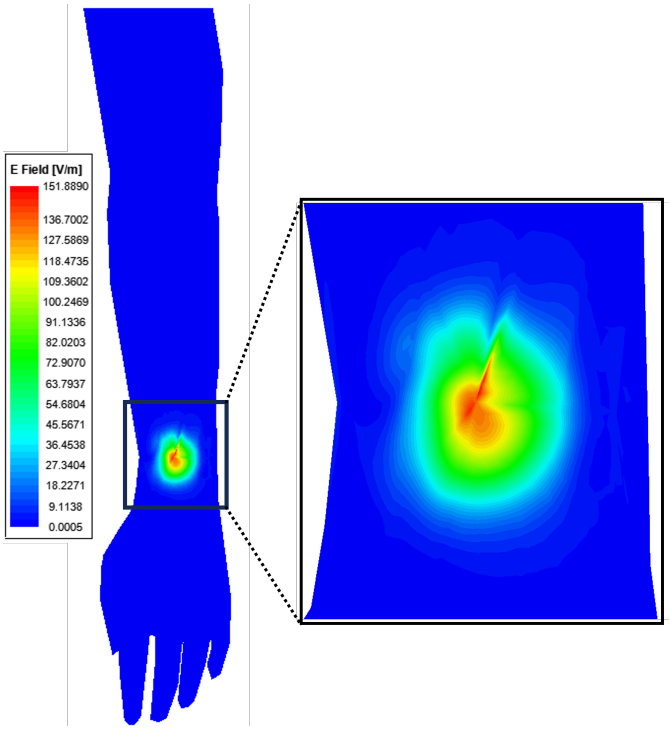

FIGURE 4.6: Distribution of the electric field on the wrist at a frequency of 2.4 GHz.

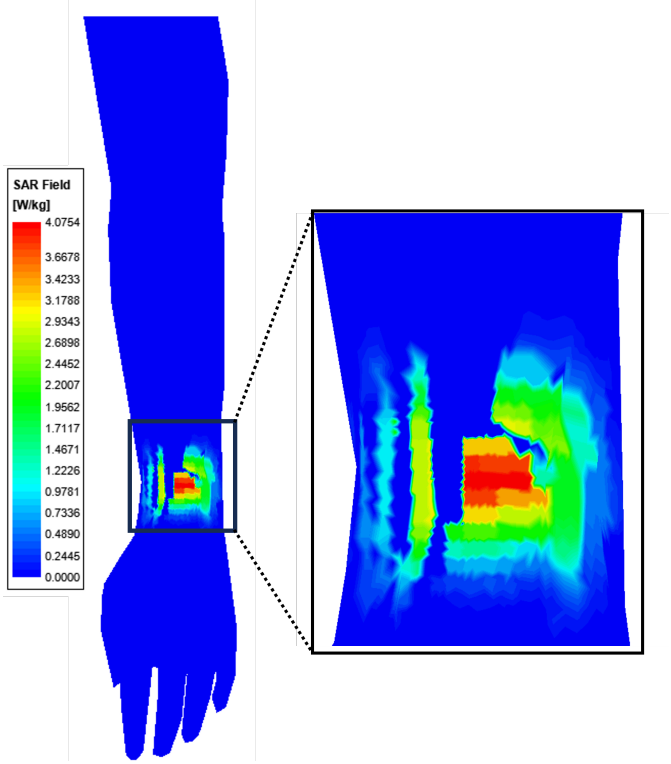

FIGURE 4.7: Spatial distribution of SAR_{10g} on the wrist at 2.4 GHz.

to its non-intrusive nature and easy accessibility. Therefore, understanding the SAR levels at the waistline is essential to ensure the safety and well-being of the many individuals who use these devices daily.

Additionally, the waistline region encompasses crucial organs and tissues sensitive to electromagnetic radiation. The antenna's proximity to the body in this area may lead to notable SAR values, especially if the antenna design is not optimal or if the wearable device is worn for extended periods.

Moreover, the waistline is a region where body composition and clothing can influence electromagnetic energy absorption. Variations in fat and muscle distribution can impact the amount of electromagnetic energy absorbed by the body. Additionally, the presence of clothing between the wearable device and the skin can alter SAR levels, underscoring the importance of evaluating SAR at the waistline under realistic conditions.

Assessing SAR at the waistline provides valuable insights into potential health risks associated with wearable devices. It enables the identification of any potential

hotspots of SAR concentration and aids in developing safe and compliant wearable devices that adhere to established exposure limits. Therefore, in this study, two distinct potential mounting positions for the wearable device are investigated. The first involves mounting the device on the side of the torso at the waistline, while the second position is placing it on the backside of the waistline. Both positions significantly impact the exposure levels experienced by the worker. For instance, positioning the wearable device on the side of the torso can lead to heightened reflections from the nearby tunnel boundaries, potentially increasing the worker's exposure.

Placing the wearable device at the back of the waistline has advantages, mainly because it reduces reflections from surrounding boundaries. This study aims to thoroughly analyze how different mounting positions affect electromagnetic exposure, specifically examining the impact of wearable device placement on the torso in hazardous environments, such as underground mines. The scenarios mentioned will be investigated individually below:

4.3.2.1 SAR for Wearable Device Positioned at the Side of the Waist in Free Space Environment

The wearable device was mounted on the side of the waistline at a distance of 5 mm, as shown in Figure 4.8. Only the relevant part of the torso (100 mm above and below the antenna structure) was selected to reduce the computational power required to simulate the complete torso. The E-field distribution represents the hotspot on the same positions where MIFA was placed, as illustrated in Figure 4.9a. Similarly, the maximum averaged SAR_{10g} value was 3.308 W/kg, and the SAR_{10g} distribution on the torso is shown in Figure 4.9b.

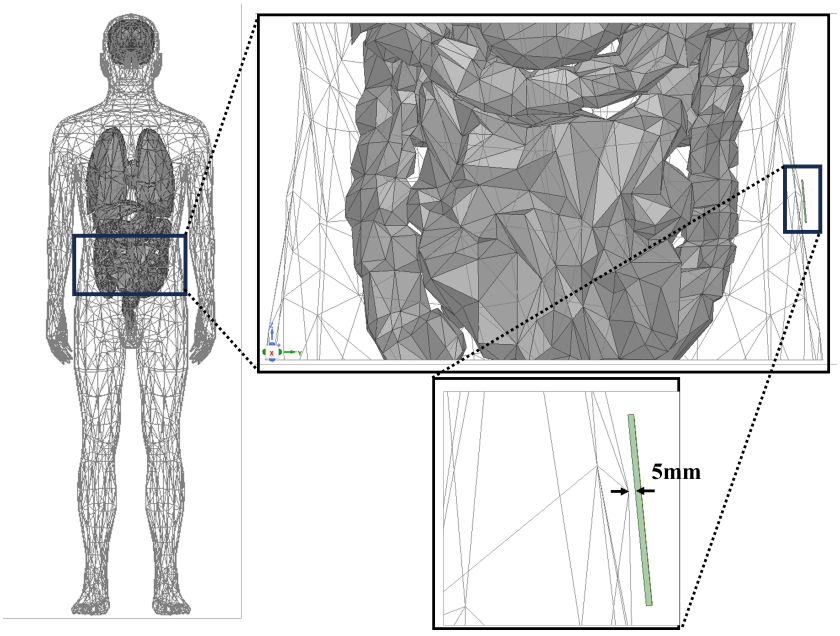

FIGURE 4.8: Simulation setup of the MIFA on the side of the waistline.

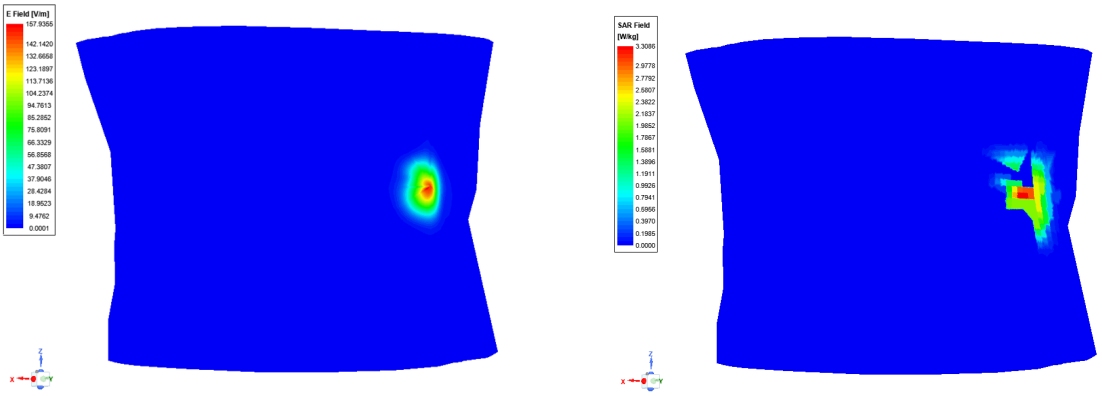

(a) (b)

FIGURE 4.9: Simulation results for MIFA placed on the side of the waistline (a) E field distribution and (b) SAR_{10g}

4.3.2.2 SAR for Wearable Device Positioned at the Back of the Waist in Free Space Environment

In this scenario, the wearable device (MIFA) was mounted on the backside of the waistline at a distance of 5 mm, as shown in Figure 4.10a. The simulated mesh was plotted as shown in Figure 4.10b. The E-field distribution shows the hotspot right under the positions where MIFA was placed on the backside of the waistline, as illustrated in Figure 4.11a. The maximum electric field on the skin tissue was 140.251 V/m. Similarly, the maximum averaged SAR_{10g} value was 2.410 W/kg,

and the SAR_{10g} distribution on the torso is shown in Figure 4.11b. The difference in SAR value between the two positions was due to the difference in the flat surface closer to the skin tissues.

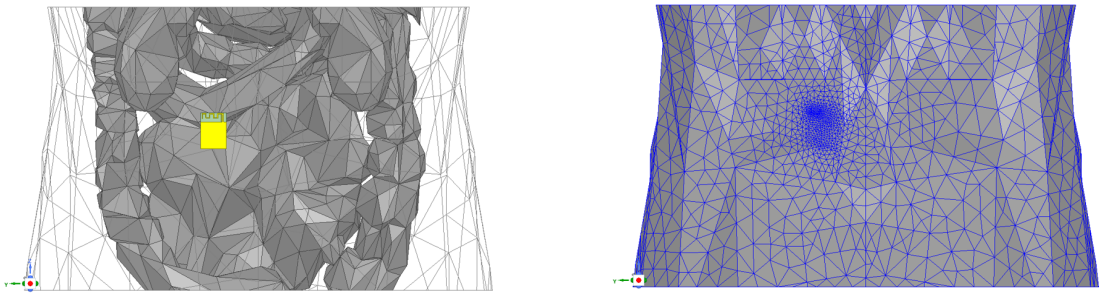

(a) (b)

FIGURE 4.10: Simulation setup when MIFA is placed (a) on the backside of the waistline (b) simulated mesh of the scenario

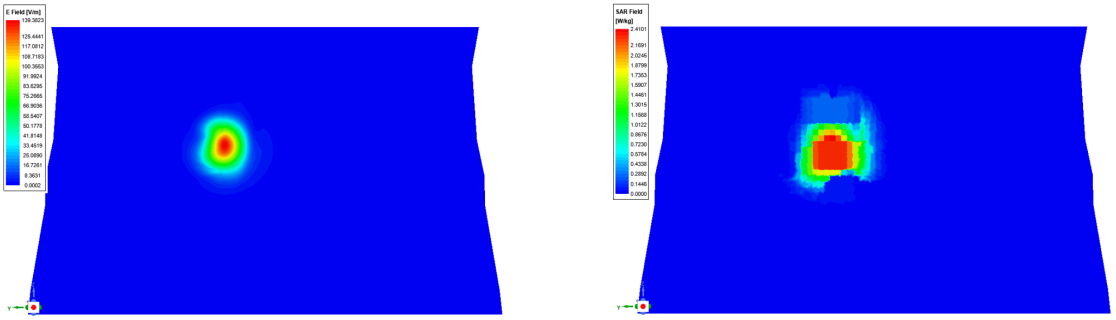

(a) (b)

FIGURE 4.11: Simulation results for MIFA placed on the backside of the waistline (a) E field distribution and (b) SAR_{10g}

The SAR values at 2.4 GHz for various scenarios and studies were compared in Table 4.1. The SAR values reported for the head in [156], using MIFA, exceeded ICNIRP levels, suggesting the need to mount the wearable device outside the safety helmet. Similarly, the results presented in our study show that the SAR values were also higher for the wrist and waistline side scenarios under conditions of RF-EMF exposure similar to those discussed in [156] (such as MIFA antenna, power level of 0.1 W, and distance between antenna and body). Consequently, the ESP32-WROOM board exhibited higher SAR values in worst-case scenarios for the wearable device's wrist and waistline mounting positions. Modifying the MIFA structure to mitigate RF-EMF exposure or adding shielding between the

antenna and body is recommended. Increasing the distance between the body and MIFA can also reduce the SAR values.

TABLE 4.1: Comparison of MIFA RF-EMF exposure for different mounting positions at 2.4 GHz

Reference	RF-EMF source	Exposure scenario	SAR_{10g} (W/kg)
[156]	ESP32-WROOM	Headband	4.0
		Helmet	0.4
This work	ESP32-WROOM	Wrist	4.0754
		Waistline side	3.308
		Waistline back	2.410

4.4 SAR Variability for Parameter Variations of RF-EMF Source

Understanding the effects of various parameters on SAR variability is paramount, as this knowledge is crucial for effectively mitigating RF-EMF exposure in both the general public and workers. SAR variability depends on multiple factors associated with the source of the RF-EMF, such as the frequency of the electromagnetic signal, the transmit power level, the distance between the source and the exposed body, and the antenna's orientation. Various studies have investigated the effects of frequencies below 6 GHz [10, 156]. Consequently, factors such as the distance between the antenna and tissues, the transmit power of the antenna, and the antenna's orientation play crucial roles in determining SAR variability for a wearable device at a specific frequency.

As the distance between the source and tissues increases, the field strength diminishes, consequently reducing the SAR in the tissues. This relationship between SAR and distance is evident in the literature, highlighting the direct correlation between the device's proximity to tissues and SAR levels. However, it is critical to determine the safe distance for mounting the wearable device on the worker.

Similarly, the transmit power of the wearable device plays a pivotal role in determining the magnitude of the electromagnetic field emitted by the antenna. Higher transmit power results in greater exposure to tissues located in proximity.

Additionally, the antenna's orientation on the body significantly impacts the distribution of electromagnetic energy. Different orientations lead to varying patterns of energy absorption and SAR values within tissues. Therefore, these factors intricately contribute to the overall RF-EMF exposure levels experienced by the tissues, necessitating careful consideration in assessing and designing wearable devices and their deployment in various scenarios, especially in confined environments such as underground mines.

4.4.1 Analysis of SAR Variation with Distance between Antenna and Tissues

The SAR was analyzed for variation in the distance between the antenna and tissues for the wrist and waistline scenario. The SAR values were analyzed at distances of 5 mm, 10 mm, 15 mm, and 20 mm from both the wrist and waistline scenarios, considering a maximum power level of 0.1 W allowed at 2.4 GHz, leading to a worst-case assessment. Figure 4.12 compares the SAR's variation for different distances. It can be seen that the SAR value decreases significantly with the increase in the distance between the tissues and the antenna. The SAR value on the wrist was lower than the ICNIRP limits of 5 mm to place it closer to the human arm tissues. At the distance of approximately 12.5 mm, the SAR value for the waistline scenario was lower than the prescribed regulatory limit of ICNIRP [4] for a torso.

In contrast, it was recommended to maximize the distance between the antenna and the body to mitigate the lower levels of exposure. The safe distance for the MIFA was approximately more than 12 mm, with a SAR value below regulatory limits for both scenarios. Due to the difference in the body's shape, the SAR value on the wrist changes more rapidly with distance than the waistline.

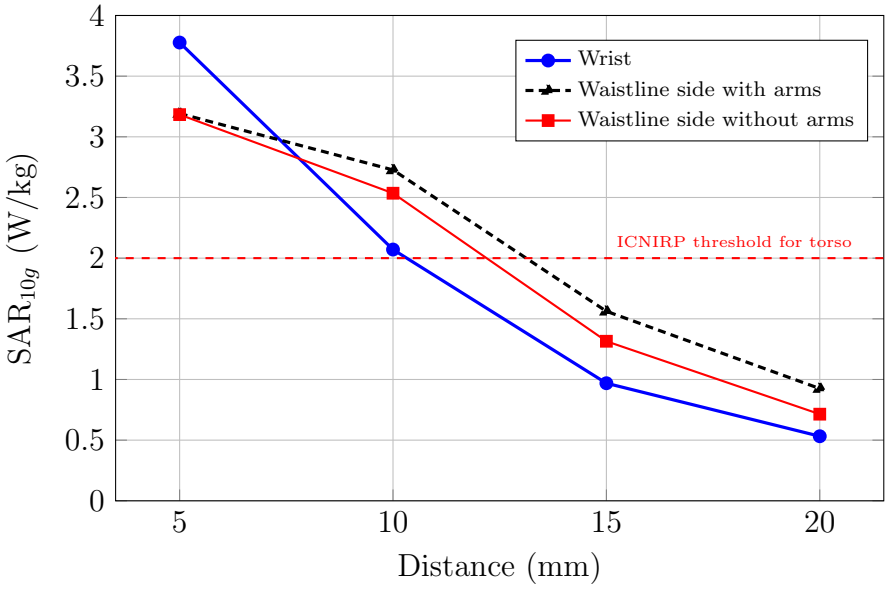

FIGURE 4.12: SAR variability to the distance between antenna and tissue for MIFA placement on Wrist and Waistline.

4.4.2 Transmitting Power and SAR variability

When the transmitting power of the antenna is increased, the intensity of the RF-EMF in the surrounding environment of the antenna is increased. The higher intensity of the electric fields increases the SAR in the biological tissues. In mathematical terms, SAR is proportional to the square of the electric field strength generated by the transmitting antenna as expressed in Eq. 2.1. The SAR variability with transmit power of the source of the RF-EMF was analyzed in different studies [10, 163]. In [163], transit power level significantly influences SAR and temperature distribution in the head tissues. Similarly, in [10] investigated the maximum power levels that can be used for wearable devices in case of emergency/ rescue operations without exceeding the ICNIRP and IEEE regulatory limits of the SAR in underground mine scenarios. Hence, conducting a thorough examination of SAR variability across different transmit power levels of the wearable device (MIFA) is crucial. Moreover, the adaptability of the ESP32 is highlighted, providing adjustable power levels ranging from 1 mW to 100 mW [164].

The investigation into SAR variability encompassed both wrist and waistline scenarios, involving manipulating power levels by the increment of 25 mW, as depicted in Figure 4.13. The SAR increases proportionally with the elevation of the power level of the MIFA antenna. Furthermore, the wrist-mounted configuration exhibited a higher maximum SAR than the waistline configuration. At the lowest power level (1 mW), the SAR values were 0.038 W/kg and 0.032 W/kg for wrist and waistline scenarios, respectively. These findings advocate for the implementation of wearable devices featuring adjustable power settings, which could serve as a mitigation strategy for controlling RF-EMF exposure levels. Furthermore, SAR values at maximum power level indicate that the MIFA is suitable for wrist positioning, whereas, for waistline positioning, it exceeds ICNIRP guidelines [4].

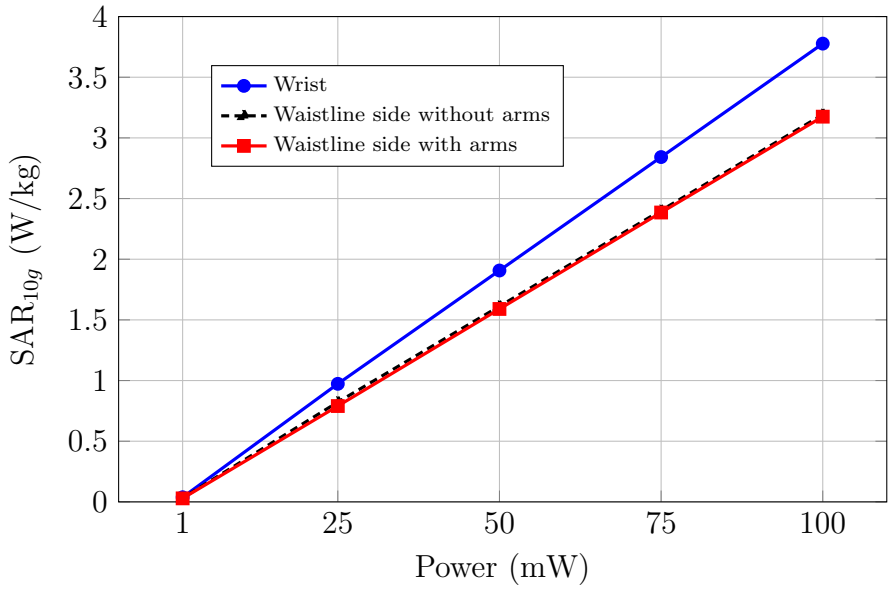

FIGURE 4.13: SAR variability with different power levels for MIFA placement on wrist and waistline.

4.4.3 Device Orientation and SAR variability

The antenna's orientation significantly influences the distribution of electromagnetic fields and subsequently impacts the SAR [165]. As the orientation of the antenna changes, the pattern of electromagnetic radiation emitted also changes,

leading to variations in SAR values [166]. Antenna orientation is critical in determining how electromagnetic waves interact with the surrounding environment and tissues. For instance, if the antenna is oriented so that the emitted waves are directed toward a specific body part, that region might experience higher SAR due to increased energy absorption. On the other hand, if the waves are not aligned with the body, lower SAR values in specific tissues may be observed. Therefore, it is essential to investigate the impact of antenna orientation on exposure metrics.

The SAR variability was analyzed across different orientations of the MIFA antenna, considering both wrist and waistline placements, with a fixed power level of 0.1 W, as shown in Figure 4.14. The MIFA antenna was rotated around its axis aligned parallel to the body, denoted as the y-axis. While the SAR displayed minimal fluctuations for the wrist scenario, it exhibited more substantial alterations for the waistline placement. Interestingly, this SAR variation remained consistent across different considerations of the tissues, i.e., with and without consideration of the arms. Specifically, the SAR value reached its minimum at a 90^0 orientation, signifying the pivotal role of antenna alignment in devising strategies for exposure mitigation for wearable devices.

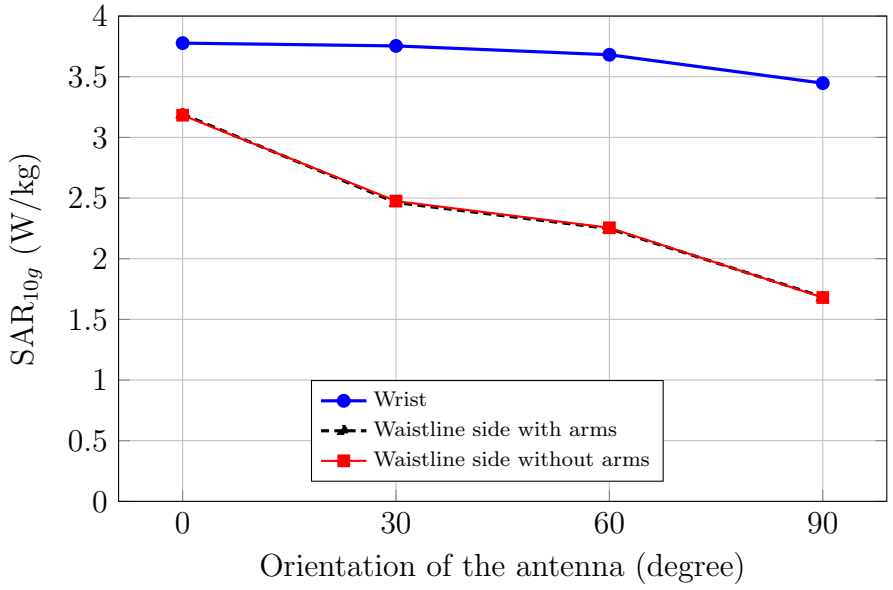

FIGURE 4.14: SAR variability with respect to antenna orientation for MIFA placement on wrist and waistline.

4.5 SAR Assessment in Tunnel Environments: Analysis and Findings

RF-EMF exposure in confined environments poses unique challenges, leading to higher exposure levels due to the reflection and scattering of electromagnetic waves from nearby objects. This elevation in exposure is influenced by various factors, such as the distance between tissues and surrounding objects, as well as the properties, shape, and orientation of the objects [10, 167–169]. Notably, research has shown that metallic walls near mobile phones can increase the SAR value by up to 7% at a distance of 394 mm [148]. Similarly, investigations into multiple Wi-Fi devices inside a metallic enclosure demonstrated that spacing, Wi-Fi device count, and relative positions in the room are crucial factors affecting RF-EMF exposure [169]. Consequently, it is essential to incorporate the surrounding environment when evaluating RF-EMF exposure of wearable devices, especially in confined spaces like the working environment of underground mine workers, where various metallic objects are present close to the worker, potentially amplifying RF-EMF exposure.

A LIDAR[1] (Light Detection and Ranging) scan model incorporates the surrounding environment in evaluating the RF-EMF exposure. Recently, a LIDAR scan model was used to study the roughness impact on the path loss exponent of the wireless signal propagation in the natural caves [49].

Similarly, a LIDAR-scanned model of the Wits mock mine was used to investigate the impact of the tunnel structure on the exposure of wearable devices worn by the worker. Therefore, a LIDAR-scanned model of the Wits mock mine with high resolution (2 mm) was used in this study. The scanned model was imported to the point cloud, and the DXF file of the LIDAR model was imported to Ansys Geometry for further processing. The LIDAR scanned model was 67 m in length

[1]LIDAR (Light Detection and Ranging) scanning is a cutting-edge technology that plays a pivotal role in various industries and applications. By emitting laser pulses and measuring the time it takes for the laser to return after hitting an object, LIDAR systems create precise 3D representations of objects and environments. This advanced scanning technique offers unparalleled accuracy and detail, making it indispensable in topographic mapping, autonomous vehicles, forestry, urban planning, archaeology, and environmental monitoring.

and approximately 3 m in width. In numerical modelling, the complexity and size of the model play a vital role in the accuracy and required computational resources. High computational resources are required to simulate such a large tunnel structure. Maintaining the model's accuracy and reducing computational resources is compulsory by selecting only relevant parts of the objects. Therefore, a slice of 2 m of the LIDAR scanned model of the Wits mock mine was selected for further processing. The facets of the geometry were converted to a solid with a thickness of 100 mm, as shown in Figure 4.15.

To further reduce the model size, it is essential to consider only relevant parts of the tunnel model, such as the wall adjacent to the wearable device, which can incorporate the reflections of the RF-EMF and potentially increase the worker's RF-EMF exposure. The roof, floor, and opposite wall have less and minimal impact on the reflections and absorption. Therefore, the model was further reduced to 1 m $\times$ 1 m (eight times larger than the wavelength at 2.4 GHz). The CAD model of the tunnel was imported to the HFSS solver to simulate the RF-EMF scenario. In HFSS, the geometry was assigned to the material properties of rock [170].

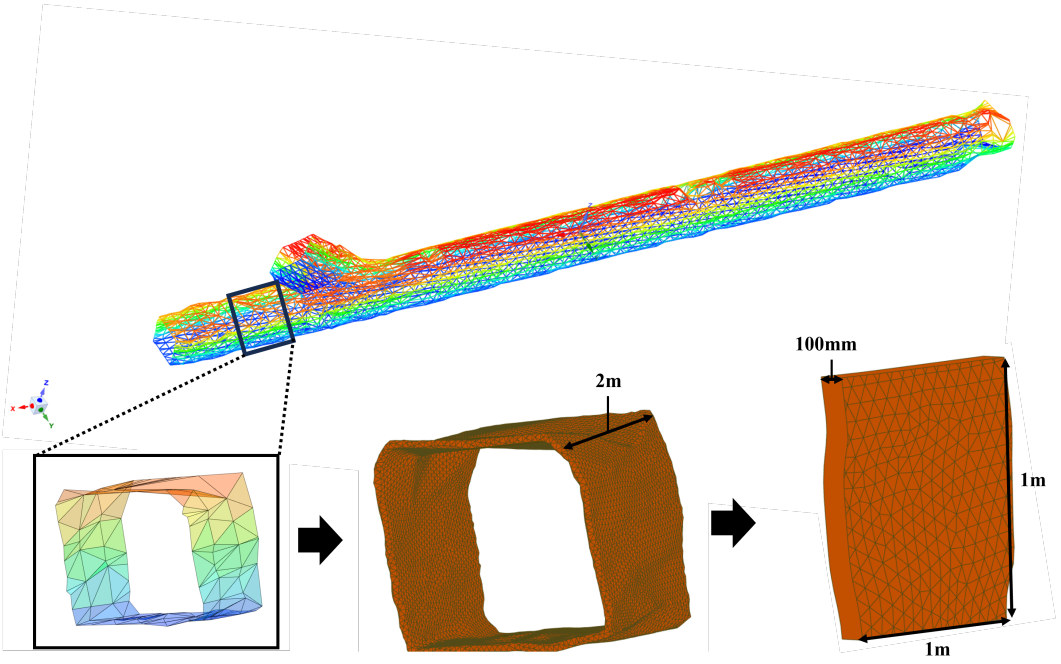

FIGURE 4.15: Processing of the LIDAR scanned model of the Wits mock mine tunnel.

TABLE 4.2: Dielectric and thermal properties of the rock utilized in this study.

	Permittivity	Electrical Conductivity (S/m)	Density (kg/m^3)	Heat Capacity (J/kg/°C)	Thermal Conductivity (W/m/°C)
Rock	12.25	0.009976	2574.88	893.25	1.40641

4.5.1 SAR for Wearable Device Positioned on the Wrist in Tunnel Environment

The CAD model of the tunnel was used to determine the realistic impact of the underground mine tunnel on the electric field and absorption of the RF-EMF in the tissues. The MIFA placed on the wrist was used in this scenario. The distance between the tunnel and the wrist was kept 100 mm, as shown in Figure 4.16. The distance between the MIFA and wrist remained the same (5 mm). The electric field and SAR_{10g} distribution on the wrist remains similar, whereas the value is marginally higher than the free space scenario. The maximum SAR_{10g} value on the wrist for the tunnel scenario was 4.101 W/kg.

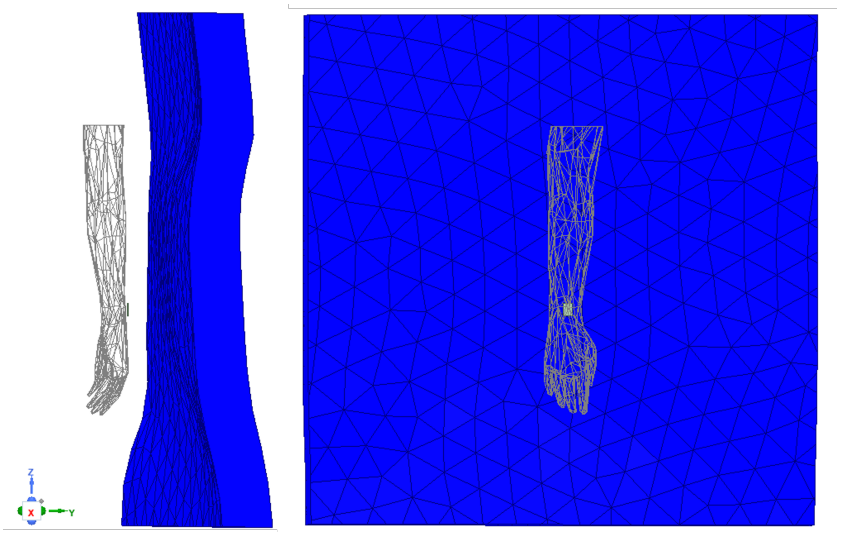

FIGURE 4.16: Simulation setup of the MIFA on the wrist for the tunnel.

4.5.2 SAR for Waistline in tunnel

4.5.2.1 SAR for Wearable Device Positioned on the Side of the Waist in Tunnel Environment

The CAD model of the tunnel structure was imported to evaluate the realistic impact of the tunnel on the absorption mechanism in the tissues. The tunnel model was kept 100 mm away from the skin tissues, whereas the distance between the MIFA and tissues was 5 mm as shown in Figure 4.17. The maximum SAR_{10g} on the skin tissues was 3.325 W/kg.

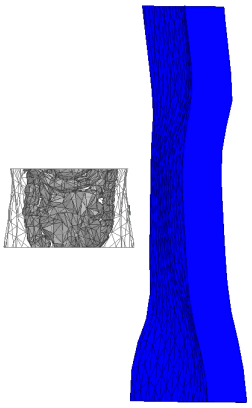

FIGURE 4.17: Simulation setup of the MIFA on the side of the waistline for the tunnel.

4.5.2.2 SAR for Wearable Device Positioned on the Back of the Waist in Tunnel Environment

Similarly, the CAD model of the tunnel was imported and kept 100 mm away from the skin tissues, as shown in Figure 4.18. The maximum SAR_{10g} on the skin tissues was 2.404 W/kg.

Table 4.3 compares SAR values for tunnel and free space environments. The SAR values were obtained for both the tunnel and free space environments and were compared to those from a previous study [10]. The SAR values were found to be slightly higher with the MIFA antenna than the dipole antenna. Additionally, the

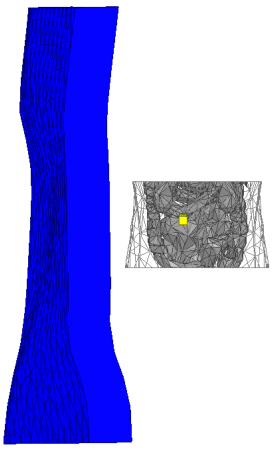

FIGURE 4.18: Simulation setup of the MIFA on the backside of the waistline for the tunnel.

SAR values in the tunnel scenario exceeded the ICNIRP guidelines for both wrist and waistline positions. Therefore, it is recommended that the ESP32-WROOM should not be operated at maximum transmit power in such environments. Further investigation into RF-EMF exposure of these wearable devices is essential. Furthermore, shielding these devices for further mitigation of RF-EMF exposure is necessary.

TABLE 4.3: Comparison of MIFA RF-EMF exposure for different tunnel scenarios at 2.4 GHz

Reference	RF-EMF source	Exposure scenario	SAR_{10g} (W/kg) (Tunnel/Free space)
[10]	Dipole antenna	Head Torso	1.54/1.5 0.94/0.89
This work	ESP32-WROOM	Wrist Waistline	4.076/4.101 3.325/3.308

4.5.3 Investigating SAR Variability in Relation to Tunnel Parameters

The SAR demonstrates notable variation due to the diverse materials present in the surrounding environment of an exposure scenario. These materials possess distinct electromagnetic properties that result in unique interactions with incident

waves. The reflections of the incident waves at material interfaces govern such variations in SAR values. Different studies have investigated the SAR variation for different surrounding materials, such as inside the elevator [171–173], indoor environment [174–176], and inside transport vehicles [177–180].

The distance between these materials and the human body also significantly influences SAR levels. As the distance increases, the material's effect on the electromagnetic field weakens, resulting in lower energy absorption by bodily tissues. In contrast, shorter distances intensify the interaction between the material and the incident wave, potentially causing higher SAR values in the adjacent tissues. The interrelation between distance and SAR underscores the significance of materials' attributes and their spatial proximity in exposure assessments.

Understanding the interaction between these materials and electromagnetic fields is essential in environments like underground mines, where various metallic structures and mineral deposits are common. It aids in predicting SAR variations in different work scenarios and guides the development of safety measures for workers, as previously investigated in the study by the author [10]. In [10], only concrete material was considered, and it was observed that the SAR values were marginally higher than the free space environment. In underground mines, the unique mineral compositions of ore bodies pose distinct challenges, requiring comprehensive investigations into SAR variation. Considering diverse material properties, such analyses thoroughly evaluate exposure levels and promote occupational safety across different environments.

4.5.3.1 SAR Variability Across Different Tunnel Properties

Various materials exhibit distinct electromagnetic properties, including permeability, dielectric constant (permittivity), and conductivity, as highlighted by studies such as [181, 182]. Coal's dielectric constant, for instance, varies between 10 and 34 in medium frequencies, while it ranges from 3.4 to 3.9 at 9 GHz [181]. Most rocks possess permeability values akin to that of vacuum ($\mu_0 = 4\pi \times 10^{-7} H/m$),

except for those with elevated concentrations of ferromagnetic metals. Rock dielectric constants span from 2 to 70, more commonly from 4 to 10, and conductivity ranges from 10^{-6} S/m to 1 S/m [182]. These attributes generally fluctuate based on material water content, with conductivity typically rising and the dielectric constant decreasing as frequency increases [181]. In studies like [183–185], rock dielectric constants fall within the 4 to 20 range, while conductivity ranges from 10^{-2} S/m to 10^{-5} S/m. As a result, a wide spectrum of dielectric constants underwent thorough analysis. The goal was to systematically investigate how these factors contribute to variations in RF-EMF absorption within the human body.

The permittivity of the rock was systematically altered across three increments, ranging from 5 to 15, for both the wrist and waistline scenarios, as illustrated in Figure **??**. Notably, the observed SAR variations were negligible as the permittivity of the rock was increased. This finding suggests that changes in the rock's permittivity within this range do not significantly influence the SAR values for both mounting positions of the MIFA antenna.

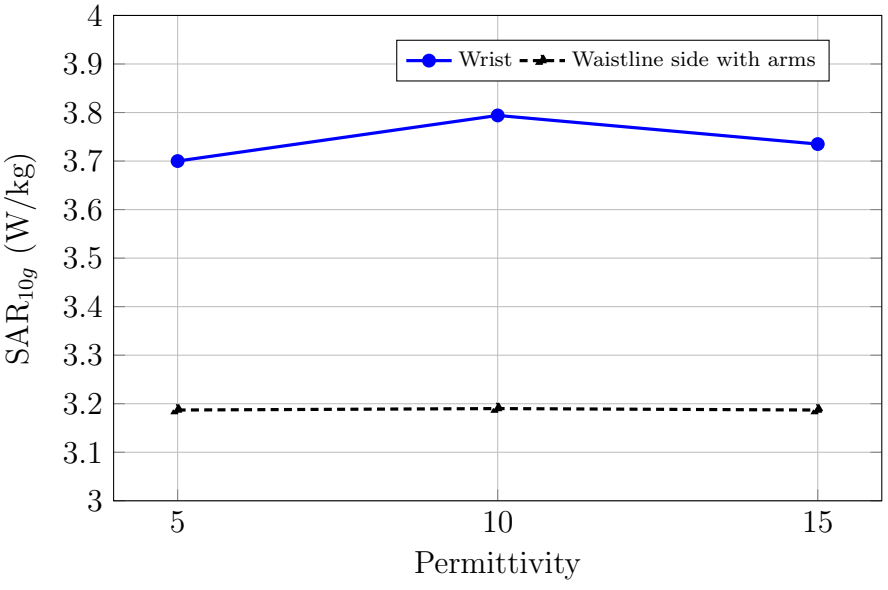

FIGURE 4.19: SAR variability with permittivity of the rock for MIFA placement on wrist and waistline

4.5.3.2 Impact of Distance on SAR Variability Between Wearable Devices and Tunnel

The distance between a wearable device and the boundary of an underground mine tunnel is crucial in minimizing exposure risks associated with RF-EMF. The closer the device is to the boundary, the higher the risk due to increased reflections. To determine the ideal distance, this study considered distances ranging from 100mm to 500mm for both wrist and waistline scenarios. The SAR variations with distance for both placements were investigated, and the results are depicted in Figure 4.20. The observed SAR fluctuations are minimal for both placements. However, in the wrist configuration, the SAR value slightly increased at a distance of 300mm, possibly due to the constructive and destructive interference of RF waves at the 2.4GHz frequency. In contrast, within the waistline setup, the SAR exhibited a minor decrease when the MIFA antenna was positioned on the backside, suggesting that the RF-EMF source was farther from the tunnel boundary, reducing its influence.

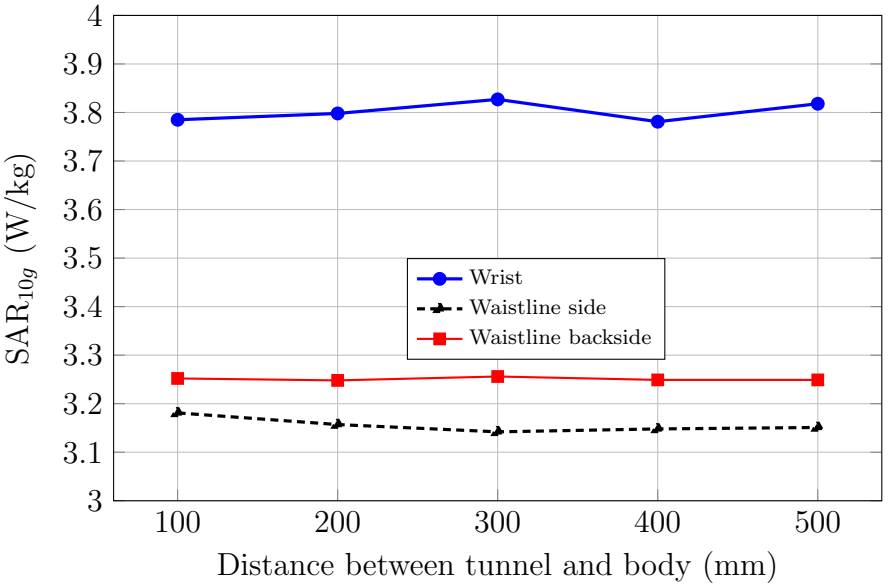

FIGURE 4.20: SAR variability with the distance between body and tunnel structure for wrist and waistline scenarios.

4.6 Conclusion

This chapter assesses the SAR for an ESP32-WROOM-based MIFA antenna in both free space and underground mine tunnel environments. Initially, the MIFA antenna was designed, and its performance was validated for use as an RF-EMF source. This type of antenna is widely used in wearable devices and IoT applications.

SAR values were assessed for the designated mounting positions of the wearable device in a free space environment, focusing on both wrist and waistline positions of the MIFA antenna, with a transmission power of 100 mW at a distance of 5 mm. The SAR values were higher for both wrist and waistline scenarios, consistent with findings from previous studies regarding head exposure [156, 158]. Therefore, it is recommended that RF-EMF exposure from wearable devices be mitigated to below the ICNIRP threshold of 2 W/kg. Potential mitigation strategies include redesigning the antenna's radiating element to reduce SAR values, increasing the distance between the device and the body, or implementing RF shielding.

The variability of SAR concerning the distance between the body and the RF-EMF source, power level, and orientation of the MIFA antenna was also investigated. The SAR values remained below ICNIRP levels at a distance of 12.5 mm between the MIFA antenna and the body, establishing this as a safe mounting distance for the wearable device. However, SAR increased with higher transmit power levels, exceeding ICNIRP limits at the maximum permissible power level. Additionally, SAR showed only minor variations with the orientation of the MIFA antenna, with similar trends observed for both wrist and waistline placements. This indicates that the orientation of the wearable device has a negligible impact on RF-EMF exposure.

Furthermore, SAR was evaluated in an underground mine tunnel using a LiDAR-scanned model for different mounting positions of the wearable device. The LiDAR

models were preprocessed to optimize computational resource requirements without affecting the RF-EMF exposure evaluation. It is evident that when a wearable device is positioned close to the tunnel boundary, the RF-EMF reflected from nearby surfaces is stronger than the reflected signals from more distant boundaries, as discussed in [10]. Consequently, the tunnel models were reduced to 1 meter by 1 meter (eight times larger than the wavelength at 2.4 GHz) to facilitate the investigation of SAR values. The SAR values were slightly higher for both the wrist and waistline mounting positions, consistent with findings from prior research [10, 11].

The impact of various surrounding environmental parameters was also examined for different mounting positions. Specifically, the variability of SAR concerning rock properties, such as the permittivity of the rock and the distance between the tunnel and the MIFA, was investigated. A range of rock permittivity values was utilized in the numerical simulations to assess SAR variability. The results indicated that changes in rock permittivity resulted in only marginal variations in SAR values for both wrist and waistline scenarios when other parameters were held constant. Similarly, SAR values showed minimal variation with increasing distance beyond 100 mm from the tunnel. Therefore, a safe distance of 100 mm between the tunnel and the wearable device is recommended to mitigate RF-EMF exposure; however, greater distances result in less reflected signal exposure to the tissues.

Chapter 5

Assessment of Temperature Elevation in Tissues Induced by Wearable Device Exposure in Underground Mine Environment

5.1 Introduction

The investigation of temperature distribution in biological tissues is essential for wearable devices in underground mines, mainly due to the elevated temperature of the environment. In the high thermal environment of underground mines, combined with wearable devices, complex interactions occur, affecting both the propagation of RF-EMF and the thermal response of tissues. Consequently, exploring temperature distribution in biological tissues is crucial, offering a significant perspective to understand and address RF-EMF exposure in the thermally intense environments of underground mines.

5.2 Steady State Thermal Analysis of the Wearable Device Exposure

Different temperatures of the underground mine environment, such as 40 and 50 ^{0} C, were considered as ambient temperatures exposed to RF-EMF. The human body's nominal temperature is approximately 37^0 C, which is lower than the working temperature of the underground mine environment. Therefore, it is crucial to investigate the temperature elevation in tissues due to RF-EMF exposure of wearable devices in high-temperature environments.

In the steady-state thermal analysis, heat conduction is investigated between bodies without considering time constraints, resulting in maximum and minimum temperature distribution on the bodies. Therefore, in this investigation, the temperature distribution in the tissues was analysed for exposure to wearable devices in the presence of underground structures for different mounting positions on the body. In Ansys Workbench, the Steady-state mechanical solver imports geometries, material properties, and electromagnetic loss from the HFSS solver. The electromagnetic loss was imported from the *HFSS* solver as volume loss density (W/m^3) and defined as a heat generation source in the *Ansys Mechanical* solver. The other boundary conditions, such as convection and radiation, were also assigned to the exposed tissues of the setup scenario. The structure of the antenna and tunnel were ignored as they generated no heat. Further analysis and results are discussed below:

5.2.1 Steady State Thermal Analysis for Wrist Position of the Wearable Device

The steady-state *Mechanical* solver was used to analyze diverse temperature scenarios for the wrist-mounted wearable device. The *Mechanical* solver dynamically adapts the mesh allocation to the targeted tissues, as illustrated in Figure 5.1. The mesh utilized linear element order with an element size of 4 mm, generating 124,014 elements for analysis. Results obtained from the HFSS solver were integrated into the mechanical solver, where a heat generation source was assigned, as shown in Figure 5.2. Notably, the highest imported loss closely corresponded to the placement of the MIFA antenna on the wrist. The thermal model embraced convection and radiation boundaries, attributing an ambient temperature of 30^0 C to the wrist region. The temperature distribution in the tissues at 30^0 C is shown in Figure 5.3. The temperature exhibited an elevation at the centre, precisely where the MIFA antenna was positioned, gradually decreasing radially from the centre. The maximum temperature registered within the wrist scenario stood at 31.735^0 C. This temperature distribution remained consistent even when subjected

to varying ambient temperatures of 40^0 C and 50^0 C, yielding maximum temperature distributions of 41.771^0 C and 51.672^0 C, respectively. Thus, the presence of an RF-EMF source induced the heating and increased the temperature of the tissues by approximately 1.7^0 C, which is lower for the ICNIRP [4].

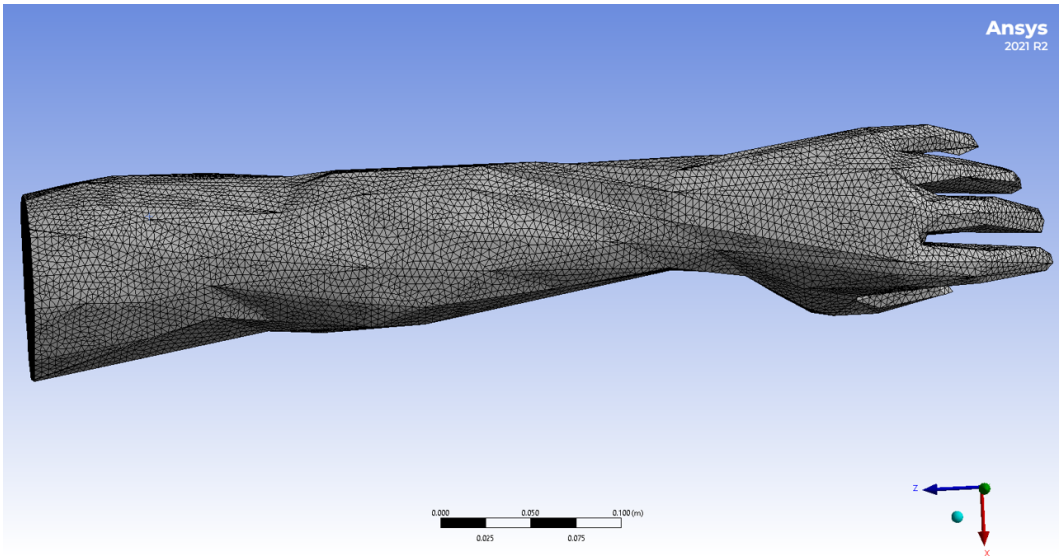

FIGURE 5.1: Meshing of mechanical solver for the wrist scenario

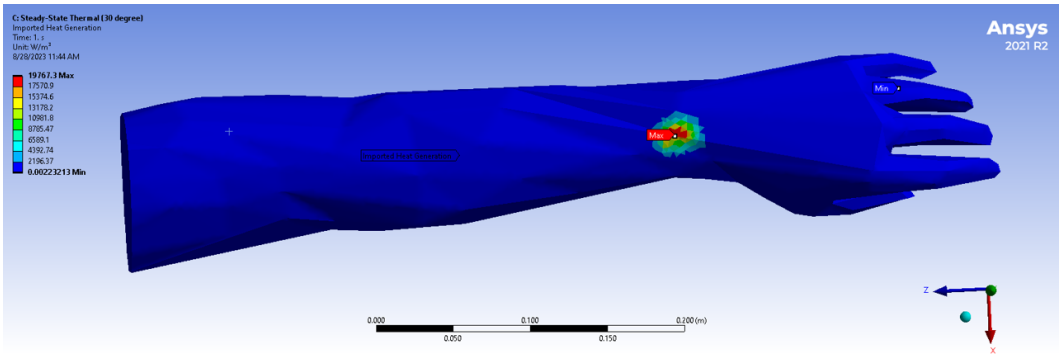

FIGURE 5.2: HFSS imported loss in the mechanical solver for the wrist scenario

5.2.2 Steady state Thermal Analysis for Waistline Position of the Wearable Device

A comparable setup and boundary conditions were implemented to compute the temperature distribution when a wearable device is affixed to the body's waistline position. This investigation considered two distinct mounting orientations of the

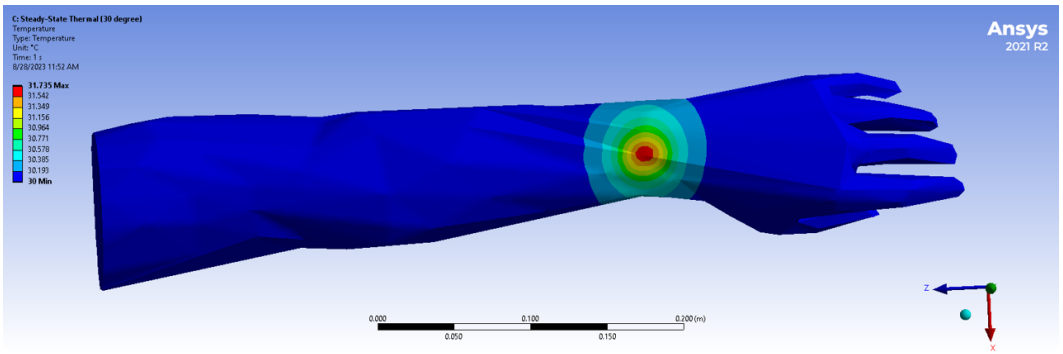

FIGURE 5.3: Thermal distribution on the wrist at 30^0 C ambient temperature

MIFA antenna: one at the side and the other at the backside of the miner's waistline. Convection and radiation boundaries were assigned to the skin of the tissues. Notably, the tunnel and antenna structure were excluded, as they do not influence temperature fluctuations within the tissues. In Figure 5.4, the body mesh for the scenario with the MIFA antenna positioned at the waistline's side comprised 400,642 elements, each with a size of 4 mm. The imported loss was assigned as the heat generation source, with a value of 0.0588486 W for skin tissues, as demonstrated in Figure 5.5. The system was solved using an iterative solver, with an ambient temperature set at 30^0 C. The temperature distribution on the skin tissues, as depicted in Figure 5.6, manifested a peak of 31.409^0 C. This temperature distribution exhibited a radial decrease from the central position of the MIFA antenna. By varying the ambient temperature to 40^0 C and 50^0 C, the corresponding maximum temperature increases in the skin tissues were 41.367^0 C and 51.367^0 C, respectively.

Similarly, temperature variations were examined within the skin tissues when the MIFA antenna was positioned on the backside of the waistline. This scenario introduced ambient temperature variations while retaining consistent boundary conditions. As depicted in Figure 5.7, the graphical representation displays the extremities of the imported electromagnetic loss on the backside of the waistline location. Notably, the highest loss corresponds precisely to the area where the MIFA antenna was installed. Additional insight is provided by the temperature distribution shown in Figure 5.8, showcasing the temperature increase at an ambient temperature of 30^0 C for the identical position. The maximum temperature

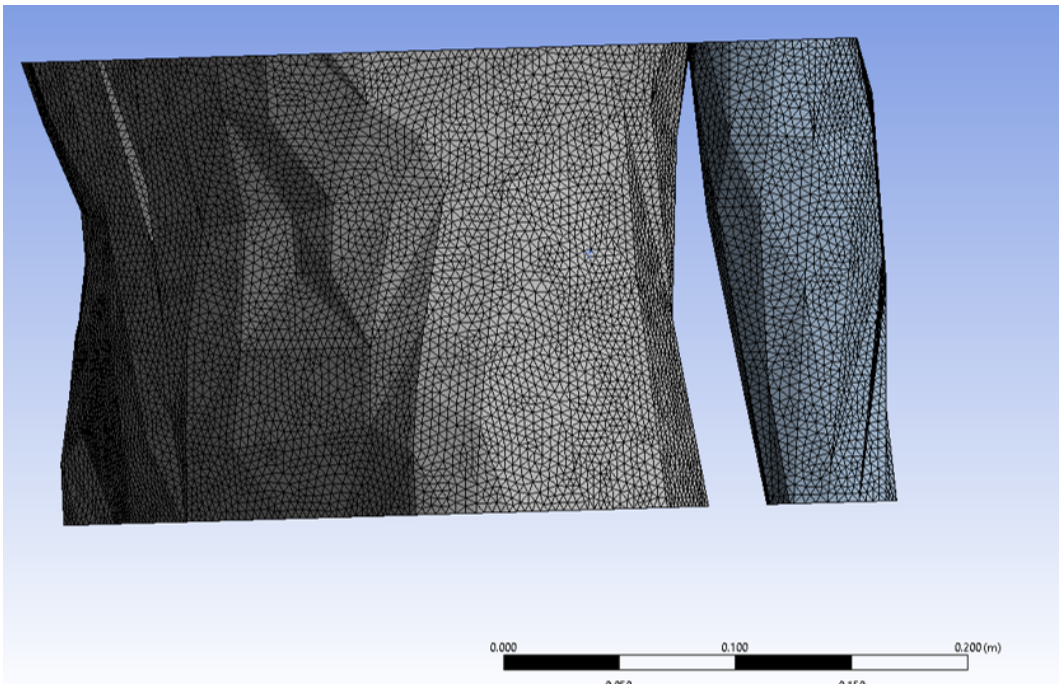

FIGURE 5.4: Meshing of mechanical solver for the waistline side scenario

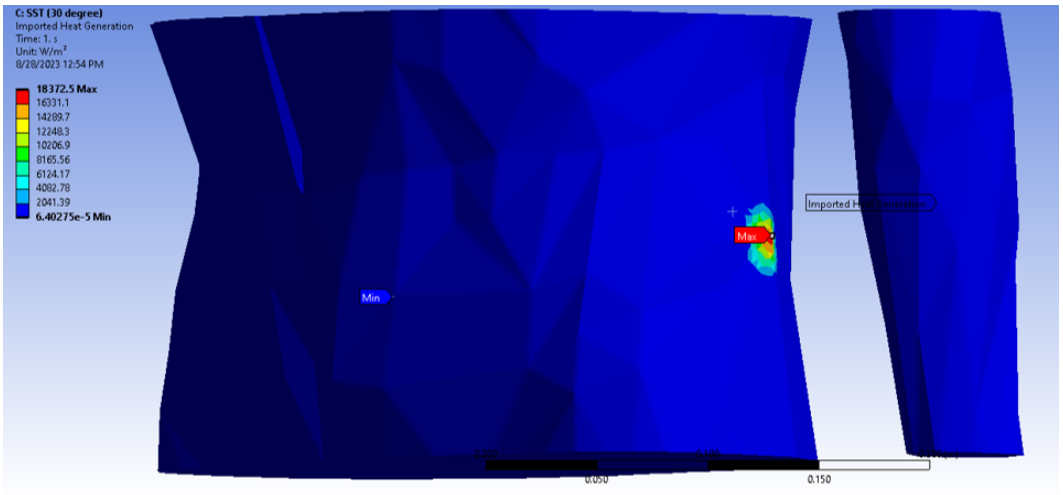

FIGURE 5.5: HFSS imported loss in the mechanical solver for the waistline side scenario

increase reached 31.272^0 C. Similarly, for ambient temperatures of 40^0 C and 50^0 C under the same boundary conditions, the maximum temperature elevation in skin tissues was 41.272^0 C and 51.272^0 C, respectively.

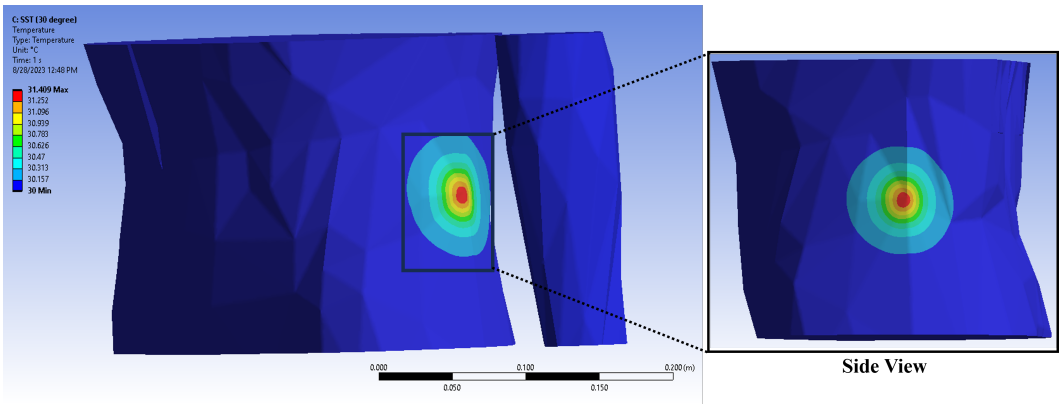

FIGURE 5.6: Thermal distribution for the waistline side scenario at 30^0 C ambient temperature

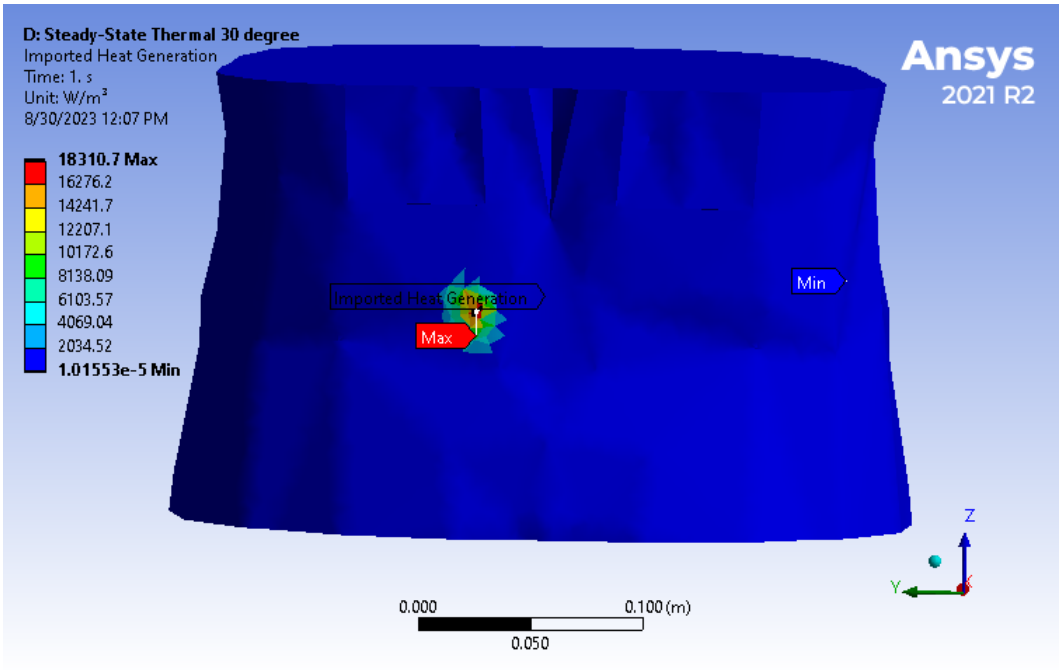

FIGURE 5.7: HFSS imported loss in the mechanical solver for the waistline side scenario

5.2.3 Comparison of Steady-State Thermal Results from Wearable Device Exposure

Table 5.1 compared the steady-state thermal results between wrist and waistline positions across various ambient temperatures within an underground mine environment. The findings indicate a consistent trend of temperature elevation due to RF-EMF exposure across different ambient temperatures. Higher ambient temperatures correspond to increased temperature elevation within tissues. This

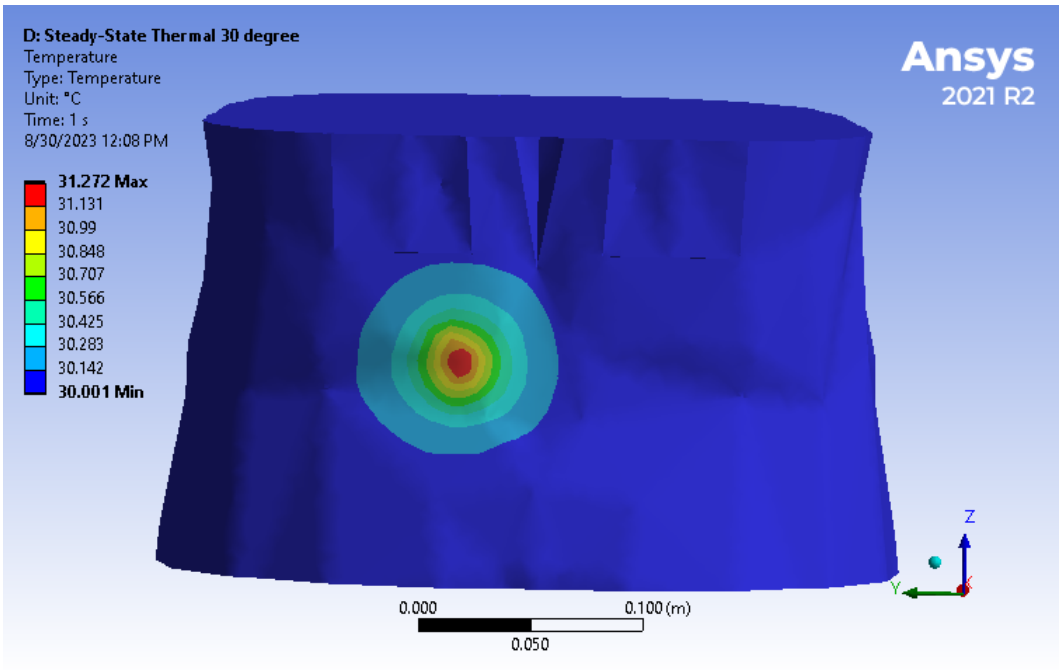

FIGURE 5.8: Temperature distribution of the MIFA antenna positioned on the back of the waistline at an ambient temperature of 30^0 C

trend persists uniformly across all mounting positions examined. The impact of diverse environmental conditions, such as elevated ambient temperature, seems to exert minimal influence on the extent of thermal response to RF-EMF exposure within underground mine settings. Notably, at a 30^0 C ambient temperature, the elevation in tissue temperature is higher compared to scenarios with ambient temperatures of 40^0 C and 50^0 C. However, the elevation in tissue temperature decreases as the ambient temperature rises to 40^0 C and 50^0 C. Importantly, all observed temperature elevations remain below the ICNIRP guidelines [4].

Additionally, it is noteworthy that the wrist consistently exhibits slightly higher temperature elevations than the waistline side and back configurations across all ambient temperature settings. This observation suggests an increased accumulation of heat in the wrist region.

The analysis of steady-state thermal results provides valuable insights into the maximum temperature elevation within tissues resulting from higher ambient temperatures and RF-EMF exposure from wearable devices. Despite higher SAR values observed in specific scenarios, the temperature elevation consistently remains

within ICNIRP guidelines across all scenarios. Moreover, the maximum temperature elevation in tissues primarily depends on ambient temperature, as temperature elevation in tissues due to RF-EMF exposure remains consistent across all ambient temperatures.

TABLE 5.1: Comparison of temperature elevation for wrist and waistline for different ambient temperature

Mounting position	Ambient temperature (^{0} C)	Maximum Temperature elevation (^{0} C)
Wrist	30	31.735
	40	41.771
	50	51.672
Waistline side	30	31.409
	40	41.367
	50	51.367
Waistline back	30	31.272
	40	41.272
	50	51.272

5.3 Transient Thermal analysis of the wearable device exposure

Transient analysis is pivotal in comprehending the temperature distribution within biological tissues. Unlike steady-state analysis, which offers insights into equilibrium conditions, transient analysis delves into the dynamic nature of temperature elevation in tissues over time. In the context of RF-EMF exposure within underground mine environments, where the RF-EMF source and the biological response can vary over time, transient analysis captures the intricate evolution of temperature patterns. This analysis not only aids in understanding the immediate effects of exposure but also allows for exploring temporal thermal responses, which can help predict potential heat accumulations or dissipation trends. Transient analysis was conducted for the tunnel environment when the wearable device (MIFA antenna) was mounted on the wrist and waistline side of the miner. Only the

waistline side position was observed in this analysis, as it consistently provided higher temperature elevation in tissues and SAR values across all scenarios, as observed in Chapter 4. The transient analysis was performed solely for a 40^0 C ambient temperature, as the observed trends remained consistent across other ambient temperatures.

5.3.1 For 1 hour of RF-EMF exposure

The exploration of temperature dynamics over time was facilitated by utilizing a transient thermal solver. Within this solver, the RF-EMF exposure and analysis duration was set at 1 hour, while the loss, imported from HFSS, served as the heat generation source. The tunnel and MIFA antenna structure were omitted as they do not contribute to heat generation. Two wearable device mounting positions on the miner's body were simulated, encompassing the wrist and waistline. As demonstrated in Figure 5.9, a temperature variation in the skin tissues of the wrist over 3600 seconds (1 hour) within a 40^0 C ambient temperature setting. Notably, the temperature of the skin tissue progressively increases with time. The culmination of this behaviour resulted in a peak temperature of 41.461^0 C at 3600 seconds for the wrist scenario. This escalating temperature trajectory reflects the ongoing thermal accumulation within the skin tissues until they eventually attain thermal equilibrium conditions, i.e., the maximum of 41.771 as observed in steady state analysis.

The temperature variation was also observed for the waistline position of the MIFA antenna at 40^0 C for 1 hour (3600 s), as shown in Figure 5.10. It can be seen that the temperature starts increasing with time, and at 3600 s, it reaches the maximum of 40.042^0 C. The variance in temperature elevation observed between wrist and waistline skin tissues is attributed to the discrepancy in imported loss and subsequent variation in SAR values, influenced by differences in body shape, as discussed in the preceding chapter.

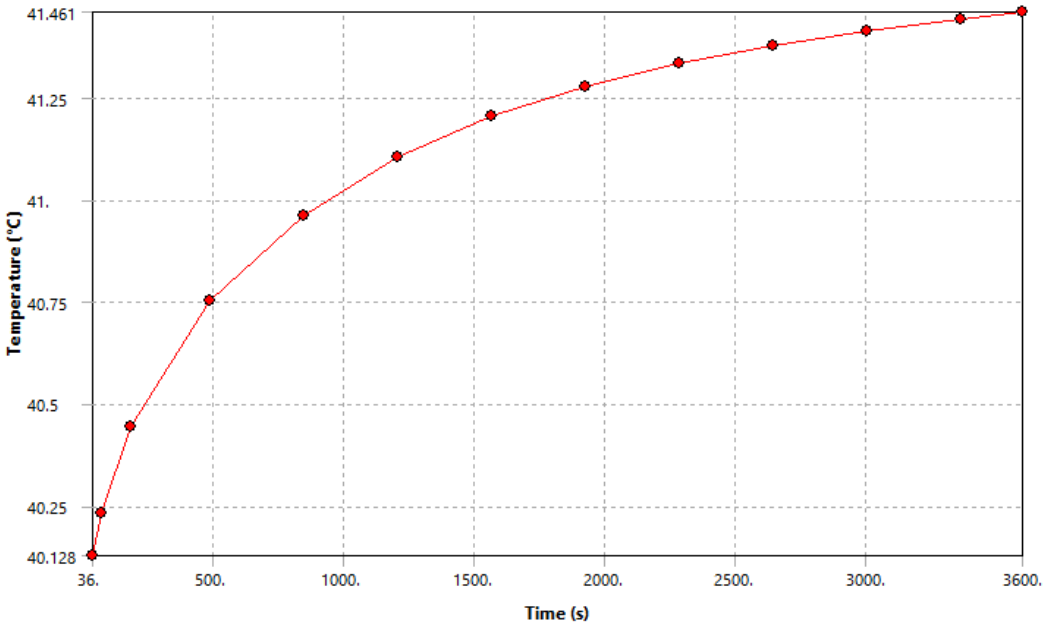

FIGURE 5.9: Time vs. temperature variation in the skin tissues of the wrist for exposure of 1 hour with the ambient temperature of 40^0 C

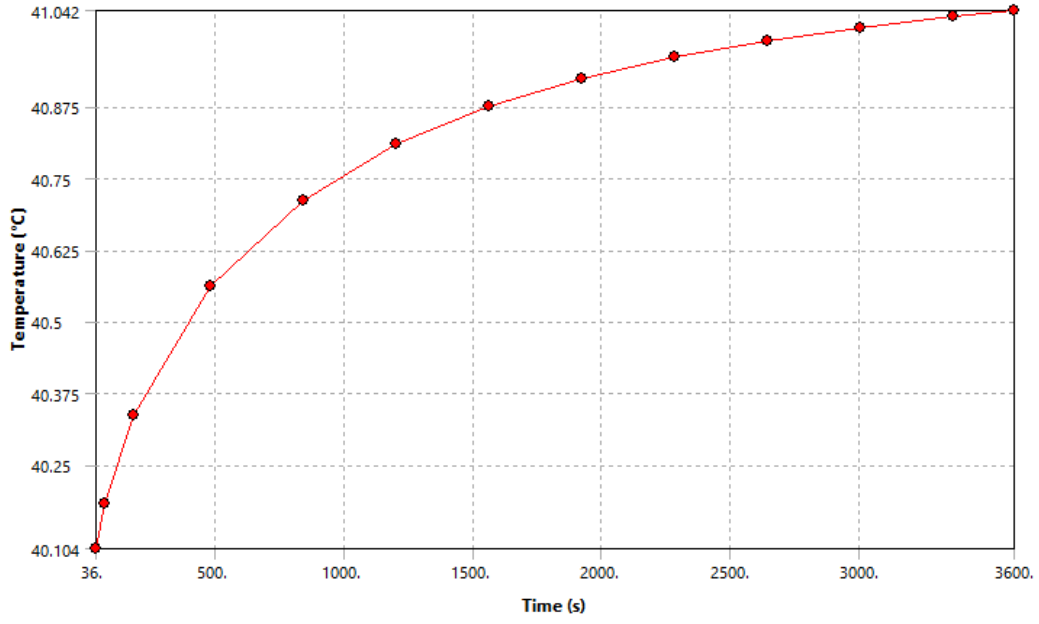

FIGURE 5.10: Time vs. temperature variation in the skin tissues of the waistline for 1 hour with an ambient temperature of 40^0 C

5.3.2 For 5 hours of exposure

The RF-EMF exposure duration was adjusted to 5 hours (18000 s) for both wearable device placements at 40^0 C ambient temperature. Notably, in both the wrist and waistline positions, the rate of temperature increase began to level off around 4.167 hours (15000 s), as depicted in Figure 5.11 and Figure 5.12. The highest temperature elevation observed in skin tissues reached 41.664^0 C for the wrist and 41.17^0 C for the waistline configuration.

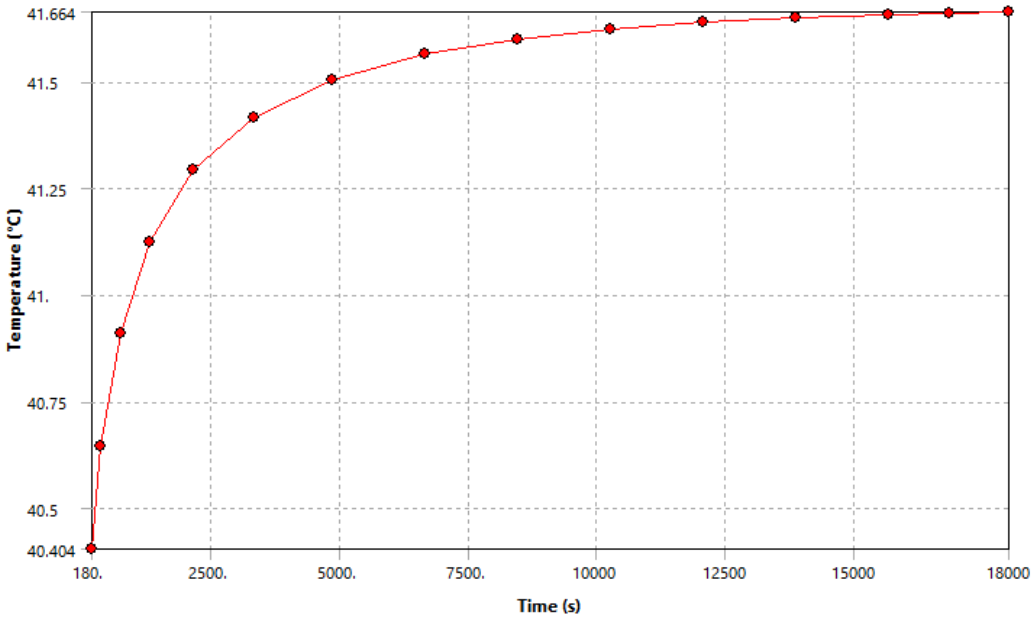

FIGURE 5.11: Time vs. temperature variation in the skin tissues of the wrist for 5 hours with an ambient temperature of 40^0 C

5.3.3 For 8 hours of exposure

In this instance, the RF-EMF exposure duration was extended to 8 hours. We investigated tissue temperature rise in both wrist and waistline configurations at a 40^0 C ambient temperature, depicted in Figure 5.13 and Figure 5.14. Remarkably, the temperature rise displayed minimal alteration between the 5-hour and 8-hour RF-EMF exposures, indicating the attainment of a thermal equilibrium state. The highest temperature increase observed at the 8-hour mark reached 41.673^0 C for the wrist scenario and 41.183^0 C for the waistline configuration.

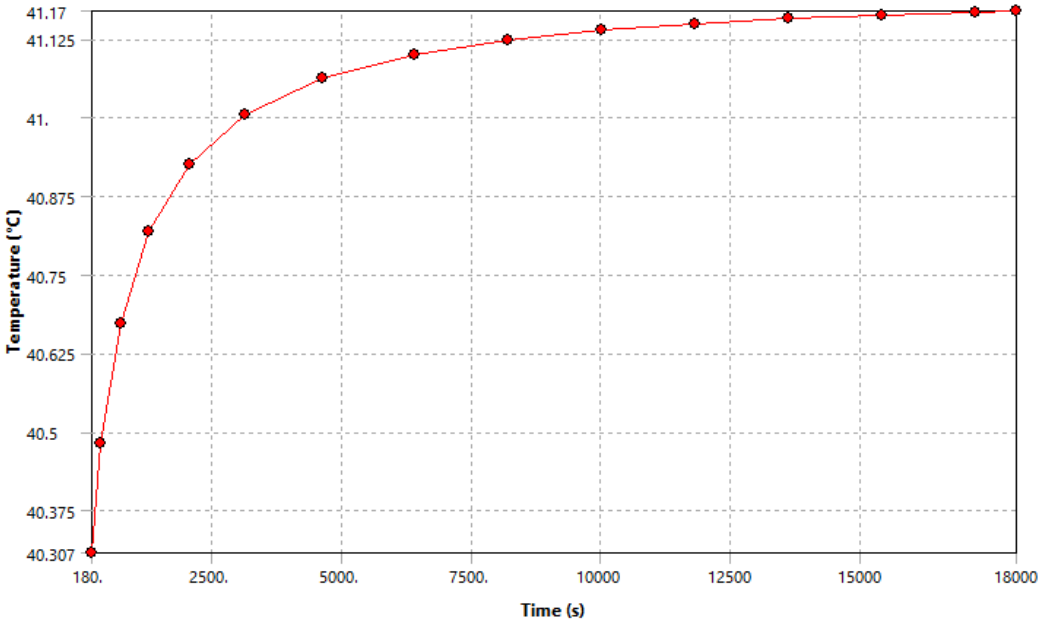

FIGURE 5.12: Time vs. temperature variation in the skin tissues of the waistline for 5 hours with an ambient temperature of 40^0 C

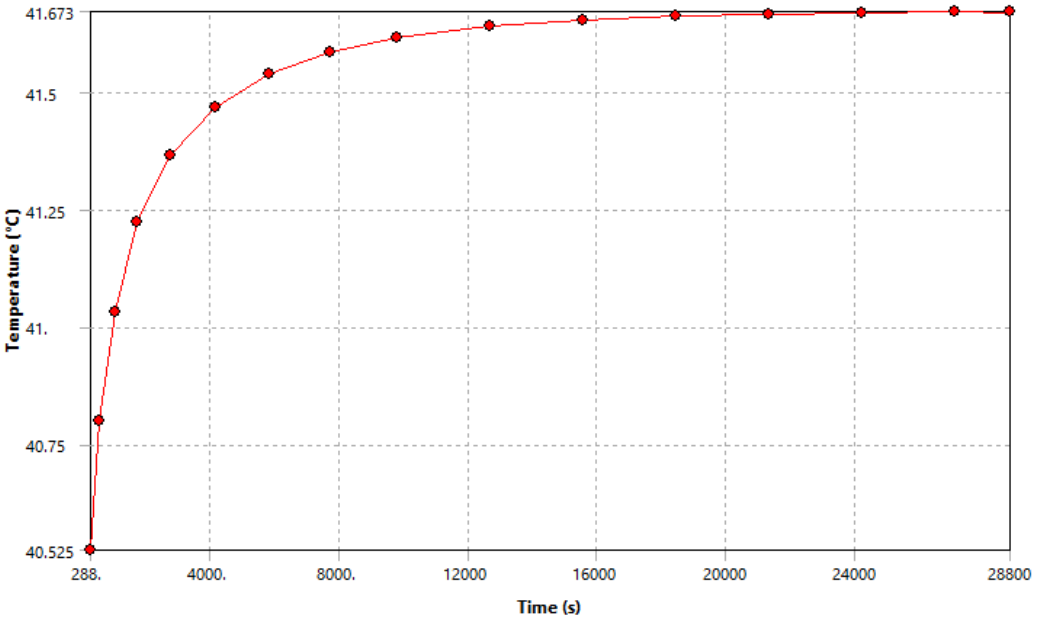

FIGURE 5.13: Time vs. temperature variation in the skin tissues of the wrist for exposure of 8 hours with ambient temperature of 40^0 C

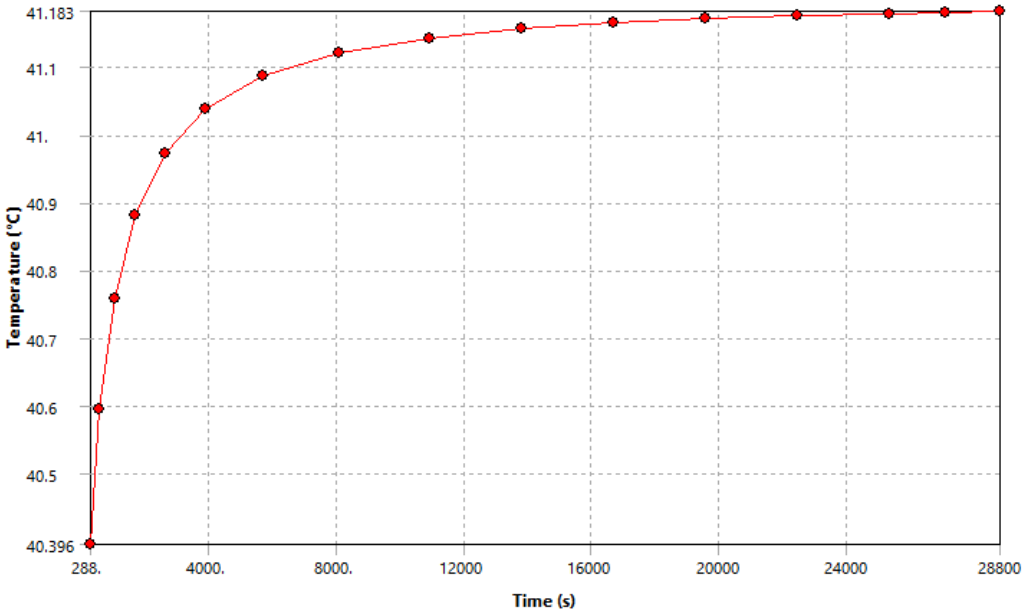

FIGURE 5.14: Time vs. temperature variation in the skin tissues of the waistline for 8 hours with an ambient temperature of 40^0 C

5.4 Comparison of the Results

Our study found that high ambient temperatures do not affect the thermal response to RF-EMF exposure in underground mine environments. This result is consistent with a prior study [25] that examined the impact of ambient temperature, humidity, and clothing on RF-EMF-induced thermal load, showing similar trends. Although our study did not consider the effects of clothing and humidity, we still observed consistent patterns. In [25], the researchers evaluated the thermal impact of RF-EMF by varying the SAR values, which captured the realistic characteristics of the RF-EMF source, including frequency, transmit power, orientation, and mounting positions. This approach limits the comparison with our study, as we kept these parameters the same. In another study by Moore et al. [24], the thermal profile of a finely discretized human body model was assessed, taking into account a 1 GHz RF-EMF at occupational safety limits in adverse environmental conditions such as high humidity and ambient temperature. This study found that while electromagnetic fields contribute to tissue temperature elevation, the impact is overshadowed by environmental factors and clothing type. Additionally,

the study compared exposure limits, as it assessed RF-EMF exposure at 1 GHz without considering the characteristics of surrounding objects.

5.5 Conclusion

The temperature elevation in tissues resulting from RF-EMF exposure of wearable devices was investigated under varying high ambient temperatures typical of underground mine environments. The evaluation focused on different mounting positions of the wearable device on the body, specifically the wrist and waistline. The SAR values obtained were used as heat sources in *ANSYS Mechanical*, where ambient temperatures relevant to the underground mine environment were set to assess temperature distribution in the tissues. The maximum temperature elevation in the tissues was calculated using the steady-state thermal solver in *ANSYS Mechanical*. This solver assumes an infinite time frame, providing a temporal and maximum temperature distribution for tissues exposed to RF-EMF from the wearable device.

The results indicated that the hotspot for temperature distribution is located directly beneath the RF-EMF source, specifically below the antenna of the wearable device. The maximum temperature elevation in the skin tissues was below the ICNIRP limits [4] for all mounting positions of the wearable devices. Notably, the temperature elevation was higher for the wrist mounting than the waistline position. However, the backside of the waistline exhibited lower temperature elevations in the tissues, suggesting that this is a preferable mounting location on the waistline. Overall, the wrist is the optimal position for the wearable device, as peripheral tissues have higher tolerance levels for RF-EMF exposure regarding both SAR and temperature elevation.

Moreover, the varying thermal loads of the surrounding environment did not affect the temperature elevation in the tissues resulting from RF-EMF exposure from the wearable device. The temperature elevations for the wrist, side waist, and backside mounting positions were recorded at 1.7°C, 1.4°C, and 1.27°C, respectively,

regardless of the ambient temperatures of 30°C, 40°C, and 50°C. This suggests that the temperature increase in tissues due to RF-EMF exposure is independent of the ambient temperature. However, it is essential to note that ambient temperature does act as a thermal load that can elevate the core temperature of the tissues.

Similarly, a transient thermal analysis of RF-EMF exposure from the wearable device was conducted to assess long-term exposure in underground mine settings. The *Ansys Mechanical* transient solver was employed to investigate temperature elevation in tissues over time for different ambient temperatures typical of underground environments. The results indicated that the tissue temperature reached its maximum elevation within one hour of continuous RF-EMF exposure from the wearable device. Notably, the analysis showed that most of the temperature rise occurred during the first hour of exposure, with the temperature curve stabilizing into a horizontal line thereafter, indicating minimal further elevation. Thus, it can be concluded that the maximum temperature rise occurs within the first hour, after which the tissues maintain thermal equilibrium. This study underscores the importance of considering antenna placement, environmental factors, and ambient temperature when assessing tissue response to RF-EMF exposure, particularly to ensure safety in confined environments like underground mines.

Chapter 6

Background: Supervised Machine Learning

This chapter introduces machine learning (ML) and classifies it into different categories. It also discusses the need for supervised ML models and their performance metrics to validate the output predictions. Different supervised ML models, such as random forest, XGBoost, linear regression, K nearest neighbor, and support vector machine, are explained using their hyperparameters and performance. Lastly, it explains the issues with supervised ML models.

6.1 Introduction

ML is a sub-field of Artificial Intelligence (AI) that uses algorithms to solve regression and classification problems. It allows systems to learn from available data and predict the output for unseen data. The algorithms used in ML are designed to perform specific tasks efficiently, using predefined mathematical models that learn from available data samples called "training data". ML is divided into three categories: supervised, unsupervised, and reinforcement learning. In supervised ML, the output of the models is known, i.e., labelled, whereas in unsupervised ML, the output is not labelled. This study focuses on supervised ML, given that the data for predicting SAR and temperature elevation in tissues due to RF-EMF exposure from the MIFA is labelled. It means that the outputs are known to have regression problems. Therefore, we will exclusively discuss supervised ML.

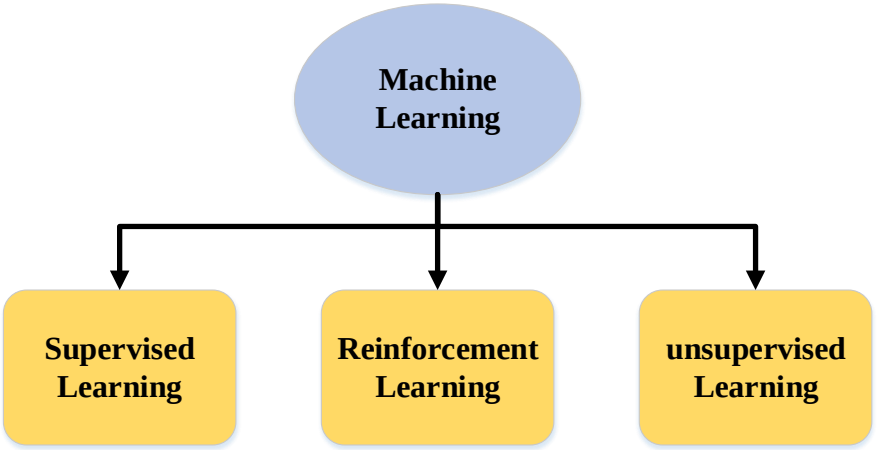

FIGURE 6.1: Major categories of machine learning.

6.2 Supervised Machine Learning

In ML, each instance in a dataset is typically represented using a consistent set of features (inputs), which may vary in nature, such as continuous, categorical, or binary. Supervised learning occurs if the correct outputs, known as labels, represent the instances. In contrast, unsupervised learning involves instances lacking such labels. Through the application of unsupervised algorithms, particularly clustering algorithms, researchers aim to unveil previously unknown but potentially valuable classes of items [186]. Numerous ML applications revolve around tasks that can be framed as supervised learning. In supervised machine learning, the model is provided with the data features and tasked with predicting the labelled output, as illustrated in Figure 6.2. Various ML models can be employed, including linear regression, random forest, and gradient boost.

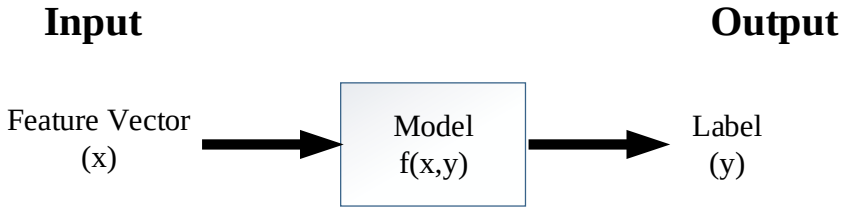

FIGURE 6.2: Supervised machine learning model.

Supervised ML problems can be broadly classified into regression and classification problems, as shown in Figure 6.3. Regression involves tasks that aim to forecast a numerical value output using unseen input data, whereas classification problems predict a discrete value output (Class label) [187].

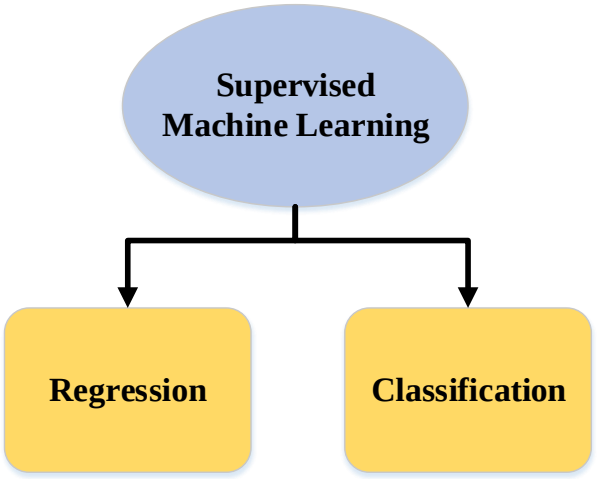

FIGURE 6.3: Types of Supervised machine learning.

Regression techniques permit the discovery of correlations between variables and predictions of continuous values based on these variables [188]. The problem is also referred to as regression when the output is continuous. The input variables (X) are mapped to the dataset's continuous outputs (Y) in regression and predicted for unknown input variables. The regression can be further divided into two main categories: simple and multiple linear regression, as shown in Figure 6.4. In simple linear, a single line represents the relationship between the input (X) and output (Y). In contrast, multiple linear regression is further divided into linear and non-linear based on the output relation of the input and output [189].

The problem is called classification when the models' output is in a categorical form. The dataset instances are categorized according to specified classes in classification problems [188, 190]. Classification can be performed on both unstructured and structured datasets. The dataset is classified into some given label or category, and for new input instances, the class or label will be assigned to it using different techniques. A *classifier* is an algorithm that learns from the training data set

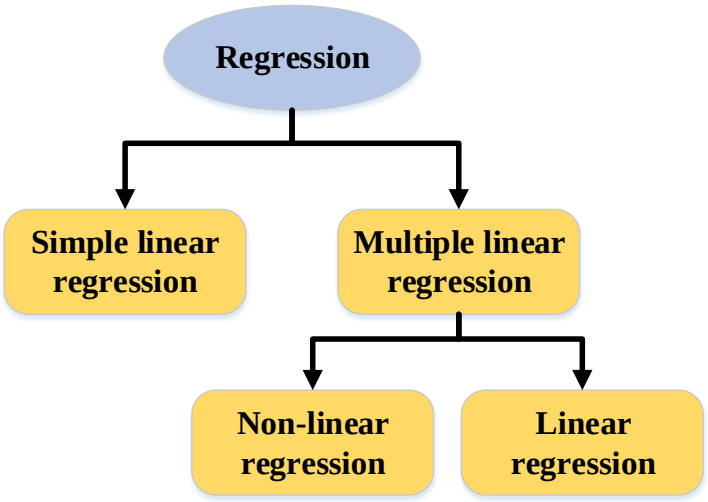

FIGURE 6.4: Categories of the regression.

and then assigns new data points to a particular class. The classification model concludes a valid mapping function from the training dataset and predicts the new data class based on mapping functions. The classification task can be further divided into binary classification or multi-label classification. In binary classification, the data is classified into two possible outcomes. For example, weather forecast (it will rain or not), and email filter (whether email is spam or not). In multi-label classification, data is classified into two or more possible outcomes. For example, to classify the students' performance into good, average, and poor.

6.2.1 Performance Metrics of Supervised ML Models

In ML regression problems, the models learn to predict continuous output values. The regression model is constructed using historical data. In the end, it defines a mathematical model that approximately fits all points in the dataset to predict the output for unseen data. The performance of the ML model can be evaluated using Mean Absolute Error (MAE), Root mean square error (RMSE), and R-squared error.

In this study, MAE, RMSE, and R-squared were used to compare the performance of the machine learning models in predicting SAR and temperature elevation in

skin tissue. These metrics were selected for the valuable insights they provide during model training. Specifically, MAE and RMSE offer distinct perspectives on prediction errors: MAE reflects the average magnitude of errors, while RMSE places more emphasis on larger errors, making it particularly useful for identifying outliers. Additionally, the R^2 metric indicates the proportion of variance explained by the model, helping to assess the overall fit and effectiveness of the model.

6.2.1.1 Root Mean Square Error

The RMSE is commonly employed to calculate the sum of regression errors for each point in the dataset during each learning iteration. A reliable regression model depends on identifying the most suitable hypothetical function by minimizing the RMSE error as much as possible. The RMSE is the square root of the average squared distance between the actual and predicted value [191].

$$RMSE = \sqrt{\frac{\sum_{i=1}^{n}(y_i - \hat{y}_i)^2}{n}} \tag{6.1}$$

where, n denotes the number of data points, y_i represents the actual value, $\hat{y}_i$ represents the predicted value.

6.2.1.2 Mean Absolute Error

Mean Absolute Error (MAE) measures how close forecasts or predictions are to the actual outcome [192]. MAE is computed by adding the absolute difference between the actual and predicted values for each observation over the entire array and dividing the result by the number of observations in the array [193], as expressed in Eq. 6.2. It determines how prediction errors vary from one predicted to the next.

$$MAE = \frac{1}{n}\sum_{i=1}^{n}|y_i - \hat{y}_i| \tag{6.2}$$

6.2.1.3 R-squared Error

R squared, also called the coefficient of determination, evaluates the extent of variation in predictions. It establishes the relationship between changes in a dependent variable and changes in an independent variable. However, it provides insights into whether the chosen model is outstanding or poor and indicates if the data and predictions are biased. The expression for R squared can be written as [194]:

$$R^2 = 1 - \frac{\sum_i^n (y - \hat{y}_i)^2}{\sum_i^n (y - \bar{y}_i)^2} \tag{6.3}$$

6.3 Supervised Learning Regression Models

The section below discusses supervised learning regression models.

6.3.1 Linear Regression

In statistics, linear regression models the relationship between a numerical output and one or more explanatory factors, also known as dependent and independent variables. It is a linear approach that aims to capture and quantify the linear relationship between these variables [193]. When dealing with one or more input variables, an iterative method can improve the coefficient values by minimising the model's error on the training data. It involves adjusting the coefficients to minimise the difference between the predicted and actual values (known as gradient descent), thereby refining the model's performance on the training dataset. This process continues until the squared error is reduced to its minimum value. For example, for a given set of inputs, consider a linear equation with a set of input variables (X) resulting in output variables (Y). The line represents one scaling factor to every input, known as the coefficient; it includes another coefficient, the intercept. LR model involves estimating the coefficient values used to illustrate available data [195]. Figure 6.5 characterises the relationship between data points

and the LR line, which is crucial for understanding how well the model fits the data.

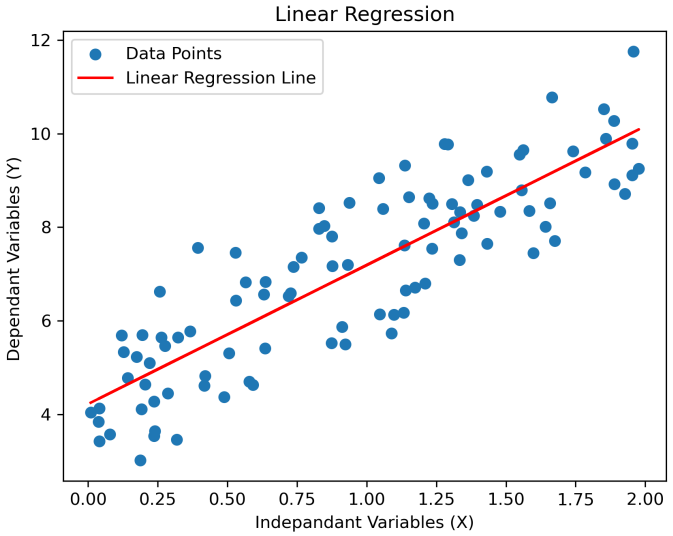

FIGURE 6.5: Linear regression.

A simple linear regression model can be represented in mathematical terms as [196]:

$$Y = \alpha + \beta X \tag{6.4}$$

where X is the independent variable, Y is the dependent variable, α and β are linear coefficients. For multiple linear regression model, the above model can be written as [196]:

$$Y = \theta_0 + \theta_1 x_1 + \theta_2 x_2 + ... + \theta_n x_n \tag{6.5}$$

where $\theta_0, \theta_1, \ldots, \theta_n$ represent the coefficients corresponding to the features indexed from 1 to n.

6.3.1.1 Learning Model

1. Simple linear regression: A single input is utilised to estimate the coefficient in the models. It includes calculating statistical parameters such as standard deviations, mean, correlations, and covariance [195].

2. Ordinary Least Squares (OLS): This technique is employed when multiple coefficients are necessary for calculation. This approach aims to minimise squared residuals' summation for a given regression line. It involves calculating the distance from every data point to the regression line, squaring these distances, and summing all the squared errors. By treating the data as a matrix, linear algebra techniques are applied to compute the coefficient values [197].

3. Gradient descent: Optimizing the coefficient values involves iteratively minimizing errors in the training data, known as gradient descent when dealing with multiple input values. It begins with random values assigned to each coefficient, and for every input-output pair, the sum of squared errors is calculated. The coefficient values are then updated in a manner that reduces the error. This iterative process continues until either a minimum sum-squared error is reached or further progress becomes unattainable (no minimization of error is possible) [197].

4. Regularization: It includes minimizing the sum squared error on the training data using OLS and also decreases the complexity in the model. These approaches are considered adequate when the input values are collinear, and traditional OLS regression tends to over-fit the training dataset [197].

6.3.2 K Nearest Neighbors

K-Nearest Neighbor (KNN) is employed when feature vectors are continuous [194]. KNN operates by storing existing data and making predictions for new data based on similarities with its neighbours. This method effectively handles noisy data and finds applicability in various real-world scenarios. However, its computational expense arises from repetitively calculating the distance to the k nearest neighbours for each new data point [189].

The KNN regressor learns by comparing the given test instances with the training set, utilizing the similarities between data points to make predictions for new

instances [198]. For example, T = (x_1, y_1), (x_2, y_2),...,(x_N, y_N) is the training set with distance metrics d, N is the number of instances, where x_i = (x_{i1}, x_{i2},....,x_{im}) is the ith instance denoted by m attributes for output y_i. For a test instance x, the kNN regressor computes the distance (d_i) between x and each instance x_i in the training set T. Subsequently, it sorts the distances d_i in ascending order. If d_i ranks in the ith place, then the instance corresponding to the distance d_i is referred to as the ith nearest neighbour $NN_{i(x)}$, and its output is denoted as $y_{i(x)}$ [198]. For an unknown pattern $x^{'}$, the KNN model predicts the output for a new instance by computing the mean of the function values of its K-nearest neighbours [199]:

$$f_{KNN}(x^{'}) = \frac{1}{K} \sum_{i \in N_K(x^{'})} y_i \tag{6.6}$$

where $N_K(x^{'})$ contains the indices of the K-nearest neighbors of $x^{'}$.

The number of neighbours k in KNN significantly impacts model flexibility and generalization. Smaller k values lead to more complex models with low bias but high variance, which are prone to overfitting. Larger k values result in smoother decision boundaries with lower variance but potentially higher bias, balancing underfitting. Choosing an appropriate k involves considering the bias-variance trade-off, computational efficiency, and data distribution [199]. Figure 6.6 shows the variation of the k value on the prediction of the KNN regressor.

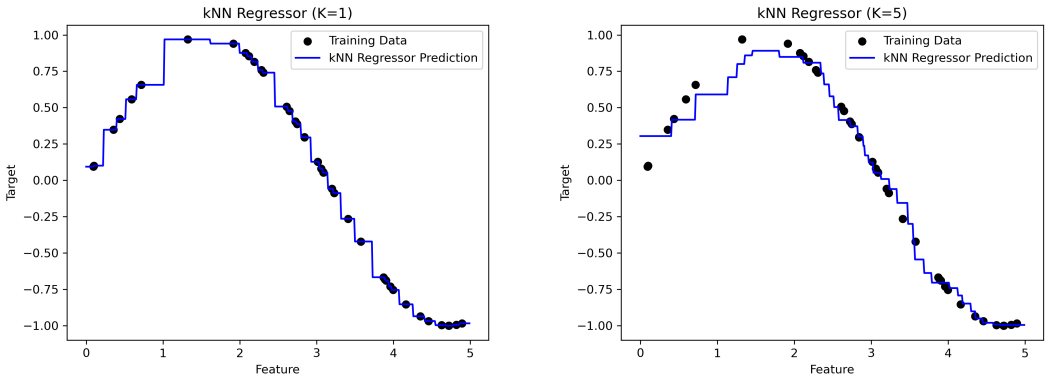

(a) (b)

FIGURE 6.6: Illustration of KNN regression for (a) K = 1 and (b) K = 5

6.3.3 Support Vector Machines

While Vapnik initially proposed Support Vector Machines (SVMs) in the late 1960s, they received significant attention in recent years when they emerged as a promising estimator in data-driven fields [200]. SVM can be used for both classification and regression problems. Support Vector Regression (SVR) works by finding a hyperplane that best fits the data while minimizing the error between the predicted and actual values, subject to a user-defined tolerance margin. SVR utilizes a subset of training points in its decision function to maximize the minimum distance from the hyperplane to neighbouring sample points. It effectively addresses overfitting by employing appropriate kernel functions (KF). These kernels transform original non-linear observations into a higher-dimensional space, enhancing data separability. The SVR's searches for a fitting function $f(x) = \langle w, x \rangle + b$, with small value ϵ from the target (y_i) for training data set (x_i). The KF is based on the radial basis function (RBF) [195, 201]. The KF is defined as the inner product of the transformed input-feature vectors:

$$K(x_i, x_j) := \langle \phi(x_i) \mid \phi(x_j) \rangle \tag{6.7}$$

The optimization of this cost function is considerably simplified by introducing kernel notation. Rather than explicitly designing a mapping function, transforming the data, and subsequently computing inner products, the SVR approach defines the kernel as a function of the input feature vector. Commonly considered KFs in SVM applications include [200]:

$$\begin{aligned} K_{linear}(x, x^{'}) &= x, x^{'} \\ K_{polynomial} &= (\gamma x x^{'} + r)^{\rho} \\ K_{RBF}(x, x^{'}) &= exp(-\gamma \parallel x - x^{'} \parallel^2) \\ K_{sigmoid}(x, x^{'}) &= tanh(\gamma x x^{'} + r) \end{aligned}$$

SVR is a powerful regression technique that can capture complex relationships

in data, especially when combined with appropriate kernel functions and hyper-parameter tuning. Unlike KNN, the accuracy and performance of the SVR are independent of the size of the data set [202]. Figure 6.7 shows the SVR with RBF KF for data different tolerances.

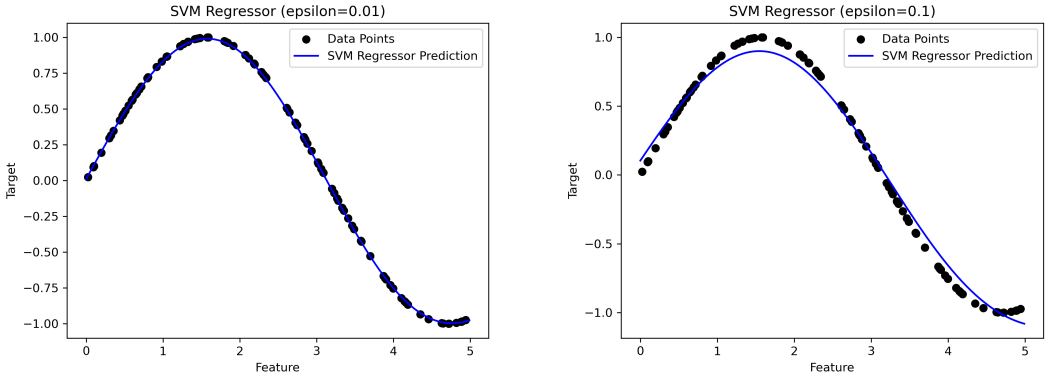

(a) (b)

FIGURE 6.7: Illustration of support vector regressor with radial basis function kernel function for epsilon (a) 0.01 and (b) 0.1

6.3.4 Random Forest

Random Forest (RF) regression technique leverages the collective performance of multiple Decision Tree (DT) algorithms to classify or predict the value of a variable [203]. When RF receives the input vector (x) consisting of different training data features, RF constructs K number of regression trees and averages the results. After K such trees $T(x)_1^k$ are grown, the RF regression predictor is given as [200]:

$$\hat{f}_{rf}^{K}(X) = \frac{1}{K}\sum_{k=1}^{K} T(x) \tag{6.8}$$

To prevent the correlation among different trees, RF enhances the diversity of the trees by growing them from various training data subsets generated through a technique called bagging. The bagging technique trains data by resampling randomly and replacing the original dataset. This makes it robust when facing slight variations in the input dataset and improves the prediction accuracy [203]. On the

contrary, when RF constructs a tree, it selects the best feature/split point within a randomly chosen subset of evidential features from the overall set. This approach can weaken the strength of individual trees but reduces the correlation between them, thus minimizing generalization error [203]. Furthermore, the samples not chosen for training the kth tree in the bagging process are included in another subset called out-of-bag (oob). These oob elements can be utilized by the kth tree to evaluate its performance [204].

RF also offers an evaluation of the relative importance of various evidential features. This capability is valuable in multi-source studies with high data dimensionality, where understanding the influence of each feature on the prediction model aids in selecting the most effective ones [205]. Figure 6.8 shows the RF regressor predictions with 100 estimators.

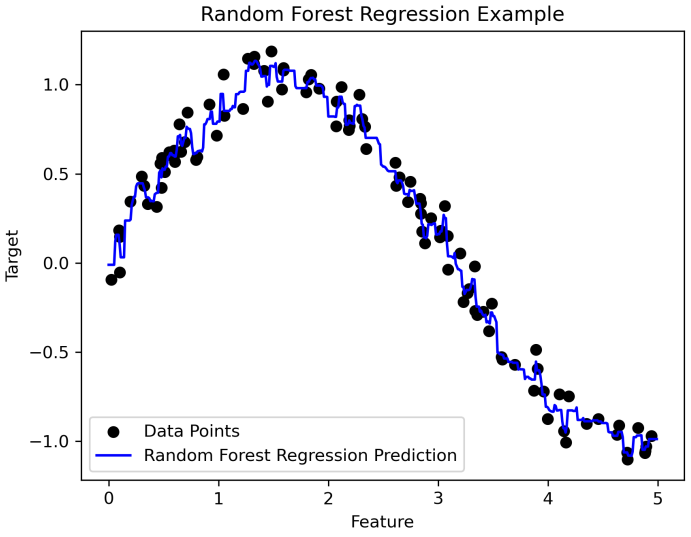

FIGURE 6.8: Random Forest Regressor with 100 tree estimators.

6.3.5 XGBoost

Chen and Guestrinis recently introduced eXtreme Gradient Boosting (XGBoost), a cutting-edge algorithm [206]. XGBoost functioning as an ensemble learning method employs gradient-boosted decision trees specifically crafted to enhance both speed and performance [207]. XGBoost aimed to enhance the computational

resources available for boosted tree algorithms. The Gradient Boosting technique employs a loss function that needs adjustment to tackle specific challenges. This loss function is referred to as cross-entropy for classification tasks, while it is termed MSE for regression problems. Utilizing a weak learner to generate predictions and an additive model to merge weak learners, XGBoost leverages the addition of weak learners to minimize the loss function and rectify residual errors from prior trees [208]. Gradient boosting involves the creation of new models to predict the errors of previous models, which are then combined to provide the final prediction. The term "gradient boosting" derives from using a gradient descent approach to diminish or minimize loss while incorporating new models.

Achieving optimal performance requires careful tuning of the model. Tuning XGBoost can be particularly challenging due to the multitude of its hyper-parameters. These parameters can be categorized into general, booster, learning task, and command line parameters. Tuning can be conducted through either grid or random search methodologies [209].

According to the original framework of gradient boosting [210], it employs K additive trees to approximate the output as follows [211]:

$$\hat{y}_i = \sum_{k=1}^{K} f_k(X_i), f_k \in F \tag{6.9}$$

Where f_k is the independent classification and regression tree (CART) at each k step, map the input variables X_i to y_i, and F is the space of functions containing all CARTs. XGBoost aims to minimize the regularized objective function defined as follows:

$$obj = \sum_{i=1}^{n} \iota(y_i, \hat{y}_i + \sum_{k=1}^{K} \Omega(f_k), f_k \in F \tag{6.10}$$

Here, $\Omega(\mathrm{f}) = \gamma \mathrm{T} + \frac{1}{2}\lambda \sum_{j=1}^{T} w_j^2$. The regularized objective function comprises two components: the training loss function ι and the regularization term Ω. The training loss ι quantifies the disparity between the predicted value $\hat{y}_i$ and the actual value y_i. Meanwhile, the regularization term Ω assesses the model's complexity,

thereby facilitating the refinement of the learned weights to prevent overfitting [211].

6.4 Issues of Supervised Learning Algorithms

The first step in supervised ML is to deal with a dataset. Experts may suggest carefully selecting features to optimize training on a dataset. In cases where specialized expertise is lacking, resorting to a "brute-force" approach involves assessing all available features to identify the most informative and relevant ones. However, datasets gathered via the "brute-force" method are not conducive to effective modelling. They often contain noise and missing feature values, thus requiring thorough preprocessing to mitigate these issues [212]. In the subsequent phase, data preparation and preprocessing are pivotal stages in supervised machine learning. Researchers play a crucial role in executing these tasks effectively. Different researchers have proposed various techniques to address the challenge of missing data. Hodge and Austin conducted a comprehensive survey of contemporary techniques for outlier (noise) detection [213]. Additionally, Karanjit and Shuchita provided insights into different outlier detection methods employed across diverse machine-learning applications [214]. Furthermore, Escalante conducted a comparative analysis of six outlier detection methods through experiments conducted on benchmark datasets and a synthetic astronomical domain [215].

6.5 Deep Learning Models

In 1980, due to invention of efficient deep learning (DL) models and network structures deep learning models became a prevalent topic in the area of ML and Artificial Intelligence (AI) [216]. DL models have grown dramatically in terms of performance in a wide range of applications in day-to-day life. The DL techniques can play a key role in building intelligent data-driven systems according to today's needs, because of their excellent learning capabilities from historical data and provide fast and efficient solution. Consequently, DL can change the world as

well as humans' everyday life through its automation power and learning from experience [217]. There are various DL models available used for different type of data. In this study, Convolutional Neural Network (CNN), Fully Connected Neural Network (FCNN), Recurrent Neural Network (RNN) and Long short-term memory (LSTM) were discussed briefly.

6.5.1 Convolutional Neural Network (CNN)

The Convolutional Neural Network (CNN) is a popular discriminative DL architecture that learns directly from the input without the need for human feature extraction. Figure 6.9 shows an example of a CNN including multiple convolutions and pooling layers. Each layer in CNN takes into account optimum parameters for a meaningful output as well as reduces model complexity. CNN also uses a *dropout* that can deal with the problem of over-fitting, which may occur in a traditional network. CNN are specifically intended to deal with a variety of 1D and 2D shapes, and are thus widely employed in visual recognition, medical image analysis, image segmentation and natural language processing [218].

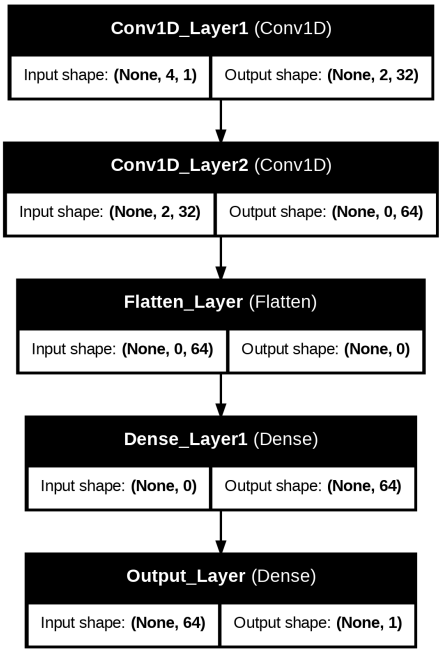

FIGURE 6.9: Example of the CNN model showcasing multiple layers, including the input and output sizes for each layer.

6.5.2 Recurrent Neural Network (RNN)

Recurrent Neural Network (RNN) are suited for sequential inputs like speech and text and generating sequence. RNN is a type of artificial neural network having the structure of feed-forward neural network. The directed cycles in RNN allows the information to be circulated in the network so that the output of each time is not related to the input at present but related to the input at previous timestamps [219].

The traditional RNNs deal with time series data having serious problem about gradient vanishing in process of back propagation. Therefore, RNN can only be used for short term memory. Figure 6.10 shows the simple RNN model which consists of a single SimpleRNN layer with 50 units to process sequential data, followed by a Dense output layer for regression. It takes input sequences of shape 10 time steps and 4 features and outputs a single numerical value.

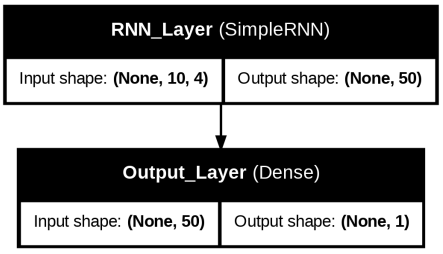

FIGURE 6.10: Example of the RNN model showcasing multiple layers, including the input and output sizes for each layer.

6.5.3 Long short-term memory (LSTM)

To address the issue of the back-flow of memory in RNNs, Hochreiter and Schmidhuber (1997) proposed Long Short-Term Memory (LSTM) [220]. A memory cell in an LSTM unit can store data for extended periods, with the flow of information into and out of the cell regulated by three gates. The *Forget Gate* decides which information from the previous cell state should be retained and which should be discarded as no longer relevant. The *Input Gate* determines which new information

is incorporated into the cell state, while the *Output Gate* controls the information transmitted as output. Figure 6.11 shows the simple LSTM model consists of a single LSTM layer with 50 units to process sequential data, followed by a Dense output layer for regression. It accepts input sequences with a shape of 10 time steps and 4 features, and outputs a single numerical value.

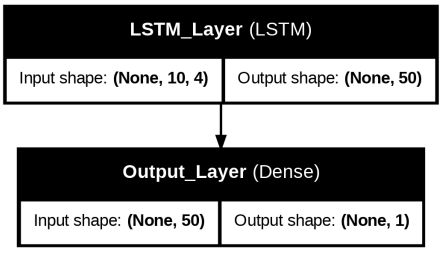

FIGURE 6.11: Example of the LSTM model showcasing multiple layers, including the input and output sizes for each layer.

6.5.4 Fully Connected Neural Network (FCNN)

A Fully Connected Neural Network (FCNN) is a type of artificial neural network where each neuron in one layer is connected to every neuron in the next layer. In the input layer, each neuron represents a feature of the data. The input is then processed through one or more hidden layers, consisting of neurons that perform computations and extract patterns. The output layer produces the network's prediction. The main characteristic of an FCNN is that information flows in a single direction—from the input layer to the output layer—without loops or cycles, enabling the model to learn complex relationships. Figure 6.12 illustrates an example of a simple FCNN model, showing the input and output shapes for each layer.

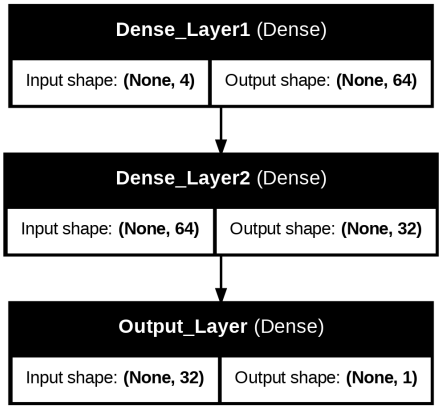

FIGURE 6.12: Example of the FCNN model showcasing multiple layers, including the input and output sizes for each layer.

Chapter 7

Prediction of SAR & Temperature Elevation in Tissues using Machine Learning

7.1 Introduction

This chapter explored the application of supervised ML models for predicting SAR and temperature elevation in tissues, considering diverse parametric variations. Different ML models were implemented such as RF, XGBoost, LR, KNN, SVM, CNN, LSTM, FCNN, RNN and a hybid model of CNN-LSTM. These models were implemented to predict the SAR and temperature elevation in the tissues.

ML models offer several advantages over traditional numerical simulations. Once trained on relevant datasets, they can accurately predict SAR and temperature elevation, bypassing the need for extensive computational simulations. Furthermore, ML models excel at distilling complex relationships from data, providing a streamlined approach to understanding the interactions between RF-EMF exposure and tissue responses.

Throughout this chapter, we evaluate the performance of various ML models using different performance metrics. Additionally, a t-test was employed to validate our results' reliability. By systematically assessing the predictive capabilities of ML models and conducting statistical validation, we aim to provide a comprehensive understanding of their effectiveness in predicting SAR and temperature elevation in tissues.

7.2 Consideration of RF-EMF Exposure Parameters for Machine Learning

This study focuses on pivotal parameters linked to RF-EMF exposure near the MIFA in proximity to humans. The findings presented in Chapter 4 and supported by existing literature establish that SAR variability is affected by parameters linked to the characteristics of RF-EMF sources. Similarly, Chapter 5 underscores the significance of the ambient temperature and the duration of exposure as pivotal factors influencing temperature elevation. Hence, it is imperative to consider these critical factors that influence RF-EMF exposure when making predictions regarding SAR and temperature elevation. Further details regarding the RF-EMF exposure parameters are discussed below.

7.2.1 Parameters for SAR Predictions

The SAR variation is notably influenced by several factors, including the distance between the RF-EMF source and the exposed tissues [26,97]. Likewise, variations in the transmit power levels of RF-EMF significantly contribute to the variation in SAR values [10]. Additionally, the frequency of the RF-EMF source emerges as a critical influence on SAR values, typically exhibiting higher values for high frequencies with reduced penetration [10]. Moreover, the mounting position on the body, antenna structure, tissues' dielectric properties, and RF-EMF source's orientation also impact the SAR value.

The variation in frequency was not studied due to the operational constraints of the MIFA, which operates within a single band (2.4 GHz), and the investigation solely focused on the MIFA antenna. Furthermore, the impact of dielectric properties was beyond the scope of this study due to the single frequency of 2.4 GHz utilised. Different mounting positions on the body, orientation of the antenna, and power level were also considered in the study. The parameters used in ML for SAR prediction are outlined below:

- Distance between MIFA and body.
- Power level of MIFA.
- Orientation of the MIFA.
- Mounting position on the body.

Identifying these parameters establishes the groundwork for predicting SAR through ML, offering valuable insights into the complex interaction dynamics between RF-EMF exposure and its various influencing factors.

7.2.2 Parameters for Temperature Elevation Predictions

The temperature increase in tissues due to exposure to RF-EMF is mainly influenced by the characteristics of the RF-EMF source, such as frequency and power level. In addition, the vital parameters that affect the temperature elevation in tissues due to RF-EMF exposure include the ambient temperature during exposure and the duration of exposure. RF-EMF sources increase the thermal load on tissues, causing their temperature to rise [24, 25]. Furthermore, the duration of exposure also plays a significant role in determining the extent of temperature elevation in tissues [221]. Therefore, this study considers different ambient temperatures within an underground mine and the duration of RF-EMF exposure to predict the temperature elevation in tissues for various mounting positions of MIFA.

7.3 Data Collection and Preprocessing

7.3.1 For SAR Predictions

The data was collected by varying the associated RF-EMF exposure parameters to predict SAR. The considered parameters were varied, and SAR was reported using numerical simulations. The distance was varied for 5 mm, 10 mm and

15 mm, whereas the power level was varied from the minimum transmit power level (0.01 W) to the maximum allowed power level at 2.4 GHz (0.1 W). The orientation of the MIFA was varied for 0^0, 30^0, 60^0 and 90^0, as these angles yielded comparable responses to other orientations of the MIFA. Two mounting positions, wrist and waistline, were selected for SAR predictions, as the focus of this study was specifically on investigating SAR for these commonly used positions, which are prevalent in wearable device applications. The variation of considered parameters is summarised below:

- **Distance** between MIFA and body: 5 mm, 10 mm and 15 mm (3 variations)
- **Power level** of MIFA: 1 mW, 50 mW and 100 mW (3 variations)
- **Orientation** of the MIFA: 0^0, 30^0, 60^0 and 90^0 (4 variations)
- **Mounting position** on the body: wrist and waistline side (2 variations)

HFSS simulations were performed using *Optimetrics* to explore parametric variations for all the above parameters for SAR values. Each mounting position of the MIFA generates 36 ($3\times$ 3 $\times$ 4) parameter combinations. Therefore, a total of 72 ($3 \times 2 \times 4 \times 2$) sets were analysed, encompassing both wrist and waistline positions for SAR predictions. The maximum average SAR_{10g} averaged over 10 grams of tissues was recorded as an output parameter, referred to as SAR in this study.

The collected data, comprising transit power level, distance, orientation, and mounting position, was consolidated into a single file, with SAR designated as the output parameter for ML models. This unified dataset provides the necessary inputs and corresponding output for training and evaluating ML algorithms to predict SAR levels based on various factors such as power level, distance, orientation, and mounting position. The ML models are trained using a portion of the (training) dataset and then evaluated for their performance using the remaining (test) data.

7.3.2 For Temperature Elevation Predictions

The data collection process involved systematically varying the parameters discussed in the previous section to predict temperature elevation using ML models. Typical ambient temperatures of the underground mine environment were considered for the RF-EMF exposure scenario, with a fixed time duration of 8 hours. Results discussed in Chapter 5 revealed that tissue temperature elevation tends to reach equilibrium following continuous RF-EMF exposure. Consequently, after 8 hours of exposure, the elevated tissue temperature remains constant under consistent RF-EMF exposure conditions. Hence, for the RF-EMF exposure duration in this study, a fixed time duration of 8 hours was utilised.

In this study, two mounting positions of the MIFA were examined under ambient temperatures of 40^0 C and 50^0 C. The RF-EMF exposure calculations were conducted at intervals of 10 seconds over a total duration of 8 hours. The *Mechanical* solver within Ansys Workbench was employed to assess parameter variations and determine the maximum temperature elevation in skin tissues. Input features for the ML models included mounting positions (wrist and waistline), time duration (10 sec), and ambient temperature (40^0 C and 50^0 C), while the maximum temperature served as the output for implementing the ML model. A total of 115,200 data points were generated for temperature prediction using ML models and used for training and testing datasets for the ML models.

7.4 Implementation of Machine Learning Models for SAR Prediction

7.4.1 Data Splitting for Machine Learning Models

The first step in implementing the ML models is splitting the data into train and test data. Splitting the data into training and testing sets was essential for assessing the ML performance on unseen data, thus avoiding over-fitting and

providing insights into its generalisation capabilities. Additionally, this process facilitates the comparison of various machine learning models' performances.

The data was divided into a 70% training dataset and a 30% dataset designated for testing and validating the ML model. The data was split randomly, ensuring that each subset (training, testing, and validation) contained a representative sample of the overall dataset. This random splitting helps prevent bias and ensures the model was evaluated on diverse data points. Random data splitting can introduce biases due to class imbalance and temporal or spatial structure, thus impacting model evaluation. Cross-validation (CV) techniques were implemented to mitigate this issue and ensure fair and consistent performance assessment of ML models.

7.4.2 Grid Search for Hyper Parameter Tuning

Grid search is a widely used method for hyperparameter optimization in machine learning models [222]. In this approach, a finite set of possible values is defined for each hyperparameter, and the algorithm performs an exhaustive search by evaluating the Cartesian product of these value sets [223]. Hyperparameters can be categorical, Boolean, real-valued, or integer-valued, each contributing to the dimensionality of the grid. A key drawback of grid search is its inefficiency in high-dimensional spaces, as the number of evaluations grows exponentially with each additional hyperparameter, a challenge known as the "curse of dimensionality" [224].

When there are k parameters, each with n possible values, the computational complexity of grid search grows exponentially at a rate of $O(n^k)$ [225]. Consequently, grid search is only practical when the hyperparameter space is relatively small. In scikit-learn, the GridSearchCV function can efficiently apply grid search to identify optimal hyperparameters [226]. To reduce overfitting and bias in the machine learning models, different k-fold cross-validation (CV) methods were implemented. Comparisons were made for 5, 10, and 15-fold CV to determine the most effective

configuration. Table 7.1 presents the hyperparameters evaluated for each model to achieve the best performance.

7.4.3 Random Forest for SAR Predictions

The data for SAR predictions was trained using the RF regressor model. Model performance was assessed using the MAE, RMSE, and R^2 parameters. The RF relies on decision trees as estimators, significantly impacting the model's performance. Usually, values ranging from 10 to 100 are commonly employed, with the exact choice influenced by the data complexity and the specific task. However, experimentation was essential for determining the optimal number of estimators tailored to a specific dataset. Other hyperparameters are maximum depth and a minimum sample of leaf. Grid CV was performed to find the best combination of hyperparameters using negative mean squared error as the scoring metric. The best hyperparameters were used to train the RF regressor and recorded the MAE, RMSE, and R^2. Table 7.2 compares different CVs for MAE, RMSE and R^2. For 10-fold cross-validation, the optimal hyperparameters, such as max depth was 10, minimum samples leaf was 1, and estimators was 10, yield lower MAE and RMSE, along with a higher R^2 value, indicating a closer fit to the data. Therefore, these hyperparameters were used to train the RF regressor and analyse the importance of the feature.

Feature importance insights into which input variables are most influential in the ML model's predictions [227]. Understanding feature importance assists in identifying relationships between variables, enhances model transparency, improves performance, and informs data collection efforts by prioritising the most relevant features. Therefore, feature importance was applied to understand the essential features contributing to the SAR prediction. The importance of features was assessed using the RF regressor, and the feature importance was sorted in descending order, as depicted in Figure 7.1. The power level emerged as the most influential feature, surpassing factors such as antenna-body distance, antenna orientation, and mounting positions.

TABLE 7.1: Machine learning models hyperparameter configuration space.

Model	Hyperparameter	Search space
RF	*n_estimator*	10, 50, 100
	max_depth	None, 10, 20
	min_samples_leaf	1, 5, 10
XGBoost	*learning_rate*	0.1, 0.01, 0.001
	max_depth	3, 6, 9
	min_child_weight	1, 3, 5
	n_estimators	10, 20, 50, 100
LR	No hyperparameter	
KNN	*n_neighbors*	3, 5, 7, 9
	weights	uniform, distance
	p	1, 2
	algorithm	auto, ball_tree, kd_tree, brute
SVM	*kernel*	linear, poly, rbf
CNN, RNN	*learningrate*	0.01, 0.001, 0.2
	droupoutrate	0.3, 0.5, 0.6
	filters	16, 32, 64
	numberoflayers	1, 2
	batchsize	16, 32, 64
	epochs	10, 20
LSTM	*learningrate*	0.01, 0.001, 0.2
	droupoutrate	0.3, 0.5, 0.6
	filters	16, 32, 64
	numberoflayers	1, 2
	numberofunits	16, 32
	batchsize	16, 32, 64
	epochs	10, 20
FCNN	*learningrate*	0.01, 0.001, 0.2
	droupoutrate	0.3, 0.5, 0.6
	denseunits	50, 100
	numberoflayers	1, 2
	batchsize	16, 32, 64
	epochs	10, 20
CNN-LSTM	*learningrate*	0.01, 0.001
	dropoutrate	0.3, 0.5
	filters	16, 32
	numberoflayers	1, 2
	LSTMunits	50, 100
	batchsize	16, 32
	epochs	10, 20

TABLE 7.2: Comparison of performance metric of random forest

Cross validation	Train Data			Test Data		
	MAE	RMS	R^2	MAE	RMS	R^2
5	0.0662	0.1123	0.9887	0.1044	0.1793	0.9585
10	0.0547	0.0915	0.9925	0.0925	0.1471	0.9721
15	0.0672	0.1077	0.9896	0.1000	0.1699	0.9627

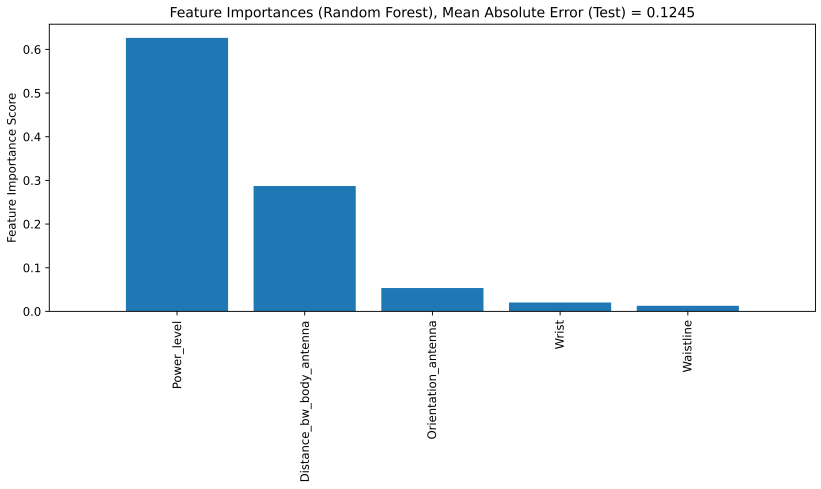

FIGURE 7.1: Feature importance for the prediction of SAR for Random Forest

7.4.4 XGBoost for SAR Predictions

The data was trained using the XGBoost regressor with its hyperparameters, such as learning rate, max depth, minimum child weight and number of estimators. The learning rate controls the step size during the optimisation process, influences the model's convergence speed and final performance, and is also considered a critical parameter. The maximum depth of the trees impacts the model's complexity and the model's ability to capture complex patterns in data. The minimum child weight helps prevent over fitting by controlling the number of instances in each node. The number of estimators specifies the number of trees to be built for the model. These hyperparameters were used to train the model and to find the best hyperparameters using grid CV with minimum MAE. The CV was performed for different values and compared to find the best hyperparameters of XGBoost as shown in Table 7.3. CV 10 outperforms the other cross-validation sets. Specifically,

for CV 10, XGBoost achieved optimised hyperparameters with a learning rate of 0.1, a max depth of 3, a min child weight of 1, and 100 estimators.

TABLE 7.3: Comparison of performance metric of XGBoost

Cross validation	Train Data			Test Data		
	MAE	RMS	R^2	MAE	RMS	R^2
5	0.0606	0.0765	0.9947	0.1379	0.1769	0.9596
10	0.0606	0.0765	0.9947	0.1379	0.1769	0.9721
15	0.0916	0.1186	0.9873	0.1197	0.1564	0.9684

Feature importance was also assessed with XGBoost to identify the significance of various features in SAR prediction. Within the XGBoost framework, the most critical feature for SAR prediction was the power level of the antenna, followed by the distance between the body and the antenna, orientation, and mounting positions (wrist or waistline), as illustrated in Figure 7.2. Hence, power level and distance variations are recommended as crucial features for accurately predicting SAR values and influencing the model's outcomes. They also aid in understanding the underlying relationships within the data, potentially offering valuable insights into domain-specific challenges.

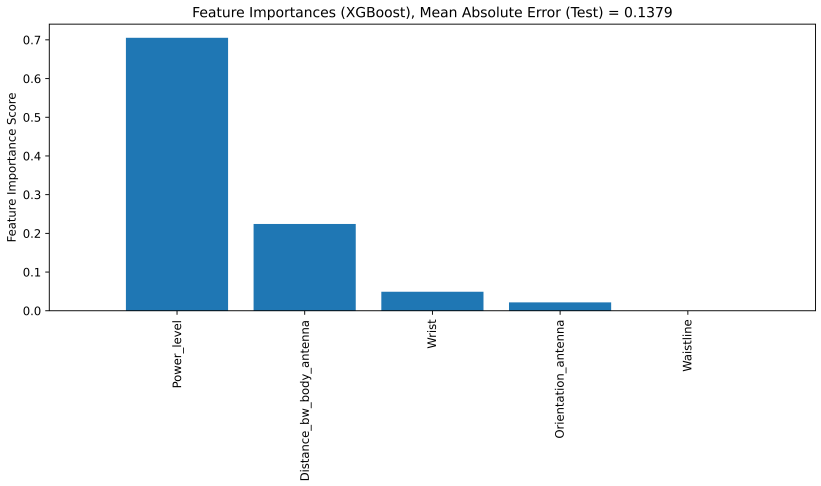

FIGURE 7.2: Feature importance for the prediction of SAR for XGBoost

7.4.5 K Nearest Neighbor for SAR Predictions

The data was trained using a KNN regressor, incorporating various hyperparameters, including the number of neighbours (3, 5, 7, 9), weight function (uniform and distance), p-value (where p=1 corresponds to Manhattan distance and p=2 corresponds to Euclidean distance), and algorithm (auto, ball tree, KD tree, and brute). A grid search CV with different cross-validation values was conducted to optimise the model's performance. Subsequently, performance metrics were compared to identify the optimal set of hyperparameters as shown in Table 7.4. It is evident that with a 10-fold CV, the training data exhibit an MAE and RMSE of 0, while the test data display the minimum MAE and RMSE values alongside a higher R-square value. In this configuration, the hyperparameters entail utilising the brute algorithm, setting the number of neighbours to 9, employing a distance-based weight function, and utilising Euclidean distance for neighbour distance calculation. Consequently, these hyperparameters were employed to train the KNN regressor.

Table 7.4: Comparison of performance metric of K Nearest Neighbor

Cross validation	Train Data			Test Data		
	MAE	RMS	R^2	MAE	RMS	R^2
5	0.3539	0.5198	0.7568	0.3064	0.4719	0.7124
10	0.0000	0.0000	1.0000	0.2281	0.4309	0.7602
15	0.0000	0.0000	1.0000	0.2288	0.4311	0.7600

7.4.6 Linear Regression for SAR Predictions

Linear regression (LR) regressor was used to train the data, and performance parameters were reported. The LR regressor has no hyperparameters for tuning. Therefore, no grid CV was performed. Table 7.5 shows the performance metrics of the LR. The LR model performs well, with lower errors and a good amount of variance explained in the training and test datasets. However, the R-squared value, particularly in the test set, was lower than other models like RF and XGBoost,

suggesting that LR may not capture as much variability as other models. LR does not inherently measure feature importance due to its simplicity and linearity. Therefore, the importance of features still needs to be considered.

Table 7.5: Comparison of performance metric of Linear Regression

Train Data			Test Data		
MAE	RMS	R^2	MAE	RMS	R^2
0.3597	0.4513	0.8166	0.3168	0.4268	0.7648

7.4.7 Support Vector Machine for SAR Predictions

The SVM regressor was trained using various kernels, including linear, polynomial, and radial basis functions (RBF). Grid CV was employed to determine the optimal hyperparameters of the SVM model across different values of k-fold validation. Table 7.6 compares performance metrics for the SVM regressor across different k-fold values. It can be noted that the linear kernel performs better for both CV values, although the SVM regressor model performance was less than that of the RF, XGBoost, LR and KNN models. The SVM regressor exhibits a lower R-square value than the RF and XGBoost models and can have less variance in the target variable compared to the other models. The SVM model might not capture the underlying patterns in the data as effectively as the RF and XGBoost models and is an unsuitable choice for this specific regression task.

Table 7.6: Comparison of performance metric of Support Vector Machine

Cross validation	Train Data			Test Data		
	MAE	RMS	R^2	MAE	RMS	R^2
5	0.3396	0.4773	0.7949	0.3482	0.4764	0.7070
10	0.3396	0.4773	0.7949	0.3482	0.4764	0.7070

7.4.8 CNN for SAR Predictions

The CNN model was implemented with input layer designed to accept a sequence of 5 features, followed by multiple convolutional layers with $ReLU$ activation and max pooling to extract relevant features. Dropout is applied after each convolutional layer to prevent overfitting. The model concludes with a flattening layer and a dense output layer with a linear activation function. The optimizer is selected from a predefined set (Adam, RMSprop, or SGD) and is adjusted based on the learning rate and gradient clipping.

The CNN model was implemented with various hyperparameter sets. These hyperparameters were tuned using different CV folds, specifically 5-fold and 10-fold. Table 7.7 presents a comparison of the performance metrics of the CNN models across these CV folds. The performance of the CNN model was superior with 10-fold cross-validation compared to 5-fold. The optimal hyperparameters after tuning were a batch size of 16, a dropout rate of 0.5, 20 epochs, 32 filters, a learning rate of 0.01, and a single layer.

Table 7.7: Comparison of performance metrics of deep learning models with different cross-validation folds

Deep Learning Models	Cross validation	Test Data		
		MAE	RMS	R^2
CNN	5	0.2964	0.4453	0.7439
	10	0.2741	0.4255	0.7662
LSTM	5	0.3644	0.6307	0.4864
	10	0.6649	0.8526	0.0612
FCNN	5	0.2958	0.4300	0.7613
	10	0.2612	0.4647	0.7211
RNN	5	0.3121	0.4184	0.7739
	10	0.1973	0.3704	0.8228
CNN-LSTM	5	0.2115	0.3331	0.8568
	10	0.2952	0.4887	0.6915

7.4.9 LSTM for SAR Predictions

The LSTM model for regression tasks is implemented using Keras and integrated with Scikit-learn's 'GridSearchCV' for hyperparameter tuning. The model includes an input layer designed to process sequences of 5 time steps, each with 1 feature. It is followed by a configurable number of LSTM layers, with adjustable units. Each LSTM layer is paired with a dropout layer to enhance regularization and prevent overfitting. After the LSTM layers, dense layers with ReLU and linear activation functions are used, making the model suitable for regression tasks. The optimizer is selected from Adam, RMSprop, or SGD, with customizable learning rates and gradient clipping. Table 7.1 lists the hyperparameter grid values searched to optimize the model and determine the best parameters. Grid search is conducted using 5-fold cross-validation, evaluating each combination of hyperparameters based on negative mean squared error. Once the optimal hyperparameters are identified, the model is retrained using the best configuration, and its performance is evaluated on test data. As shown in Table 7.7, a 10-fold cross-validation provides robust performance on the test data.

7.4.10 FCNN for SAR Predictions

The FCNN model for regression tasks was implemented, and *GridSearchCV* was integrated for hyperparameter tuning. The model features an input layer that accepts five input features for SAR predictions, followed by a dense layer with *ReLU* activation and dropout for regularization. The output layer uses a linear activation function, making it suitable for regression. Table 7.1 outlines the hyperparameters used in tuning the FCNN model for optimal performance. The GridSearchCV identified the best hyperparameters for both 5-fold and 10-fold cross-validation, as shown in Table 7.7. After the grid search, the model was trained with the optimal parameters and evaluated on the test data. The best hyperparameters were a batch size of 16, a dropout rate of 0.2, 20 epochs, and a learning rate of

0.01. The results revealed that the 10-fold CV provided the optimal performance for the FCNN model.

7.4.11 RNN for SAR Predictions

The RNN architecture consists of an input layer that accepts sequences with a fixed length of 5 time steps and a single feature per step. It includes multiple LSTM layers, where each LSTM unit uses the *tanh* activation function, with dropout applied to mitigate overfitting. The final LSTM layer does not return sequences, while intermediate layers return sequences, enabling the stacking of multiple LSTM layers. After the LSTM layers, a *Dense layer* with *ReLU* activation was used for further feature processing, followed by an output layer with a *linear* activation function, making the model suitable for regression tasks. To optimize the model, *GridSearchCV* was employed to explore different combinations of hyperparameters for 5 and 10 folds and tuned hyperparameters are provided in Table 7.1. The GridSearchCV identified the optimal hyperparameters, including a batch size of 16, a dropout rate of 0.3, 20 epochs, a learning rate of 0.01, 32 units, and a single layer. The RNN model was ultimately trained using the best hyperparameters on the training data, and its performance metrics were evaluated on the test data, as shown in Table 7.7. The results indicate that, for the 10-fold cross-validation, the RNN model delivers more robust performance.

7.4.12 CNN-LSTM for SAR Predictions

A hybrid model was implemented to predict SAR, leveraging the strengths of individual models: CNNs for feature extraction and LSTMs for learning sequential data. The CNN-LSTM architecture was designed to benefit from both deep learning techniques. The model consists of an input layer that accepts sequences of fixed length, followed by several 1D convolutional layers with ReLU activation, MaxPooling, and Dropout layers to extract features and prevent overfitting. The LSTM layer then learns the sequential dependencies, and the output layer is a

Dense layer with a linear activation function, suitable for regression tasks. A custom Keras regressor class, CustomKerasRegressor, was used to wrap the model, enabling it to work with GridSearchCV for hyperparameter optimization. The grid search evaluates various hyperparameter combinations, as detailed in Table 7.1. The GridSearchCV identified the best parameters as follows: a batch size of 16, a dropout rate of 0.3, 20 epochs, 32 filters, a learning rate of 0.01, 50 LSTM units, and a single CNN layer. Finally, the CNN-LSTM model was trained on the training data using the best hyperparameters, and the model was tested on the test data to evaluate performance metrics. Table 7.7 compares the performance metrics across different cross-validation folds, showing that the 5-fold cross-validation yields better performance than the 10-fold, indicating that the model begins to overfit.

7.4.13 T-Test for SAR Predictions

A t-test helps assess the statistical significance of differences in comparing the performance of different ML models on a similar dataset, particularly regarding model performance, feature selection, and error analysis. Furthermore, a t-test can reveal variability in model performance due to factors such as random initialization or differences in the dataset, offering insights into model generalization and overfitting.

The discrepancy between actual and predicted SAR values in the t-test can be attributed to several factors. Model complexity significantly influences the variations observed between these values. Complex models may overfit the training data, capturing noise instead of the underlying patterns, which leads to poor predictions on unseen data. Conversely, simpler models may overlook essential features, resulting in high bias and prediction inaccuracies. Additionally, variability in the SAR and temperature parameters can introduce noise into the model predictions. Together, these factors contribute to the discrepancies between actual and predicted SAR values, thereby affecting the results of statistical tests like the t-test that evaluate model performance.

The t-test was used to access errors between actual and predicted SAR values generated by ML models that were significantly different from 0. The null hypothesis (H_0) was a mean error between the actual and predicted SAR values generated by the ML model is equal to 0, or the alternative hypothesis (H_1) represents the error is not equal to 0. T-test calculates t-statistic and p-value. If the p-value is less than the significance level (<0.05), it suggests that there is significant evidence to reject the null hypothesis. It concludes that the mean error between actual and predicted SAR values generated by the ML model significantly differs from 0. Therefore, the alternative hypothesis (H_1: >0.05) is valid, suggesting that the mean error between actual and predicted SAR values generated by the ML model is not significantly different from 0. The t-test allows us to conclude which ML model performs better and exhibits satisfactory performance. Hence, a t-test was conducted across all ML models, and the outcomes were visualised by plotting their mean errors.

The chosen significance level, often represented as the p-value was set at 0.05. If the p-value is less than 0.05, the mean error between actual and predicted SAR values deviates significantly from zero, suggesting poor performance of the specific ML model. Conversely, if the p-value exceeds 0.05, it implies that the mean error is closer to zero, indicating good performance of the ML models for SAR prediction. The t-test results were illustrated in Figure 7.3, displaying the p-values for all implemented ML models for SAR prediction. The comparison demonstrates that the p-values for RF, XGBoost, LR, and KNN exceeded 0.05, affirming their strong performance and suitability for SAR prediction. Conversely, the p-value for SVM fell below 0.05, indicating subpar performance of the SVM ML model in SAR prediction.

A t-test was also conducted on the deep learning models to validate the results. Figure 7.4 presents the t-test results for the CNN, LSTM, FCNN, RNN, and hybrid CNN-LSTM models. The results indicate that all implemented deep learning models passed the t-test, confirming that the predicted SAR values are close to zero. However, the LSTM model exhibited a low p-value, which may be attributed to the small variance in the error.

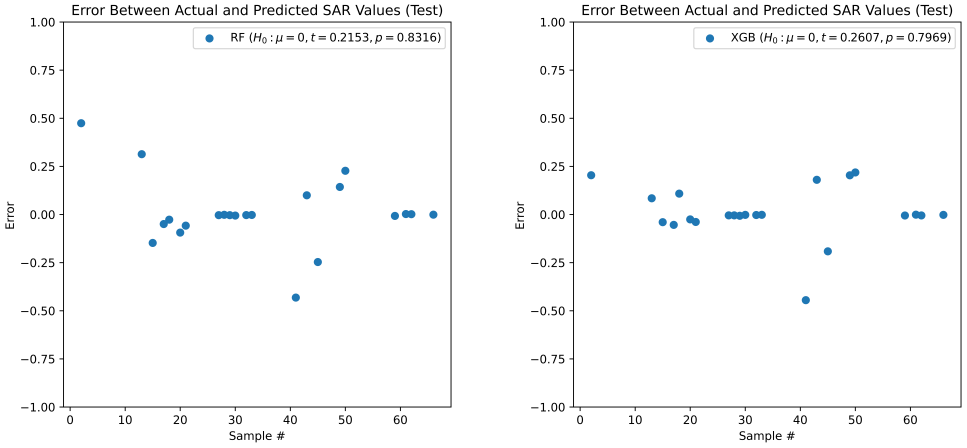

(a)

(b)

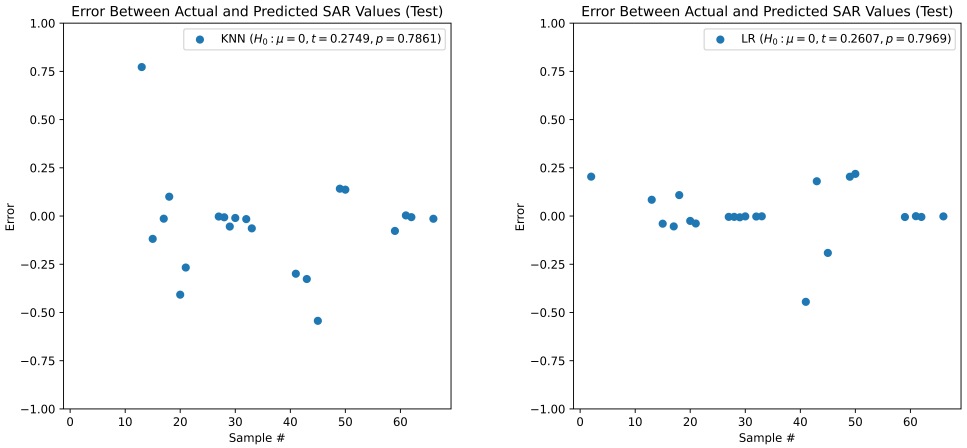

(c)

(d)

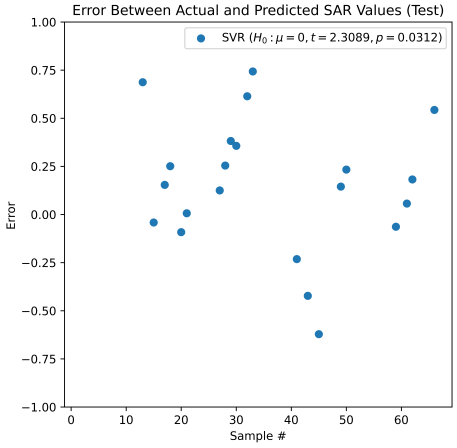

(e)

FIGURE 7.3: Error between actual and predicted value of SAR for t-test when (a) random forest, (b) XGBoost, (c) KNN, (d) linear regression and (e) SVM models were used.

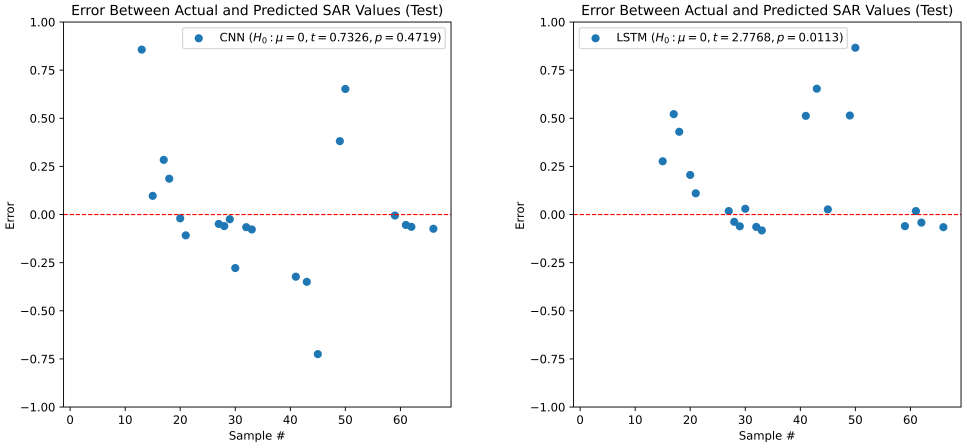

(a)

(b)

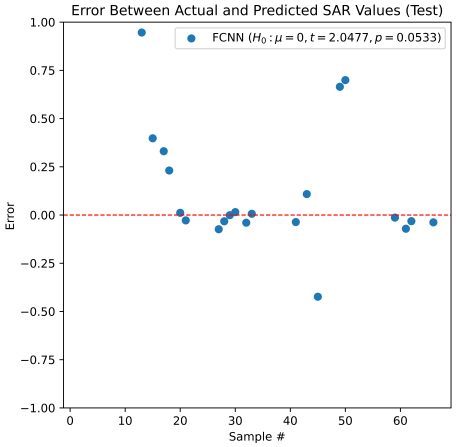

(c)

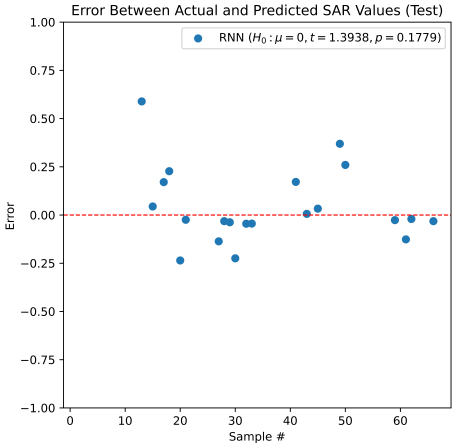

(d)

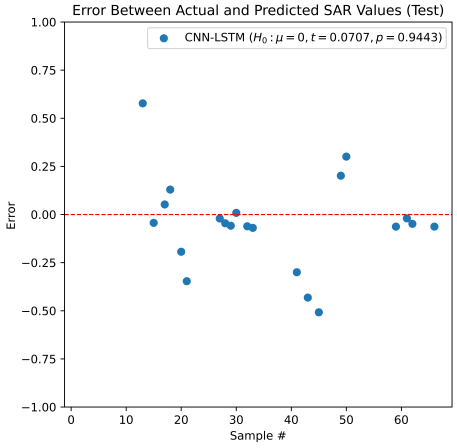

(e)

FIGURE 7.4: Error between the actual and predicted SAR values for the t-test across different deep learning models: (a) CNN, (b) LSTM, (c) FCNN, (d) RNN, and (e) CNN-LSTM.

7.5 Implementation of Machine Learning Models for Prediction of Maximum Temperature Elevation in Tissues

7.5.1 Data Splitting for Machine Learning Models

The dataset was divided into two subsets to predict maximum tissue temperature elevation. One subset was designated for training the model, while the other was reserved for evaluating its performance. The training set comprises 70% of the total data, while the remaining 30% was utilised to test various ML models to assess their effectiveness. A random state of 7 was set to ensure consistent data splitting every time the code runs, thereby maintaining result consistency.

7.5.2 Random Forest for Temperature Elevation Predictions

The data for maximum temperature elevation predictions was trained using the RF regressor model. The hyperparameters of RF varied, and the best hyperparameters were selected using a grid search CV. The RF hyperparameters used in temperature prediction were the number of estimators, maximum depth of the tree, and minimum sample leaf. The grid CV search was performed with different k-fold values to remove the biases in the training data set of the RF model. Grid CV used negative mean squared error as the scoring metric for selecting the best hyperparameters of the ML model. The best hyperparameters were used to train the RF regressor and recorded the MAE, RMSE, and R^2. Table 7.8 compares k-fold CV values with MAE, RMSE and R^2.

The analysis conducted through 5-fold cross-validation revealed the optimal hyperparameters for the RF model as a maximum depth of 20, a minimum sample leaf of 1, and 100 estimators. This configuration resulted in lower MAE and RMSE values and a higher R^2 value. These metrics collectively indicate a closer fit of the

model to the data. Similar results were also observed for 10 and 15-fold CV, suggesting consistent performance across different fold values. However, the specified hyperparameters consistently outperformed others, reaffirming their effectiveness in capturing the underlying patterns within the dataset and emphasising their suitability for predictive modelling of temperature elevation.

TABLE 7.8: Comparison of performance metric of random forest for predictions of temperature elevation

Cross validation	Train Data			Test Data		
	MAE	RMS	R^2	MAE	RMS	R^2
5	0.0001	0.0007	1.0000	0.0003	0.0016	1.0000
10	0.0001	0.0007	1.0000	0.0003	0.0016	1.0000
15	0.0001	0.0007	1.0000	0.0003	0.0017	1.0000

Similarly, the importance of features was applied to understand the essential features contributing to temperature elevation prediction. The importance of features was assessed using the RF regressor and sorted in descending order, as depicted in Figure 7.5. The findings indicate that ambient temperature is the primary factor influencing the maximum temperature elevation observed in tissues. This elevation can be determined by the combined effect of ambient temperature and the temperature increase resulting from exposure to RF-EMF. While the temperature rise due to RF-EMF exposure contributes to the thermal load experienced by the tissues, the predominant variation in maximum temperature elevation is attributed to higher ambient temperature levels exceeding 37^0 C. It highlights the considerable influence of environmental conditions, particularly ambient temperature, on the dynamics of tissue temperature. In comparison, RF-EMF exposure is supplementary in affecting tissue temperature dynamics. Furthermore, the duration of RF-EMF exposure exhibits minimal impact on temperature elevation. Even with 0 seconds to 8 hours of RF-EMF exposure variations, the observed elevation remains below 1^0 C.

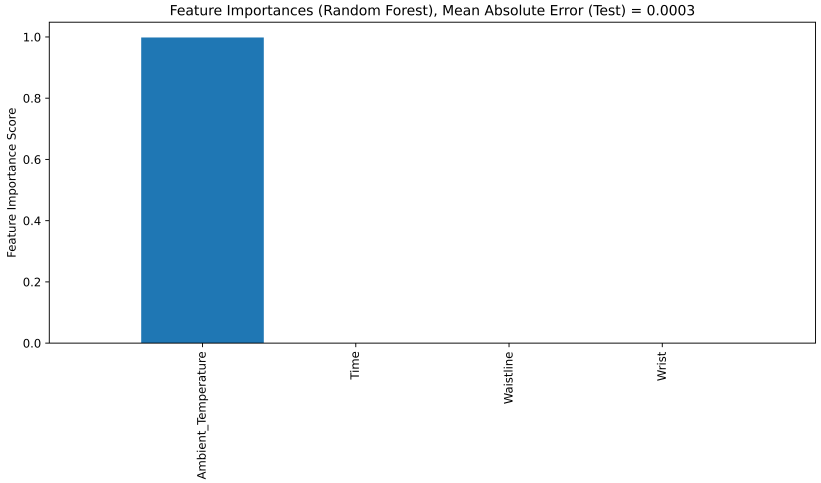

FIGURE 7.5: Feature importance for the prediction of maximum temperature elevation for Random Forest

7.5.3 XGBoost for Temperature Elevation Predictions

The data underwent training using the XGBoost regressor, employing similar hyperparameters such as learning rate, max depth, minimum child weight, and several estimators. The best hyperparameters, determined through grid CV with minimum MAE, were explored across various k-fold values, as outlined in Table 7.9. The k-fold values of 5 and 10 yielded identical performance metrics, albeit with different sets of hyperparameters for XGBoost. Specifically, for 5-fold cross-validation, the optimal hyperparameters were a learning rate of 0.1, maximum depth of 9, minimum child weight of 1, and 100 estimators. The resulting MAE and RMSE values were minimised, with an R-squared value of 1, indicating that the XGBoost regressor exhibited superior accuracy in predicting temperature elevation compared to RF. Consequently, the XGBoost regressor was trained using the optimal hyperparameters from 5-fold cross-validation, followed by a feature importance analysis.

Feature importance analysis was conducted using XGBoost to identify the significance of different features in predicting temperature elevation, as depicted in Figure 7.6. Consistently with previous findings, the analysis revealed that ambient

TABLE 7.9: Comparison of performance metric of XGBoost for predictions of temperature elevation in tissues

Cross validation	Train Data			Test Data		
	MAE	RMS	R^2	MAE	RMS	R^2
5	0.0016	0.0067	1.0000	0.0018	0.0077	1.0000
10	0.0016	0.0067	1.0000	0.0018	0.0077	1.0000

temperature emerged as the most crucial feature in determining maximum temperature elevation in tissues. Conversely, the impact of other factors on temperature elevation was found to be negligible.

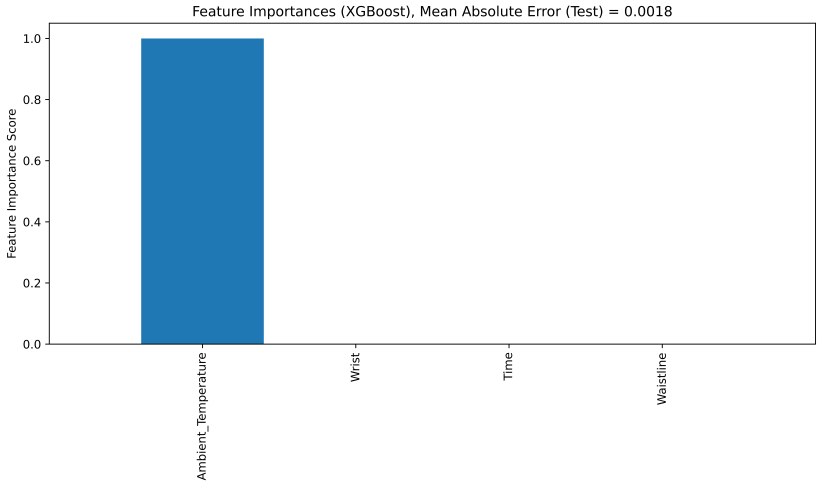

FIGURE 7.6: Feature importance for the prediction of temperature elevation for XGBoost

7.5.4 K Nearest Neighbor for Temperature Elevation Predictions

The data was trained using a KNN regressor, with optimisation conducted via grid search CV across various hyperparameters. The number of neighbors, weight function, p-value, and algorithm were among these parameters. When comparing performance metrics, it was discovered that with a 5-fold CV, the training data achieved an MAE and RMSE of 0, as shown in Table 7.10. The test data exhibited minimal MAE and RMSE values and a higher R-squared value. The optimal hyperparameters included using the brute algorithm, setting the number

of neighbors to 3, employing a distance-based weight function, and utilising Euclidean distance for neighbour distance calculation. These hyperparameters were subsequently employed to train the KNN regressor.

TABLE 7.10: Comparison of performance metric of K Nearest Neighbor for temperature elevation prediction

Cross validation	Train Data			Test Data		
	MAE	RMS	R^2	MAE	RMS	R^2
5	0.0000	0.0000	1.0000	1.7476	2.3486	0.7887
10	0.0000	0.0000	1.0000	1.7903	2.3965	0.7800
15	0.0000	0.0000	1.0000	1.7903	2.3965	0.7800

7.5.5 Linear Regression for Temperature Elevation Predictions

LR regressor was used to train the data, and performance parameters such as MAE, RMSE and R-square values were reported. The LR regressor has no hyperparameters for tuning. Therefore, no grid CV was performed. Table 7.11 shows the performance metrics of the LR. The LR model performs well, with lower errors and much variance explained in the training and test datasets. However, the R-squared value, particularly in the test set, is lower than other models like RF and XGBoost, suggesting that LR may not capture as much variability as other models.

TABLE 7.11: Comparison of performance metric of Linear Regression for temperature elevation predictions

Train Data			Test Data		
MAE	RMS	R^2	MAE	RMS	R^2
0.1309	0.1638	0.9990	0.1311	0.1625	0.9990

7.5.6 Support Vector Machine for Temperature Elevation Predictions

The SVM regressor was trained with linear, polynomial, and RBF kernels. Due to the prolonged training time with the linear kernel, polynomial and RBF kernels were only employed, delivering faster performance metrics for the SVM regressor. Table 7.6 illustrates the performance comparison across various kernel functions. The SVR model's performance metrics reveal notable shortcomings. Across both training and test datasets, the model exhibits the MAE of approximately five units, indicating a consistent discrepancy between predicted and actual values.

The RMSE values were also around 6.9, suggesting a spread of errors around the mean prediction. Most concerning, however, are the negative R-squared values of -0.8270 for training and -0.8619 for testing, indicating that the SVR model fails to explain the variability in the data around its mean. This discrepancy underscores the model's inability to capture the underlying patterns effectively, signalling poor performance across the training and testing phases.

Table 7.12: Comparison of performance metric of Support Vector Machine for temperature elevation prediction

Kernel function	Train Data			Test Data		
	MAE	RMS	R^2	MAE	RMS	R^2
polynomial	5.0773	6.9072	-0.8270	5.1678	6.9723	-0.8619
RBF	5.0775	6.6280	-0.6822	5.1589	6.6943	-0.7164

7.5.7 CNN for Temperature Elevation Predictions

The CNN was designed to predict temperature elevation in regression tasks, with hyperparameter optimization performed using *GridSearchCV*. The input features were normalized using *MinMaxScaler* and reshaped into a 3D format suitable for CNN processing. The architecture consisted of an input layer for time-series data, a convolutional layer with adjustable filters and a kernel size of 2, followed

by a max-pooling layer, a flattening layer, and fully connected dense layers for regression output. A 5-fold CV using *GridSearchCV* yielded optimal performance, with the best hyperparameters outlined in Table 7.13. These included a batch size of 128, 20 epochs, 256 filters, and the *sgd* optimizer.

Table 7.13: Comparison of performance metrics of Deep learning models with different cross-validation folds

Deep Learning Models	Cross validation	Test Data		
		MAE	RMS	R^2
CNN	3	0.2416	0.3216	0.4639
	5	0.2326	0.3210	0.4659
LSTM	3	0.0012	0.0018	1.0000
	5	0.0017	0.0029	1.0000
FCNN	3	0.0030	0.0045	0.9999
	5	0.0019	0.0031	1.0000
RNN	3	0.0023	0.0036	1.0000
	5	0.0014	0.0027	1.0000
CNN-LSTM	3	0.0053	0.0081	0.9997
	5	0.0126	0.0148	0.9989

7.5.8 LSTM for Temperature Elevation Predictions

The LSTM model was implemented to predict temperature and optimized using *GridSearchCV*. To enhance training efficiency, the dataset features were normalized using *MinMaxScaler*, and the input data was reshaped into a 3D structure, e.g., [samples, timesteps, features]. The LSTM architecture included an input layer for sequential data, an LSTM layer with tunable units, a fully connected dense layer with 64 neurons, and a final dense output layer. The model, compiled with the mean squared error loss and either *adam* or *sgd* optimizers, was wrapped in *KerasRegressor* to enable systematic hyperparameter tuning. Grid search was performed with 3-fold and 5-fold CV to evaluate combinations of batch size, epochs, optimizer, and LSTM units. The model was trained using the best hyperparameters, and its performance was evaluated. Results showed that the test data performed better with 3-fold CV, as the 5-fold resulted in higher MAE and RMSE, indicating that the model began to overfit the data.

7.5.9 FCNN for Temperature Elevation Predictions

The FCNN model was implemented to predict temperature elevation in tissues using regression. The data was normalized with *MinMaxScaler* to ensure consistent scaling. The model architecture consisted of an input layer, a hidden layer with tunable neurons and *ReLU* activation, and a final dense output layer for regression. It was compiled using mean squared error (MSE) as the loss function and wrapped in *KerasRegressor* for hyperparameter tuning. The optimal model, trained on the test data, was evaluated for performance. Table 7.13 showed that the 5-fold CV performed better, with the best hyperparameters being a batch size of 16, 20 epochs, 32 neurons, and the *adam* optimizer.

7.5.10 RNN for Temperature Elevation Predictions

The Simple RNN was implemented to predict temperature elevation, with the data scaled using *MinMaxScaler*. Without rescaling, the RNN model's performance was worse. The input data was reshaped into a suitable format for the RNN model. The architecture consisted of an input layer for sequential data, a SimpleRNN layer with tunable units, followed by a dense layer, and a final dense output layer for regression. Hyperparameter tuning was performed using *KerasRegressor* and *GridSearchCV* to optimize the model. After training with the best hyperparameters, the optimal model was used to make predictions. The results indicated that the best hyperparameters, achieved with 5-fold cross-validation as shown in Table 7.13, were a batch size of 32, 20 epochs, 32 units, and the *adam* optimizer.

7.5.11 CNN-LSTM for SAR Predictions

In this hybrid model, CNN and LSTM layers were combined to predict temperature elevation. The features were normalized using *MinMaxScaler* to ensure consistent scaling. The input data was then reshaped into a 3D format suitable for CNN-LSTM models. The architecture includes a CNN layer with tunable filters

for feature extraction, followed by a max-pooling layer to reduce dimensionality. The extracted features are processed through an LSTM layer to capture temporal dependencies. The model's output is connected to a fully connected dense layer, culminating in a regression output layer. Hyperparameter optimization was conducted using *GridSearchCV*, tuning the model across various combinations of batch size, epochs, optimizer, CNN filters, and LSTM units. The model was trained with the best hyperparameters, and performance was evaluated on the test data. As shown in Table 7.13, the optimal performance was achieved with a 3-fold cross-validation, using a batch size of 32, 10 epochs, 32 filters, 10 LSTM units, and the *adam* optimizer.

7.5.12 T-Test for Temperature Elevation Predictions

The t-test was used to access errors between actual and predicted temperature elevation values generated by various ML models that were significantly different from 0. The t-test allows us to conclude which ML model performs better and exhibits satisfactory performance. Hence, a t-test was conducted across all ML models, and the outcomes were visualised by plotting their mean errors.

The chosen significance level (often represented as the p-value) for the t-test was set at 0.05. If the p-value is less than 0.05, it indicates that the mean error between actual and predicted temperature elevation values deviates significantly from zero. In contrast, if the p-value exceeds 0.05, the mean error is closer to zero, indicating the excellent performance of the ML models. The t-test results for temperature elevation were illustrated in Figure 7.7, displaying the p-values for all implemented ML models for temperature elevation prediction. The results indicate that KNN and LR exhibited high p-values, suggesting strong performance in temperature prediction compared to other ML models, which performed poorly in the task.

A t-test was also performed to evaluate the performance of the deep learning models used for predicting temperature elevation in tissues. The results of the t-test are shown in Figure 7.8. It can be observed that all deep learning models

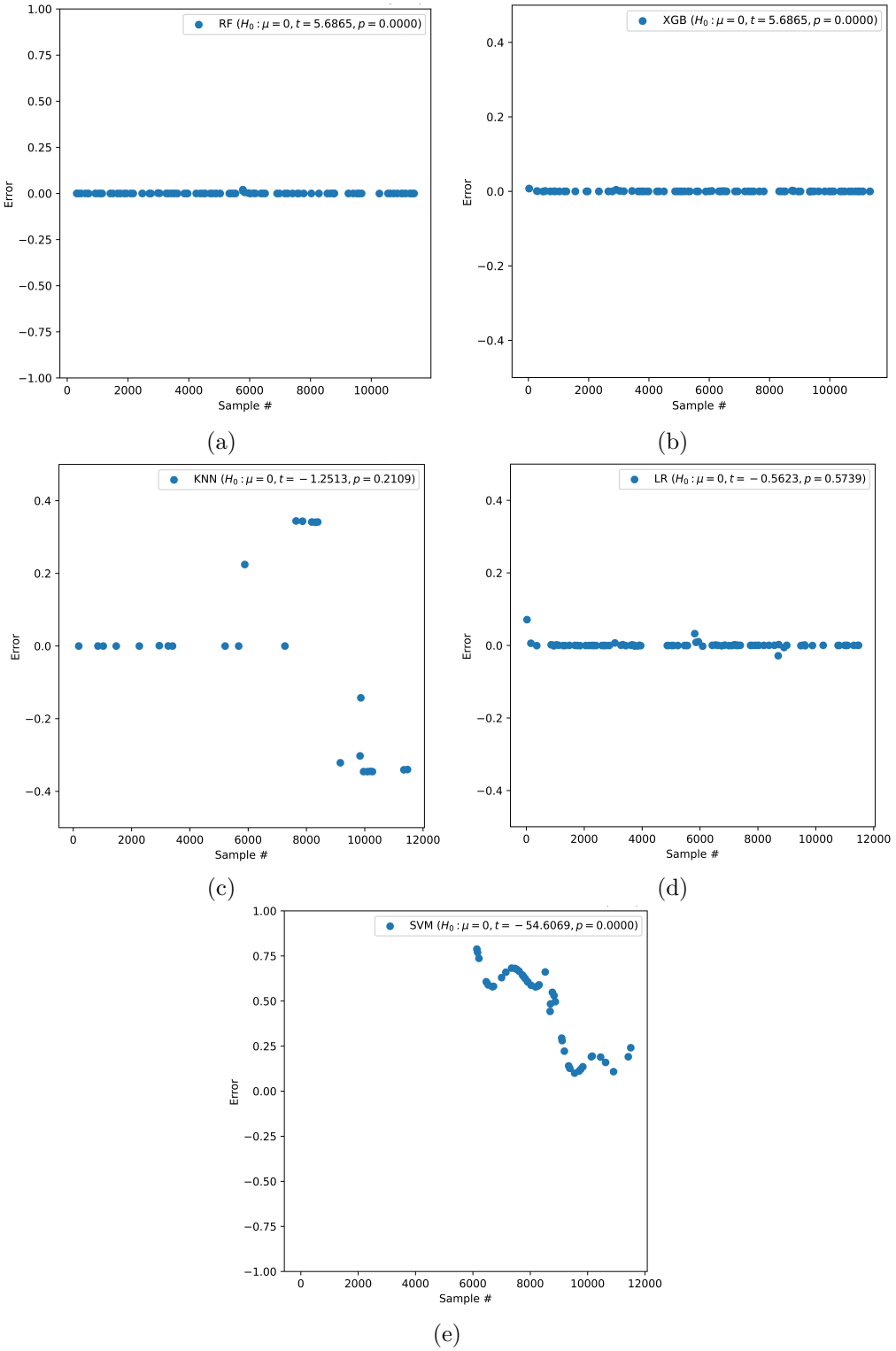

FIGURE 7.7: Error between actual and predicted value of temperature elevation for t-test when (a) random forest, (b) XGBoost, (c) KNN, (d) linear regression and (e) SVM models were used.

outperform the t-test, with errors close to zero. However, the p-value is zero, indicating that the t-test failed to show significant differences. This could be due to the small variance in the errors, making the p-value negligible. To validate this, the error variance for each model was also measured. The error variance for the CNN model was 0.1030, while for the LSTM, FCNN, RNN, and CNN-LSTM models, it was zero. Consequently, the small error variance led to a zero p-value in the t-test.

7.6 Conclusion

This chapter utilised supervised ML models to predict SAR and temperature elevation from RF-EMF exposure emitted by wearable devices. Various parameters associated with RF-EMF were carefully considered to enhance the accuracy of our predictions. These parameters varied systematically, were recorded through numerical simulations, and were used as training and validation datasets for the ML models.

A range of ML algorithms, including RF, XGBoost, KNN, LR, and SVM and deep learning models CNN, LSTM, FCNN, RNN and CNN-LSTM were used to analyse SAR and temperature data. The performance of each model was assessed using standard metrics, such as MAE, RMSE, and R-square values. Grid cross-validation was conducted to select the best hyperparameters, compare results across different k-fold cross-validation configurations, and optimise model performance.

Our findings showed that RF, XGBoost, LR, and KNN models performed excellently in SAR prediction, while LR and KNN models excelled in predicting temperature elevation. However, all the deep learning Including CNN, LSTM, FCNN, RNN and CNN-LSTM showed good performance for SAR and temperature predictions. We optimised model performance using grid cross-validation and validated our predictions through t-tests.

Our study demonstrates the potential of ML models with optimised hyperparameters to predict SAR and temperature elevation accurately. We found that power

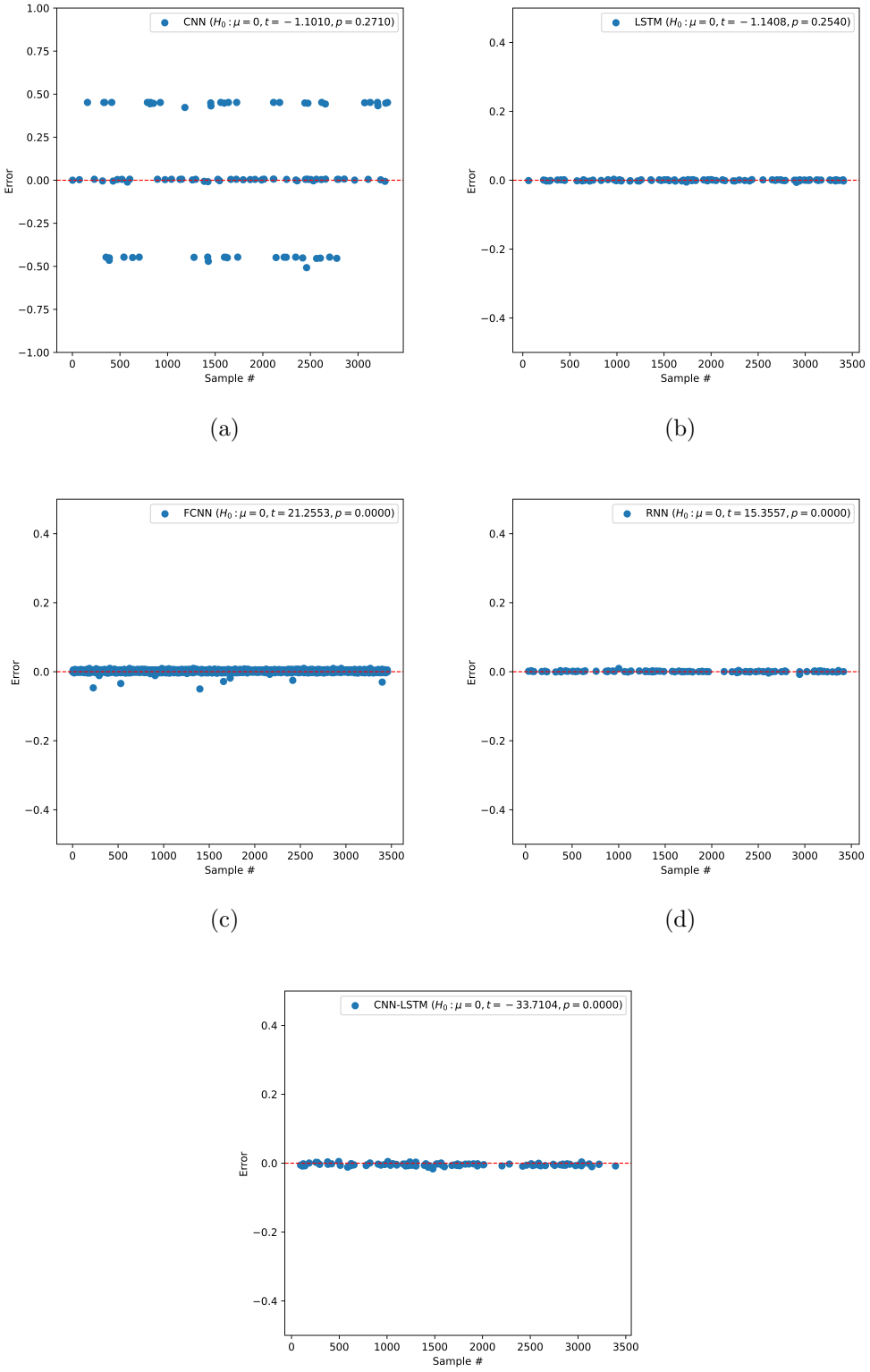

(a) (b)

(c) (d)

(e)

FIGURE 7.8: Error between the actual and predicted temperature values for the t-test across different deep learning models: (a) CNN, (b) LSTM, (c) FCNN, (d) RNN, and (e) CNN-LSTM.

level significantly influences SAR evaluation, and ambient temperature is crucial in predicting temperature elevation. It is important to note that the maximum temperature elevation in tissues is the cumulative effect of ambient temperature and the thermal load induced by RF-EMF exposure.

In general, the ML and deep learning models can be used to predict SAR and maximum temperature elevation in tissues using numerically collected data for different variations of parameters associated with RF-EMF exposure.

Chapter 8

Measurement of RF-EMF Exposure of Wearable Device

This chapter thoroughly examines the measurement of RF-EMF exposure in underground mine tunnels by developing a prototype wearable device. No existing literature measures the RF-EMF exposure of wearable devices, especially in the underground mine environment. The wearable device's power density (PD) was measured at various distances in a realistic underground mine tunnel. The PDs were also simulated using the MIFA model and calculated analytically to compare with the measured values across different distances. This comparison allows for the validation of the accuracy of the simulation and analytical methods against real-world measurements, providing insights into their reliability and effectiveness for predicting power densities.

8.1 Addressing the Gap for Comprehensive RF-EMF Exposure Measurement

In [156, 158], the focus was on measuring the variation in the reflection coefficient (S_{11}) of the MIFA for different mounting positions on the body and comparing these measurements with simulated values. However, the study did not involve measuring the RF-EMF exposure of the ESP32-WROOM board. The analysis of the reflection coefficient presented in [156] solely pertains to evaluating the performance of the MIFA across various body parts and does not directly address the absorption of RF-EMF within the body. Furthermore, the simulation

and measurement of the ESP32-WROOM, as presented in [156, 158], did not consider the realistic deployment environment for wearable devices. This limitation restricts the applicability and relevance of the study's findings to real-world scenarios. Therefore, our current study aims to address this gap by comprehensively measuring realistic RF-EMF exposure specifically for the ESP32-WROOM device in the underground mine tunnel.

8.1.1 Schematic and Prototyping of the Wearable Device

The schematic diagram for the ESP32-WROOM-based wearable device is depicted in Figure 8.1. Utilizing the *GPIO* pin of the ESP32 board, we collected temperature and humidity data from the DHT11 sensor. This recorded data was transmitted to a mobile web server for temperature and humidity data visualization. The ESP32 transmits data using Wi-Fi protocol to the mobile hotspot network of the mobile phone. Users can visualize the data by entering the IP address of the ESP32 into the browser's search bar on the mobile phone. The screenshots of the Arduino IDE COM port and mobile web server are depicted in Figure 8.2 and Figure 8.3, respectively. The transmit power is indicated by the numeric value of 72 (as depicted in Figure 8.2), which was converted using the *Wi-FiGenric* library and corresponds to 18 dBm (0.063 W). Therefore, the wearable device is transmitting at a power level of 0.063 W. The web server updates the data for every 1 second. The prototype of the wearable device is shown in Figure 8.4. The ESP32 board and DHT 11 sensor were powered using a Lithium-ion battery. The programming of the ESP32 board was carried out using Arduino IDE 1.8.19, utilizing the C language.

8.2 Components of the Wearable Device

To evaluate the RF-EMF exposure of the MIFA in an underground mine setting, a prototype of the wearable device utilizing ESP32-WROOM was assembled. The wearable device prototype was constructed to mimic a wearable device that uses

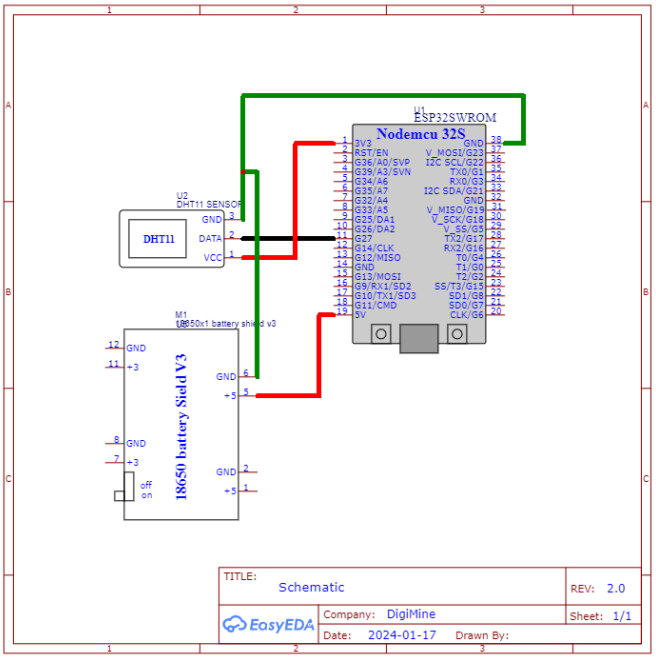

FIGURE 8.1: Schematic diagram of the prototype wearable device.

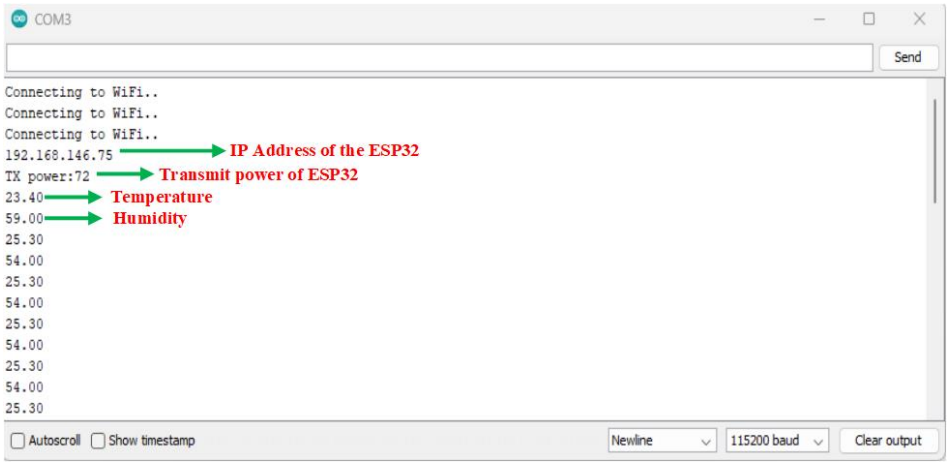

FIGURE 8.2: Screenshot of Arduino IDE COM port displaying ESP32 IP, transmit power (as per the Wi-FiGeneric library i.e., 72 = 18 dBm = 0.063 W), temperature, and humidity data.

the MIFA antenna for communication, enabling the measurement of RF-EMF exposure. The wearable device's monitoring parameters are beyond this study's scope, as they can encompass various functionalities and sensors, such as tracking location, heart rate, and monitoring of the environmental parameters. Hence, we assembled the wearable device prototype, employing a primary temperature and humidity sensor and integrating a Lithium battery shield with a Lithium-ion battery to provide power to the ESP32-WROOM. These components were selected

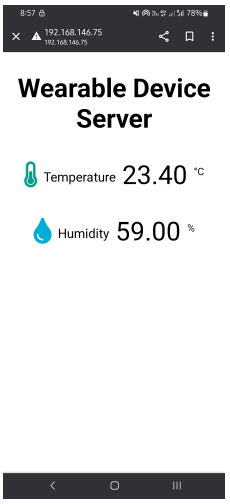

FIGURE 8.3: Screenshots of the mobile web server displaying temperature and humidity data from the wearable device.

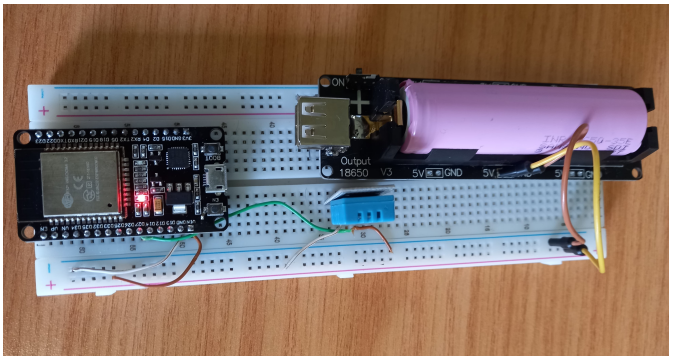

FIGURE 8.4: Prototype of the wearable device utilizing ESP32.

for the wearable device prototype based on their functionality and suitability for the intended purpose. The temperature and humidity sensor (DHT11) was chosen to provide environmental monitoring capabilities, which could be relevant for assessing conditions within the underground mine tunnel. Additionally, we integrated a Lithium battery shield (Battery Shield 18650) with a Lithium-ion battery (Rechargeable Battery 18650 (3000mAh)) to power the ESP32-WROOM, ensuring long-lasting operation and portability for the device.

The following components were used to assemble the prototype of the wearable device:

1. ESP32 NodeMCU 32S (ESP32-WROOM)
2. Battery Shield 18650 Lithium (Battery Holder + Cable)

3. Lithium-Ion Rechargeable Battery 18650 (Capacity 3000mAh)
4. DHT 11 sensor (Temperature and Humidity Sensor)
5. Jumper wires (Male to Male)
6. Breadboard

8.3 Measurements of RF-EMF Exposure

Different RF-EMF meters are available to measure RF-EMF exposure, ranging from different frequency bands, costs, and functionalities. As discussed in Chapter 2, Table 2.5 presents the utilization of different RF-EMF meters for measuring exposure across various settings. In this study, a Cornet (ED88TPLUS 5G) RF-EMF meter [228] was utilized to quantify the RF-EMF exposure of the wearable device. The Cornet RF-EMF meter is a low-cost and handy device that provides accurate RF-EMF exposure. Various studies employed Cornet RF-EMF meters for measurements of RF [109, 229–233] and extremely low-frequency [234] exposure. Singh et al. measured the RF-EMF exposure of mobile phones for different communication settings, such as incoming/outgoing calls, Wi-Fi, and Wi-Fi hotspots, using Cornet ED-75 RF-EMF meter [229]. In [230, 232], measure RF-EMF exposure of base station antennas at 1800 MHz for different distances using Cornet ED78S RF-EMF meter. Similarly, in [231], the Cornet ED15CV30L meter was used to compare the RF-EMF exposure for two locations. These measurements involved researchers using different Cornet RF-EMF meters to assess RF-EMF exposure in diverse settings, encompassing indoor and outdoor environments and covering various RF-EMF frequency bands.

The Cornet ED88TPLUS 5G RF-EMF meter is designed to measure high-frequency (RF) field strength and PD, as well as low-frequency magnetic field levels (measured in Gauss and Tesla) and extremely low-frequency electric fields (measured in V/m) in different environments. It features an RF bandwidth spanning 100 MHz to 8 GHz (5G band except for mm-meter wave band), exhibiting high sensitivity ranging from 0.5 $\mu W/m^2$ to 1.8 W/m^2. Further specifications can be found

in [228]. In the subsequent section, the extended measurement plan and analyses of the gathered data were discussed in detail.

8.3.1 Data Collection Procedure

The Cornet ED88TPLUS 5G RF-EMF meter has buffer memory (1024 cells of Data Logging Flash memory) for RF mode data logging and cannot retain the data when the meter is powered off [228]. Therefore, the RF-EMF meter was connected to the PC, which uses "Teraterm" software to log the data and store it in a log file. The step-by-step procedure for connecting the Cornet RF-EMF meter to the PC is outlined in [235].

8.3.2 Consideration of Measurement Environment for RF-EMF Exposure Assessment

The measurements were performed in the Wits mock mine tunnel at the University of the Witwatersrand and constructed with underground materials. The 66.2-meter-long tunnel enables realistic testing and mirrors environments found in deep hard-rock mines. The tunnel is also equipped with a steel ventilation duct, which closely simulates real-world conditions of the underground mine environment [236]. Various studies have leveraged the facility to evaluate diverse communication technologies [30, 237].

Measuring RF-EMF exposure in a realistic environment is crucial due to variations influenced by surrounding conditions, as highlighted in studies conducted in elevators [171–173], indoor settings [174–176], and transport vehicles [177–180]. Reflections of RF-EMF are affected by factors like distance, shape, orientation, and material properties, underscoring the importance of realistic measurements. Therefore, the Wits mock mine tunnel provides a suitable setting to conduct RF-EMF measurements in a realistic underground mine environment.

8.3.3 Measurement Campaign

The Cornet ED88TPLUS 5G RF-EMF meter and wearable device were placed on the table close to the Wits mock tunnel boundary, as shown in Figure 8.5. The RF-EMF meter was connected to the PC via cable for data logging. The PC was set to airplane mode to mitigate potential interference, while the mobile phone serving as a hotspot was positioned approximately 10 meters away from the device with its data mode switched off to minimize any potential disruption. Furthermore, the positioning of the mobile phone was carefully chosen to ensure that the RF-EMF signal emitted by the mobile phone's Wi-Fi would have no impact on the measurements being conducted. The distance was carefully chosen to ensure that the mobile phone's Wi-Fi signal would not interfere with the measurements while maintaining a connection between the wearable device and the mobile web server.

The RF-EMF exposure data was collected for various distances between the RF-EMF meter and wearable device, spanning 5 mm, 10 mm, 15 mm, and 20 mm. A ruler was utilized to accurately measure the distance between the RF-EMF meter and the wearable device as depicted in Figure 8.6. The close view of the measurement setups for distances of 5 mm and 20 mm are illustrated in Figure 8.6a and Figure 8.6b, respectively. The data was collected for 3-minute intervals for each instance.

8.3.4 Analysis of Measured Data

The raw data obtained from measurements was visualized in Figure 8.7. The raw data exhibited distinct frequency bands such as 900 MHz, 1800 MHz, 2100 MHz, 2400 MHz, and 2900 MHz. However, it is essential to note that the ESP32 board transmits RF-EMF signals within the 2400 MHz to 2484 MHz range, as specified in the ESP32 datasheet [238]. Therefore, to analyze the RF-EMF exposure data of the wearable device, other frequency signals need to be excluded. Additionally, the analysis revealed that the highest PD peaks for distances of 5 mm, 10 mm, 15 mm, and 20 mm were observed at 900 MHz and 1800 MHz, corresponding to



FIGURE 8.5: Setup for measuring RF-EMF exposure of the wearable device in the tunnel.

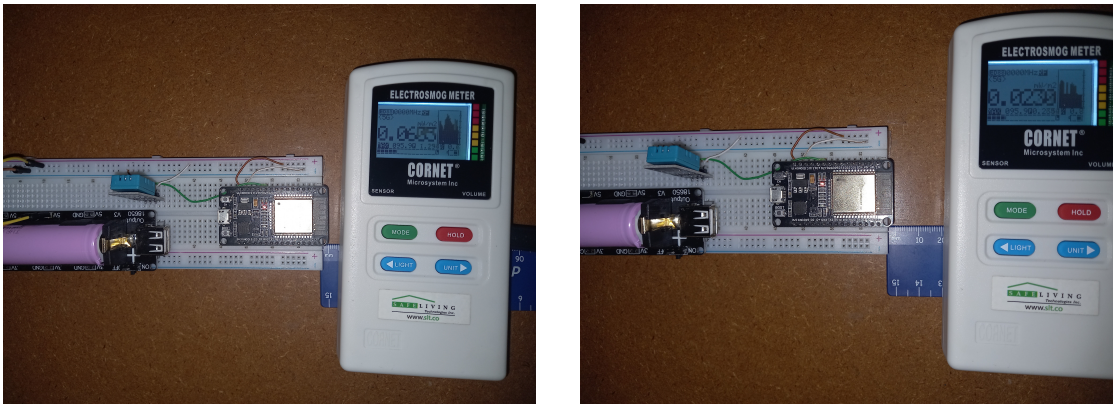

(a) (b)

FIGURE 8.6: RF-EMF exposure data collection at various distances between the RF-EMF meter and wearable device (a) 5 mm, and (b) 20 mm.

standard mobile phone frequencies. However, these frequency signals fall outside the scope of this study as they are likely attributable to the presence of other communication devices installed in the tunnel, as enlisted in [30].

For subsequent analysis, the raw data files were screened for frequencies ranging from 2400 MHz to 2500 MHz to focus on the frequency range where the

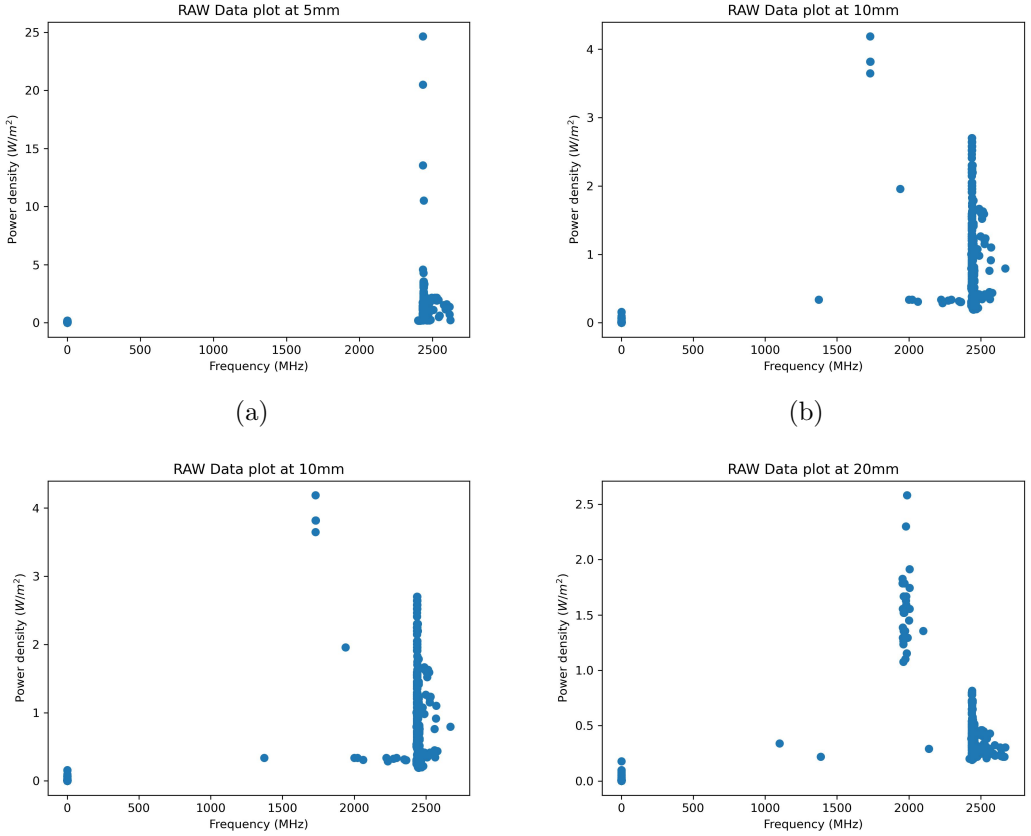

FIGURE 8.7: Plot of measured raw data at diverse distances between the RF-EMF meter and the wearable device (a) 5 mm, (b) 10 mm, (c) 15 mm, and (d) 20 mm

ESP32WROOM operates. This screening process ensures that only relevant frequency data is retained for subsequent analysis. The screened data for all observed distances in this study are shown in Figure 8.8, highlighting a peak in the PD at 2440 MHz, corresponding to the transmitted frequency of the ESP32-based wearable devices. The measured PD of RF-EMF was significantly higher at a distance of 5 mm from the wearable device, as illustrated in Figure 8.8a. The PD decreases with increased distance between the wearable device and the RF-EMF meter.

The maximum peak and average power densities for all distances were extracted from the data and are presented in Table 8.1. Notably, the power densities at distances of 5 mm and 10 mm exhibit a rapid decrease compared to those at 15 mm and 20 mm. Hence, the impact of the wearable device is minimized when

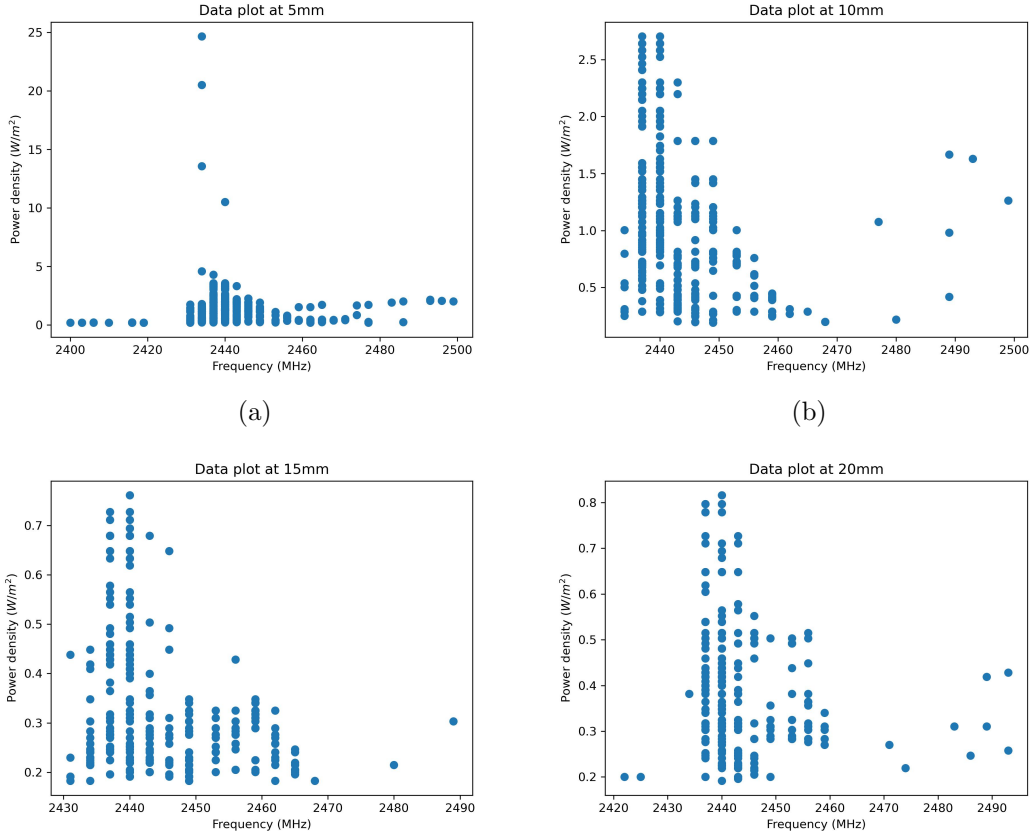

FIGURE 8.8: Plot of measure data at diverse distances between the RF-EMF meter and the wearable device (a) 5 mm, (b) 10 mm, (c) 15 mm, and (d) 20 mm

the device is positioned at a distance of 10 mm or greater, which can be considered a safe distance from the source of RF-EMF.

TABLE 8.1: Measured maximum and average power density at different distances in the range of 2400 MHz to 2500 MHz.

Distance	Power density (W/m^2)	
	Maximum	Average
5 mm	24.65	1.49
10 mm	2.70	1.13
15 mm	0.76	0.76
20 mm	0.82	0.39

8.3.5 Evaluation of Simulated Power Densities

The modelled MIFA antenna in HFSS was evaluated to assess PD at various distances from the antenna. A rectangular area above the MIFA at distances of 5 mm, 10 mm, 15 mm, and 20 mm was selected to plot PD with an input power of 0.06 W, as shown in Figure 8.9. The input power was calculated using the "compute antenna parameters" option in HFSS, which specifies different antenna performance parameters. The maximum simulated power densities were observed and summarized in Table 8.2. The power densities decrease rapidly with an increase in distance from the MIFA. Figure 8.10 plots the PD distributions for each distance.

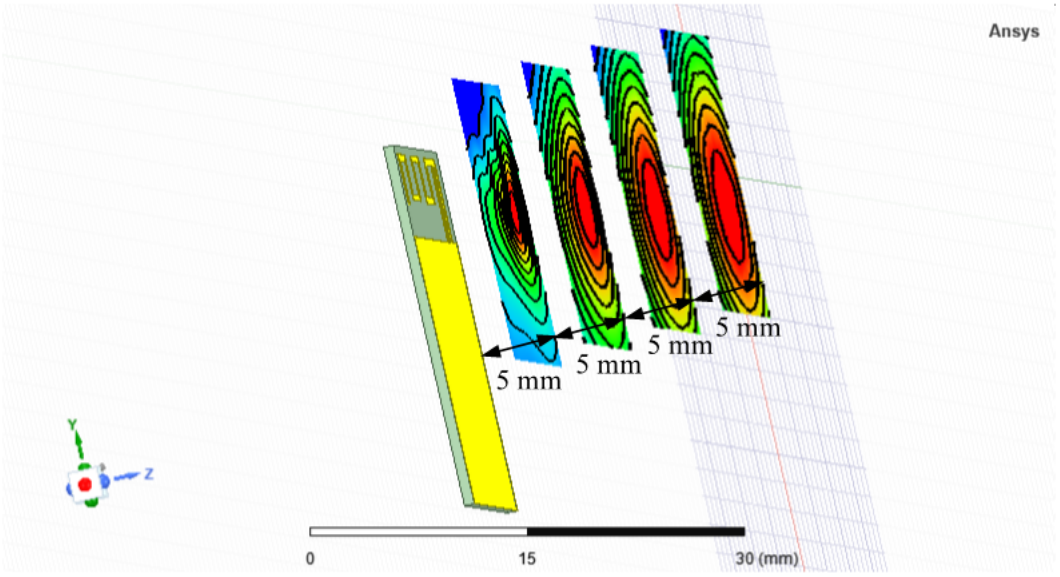

FIGURE 8.9: Simulated power density for all considered distance with MIFA.

TABLE 8.2: Simulated power density for different distances.

Distance	Maximum power density (W/m^2)
5 mm	89.99
10 mm	29.55
15 mm	16.49
20 mm	10.85

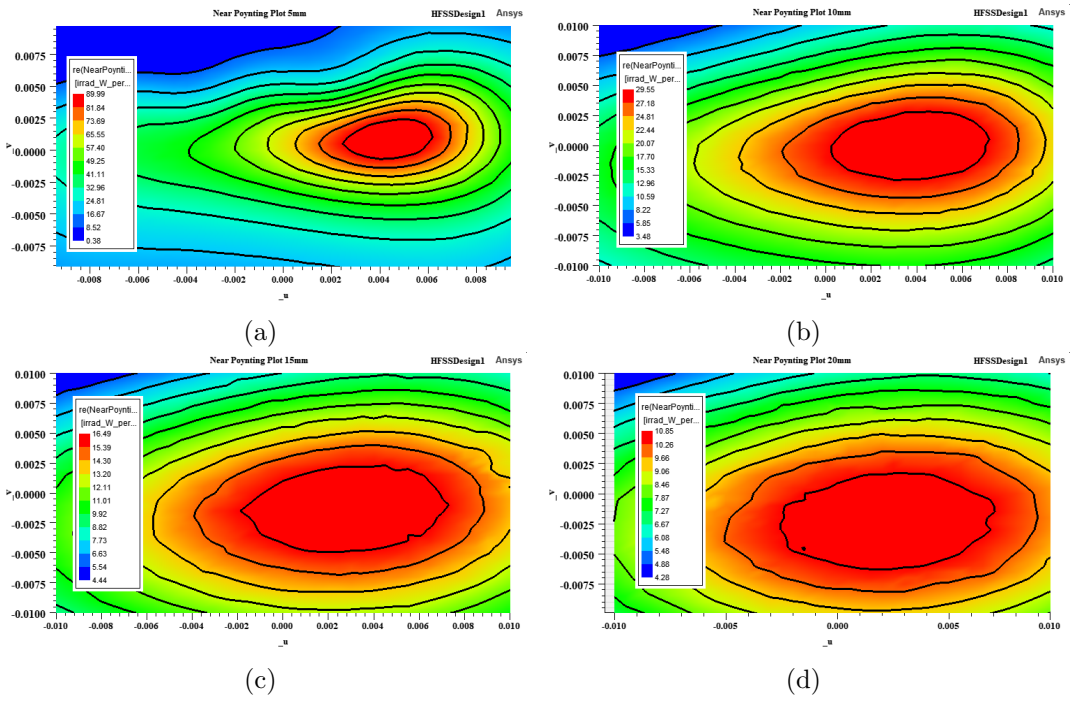

FIGURE 8.10: Simulated power densities at distance (a) 5 mm, (b) 10 mm, (c) 15 mm and (d) 20 mm

8.3.6 Analytical Calculation of Power Densities

The PD was computed at 2.4 GHz with a peak gain of 1.32 and an output power of 48.06 mW, derived from the simulated MIFA antenna. The classical equation for PD in the far-field region was employed as follows [239, 240]:

$$P_D = \frac{P_{out} \times G_{tx}}{4 \times \pi \times D^2} \tag{8.1}$$

Where P_D represents the PD, P_{out} denotes the transmitted power, G_{tx} is the gain of the antenna, and D is the distance from the antenna. The calculated values for observed distances are presented in Table 8.3.

TABLE 8.3: Analytical power density for different distances.

Distance	Maximum power density (W/m^2)
5 mm	201.7
10 mm	50.42
15 mm	22.41
20 mm	12.61

8.3.7 Comparison of Results

The maximum PD of the MIFA at specific distances (5 mm, 10 mm, 15 mm, and 20 mm) were compared between measured, simulated, and analytically evaluated data, as shown in Figure 8.11. The observed decrease in PDs with increasing distance is consistent and aligned with similar trends reported in other studies [241–244].

In [241], PD was investigated for a 5G mm-wave array antenna, and PD was plotted for distances of 5, 10, 15, and 20 mm for different antenna beams. The findings confirmed a reduction in PD as the distance from the antenna increased, aligning with existing literature on the subject. Similarly, in [242], PD was calculated for distances of 5, 10, and 15 mm in various body tissues for a frequency range of 10 to 90 GHz. A similar trend was observed, with PD increasing with increased signal frequency but decreasing with distance from the antenna.

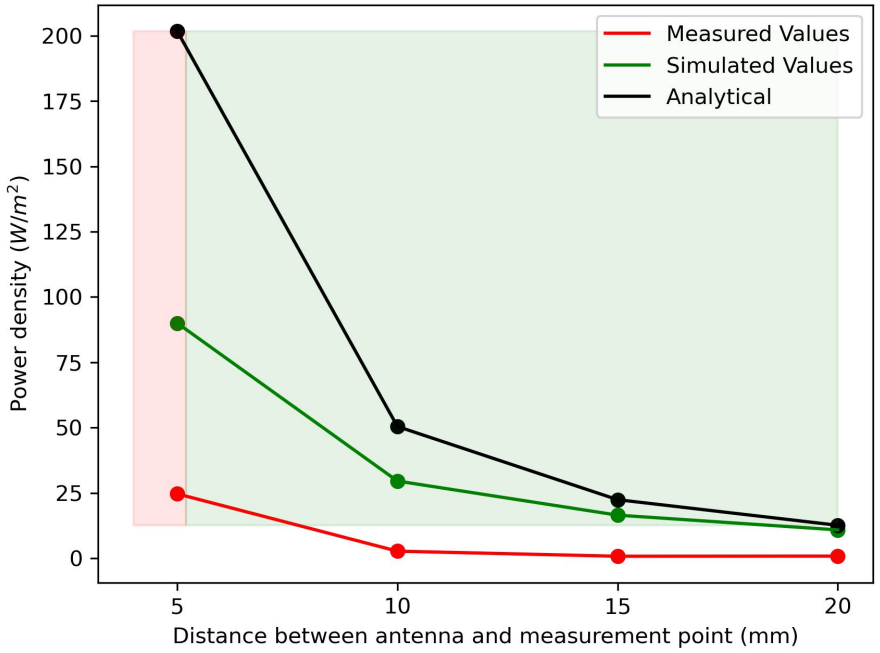

FIGURE 8.11: Comparison of the measured, simulated, and analytically evaluated power density for different distances, where red area represents near field region and green area presents far-field region.

The discrepancy in PD values at 5 mm compared to other distances (10 mm, 15 mm, and 20 mm) is attributed to the near-field radiation region of the MIFA antenna, extending up to 5.188 mm, beyond which the far-field radiation region begins. Simulated PD values may differ due to polarization mismatch between the MIFA and Cornet RF-EMF meter, as the MIFA transmits linearly polarized waves, necessitating alignment with the receiving antenna for optimal reception. Real-world conditions, including surrounding structures and electromagnetic interference, can further influence measured values, introducing complexities not fully captured in simulations or analytical calculations.

According to the ICNIRP guidelines [4], the limits for PD for frequencies ranging from 2 GHz to 300 GHz were set at 10 W/m^2. It is evident from the measurements that the measured values for the ESP32 were below the ICNIRP limits for a distance of 10 mm. Therefore, it is recommended to maintain a minimum distance of 10 mm as a safe distance to minimize the impact of RF-EMF exposure on the body when a wearable device is worn. However, at a distance of 5 mm, the PD value was higher than the ICNIRP guidelines [4].

Hence, it is recommended to maintain a 10 mm distance between the wearable device and the body when worn by miners in underground mine environments. However, this study did not assess factors like high temperature, humidity, or sweating during mine work, which is crucial for real-world implications. Investigating these parameters in underground mines is vital, especially considering temperature variations with depth. Additionally, conducting thorough investigations into long-term RF-EMF exposure in realistic working environments is crucial. This includes assessing potential biological health risks, emphasizing the importance of comprehensive studies integrating exposure measurement and health impact evaluation.

8.4 Conclusion

This chapter shows realistic measurements of the wearable device's RF-EMF exposure in a Wits mock mine tunnel using a Cornet RF-EMF meter at 2.4 GHz. The measurements were conducted to measure RF-EMF exposure of the wearable device in underground mock mine tunnel. The power densities were simulated and analytically calculated to compare the measured data for different distances from the wearable device. However, it is essential to note the inherent limitations of the RF-EMF meter, which preclude the assessment of RF-EMF exposure in terms of SAR and temperature elevation, given their dependence on tissue properties.

To the author's best knowledge, no study has measured the RF-EMF exposure of the wearable device in a realistic environment. Therefore, the main focus was measuring RF-EMF exposure from wearable devices in a realistic underground mine environment. To facilitate these measurements, we developed a prototype of the ESP32-WROOM wearable device tailored for the RF-EMF measurements. While our primary focus was on RF-EMF exposure, we integrated a temperature and humidity sensor into the prototype for supplementary data collection. Additionally, the wearable device is powered by a rechargeable battery, ensuring ease of mobility.

Our measurement campaign was conducted at varying distances of 5 mm, 10 mm, 15 mm, and 20 mm from the wearable device, systematically recorded using the Cornet ED88T Plus 5G meter in the Wits mock mine tunnel (a realistic simulated underground mine environment). Subsequently, the collected data underwent rigorous analysis and comparison with simulated and analytical data sets. Discrepancies observed between simulated and measured PD values were attributed to real-world variables such as the presence of surrounding structures and electromagnetic interference from other wireless communication systems operating within the mine tunnel.

Furthermore, it is important to recognize that analytical calculations have limited

applicability, primarily in the far-field region of the MIFA, which begins at approximately 5.2 mm. Consequently, the differences between simulated and measured power density values decrease as the distance from the source increases. Furthermore, the polarization mismatch between the MIFA and the Cornet RF-EMF meter's antenna significantly affects the accuracy of the results. Therefore, using an RF-EMF meter capable of measuring power density values in three-dimensional planes (i.e., in the x, y, and z axes) is advisable.

At the distance of 5 mm, the measured PD was higher than the ICNIRP guidelines [4]. However, these values were below the recommended limits for 10 mm, 15 mm, and 20 mm distances. Therefore, 10 mm is a safer distance for RF-EMF exposure in the underground mine environment. Additionally, when a wearable device is in contact with a miner's body, it is crucial to maintain a safe distance of at least 10 mm. To further reduce RF-EMF exposure, shielding and directional antennas are recommended, as these can help redirect radiation away from the human body.

Chapter 9

Conclusion

This chapter summarizes the research findings on RF-EMF exposure from wearable devices in underground mine environments and recommends strategies for mitigating these effects. Additionally, it discusses future directions for further investigation and measurement of RF-EMF exposure in underground settings.

9.1 Key Findings and Insights: Addressing the Research Questions

This study investigated RF-EMF exposure from wearable devices to assess SAR and temperature elevation in tissues across various underground mine environments. It also explored the application of ML models to predict SAR and temperature elevations to reduce the extensive computational demands associated with numerical simulations. Furthermore, a wearable device prototype was developed to measure realistic RF-EMF exposure within an underground tunnel.

A commonly used IoT wearable device, ESP32-WROOM, equipped with an omnidirectional MIFA antenna operating at 2.4 GHz, was considered to evaluate RF-EMF exposure in an underground mine environment. The LiDAR scan model of the Wits mock mine tunnel was incorporated to evaluate RF-EMF exposure accurately and determine its impact on SAR values in a simulated environment. The SAR variability for different parameters associated with RF-EMF exposure and the underground mine environment was also investigated. Furthermore, the temperature elevation in tissues was examined for different ambient temperatures

in underground mine environments. The maximum temperature elevation in tissues was compared across various ambient temperature variations and durations of RF-EMF exposure.

The numerical simulations are computationally intensive and time-consuming, especially when exploring various parameters associated with RF-EMF exposure. For example, running a parametric sweep for 50 parameter variations can increase simulation time by 50. Therefore, an alternative solution is needed to reduce simulation time and workload. Additionally, evaluating temperature elevation due to RF-EMF exposure requires using a mechanical solver and importing results from an electromagnetic solver, which demands expertise, extensive data storage, increased simulation time and additional license.

ML can address these challenges by predicting SAR and temperature elevation across various parameters. Recent advancements have demonstrated that ML models can estimate SAR from MRI images, providing a quicker alternative to numerical simulations for assessing RF-EMF exposure. In this study, ML models were utilized to predict SAR and temperature elevation under different parameter variations, and their performance was evaluated to ensure accuracy. Finally, RF-EMF exposure was measured using a Cornet RF-EMF meter in an underground tunnel, enabling a comparison of power densities between analytical and simulated setups. The following conclusions were derived from the results obtained through numerical simulations, machine learning, and measurements:

- The findings indicate that SAR values exceeded the ICNIRP guidelines [4] for both wrist and waistline scenarios when the device was placed 5 mm away from the body and operated at its maximum power level of 0.1 W. However, the SAR values decreased below the ICNIRP guidelines for distances greater than 12 mm for all scenarios, indicating it as a safe mounting distance for the wearable device.

  Furthermore, SAR values are influenced by the power level and show marginal variation with the antenna's orientation. Therefore, careful consideration of

the placement of the wearable device is essential, and maintaining a safer distance is recommended to mitigate RF-EMF exposure. Additionally, the use of directional antennas in wearable devices, which transmit less RF-EMF towards human tissues, is also recommended for minimizing the impact of RF-EMF exposure.

- The SAR values were marginally higher in underground mine scenarios for all considered mounting positions of the wearable device compared to the free space environment. Additionally, SAR values exhibited marginal variation with changes in the permittivity of the rock properties. The results indicate that distances greater than 100 mm between the RF-EMF source and the tunnel structure do not affect SAR values in simulated scenarios. This is because the reflections from the tunnel boundaries had weak power, leading to low reflected power RF-EMF from those boundaries. Therefore, distances greater than 100 mm are considered safe from the RF-EMF source.

- The temperature elevation in tissues due to RF-EMF exposure was evaluated at various ambient temperatures within the underground mine environment, specifically 40^0 C and 50^0 C. The maximum temperature increase in tissues remained below the ICNIRP guidelines for both wrist and waistline mounting positions across all ambient temperatures. Furthermore, the impact of varying temperatures had minimal influence on the wearable device's thermal response to the RF-EMF source. Notably, the temperature elevation in tissues was higher for the wrist than for the waistline scenarios, attributed to the differing shapes of the tissues in these areas. This suggests that the waistline is a more suitable mounting position for the wearable device. However, it is crucial to note that the wrist tissues are categorised as peripheral. SAR and temperature elevation limits for these tissues are higher than those of the waistline tissues, providing more room for RF-EMF exposure to reach the threshold. Considering the ICNIRP limit, the wrist is the best place to mount the wearable device in underground mine settings.

- The RF-EMF exposure for various time durations was also explored for wrist and waistline scenarios at 40^0 C. In this scenario, only 40^0 C was explored because the change in ambient temperature does not alter the temperature elevation in tissues due to RF-EMF exposure. Therefore, the results for 40^0 C also validate the evaluation at 50^0 C for different durations of RF-EMF exposure. It was noted that the maximum temperature elevation in tissues increased rapidly and reached close to its maximum value after approximately one hour of continuous RF-EMF exposure. Interestingly, the temperature elevation in tissues did not reach its maximum value even after 8 hours of RF-EMF exposure. Long-term exposure to the wearable device indicates that after one hour of continuous exposure, the temperature increase in the tissues becomes minimal. Consequently, the wearable device can be used continuously throughout the shift of 8 hours if the SAR values are less than the ICNIRP guidelines. Nevertheless, increasing the distance between the tissues and the RF-EMF source can further mitigate temperature elevations.

- This study also demonstrates the application of supervised ML and deep learning models in predicting SAR and temperature elevation resulting from RF-EMF exposure. Through systematic variation of RF-EMF parameters and rigorous validation, we established ML algorithms' reliability in predicting SAR and temperature elevation in tissues. The Grid search CV was applied to tune the best hyperparameters of the ML and deep learning models. The statistical t-test was also performed to validate the hypothesis for the performance of ML models. The random forest, XGBoost, K nearest neighbor and linear regression predict SAR accurately and validate the t-test hypothesis that the error between actual and predicted values was close to zero. The random forest, XGBoost, K nearest neighbor, and linear regression also accurately predict temperature elevation in tissues with low mean absolute and root mean square errors. However, the random forest, XGBoost, and SVM failed to validate the t-test, which can be due to model

complexity and high variability. The linear regression and K nearest neighbor validate the t-test null hypothesis that the actual and predicted values were closer to zero. The deep learning models such as CNN, LSTM, FCNN, RNN and CNN-LSTM also performed well in the prediction of SAR and temperature elevation in tissues. However, some models failed to pass t test and showed zero p value which is due small variance of the error (0.0000). These findings underscore the potential of ML techniques to inform risk assessment and management strategies for RF-EMF exposure in occupational settings. Leveraging ML algorithms offers a promising avenue for future research to enhance predictive accuracy and develop targeted interventions to mitigate RF-EMF hazards.

- Realistic measurements were taken in an underground mine tunnel using a Cornet ED88T Plus 5G RF-EMF meter (also called an exposimeter) operating at 2.4 GHz. The exposimeter assesses RF-EMF exposure by measuring the strength of electric and magnetic fields and power density at various frequencies. Due to this, comparing with all the simulated SAR and temperature elevation results was restricted. Despite the above simulated SAR and temperature elevation assessment limitations, comparisons were drawn between measured, simulated, and analytically calculated power densities. The power densities were simulated at a distance of 5 mm, 10 mm, 15 mm, and 20 mm from the MIFA.

- Similarly, analytical power densities were calculated using a classical expression that includes only distance from the device, output power, and antenna gain. Based on our findings, the observed discrepancies between simulated and measured power densities suggest that the simulated results serve as an upper bound for the actual measurements. This discrepancy can be attributed to real-world variables and antenna polarization mismatch as MIFA and exposimeter are linearly polarized. Therefore, it underscores the need for RF-EMF meters to measure power density in three-dimensional planes. Moreover, the analytical calculations can only be used for the far-field region

calculations and do not account for polarization and frequency. Hence, although the simulation results offer valuable insights, it is crucial to recognize the impact of real-world variables and employ advanced measurement techniques to measure RF-EMF exposure precisely. Measured results indicated safer RF-EMF exposure distances of 10 mm or greater from the device, aligning with ICNIRP guidelines [4]. The findings highlight the importance of maintaining safe distances and exploring shielding and directional antennas to mitigate RF-EMF exposure risks in underground mine environments.

9.2 Improving Mining Safety: Insights from RF-EMF Exposure

The findings of this study on RF-EMF exposure from wearable devices have several implications for the South African mining industry. The key benefits are provided below:

Improved Worker Safety: By identifying safe mounting distances for wearable devices and ensuring that RF-EMF exposure remains below the ICNIRP guidelines, mining companies can implement safer practices that protect workers from potential health risks associated with RF-EMF exposure. This is especially crucial in underground environments, where workers may encounter various RF-EMFs in challenging conditions.

Enhanced Monitoring and Risk Assessment: Using ML models to predict SAR and temperature elevations offers a more efficient way to assess RF-EMF exposure. This technology can be integrated into real-time monitoring systems, allowing for proactive risk management and timely interventions when RF-EMF exposure levels approach safety thresholds. It can also be integrated with wearable device technology.

Optimized Device Design: The recommendations for using directional antennas, RF shielding and maintaining safe distances can guide the design of

future wearable devices used in the mining sector. It can lead to the development of devices that minimize RF-EMF emissions while maintaining functionality and enhancing worker comfort and safety.

Regulatory Compliance and Contribution to Industry Standards: The insights gained from this research can help South African mining companies ensure compliance with health and safety regulations regarding RF-EMF exposure. The research findings can also contribute to establishing industry standards and best practices for RF-EMF exposure in mining. This can lead to a safer work environment and improve the overall reputation of the mining sector in South Africa. However, the urgency of the matter is underscored by the need for more studies to measure RF-EMF exposure in a real underground mine environment.

Awareness and Training: This study emphasizes the critical need for awareness of RF-EMF exposure among workers and management. By offering training informed by these findings, mining companies can cultivate a culture of safety and health consciousness among employees. Additionally, this initiative can help mitigate misunderstandings regarding the potential risks associated with RF-EMF exposure among workers and public health.

9.3 Limitation of the Research

This study evaluated SAR and temperature elevation in tissues using the ESP32-WROOM-based MIFA antenna. Given that variations in the antenna's structure influence RF-EMF exposure metrics, the results presented here apply to all variations of the ESP32 board utilizing similar antenna structures. Although associated parameters may vary, their generalization remains feasible as they are independent of the antenna's structure.

The influence of sweating, clothing, and other environmental factors on RF-EMF exposure was not accounted for in the evaluation process. Prior research, such as Moore et al., indicates that clothing can elevate tissue temperature, emphasizing

the importance of considering these variables in RF-EMF exposure assessments [25].

Additionally, the measurement conditions in this study may differ from real-world conditions in underground mines. Consequently, the findings presented here are restricted to using the ESP32 devices. It is imperative to incorporate various wearable devices used in underground mines to assess their RF-EMF exposure comprehensively. Furthermore, the RF-EMF measurement meter employed in this study features a single-axis RF sensor, potentially reducing measurement accuracy.

9.4 Future Directions

Evaluating RF-EMF exposure from wearable devices is crucial, especially in underground mining environments where workers use these devices for extended shifts. This study evaluated the RF-EMF exposure at 2.4 GHz for wearable devices. There is a need to consider the following parameters for future work to investigate SAR and temperature elevation in workers due to RF-EMF exposure wearable device:

- Frequencies, such as 5.8 GHz (5G Wi-Fi) and those used for LoRa (Long Range wireless communication).
- Polarization of the electromagnetic radiation (linear and circular) in confined environments. Literature indicates that circular polarization provides better coverage than linearly polarized electromagnetic waves, potentially increasing the RF-EMF exposure to the worker.
- A broader range of human models that consider variations in age, gender, and weight.
- Working conditions include sweating, clothing, blood flow, and metabolic rate.

There is a need to incorporate ML models to mitigate RF-EMF exposure in such environments more effectively. These ML models could be integrated into existing wearable devices to estimate RF-EMF exposure, thereby enhancing public health and ensuring the safety of workers. Future research can also incorporate additional parameters into the ML models to predict SAR and temperature elevation in tissues. Furthermore, it can be expanded to include other frequencies, creating robust datasets for training the ML models. Additionally, incorporating more advanced techniques with more RF-EMF exposure parameters and employing robust hyperparameter tuning for the ML models could further enhance prediction accuracy.

This study investigated only the near-field RF-EMF exposure from the wearable device. However, it is also essential to measure RF-EMF exposure to workers from far-field sources, such as other wireless communication systems deployed in the confined environment of underground mines.

There is an urgent need to conduct RF-EMF exposure measurements in real working underground mine environments to improve risk assessment and develop effective mitigation strategies. The author conducted multiple investigations based on numerical simulations, emphasizing the necessity of measuring RF-EMF exposure in these settings. Such measurements can assist underground mines in mitigating risks and raising awareness about RF-EMF exposure among workers.

References

[1] S. Gabriel, R. Lau, and C. Gabriel, "The dielectric properties of biological tissues: Ii. measurements in the frequency range 10 hz to 20 ghz," *Physics in medicine & biology*, vol. 41, no. 11, p. 2251, 1996.

[2] J. C. Lin, "Specific absorption rates induced in head tissues by microwave radiation from cell phones," *IEEE Microwave Magazine*, vol. 2, no. 1, pp. 22–25, 2001.

[3] International Commission on Non-Ionizing Radiation Protection and others, "Guidelines for limiting exposure to time-varying electric, magnetic, and electromagnetic fields (up to 300 ghz)," *Health physics*, vol. 74, no. 4, pp. 494–522, 1998.

[4] International Commission on Non-Ionizing Radiation Protection, "Guidelines for limiting exposure to electromagnetic fields (100 kHz to 300 GHz)," *Health physics*, vol. 118, no. 5, pp. 483–524, 2020.

[5] S. Yarkan, S. Guzelgoz, H. Arslan, and R. R. Murphy, "Underground mine communications: A survey," *IEEE Communications Surveys & Tutorials*, vol. 11, no. 3, pp. 125–142, 2009.

[6] Minerals Council South Africa, "Mining in SA - Gold," https://www.mineralscouncil.org.za/sa-mining/gold, [accessed January 25, 2024].

[7] Energy Mineral Resources and Energy, "Mine Health and Safety Inspectorate ANNUAL REPORT 2019/2020," https://static.pmg.org.za/MHSI_AR_2019-2020_Proof_1_2020-10-21.pdf, [accessed January 25, 2024].

[8] Reuters, "Spike in South Africa's mining fatalities continues into 2021," https://www.reuters.com/article/safrica-mining-casualties-idAFL5N2ND4XC, [accessed January 25, 2024].

[9] M. Li and Y. Liu, "Underground coal mine monitoring with wireless sensor networks," *ACM Transactions on Sensor Networks (TOSN)*, vol. 5, no. 2, pp. 1–29, 2009.

[10] M. A. Ashraf, A. Mahmood, and M. A. Mahboob, "Numerical evaluation of specific absorption rate in human head and torso for wearable wireless devices in underground mine scenarios," *Radiation Protection Dosimetry*, vol. 198, no. 8, pp. 491–502, 2022.

[11] M. A. Ashraf, "Analysis of specific absorption rate in humans for wearable wireless devices in underground mines," Ph.D. dissertation, School of Electrical & Information Engineering, 2020.

[12] R. Baan, Y. Grosse, B. Lauby-Secretan, F. El Ghissassi, V. Bouvard, L. Benbrahim-Tallaa, N. Guha, F. Islami, L. Galichet, and K. Straif, "Carcinogenicity of radiofrequency electromagnetic fields," *The lancet oncology*, vol. 12, no. 7, pp. 624–626, 2011.

[13] J. H. Kim, J.-K. Lee, H.-G. Kim, K.-B. Kim, and H. R. Kim, "Possible effects of radiofrequency electromagnetic field exposure on central nerve system," *Biomolecules & therapeutics*, vol. 27, no. 3, p. 265, 2019.

[14] A. Di Ciaula, "Towards 5g communication systems: Are there health implications?" *International journal of hygiene and environmental health*, vol. 221, no. 3, pp. 367–375, 2018.

[15] D. Belpomme, L. Hardell, I. Belyaev, E. Burgio, and D. O. Carpenter, "Thermal and non-thermal health effects of low intensity non-ionizing radiation: An international perspective," *Environmental pollution*, vol. 242, pp. 643–658, 2018.

[16] D. J. Panagopoulos, "Comparing dna damage induced by mobile telephony and other types of man-made electromagnetic fields," *Mutation Research/Reviews in Mutation Research*, vol. 781, pp. 53–62, 2019.

[17] C. L. Russell, "5 g wireless telecommunications expansion: Public health and environmental implications," *Environmental research*, vol. 165, pp. 484–495, 2018.

[18] A. Nefzi, "Analysis and dosimetry of the coupling of electromagnetic waves with biological tissues: application to applicator design for biomedical and study of health effects," Ph.D. dissertation, Université de Limoges, 2021.

[19] W. P. Cheshire Jr, "Thermoregulatory disorders and illness related to heat and cold stress," *Autonomic Neuroscience*, vol. 196, pp. 91–104, 2016.

[20] J. D. Ramsey, C. L. Burford, M. Y. Beshir, and R. C. Jensen, "Effects of workplace thermal conditions on safe work behavior," *Journal of safety Research*, vol. 14, no. 3, pp. 105–114, 1983.

[21] Y. Takashima, H. Hirose, S. Koyama, Y. Suzuki, M. Taki, and J. Miyakoshi, "Effects of continuous and intermittent exposure to RF fields with a wide range of SARs on cell growth, survival, and cell cycle distribution," *Bioelectromagnetics: Journal of the Bioelectromagnetics Society, The Society for Physical Regulation in Biology and Medicine, The European Bioelectromagnetics Association*, vol. 27, no. 5, pp. 392–400, 2006.

[22] K. Hossmann and D. Hermann, "Effects of electromagnetic radiation of mobile phones on the central nervous system," *Bioelectromagnetics: Journal of the Bioelectromagnetics Society, The Society for Physical Regulation in Biology and Medicine, The European Bioelectromagnetics Association*, vol. 24, no. 1, pp. 49–62, 2003.

[23] R. Santini, P. Santini, J. Danze, P. Le Ruz, and M. Seigne, "Study of the health of people living in the vicinity of mobile phone base stations: I. influences of distance and sex," *Pathol Biol*, vol. 50, no. 369, pp. 369–373, 2002.

[24] S. M. Moore, R. L. McIntosh, S. Iskra, and A. W. Wood, "Modeling the effect of adverse environmental conditions and clothing on temperature rise in a human body exposed to radio frequency electromagnetic fields," *IEEE Transactions on Biomedical Engineering*, vol. 62, no. 2, pp. 627–637, 2014.

[25] S. M. Moore, R. L. McIntosh, S. Iskra, A. Lajevardipour, and A. W. Wood, "Effect of adverse environmental conditions and protective clothing on temperature rise in a human body exposed to radiofrequency electromagnetic fields," *Bioelectromagnetics*, vol. 38, no. 5, pp. 356–363, 2017.

[26] D. Bhargava, P. Rattanadecho, and T. Wessapan, "The effect of metal objects on the SAR and temperature increase in the human head exposed to dipole antenna (numerical analysis)," *Case Studies in Thermal Engineering*, vol. 22, p. 100789, 2020.

[27] X. Xusheng, M. Kun, M. Hongwei, S. Wanfeng, and F. Hongwei, "Analysis of wireless electromagnetic wave propagation mechanism for coal mine rescue robot," in *2018 IEEE International Conference on Real-time Computing and Robotics (RCAR)*. IEEE, 2018, pp. 64–67.

[28] M. El Khaled, P. Fortier, and M. L. Ammari, "A performance study of line-of-sight millimeter-wave underground mine channel," *IEEE Antennas and Wireless Propagation Letters*, vol. 13, pp. 1148–1151, 2014.

[29] A. Ranjan, P. Misra, B. Dwivedi, and H. B. Sahu, "Studies on propagation characteristics of radio waves for wireless networks in underground coal mines," *Wireless Personal Communications*, vol. 97, no. 2, pp. 2819–2832, 2017.

[30] I. Hussain, F. Cawood, and R. van Olst, "Effect of tunnel geometry and antenna parameters on through-the-air communication systems in underground mines: Survey and open research areas," *Physical Communication*, vol. 23, pp. 84–94, 2017.

[31] Y. Diao, E. A. Rashed, and A. Hirata, "Large-scale analysis of the head proximity effects on antenna performance using machine learning based models," *IEEE Access*, vol. 8, pp. 154 060–154 071, 2020.

[32] G. Tognola, M. Bonato, E. Chiaramello, S. Fiocchi, I. Magne, M. Souques, M. Parazzini, and P. Ravazzani, "Use of machine learning in the analysis of indoor ELF MF exposure in children," *International Journal of Environmental Research and Public Health*, vol. 16, no. 7, p. 1230, 2019.

[33] Y. Kiouvrekis, A. Alexias, Y. Filipopoulos, V. Softa, C. D. Tyrakis, and C. Kappas, "Unsupervised machine learning and EMF radiation in schools: a study of 205 schools in Greece," *arXiv preprint arXiv:2007.13208*, 2020.

[34] W. Schiffbauer and J. Brune, "Underground coal mine communications for emergencies and everyday operation," in *Symposium on the capabilities and availability of wireless communication and tracking systems for underground coal mines*. sn, 2006.

[35] A. Patri, A. Nayak, and S. Jayanthu, "Wireless communication systems for underground mines–a critical appraisal," *International Journal of Engineering Trends and Technology*, vol. 4, no. 7, pp. 3149–3153, 2013.

[36] B. Austin, "Medium frequency body loop antenna for use underground," in *IEE Colloquium on Electrically Small Antennas*. IET, 1990, pp. 3–1.

[37] T. Wadley, "Underground communication by rocks in gold mines on the witwaterrand," *South Africa wet. Ny-werheid-Navorsingsraad, Johannesburg, South Africa, Telekommunikasies Navorsing Laboratorium TRL*, 1946.

[38] H. Aniss, P. Tardif, R. Ouedraogo, and P. Fortier, "Communications network for underground mines based on the IEEE 802.11 and DOCSIS standards," in *IEEE 60th Vehicular Technology Conference*, vol. 5. IEEE, 2004, pp. 3605–3609.

[39] A. Chehri, P. Fortier, and P. M. Tardif, "Geolocation for UWB networks in underground mines," in *2006 IEEE Annual Wireless and Microwave Technology Conference*. IEEE, 2006, pp. 1–4.

[40] Z. Xu, Y. Huo, and H. d. Zheng, "The effect of the wall roughness on the electromagnetic wave propagation in coal mine underground," in *2008 IEEE International Symposium on Knowledge Acquisition and Modeling Workshop*. IEEE, 2008, pp. 482–485.

[41] L. Cheng, L. Zhang, and J. Li, "Influence of mine tunnel wall humidity on electromagnetic waves propagation," *International Journal of Antennas and Propagation*, vol. 2012, 2012.

[42] X. Zheng, H. Wang, H. Wen, and J. Guo, "Propagation characteristics of electromagnetic waves in mine roadways," *Journal of Applied Geophysics*, vol. 173, p. 103922, 2020.

[43] L. F. Cheng, J. Li, and L. L. Zhang, "Dust in tunnel influenced to propagation characteristic of UHF electromagnetic waves," in *Applied Mechanics and Materials*, vol. 143. Trans Tech Publ, 2012, pp. 828–832.

[44] Y. Rissafi, L. Talbi, and M. Ghaddar, "Experimental characterization of an UWB propagation channel in underground mines," *IEEE Transactions on Antennas and Propagation*, vol. 60, no. 1, pp. 240–246, 2011.

[45] N. Hakem, G. Delisle, and Y. Coulibaly, "Radio-wave propagation into an underground mine environment at 2.4 GHz, 5.8 GHz and 60 GHz," in *The 8th European Conference on Antennas and Propagation (EuCAP 2014)*. IEEE, 2014, pp. 3592–3595.

[46] S. A. M. Tariq, C. L. Despins, S. Affes, and C. Nerguizian, "Angular dispersion of a scattered underground wireless channel at 60 GHz," *IEEE Access*, vol. 8, pp. 67 572–67 580, 2020.

[47] A. Issa, N. Hakem, and N. Kandil, "Experimental performances for LTE operating on 2.6 GHz in underground gold mine," in *2020 IEEE International Symposium on Antennas and Propagation and North American Radio Science Meeting*. IEEE, 2020, pp. 1219–1220.

[48] L. Muduli, D. P. Mishra, and P. K. Jana, "Application of wireless sensor network for environmental monitoring in underground coal mines: A systematic review," *Journal of Network and Computer Applications*, vol. 106, pp. 48–67, 2018.

[49] M. D. Bedford, A. Hrovat, G. Kennedy, T. Javornik, and P. Foster, "Modeling microwave propagation in natural caves using LiDAR and ray tracing," *IEEE Transactions on Antennas and Propagation*, vol. 68, no. 5, pp. 3878–3888, 2019.

[50] H. Zhang, M. Zhu, X. Li, W. Han, and Z. Liu, "Very low frequency propagation characteristics analysis in coal mines," *IEEE Access*, vol. 8, pp. 95 483–95 490, 2020.

[51] U. I. Minhas, I. H. Naqvi, S. Qaisar, K. Ali, S. Shahid, and M. A. Aslam, "A WSN for monitoring and event reporting in underground mine environments," *IEEE Systems Journal*, vol. 12, no. 1, pp. 485–496, 2017.

[52] X. Li, Y. Sun, Z. Liu, and M. Portfleet, "A wearable system for situational awareness estimation in underground mines," in *2018 IEEE/ACM International Conference on Connected Health: Applications, Systems and Engineering Technologies (CHASE)*. IEEE, 2018, pp. 31–32.

[53] G. E. M. Abro, S. A. Shaikh, S. Soomro, G. Abid, K. Kumar, and F. Ahmed, "Prototyping IoT based smart wearable jacket design for securing the life of coal miners," in *2018 International Conference on Computing, Electronics & Communications Engineering (iCCECE)*. IEEE, 2018, pp. 134–137.

[54] S. Indra, S. Barik, and U. C. Pati, "Design of portable indicator for underground mines using 433 MHz wireless communication," in *2018 2nd International Conference on Electronics, Materials Engineering & Nano-Technology (IEMENTech)*. IEEE, 2018, pp. 1–5.

[55] Y. Kim, J. Baek, and Y. Choi, "Smart helmet-based personnel proximity warning system for improving underground mine safety," *Applied Sciences*, vol. 11, no. 10, p. 4342, 2021.

[56] V. Ramya, N. Kavya, N. Kavana, G. Kavya, and K. Kavya, "Intelligent helmet for miners," in *2021 International Conference on Design Innovations for 3Cs Compute Communicate Control (ICDI3C)*. IEEE, 2021, pp. 234–238.

[57] R. Suganya and S. Gowtham, "Individual health and safety monitoring of workers in deep underground mines using IoT," in *Journal of Physics: Conference Series*, vol. 1717, no. 1. IOP Publishing, 2021, p. 012044.

[58] N. V. K. Reddy, G. M. Varma, and P. Visalakshi, "Design of IoT based coal mine safety system using arduino UNO," *Annals of the Romanian Society for Cell Biology*, pp. 5663–5670, 2021.

[59] S. Suganthi, G. Valarmathi, V. Subashini, R. Janaki, and R. Prabha, "Coal mine safety system for mining workers using LORA and WUSN," *Materials Today: Proceedings*, vol. 46, pp. 3803–3808, 2021.

[60] M. Ramya and M. Kousalya, "Investigation and design of helmet for coal miners," *Indo-Iranian Journal of Scientific Research (IIJSR)*, vol. 2, no. 2, pp. 136–142, 2018.

[61] J. Baek and Y. Choi, "Smart glasses-based personnel proximity warning system for improving pedestrian safety in construction and mining sites," *International journal of environmental research and public health*, vol. 17, no. 4, p. 1422, 2020.

[62] N. Singh, V. K. Gunjan, G. Chaudhary, R. Kaluri, N. Victor, and K. Lakshmanna, "IoT enabled helmet to safeguard the health of mine workers," *Computer Communications*, vol. 193, pp. 1–9, 2022.

[63] T. Porselvi, S. Ganesh, B. Janaki, K. Priyadarshini *et al.*, "IoT based coal mine safety and health monitoring system using LoRaWAN," in *2021 3rd International Conference on Signal Processing and Communication (ICPSC)*. IEEE, 2021, pp. 49–53.

[64] M. Noorin and K. Suma, "IoT based wearable device using WSN technology for miners," in *2018 3rd IEEE International Conference on Recent Trends in Electronics, Information & Communication Technology (RTEICT)*. IEEE, 2018, pp. 992–996.

[65] H. H. Pennes, "Analysis of tissue and arterial blood temperatures in the resting human forearm," *Journal of applied physiology*, vol. 1, no. 2, pp. 93–122, 1948.

[66] A. Hirata, K. Shirai, and O. Fujiwara, "On averaging mass of SAR correlating with temperature elevation due to a dipole antenna," *Progress In Electromagnetics Research*, vol. 84, pp. 221–237, 2008.

[67] J. Cooper, B. Marx, J. Buhl, and V. Hombach, "Determination of safety distance limits for a human near a cellular base station antenna, adopting the IEEE standard or ICNIRP guidelines," *Bioelectromagnetics: Journal of the Bioelectromagnetics Society, The Society for Physical Regulation in Biology and Medicine, The European Bioelectromagnetics Association*, vol. 23, no. 6, pp. 429–443, 2002.

[68] C. Chakraborty and A. Singh, "Determination of safe distance limit from cellular base station radiation exposure using SAR analysis," *Int J Comput Appl*, vol. 55, pp. 18–22, 2013.

[69] IEEE C95. 1-2019, "IEEE standard for safety levels with respect to human exposure to electric, magnetic, and electromagnetic fields, 0 Hz to 300 GHz,"

IEEE Std C95. 1-2019 (Revision of IEEE Std C95. 1-2005/Incorporates IEEE Std C95. 1-2019/Cor 1-2019), pp. 1–312, 2019.

[70] G. Vermeeren, W. Joseph, and L. Martens, "Whole-body SAR in spheroidal adult and child phantoms in realistic exposure environment," *Electronics Letters*, vol. 44, no. 13, pp. 790–791, 2008.

[71] J. Bakker, M. Paulides, A. Christ, N. Kuster, and G. C. van Rhoon, "Assessment of induced SAR in children exposed to electromagnetic plane waves between 10 MHz and 5.6 GHz," *Physics in Medicine & Biology*, vol. 55, no. 11, p. 3115, 2010.

[72] S. Iskra, R. McKenzie, and I. Cosic, "Monte Carlo simulations of the electric field close to the body in realistic environments for application in personal radiofrequency dosimetry," *Radiation protection dosimetry*, vol. 147, no. 4, pp. 517–527, 2011.

[73] J. Bakker, M. Paulides, E. Neufeld, A. Christ, N. Kuster, and G. Van Rhoon, "Children and adults exposed to electromagnetic fields at the ICNIRP reference levels: Theoretical assessment of the induced peak temperature increase," *Physics in Medicine & Biology*, vol. 56, no. 15, p. 4967, 2011.

[74] W. Joseph, G. Vermeeren, L. Verloock, M. M. Heredia, and L. Martens, "Characterization of personal RF electromagnetic field exposure and actual absorption for the general public," *Health physics*, vol. 95, no. 3, pp. 317–330, 2008.

[75] L. Verloock, W. Joseph, G. Vermeeren, and L. Martens, "Procedure for assessment of general public exposure from WLAN in offices and in wireless sensor network testbed," *Health Physics*, vol. 98, no. 4, pp. 628–638, 2010.

[76] M. J. van Wyk, M. Bingle, and F. J. Meyer, "Antenna modeling considerations for accurate SAR calculations in human phantoms in close proximity to GSM cellular base station antennas," *Bioelectromagnetics*, vol. 26, no. 6, pp. 502–509, 2005.

[77] P. Frei, E. Mohler, G. Neubauer, G. Theis, A. Bürgi, J. Fröhlich, C. Braun-Fahrländer, J. Bolte, M. Egger, and M. Röösli, "Temporal and spatial variability of personal exposure to radio frequency electromagnetic fields," *Environmental research*, vol. 109, no. 6, pp. 779–785, 2009.

[78] M. Röösli, P. Frei, E. Mohler, C. Braun-Fahrländer, A. Bürgi, J. Fröhlich, G. Neubauer, G. Theis, and M. Egger, "Statistical analysis of personal radiofrequency electromagnetic field measurements with nondetects," *Bioelectromagnetics: Journal of the Bioelectromagnetics Society, The Society for Physical Regulation in Biology and Medicine, The European Bioelectromagnetics Association*, vol. 29, no. 6, pp. 471–478, 2008.

[79] J.-F. Viel, E. Cardis, M. Moissonnier, R. de Seze, and M. Hours, "Radiofrequency exposure in the French general population: band, time, location and activity variability," *Environment International*, vol. 35, no. 8, pp. 1150–1154, 2009.

[80] E. Brillaud, A. Piotrowski, and R. De Seze, "Effect of an acute 900 MHz GSM exposure on glia in the rat brain: a time-dependent study," *Toxicology*, vol. 238, no. 1, pp. 23–33, 2007.

[81] Q. Balzano, C. Chou, R. Cicchetti, A. Faraone, and R. S. Tay, "An efficient RF exposure system with precise whole-body average SAR determination for in vivo animal studies at 900 MHz," *IEEE Transactions on Microwave Theory and Techniques*, vol. 48, no. 11, pp. 2040–2049, 2000.

[82] J. Choi, J. H. Hwang, H. Lim, H. Joo, H. S. Yang, Y. H. Lee, M. Eeftens, B. Struchen, M. Röösli, A. K. Lee *et al.*, "Assessment of radiofrequency electromagnetic field exposure from personal measurements considering the body shadowing effect in Korean children and parents," *Science of the Total Environment*, vol. 627, pp. 1544–1551, 2018.

[83] J. Karpowicz, S. de Miguel-Bilbao, P. Zradzńnski, K. Gryz, F. Falcone, and V. Ramos, "Comparative study of radiofrequency electromagnetic exposure

in the public shopping centers," in *2018 International Symposium on Electromagnetic Compatibility (EMC EUROPE)*. IEEE, 2018, pp. 972–975.

[84] S. Sagar, S. M. Adem, B. Struchen, S. P. Loughran, M. E. Brunjes, L. Arangua, M. A. Dalvie, R. J. Croft, M. Jerrett, J. M. Moskowitz *et al.*, "Comparison of radiofrequency electromagnetic field exposure levels in different everyday microenvironments in an international context," *Environment international*, vol. 114, pp. 297–306, 2018.

[85] M. Smondrk, M. Benova, and Z. Psenakova, "Specific absorption rate evaluation in human body model comprising of metallic implant," in *19th International Conference Computational Problems of Electrical Engineering*. IEEE, 2018, pp. 1–4.

[86] J. Michalowska, A. Tofil, J. Józwik, J. Pytka, P. Budzyński, and E. Korzeniewska, "Measurement of high-frequency electromagnetic fields in CNC machine tools area," in *2018 IEEE 4th International Symposium on Wireless Systems within the International Conferences on Intelligent Data Acquisition and Advanced Computing Systems (IDAACS-SWS)*. IEEE, 2018, pp. 162–165.

[87] R. Sen, A. K. Sarkar, A. K. Mandal, and L. C. Paul, "The analysis of EM absorption for biological tissue due to RF radiation measured inside the enclosed metallic chamber," in *2018 International Conference on Innovation in Engineering and Technology (ICIET)*. IEEE, 2018, pp. 1–5.

[88] D. Kljajic and N. Djuric, "The adaptive boundary exposure assessment approach for broadband EMF measurements," in *2018 26th Telecommunications Forum (TELFOR)*. IEEE, 2018, pp. 420–425.

[89] O. Bejenaru, C. Lazarescu, M. V. Paulet, and A. Salceanu, "Study upon specific absorption rate: Far field source outside and subject inside the building," in *24th IMEKO TC4 International Symposium Electrical & Electronic Measurements Promote Inudstry*, vol. 4, pp. 17–20.

[90] T. H. Loh, D. Cheadle, F. Heliot, A. Sunday, and M. Dieudonne, "A study of experiment-based radio frequency electromagnetic field exposure evidence on stochastic nature of a massive MIMO system," in *2021 15th European Conference on Antennas and Propagation (EuCAP)*. IEEE, 2021, pp. 1–5.

[91] J. M. Paniagua, M. Rufo, A. Jiménez, and A. Antolín, "Dimensionless coefficients for assessing human exposure to radio-frequency electromagnetic fields indoors and outdoors in urban areas," *Environmental research*, vol. 183, p. 109188, 2020.

[92] S. Keshmiri, N. Gholampour, and V. Mohtashami, "Assessing the compliance of electromagnetic fields radiated by base stations and WiFi access points with international guidelines on university campus," *Radiation Protection Dosimetry*, vol. 192, no. 1, pp. 1–13, 2020.

[93] D. Jovanović, V. Stanković, D. Živaljević, D. Vučković, and S. Ilie, "Effects of using metal frame glasses exposed to electromagnetic radiation from mobile phone," *Safety Engineering*, vol. 10, no. 1, pp. 1–8, 2020.

[94] L. R. Harris, "Electric field and SAR estimation for multiple wireless device usage in capsule environment," in *2020 Wireless Telecommunications Symposium (WTS)*. IEEE, 2020, pp. 1–5.

[95] N. Moraitis, I. Popescu, and K. S. Nikita, "Frequency selective EMF measurements and exposure assessment in indoor office environments," in *2020 14th European Conference on Antennas and Propagation (EuCAP)*. IEEE, 2020, pp. 1–5.

[96] O. Bejenaru, C. Lazarescu, M. V. Ursachianu, and A. Salceanu, "SAR determination for indoor, far field exposure," in *2020 International Conference and Exposition on Electrical And Power Engineering (EPE)*. IEEE, 2020, pp. 322–326.

[97] G. Lieli and J. Pingli, "Safety assessment of electromagnetic exposure of superconducting magnetic levitation track," in *IOP Conference Series: Earth*

and Environmental Science, vol. 812, no. 1. IOP Publishing, 2021, p. 012004.

[98] A. Huss, S. Dongus, R. Aminzadeh, A. Thielens, M. Van den Bossche, P. Van Torre, R. de Seze, E. Cardis, M. Eeftens, W. Joseph *et al.*, "Exposure to radiofrequency electromagnetic fields: Comparison of exposimeters with a novel body-worn distributed meter," *Environment International*, vol. 156, p. 106711, 2021.

[99] G. Göcsei, B. Németh, and I. Kiss, "Results of risk assessment for occupational electromagnetic exposures," *Journal of Electrostatics*, vol. 115, p. 103678, 2022.

[100] B. M. Zeleke, C. Brzozek, C. R. Bhatt, M. J. Abramson, R. J. Croft, F. Freudenstein, P. Wiedemann, and G. Benke, "Personal exposure to radio frequency electromagnetic fields among Australian adults," *International Journal of Environmental Research and Public Health*, vol. 15, no. 10, p. 2234, 2018.

[101] B. M. Zeleke, C. R. Bhatt, C. Brzozek, M. J. Abramson, F. Freudenstein, R. J. Croft, P. Wiedemann, and G. Benke, "Radiofrequency electromagnetic field exposure and risk perception: A pilot experimental study," *Environmental research*, vol. 170, pp. 493–499, 2019.

[102] A. Massardier-Pilonchery, E. Nerrière, S. Croidieu, F. Ndagijimana, F. Gaudaire, C. Martinsons, N. Noé, and M. Hours, "Assessment of personal occupational exposure to radiofrequency electromagnetic fields in libraries and media libraries, using calibrated on-body exposimeters," *International Journal of Environmental Research and Public Health*, vol. 16, no. 12, p. 2087, 2019.

[103] L. Hardell, M. Carlberg, and L. K. Hedendahl, "Radiofrequency radiation from nearby base stations gives high levels in an apartment in Stockholm, Sweden: A case report," *Oncology Letters*, vol. 15, no. 5, pp. 7871–7883, 2018.

[104] R. Ramirez-Vazquez, J. Gonzalez-Rubio, E. Arribas, and A. Najera, "Characterisation of personal exposure to environmental radiofrequency electromagnetic fields in Albacete (Spain) and assessment of risk perception," *Environmental research*, vol. 172, pp. 109–116, 2019.

[105] R. N. Iyare, V. Volskiy, and G. A. Vandenbosch, "Study of the correlation between outdoor and indoor electromagnetic exposure near cellular base stations in Leuven, Belgium," *Environmental research*, vol. 168, pp. 428–438, 2019.

[106] M. Benini, M. Parazzini, M. Bonato, S. Gallucci, E. Chiaramello, S. Fiocchi, and G. Tognola, "Road user exposure from ITS-5.9 GHz vehicular connectivity," *Sensors*, vol. 22, no. 18, p. 6986, 2022.

[107] R. Ramirez-Vazquez, I. Escobar, A. Thielens, and E. Arribas, "Measurements and analysis of personal exposure to radiofrequency electromagnetic fields at outdoor and indoor school buildings: A case study at a Spanish school," *IEEE Access*, vol. 8, pp. 195 692–195 702, 2020.

[108] M. Colella, M. Biscarini, M. de Meis, R. Patrizi, T. Ciallella, D. Ferrante, A. De Gaetano, M. Capuano, G. Pellegrino, E. Martini *et al.*, "Numerical evaluation of human body near field exposure to a vehicular antenna for military applications," *Frontiers in Public Health*, vol. 9, 2021.

[109] A. Wafik, A. Abdin, and I. Karim, "Assessment of electromagnetic frequencies in office spaces," *Journal of Al-Azhar University Engineering Sector*, vol. 17, no. 63, pp. 653–666, 2022.

[110] Z. Wang and W. Liu, "Influence of materials, windows and shielding layers on low-frequency electromagnetic environment of subway vehicle and human exposure research," *Progress in Electromagnetics Research M*, vol. 105, pp. 151–160, 2021.

[111] R. Ramirez-Vazquez, J. Gonzalez-Rubio, I. Escobar, C. d. P. Suarez Rodriguez, and E. Arribas, "Personal exposure assessment to Wi-Fi radiofrequency electromagnetic fields in Mexican microenvironments," *International*

Journal of Environmental Research and Public Health, vol. 18, no. 4, p. 1857, 2021.

[112] P. Di Barba, Ł. Januszkiewicz, J. Kawecki, and M. E. Mognaschi, "Electromagnetic wave absorption in the human head: A virtual sensor based on a deep-learning model," *Sensors*, vol. 23, no. 6, p. 3131, 2023.

[113] Z. Pala, İ. Bozkurt, and T. Etem, "Estimation of low frequency electromagnetic values using machine learning," in *2017 XIIIth International Conference on Perspective Technologies and Methods in MEMS Design (MEMSTECH)*. IEEE, 2017, pp. 136–139.

[114] E. Meliadò, A. Raaijmakers, A. Sbrizzi, B. Steensma, M. Maspero, M. Savenije, P. Luijten, and C. van den Berg, "A deep learning method for image-based subject-specific local SAR assessment," *Magnetic Resonance in Medicine*, vol. 83, no. 2, pp. 695–711, 2020.

[115] S. Gokyar, F. J. Robb, W. Kainz, A. Chaudhari, and S. A. Winkler, "Mrsaife: an ai-based approach towards the real-time prediction of specific absorption rate," *IEEE Access*, vol. 9, pp. 140 824–140 834, 2021.

[116] E. Gothai, A. Baseera, P. Prabu, K. Venkatachalam, K. Saravanan, and S. SathishKumar, "Machine learning technique to detect radiations in the brain." *Comput. Syst. Sci. Eng.*, vol. 42, no. 1, pp. 149–163, 2022.

[117] O. Cerezci, B. Kanberoglu, and S. C. Yener, "Assessment of occupational exposure levels of cleaning product manufacturing factory workers to electromagnetic fields," *Radiation Protection Dosimetry*, vol. 198, no. 4, pp. 197–207, 2022.

[118] M. Mannan, Y. W. Weldu, and S. G. Al-Ghamdi, "Health impact of energy use in buildings: Radiation propagation assessment in indoor environment," *Energy Reports*, vol. 6, pp. 915–920, 2020.

[119] M. Colella, M. Biscarini, M. de Meis, R. Patrizi, T. Ciallella, M. Cavagnaro, F. Apollonio, and M. Liberti, "Human body exposure to a vehicular antenna: A numerical study in a realistic military scenario," in *2022 Microwave Mediterranean Symposium (MMS)*. IEEE, 2022, pp. 1–4.

[120] T. N. Kapetanakis, M. P. Ioannidou, A. T. Baklezos, C. D. Nikolopoulos, E. S. Sergaki, A. J. Konstantaras, and I. O. Vardiambasis, "Assessment of radiofrequency exposure in the vicinity of school environments in Crete Island, South Greece," *Applied Sciences*, vol. 12, no. 9, p. 4701, 2022.

[121] Z. Psenakova, M. Benova, and J. Mydlova, "Investigation of SAR (Specific absorbtion rate) in different head models placed in shielded space," in *2019 IEEE 20th International Conference on Computational Problems of Electrical Engineering (CPEE)*. IEEE, 2019, pp. 1–4.

[122] E. Chiaramello, D. Plets, S. Fiocchi, M. Bonato, G. Tognola, M. Parazzini, L. Le Brusquet, L. Martens, W. Joseph, and P. Ravazzani, "Innovative stochastic modeling of residential exposure to radio frequency electromagnetic field sources," *IEEE Journal of Electromagnetics, RF and Microwaves in Medicine and Biology*, vol. 5, no. 1, pp. 62–69, 2020.

[123] J. P. O. Bustillo, R. J. G. Fernandez, and H. B. Domingo, "Assessment of a localized deterministic spatial interpolation method in generating an indoor radiofrequency radiation map," in *Journal of Physics: Conference Series*, vol. 1248, no. 1. IOP Publishing, 2019, p. 012075.

[124] M. Celaya-Echarri, L. Azpilicueta, P. Lopez-Iturri, E. Aguirre, S. De Miguel-Bilbao, V. Ramos, and F. Falcone, "Spatial characterization of personal RF-EMF exposure in public transportation buses," *IEEE Access*, vol. 7, pp. 33 038–33 054, 2019.

[125] M. Celaya-Echarri, L. Azpilicueta, V. Ramos, P. Lopez-Iturri, and F. Falcone, "Empirical and modeling approach for environmental indoor RF-EMF assessment in complex high-node density scenarios: Public shopping malls case study," *IEEE Access*, vol. 9, pp. 46 755–46 775, 2021.

[126] M. Celaya-Echarri, L. Azpilicueta, F. A. Rodríguez-Corbo, P. Lopez-Iturri, R. M. Shubair, V. Ramos, and F. Falcone, "5G spatial modeling of personal RF-EMF assessment within aircrafts cabin environments," *IEEE Access*, vol. 10, pp. 78 860–78 874, 2022.

[127] A. Martínez-González, J. Monzó-Cabrera, A. Martínez-Sáez, and A. Lozano-Guerrero, "Minimization of measuring points for the electric field exposure map generation in indoor environments by means of kriging interpolation and selective sampling," *Environmental Research*, p. 113577, 2022.

[128] T. Onishi, M. Ikuyo, K. Tobita, S. Liu, M. Taki, and S. Watanabe, "Radiofrequency exposure levels from mobile phone base stations in outdoor environments and an underground shopping mall in Japan," *International Journal of Environmental Research and Public Health*, vol. 18, no. 15, p. 8068, 2021.

[129] R. Maurya, N. Singh, T. Jindal, V. K. Pathak, and M. K. Dutta, "Machine learning–based identification of radiofrequency electromagnetic radiation (RF-EMR) effect on brain morphology: a preliminary study," *Medical & Biological Engineering & Computing*, vol. 58, no. 8, pp. 1751–1765, 2020.

[130] S. Kodera, A. Hirata, D. Funahashi, S. Watanabe, K. Jokela, and R. J. Croft, "Temperature rise for brief radio-frequency exposure below 6 GHz," *IEEE Access*, vol. 6, pp. 65 737–65 746, 2018.

[131] Z. Lwin and M. Yokota, "Numerical analysis of specific absorption rate and temperature rise in human head model using FDTD method," in *2018 IEEE 7th Global Conference on Consumer Electronics (GCCE)*. IEEE, 2018, pp. 1–2.

[132] F. Kaburcuk and A. Z. Elsherbeni, "SAR and temperature rise distributions in a human head due to a multi-frequency antenna source," in *2018 International Applied Computational Electromagnetics Society Symposium (ACES)*. IEEE, 2018, pp. 1–2.

[133] G. Sacco, S. Pisa, and M. Zhadobov, "Impact of textile on electromagnetic power and heating in near-surface tissues at 26 GHz and 60 GHz," *IEEE Journal of Electromagnetics, RF and Microwaves in Medicine and Biology*, vol. 5, no. 3, pp. 262–268, 2020.

[134] D. H. Gultekin and P. H. Siegel, "Absorption of 5G radiation in brain tissue as a function of frequency, power and time," *IEEE Access*, vol. 8, pp. 115 593–115 612, 2020.

[135] B. Christopher, M. U. Khandaker, P. Jojo *et al.*, "Empirical study on specific absorption rate of head tissues due to induced heating of 4G cell phone radiation," *Radiation Physics and Chemistry*, vol. 178, p. 108910, 2021.

[136] H. Matikka, J. Keshvari, and R. Lappalainen, "Temperature changes associated with radiofrequency exposure near authentic metallic implants in the head phantom—a near field simulation study with 900, 1800 and 2450 MHz dipole," *Physics in Medicine & Biology*, vol. 55, no. 19, p. 5867, 2010.

[137] G. B. Gajda, J. Paradis, and E. Lemay, "Steady state temperature rise in multilayered tissue due to arbitrary periodic SAR using finite difference FFT and transfer function method," *Biomedical Physics & Engineering Express*, vol. 7, no. 4, p. 045021, 2021.

[138] M. Cavagnaro and J. C. Lin, "Importance of exposure duration and metrics on correlation between RF energy absorption and temperature increase in a human model," *IEEE Transactions on Biomedical Engineering*, vol. 66, no. 8, pp. 2253–2258, 2018.

[139] E. A. Rashed, Y. Diao, and A. Hirata, "Learning-based estimation of dielectric properties and tissue density in head models for personalized radiofrequency dosimetry," *Physics in Medicine & Biology*, vol. 65, no. 6, p. 065001, 2020.

[140] M. N. Halgamuge, "Machine learning for bioelectromagnetics: Prediction model using data of weak radiofrequency radiation effect on plants," *International Journal of Advanced Computer Science and Applications*, vol. 8, no. 11, 2017.

[141] M. Halgamuge, "Supervised machine learning algorithms for bioelectromagnetics: Prediction models and feature selection techniques using data from weak radiofrequency radiation effect on human and animals cells," *International Journal of Environmental Research and Public Health*, vol. 17, no. 12, 2020. [Online]. Available: https://www.mdpi.com/1660-4601/17/12/4595

[142] Y. Kiouvrekis, V. Softa, Y. Filippopoulos, and K. Kappas, "Unsupervised machine learning and EMF radiation in schools: A study of 205 schools in Greece," *Physica Medica: European Journal of Medical Physics*, vol. 92, p. S239, 2021.

[143] Ansys, "Ansys HFSS Best-In-Class 3D high frequency electromagnetic simulation software," https://www.ansys.com/products/electronics/ansys-hfss, [accessed January 25, 2024].

[144] G. A. E. Vandenbosch and A. Vasylchenko, "A practical guide to 3D electromagnetic software tools," https://cdn.intechopen.com/pdfs/14726.pdf, [accessed January 25, 2024].

[145] M. Vogel, "Electromagnetic safety in wireless communications and biomedical technologies," *Canonsburg, PA, USA, ANSYS, Inc., White Paper*, 2014.

[146] Ansys, "Ansys human body model v3," https://catalog.ansys.com/product/5bfec4c8393ff6c28c1997da/ansys-human-body-m, [accessed January 25, 2024].

[147] M. Khabiri, "Design and simulation of implantable PIFA in presence of ansys human body model for biomedical telemetry using ANSYS HFSS," *Ozen Engineering, Inc*, no. 408, pp. 1–11, 2015.

[148] S. N. Makarov, G. M. Noetscher, J. Yanamadala, M. W. Piazza, S. Louie, A. Prokop, A. Nazarian, and A. Nummenmaa, "Virtual human models for electromagnetic studies and their applications," *IEEE Reviews in Biomedical Engineering*, vol. 10, pp. 95–121, 2017.

[149] INDEPENDENT COMMUNICATIONS AUTHORITY OF SOUTH AFRICA, "NOTICE OF INTENTION TO AMEND ANNEXURE B OF THE RADIO FREQUENCY SPECTRUM REGULATIONS," http://www.icasa.org.za/legislation-and-regulations/notice-of-intention-to-amend-annexure-b-of-the-radio-frequency-spectrum-regulations, [accessed January 25, 2024].

[150] M. Mardonova and Y. Choi, "Review of wearable device technology and its applications to the mining industry," *Energies*, vol. 11, no. 3, p. 547, 2018.

[151] T. Khoa, "Wearable smart technologies: New era of technology," Ph.D. dissertation, Lapland University of Applied Sciences Lapland, Finland, 2015.

[152] A. Parate and D. Ganesan, "Detecting eating and smoking behaviors using smartwatches," *Mobile Health: Sensors, Analytic Methods, and Applications*, pp. 175–201, 2017.

[153] A. Hanuska, B. Chandramohan, L. Bellamy, P. Burke, R. Ramanathan, and V. Balakrishnan, "Smart clothing market analysis report," *Berkley University of California: Berkley, CA, USA*, pp. 1–47, 2016.

[154] J. Teizer, "Wearable, wireless identification sensing platform: Self-monitoring alert and reporting technology for hazard avoidance and training (smarthat)," *Journal of Information Technology in Construction (ITcon)*, vol. 20, no. 19, pp. 295–312, 2015.

[155] B. Mayton, G. Dublon, S. Palacios, and J. A. Paradiso, "Truss: Tracking risk with ubiquitous smart sensing," in *SENSORS, 2012 IEEE*. IEEE, 2012, pp. 1–4.

[156] P. Zradziński, J. Karpowicz, K. Gryz, L. Morzyński, R. Młyński, A. Swidziński, K. Godziszewski, and V. Ramos, "Modelling the influence of electromagnetic field on the user of a wearable IoT device used in a WSN for monitoring and reducing hazards in the work environment," *Sensors*, vol. 20, no. 24, p. 7131, 2020.

[157] IT'IS Foundation, "Tissue properties database v4.1," 2022.

[158] P. Zradziński, J. Karpowicz, K. Gryz, L. Morzyński, R. Młyński, A. Swidziński, K. Godziszewski, and V. Ramos, "Modelling the influence of the 2.4 GHz electromagnetic field on the user of a wearable internet of things (IoT) device for monitoring hazards in the work environment," *Engineering Proceedings*, vol. 2, no. 1, p. 39, 2020.

[159] A. Y. I. Ashyap, Z. Zainal Abidin, S. H. Dahlan, H. A. Majid, M. R. Kamarudin, A. Alomainy, R. A. Abd-Alhameed, J. S. Kosha, and J. M. Noras, "Highly efficient wearable CPW antenna enabled by EBG-FSS structure for medical body area network applications," *IEEE Access*, vol. 6, pp. 77 529–77 541, 2018.

[160] J. R. Flores-Cuadras, J. L. Medina-Monroy, R. A. Chavez-Perez, and H. Lobato-Morales, "Novel ultra-wideband flexible antenna for wearable wrist worn devices with 4G LTE communications," *Microwave and Optical Technology Letters*, vol. 59, no. 4, pp. 777–783, 2017.

[161] E. T. S. I. E. E. . . v2. 2.2 (2019-07), "Wideband transmission systems; data transmission equipment operating in the 2.4 GHz band; harmonised standard for access to radio spectrum," 2019.

[162] C. A. Balanis, *Antenna theory: Analysis and Design*. John wiley & sons, 2016.

[163] T. Wessapan and P. Rattanadecho, "Numerical analysis of specific absorption rate and heat transfer in human head subjected to mobile phone radiation: Effects of user age and radiated power," *Journal of Heat Transfer*, vol. 134, no. 12, p. 121101, 2012.

[164] M. S. Abdul, S. M. Sam, N. Mohamed, N. H. Hassan, A. Azizan, and Y. M. Yusof, "Peer to peer communication for the internet of things using ESP32 microcontroller for indoor environments," in *2022 13th International Conference on Information and Communication Technology Convergence (ICTC)*. IEEE, 2022, pp. 1–6.

[165] E. Cocherova, J. Surda, O. Ondracek, and V. Stofanik, "RF field orientation influence on the specific absorption rate in a biological object," in *2008 14th Conference on Microwave Techniques*. IEEE, 2008, pp. 1–3.

[166] G. Akram and Y. Jasmy, "Specific absorption rate (SAR) on the human head as function of orientation of plane wave radiation: FDTD-based analysis," in *2008 Second Asia International Conference on Modelling & Simulation (AMS)*. IEEE, 2008, pp. 959–962.

[167] H. Dominguez, A. Raizer, and W. Carpes, "Electromagnetic fields radiated by a cellular phone in close proximity to metallic walls," *IEEE Transactions on Magnetics*, vol. 38, no. 2, pp. 793–796, 2002.

[168] A. Y. Simba, S. Watanabe, T. Hikage, and T. Nojima, "Measurement of the maximum SAR in a spherical phantom when operating a mobile phone near a metallic wall," in *2008 First International Symposium on Applied Sciences on Biomedical and Communication Technologies*, 2008, pp. 1–4.

[169] S. U. Hwu, B. A. Rhodes, B. K. deSilva, C. C. Sham, and J. R. Keiser, "RF exposure analysis for multiple Wi-Fi devices in enclosed environment," in *2013 IEEE Sensors Applications Symposium Proceedings*, 2013, pp. 109–112.

[170] A. E. Forooshani, S. Bashir, D. G. Michelson, and S. Noghanian, "A survey of Wireless Communications and Propagation modeling in underground mines," *IEEE Communications Surveys & Tutorials*, vol. 15, no. 4, pp. 1524–1545, 2013.

[171] T. A. J. Mary and C. Ravichandran, "Effect of SAR on human head modelling inside cylindrical enclosures," *Electromagnetic Biology and Medicine*, vol. 32, no. 3, pp. 382–389, 2013.

[172] C. K. Tang, K. H. Chan, L. C. Fung, and S. Leung, "Effect on radio frequency human exposure of mobile phone inside an enclosed metallic elevator," *Microwave and Optical Technology Letters*, vol. 50, no. 8, pp. 2207–2210, 2008.

[173] I. Karatsi, S. Bakogianni, and S. Koulouridis, "SAR and thermal distribution of pregnant woman and child inside elevator cabin," *International Journal of Microwave and Wireless Technologies*, vol. 15, no. 2, pp. 213–226, 2023.

[174] G. N. Vizi and G. A. Vandenbosch, "Building materials and electromagnetic radiation: The role of material and shape," *Journal of Building Engineering*, vol. 5, pp. 96–103, 2016.

[175] T. Koppel, A. Shishkin, H. Haldre, N. Toropovs, I. Vilcane, and P. Tint, "Reflection and transmission properties of common construction materials at 2.4 GHz frequency," *Energy Procedia*, vol. 113, pp. 158–165, 2017.

[176] O. Bejenaru, C. Lazarescu, M. V. Paulet, A. Salceanu, and M. V. Ursachianu, "Factors influencing the distribution of maximum specific absorption rates in far field human exposure scenarios," *ACTA IMEKO*, vol. 9, no. 3, pp. 59–64, 2020.

[177] D. O. McCoy, D. M. Zakharia, and Q. Balzano, "Field strengths and specific absorption rates in automotive environments," *IEEE Transactions on Vehicular Technology*, vol. 48, no. 4, pp. 1287–1303, 1999.

[178] S. W. Leung, Y. Diao, K. H. Chan, Y.-M. Siu, and Y. Wu, "Specific absorption rate evaluation for passengers using wireless communication devices inside vehicles with different handedness, passenger counts, and seating locations," *IEEE Transactions on Biomedical Engineering*, vol. 59, no. 10, pp. 2905–2912, 2012.

[179] K. Chan, S. Leung, and Y. Siu, "Specific absorption rate evaluation for people using wireless communication device in vehicle," in *2010 IEEE International Symposium on Electromagnetic Compatibility*. IEEE, 2010, pp. 706–711.

[180] M. Bonato, G. Tognola, M. Benini, S. Gallucci, E. Chiaramello, S. Fiocchi, and M. Parazzini, "Assessment of SAR in road-users from 5G-V2X vehicular connectivity based on computational simulations," *Sensors*, vol. 22, no. 17, p. 6564, 2022.

[181] P. Delogne, "Leaky feeders and subsurface radio communication," 1982.

[182] A. E. Forooshani, S. Bashir, D. G. Michelson, and S. Noghanian, "A survey of wireless communications and propagation modeling in underground mines," *IEEE Communications surveys & tutorials*, vol. 15, no. 4, pp. 1524–1545, 2013.

[183] R. J. Lytle, "Measurement of earth medium electrical characteristics: Techniques, results, and applications," *IEEE Transactions on Geoscience Electronics*, vol. 12, no. 3, pp. 81–101, 1974.

[184] E. Parkhomenko, "Electrical Properties of Rocks Plenum Press," *New York 314p*, 1967.

[185] R. J. Lytle and D. L. Lager, "The yosemite experiments: HF propagation through rock," *Radio Science*, vol. 11, no. 4, pp. 245–252, 1976.

[186] I. G. Maglogiannis, *Emerging artificial intelligence applications in computer engineering: real word AI systems with applications in ehealth, hci, information retrieval and pervasive technologies*. Ios Press, 2007, vol. 160.

[187] M. A. El Mrabet, K. El Makkaoui, and A. Faize, "Supervised machine learning: A survey," in *2021 4th International Conference on Advanced Communication Technologies and Networking (CommNet)*. IEEE, 2021, pp. 1–10.

[188] P. C. Sen, M. Hajra, and M. Ghosh, "Supervised classification algorithms in machine learning: A survey and review," in *Emerging Technology in Modelling and Graphics: Proceedings of IEM Graph 2018.* Springer, 2020, pp. 99–111.

[189] S. Dridi, "Supervised learning-a systematic literature review," *preprint, Dec*, 2021.

[190] A. I. Kadhim, "Survey on supervised machine learning techniques for automatic text classification," *Artificial Intelligence Review*, vol. 52, no. 1, pp. 273–292, 2019.

[191] K. Yeturu, "Machine learning algorithms, applications, and practices in data science," in *Handbook of Statistics.* Elsevier, 2020, vol. 43, pp. 81–206.

[192] F. Osisanwo, J. Akinsola, O. Awodele, J. Hinmikaiye, O. Olakanmi, J. Akinjobi *et al.*, "Supervised machine learning algorithms: Classification and Comparison," *International Journal of Computer Trends and Technology (IJCTT)*, vol. 48, no. 3, pp. 128–138, 2017.

[193] B. Panigrahi, K. C. R. Kathala, and M. Sujatha, "A machine learning-based comparative approach to predict the crop yield using supervised learning with regression models," *Procedia Computer Science*, vol. 218, pp. 2684–2693, 2023.

[194] G. O. Barrionuevo, J. A. Ramos-Grez, M. Walczak, and C. A. Betancourt, "Comparative evaluation of supervised machine learning algorithms in the prediction of the relative density of 316l stainless steel fabricated by selective laser melting," *The International Journal of Advanced Manufacturing Technology*, vol. 113, pp. 419–433, 2021.

[195] P. Singh, *Fundamentals and methods of machine and deep learning: algorithms, tools, and applications.* John Wiley & Sons, 2022.

[196] V. Gupta, V. K. Mishra, P. Singhal, and A. Kumar, "An overview of supervised machine learning algorithm," in *2022 11th International Conference*

on System Modeling & Advancement in Research Trends (SMART). IEEE, 2022, pp. 87–92.

[197] R. Anitha and D. Siva Sundhara Raja, "Development of computer-aided approach for brain tumor detection using random forest classifier," *International Journal of Imaging Systems and Technology*, vol. 28, no. 1, pp. 48–53, 2018.

[198] Y. Song, J. Liang, J. Lu, and X. Zhao, "An efficient instance selection algorithm for K-nearest neighbor regression," *Neurocomputing*, vol. 251, pp. 26–34, 2017.

[199] O. Kramer *et al.*, *Dimensionality reduction with unsupervised nearest neighbors*. Springer, 2013, vol. 51.

[200] V. Rodriguez-Galiano, M. Sanchez-Castillo, M. Chica-Olmo, and M. Chica-Rivas, "Machine learning predictive models for mineral prospectivity: An evaluation of neural networks, random forest, regression trees and support vector machines," *Ore Geology Reviews*, vol. 71, pp. 804–818, 2015.

[201] M. Awad, R. Khanna, M. Awad, and R. Khanna, "Support vector regression," *Efficient Learning Machines: Theories, Concepts, and Applications for Engineers and System Designers*, pp. 67–80, 2015.

[202] A. Singh, N. Thakur, and A. Sharma, "A review of supervised machine learning algorithms," in *2016 3rd International Conference on Computing for Sustainable Global Development (INDIACom)*. IEEE, 2016, pp. 1310–1315.

[203] L. Breiman, "Random forests," *Machine Learning*, vol. 45, pp. 5–32, 2001.

[204] J. Peters, B. De Baets, N. E. Verhoest, R. Samson, S. Degroeve, P. De Becker, and W. Huybrechts, "Random forests as a tool for ecohydrological distribution modelling," *Ecological Modelling*, vol. 207, no. 2-4, pp. 304–318, 2007.

[205] M. Pal, "Random forest classifier for remote sensing classification," *International journal of remote sensing*, vol. 26, no. 1, pp. 217–222, 2005.

[206] T. Chen and C. Guestrin, "XGBoost: A scalable tree boosting system," in *Proceedings of the 22nd ACM SIGKDD International Conference on Knowledge Discovery and Data Mining*, 2016, pp. 785–794.

[207] C. N. Obiora, A. Ali, and A. N. Hasan, "Implementing extreme gradient boosting (XGBoost) algorithm in predicting solar irradiance," in *2021 IEEE PES/IAS PowerAfrica*. IEEE, 2021, pp. 1–5.

[208] S. Badirli, X. Liu, Z. Xing, A. Bhowmik, K. Doan, and S. S. Keerthi, "Gradient boosting neural networks: Grownet," *arXiv preprint arXiv:2002.07971*, 2020.

[209] A. Ogunleye and Q.-G. Wang, "XGBoost model for chronic kidney disease diagnosis," *IEEE/ACM Transactions on Computational Biology and Bioinformatics*, vol. 17, no. 6, pp. 2131–2140, 2019.

[210] J. H. Friedman, "Greedy function approximation: A Gradient boosting machine," *Annals of statistics*, pp. 1189–1232, 2001.

[211] Y. Meng, N. Yang, Z. Qian, and G. Zhang, "What makes an online review more helpful: An interpretation framework using XGBoost and SHAP values," *Journal of Theoretical and Applied Electronic Commerce Research*, vol. 16, no. 3, pp. 466–490, 2020.

[212] S. B. Kotsiantis, I. Zaharakis, P. Pintelas *et al.*, "Supervised machine learning: A review of classification techniques," *Emerging Artificial Intelligence Applications in Computer Engineering*, vol. 160, no. 1, pp. 3–24, 2007.

[213] V. Hodge and J. Austin, "A survey of outlier detection methodologies," *Artificial Intelligence Review*, vol. 22, pp. 85–126, 2004.

[214] K. Singh and S. Upadhyaya, "Outlier detection: Applications and techniques," *International Journal of Computer Science Issues (IJCSI)*, vol. 9, no. 1, p. 307, 2012.

[215] H. J. Escalante, "A comparison of outlier detection algorithms for machine learning," in *Proceedings of the International Conference on Communications in Computing*, 2005, pp. 228–237.

[216] J. Karhunen, T. Raiko, and K. Cho, "Unsupervised deep learning: A short review," *Advances in independent component analysis and learning machines*, pp. 125–142, 2015.

[217] I. H. Sarker, "Deep learning: a comprehensive overview on techniques, taxonomy, applications and research directions," *SN computer science*, vol. 2, no. 6, p. 420, 2021.

[218] ——, "Data science and analytics: an overview from data-driven smart computing, decision-making and applications perspective," *SN Computer Science*, vol. 2, no. 5, p. 377, 2021.

[219] X. Du, Y. Cai, S. Wang, and L. Zhang, "Overview of deep learning," in *2016 31st Youth Academic Annual Conference of Chinese Association of Automation (YAC)*. IEEE, 2016, pp. 159–164.

[220] S. Hochreiter, "Long short-term memory," *Neural Computation MIT-Press*, 1997.

[221] C. K. Chou, H. Bassen, J. Osepchuk, Q. Balzano, R. Petersen, M. Meltz, R. Cleveland, J. Lin, and L. Heynick, "Radio frequency electromagnetic exposure: Tutorial review on experimental dosimetry," *Bioelectromagnetics: Journal of the Bioelectromagnetics Society, The Society for Physical Regulation in Biology and Medicine, The European Bioelectromagnetics Association*, vol. 17, no. 3, pp. 195–208, 1996.

[222] J. Bergstra and Y. Bengio, "Random search for hyper-parameter optimization." *Journal of machine learning research*, vol. 13, no. 2, 2012.

[223] F. Hutter, L. Kotthoff, and J. Vanschoren, *Automated machine learning: methods, systems, challenges*. Springer Nature, 2019.

[224] M. Claesen, J. Simm, D. Popovic, Y. Moreau, and B. De Moor, "Easy hyperparameter search using optunity," *arXiv preprint arXiv:1412.1114*, 2014.

[225] P. R. Lorenzo, J. Nalepa, M. Kawulok, L. S. Ramos, and J. R. Pastor, "Particle swarm optimization for hyper-parameter selection in deep neural networks," in *Proceedings of the genetic and evolutionary computation conference*, 2017, pp. 481–488.

[226] F. Pedregosa, G. Varoquaux, A. Gramfort, V. Michel, B. Thirion, O. Grisel, M. Blondel, P. Prettenhofer, R. Weiss, V. Dubourg *et al.*, "Scikit-learn: Machine learning in python," *the Journal of machine Learning research*, vol. 12, pp. 2825–2830, 2011.

[227] S. Hooker, D. Erhan, P. Kindermans, and B. Kim, "A benchmark for interpretability methods in deep neural networks," *Advances in Neural Information Processing Systems*, vol. 32, 2019.

[228] CORNET Microsystem, "CORNET ED-88TPlus5G2 Electrosmog meter user's manual," https://safelivingtechnologies.com/content/Products/ED88TPlus5G2%20UserManualQeng1.0.pdf, [accessed January 25, 2024].

[229] T. Singh, R. Devi, A. Kumar, S. S. Jambagi, and B. Singh, "Transmission of electromagnetic radiations from mobile phones: A critical analysis," in *Smart Innovations in Communication and Computational Sciences: Proceedings of ICSICCS 2017, Volume 1*. Springer, 2019, pp. 229–238.

[230] O. Osahon, P. Ushie, and O. Ojo, "Comparative analysis of SAR and temperature rise within head tissues exposed to RF radiation from GSM transceiver base station in South-South Nigeria," *Journal of Advances in Physics*, vol. 13, no. 6, 2017.

[231] O. Florence, "Radio propagation in outdoor suburban environment: Effect on GSM signal strength," *International Journal of Engineering and Science*, vol. 3, no. 2014, pp. 73–79, 2014.

[232] O. Osahon, P. Ushie, and O. Ojo, "Investigation of the main lobe distance of transmitted power density from GSM transceiver base stations in South-South Nigeria," *International Journal of Biophysics*, vol. 7, no. 2, pp. 17–23, 2017.

[233] W. B. Al Smadi, "The environmental radiation pollution in urban buildings," Ph.D. dissertation, The British University in Dubai (BUiD), 2015.

[234] M. Haque and M. Quamruzzaman, "Measurement of magnetic field from electrical appliances in EEE classrooms of Southeast University Bangladesh," *Univ. J. Electr. Electron. Eng*, vol. 4, no. 2, pp. 51–56, 2016.

[235] CORNET Microsystem, "CORNET Microsystem ED88TPlus5G2 (ED88TP5G2) Data Logging/recording function description and user guide," https://safelivingtechnologies.com/content/Products/ED88TPlus5G2%20Data%20Logging-v1.0.pdf, [accessed January 25, 2024].

[236] F. Cawood, "Wits digital mine taking satellite communication underground," 2016.

[237] I. Zaman, A. Förster, A. Mahmood, and F. Cawood, "Finding trapped miners with wireless sensor networks," in *2018 5th International Conference on Information and Communication Technologies for Disaster Management (ICT-DM)*. IEEE, 2018, pp. 1–8.

[238] Espressif Systems, "ESP32 Series Datasheet," https://www.espressif.com/sites/default/files/documentation/esp32_datasheet_en.pdf, [accessed January 25, 2024].

[239] P. van der Walt, "The power density in the radiating near field region of directive antennas," in *2012 IEEE-APS Topical Conference on Antennas and Propagation in Wireless Communications (APWC)*. IEEE, 2012, pp. 1165–1168.

[240] I. Kim and J. Lee, "Theoretical calculation of power densities in the near-field region of phased array antenna," *Microwave and Optical Technology Letters*, vol. 63, no. 1, pp. 367–371, 2021.

[241] D. Qi, F. Zou, J. Zhao, S. Sun, H. Wei, Y. Chen, and Z. Xia, "Power density case study for 5G mmWave array antennas," *Wireless Communications and Mobile Computing*, vol. 2021, pp. 1–14, 2021.

[242] K. Li, S. Kodera, D. Poljak, Y. Diao, K. Sasaki, A. Šušnjara, A. Prokop, K. Taguchi, J. Xi, S. Zhang *et al.*, "Calculated epithelial/absorbed power density for exposure from antennas at 10–90 GHz: Intercomparison study using a planar skin model," *IEEE Access*, vol. 11, pp. 7420–7435, 2023.

[243] L. Scialacqua, F. Mioc, A. Scannavini, and L. Foged, "Simulated and measured power density using equivalent currents for 5G applications," in *2020 IEEE International Symposium on Antennas and Propagation and North American Radio Science Meeting*. IEEE, 2020, pp. 1827–1828.

[244] F. Mioc, L. Scialacqua, A. Scannavini, S. Anwar, and L. Foged, "Power density evaluation of simulated and measured data based on equivalent currents method," in *2021 15th European Conference on Antennas and Propagation (EuCAP)*. IEEE, 2021, pp. 1–4.